Astrophysical Frontiers: The Indirect Detection of Dark Matter & the Analysis of Gamma-ray Binary Systems

Dissertation

der Mathematisch-Naturwissenschaftlichen Fakultät

der Eberhard Karls Universität Tübingen

zur Erlangung des Grades eines

Doktors der Naturwissenschaften

(Dr. rer. nat.)

vorgelegt von

Charles Richard Thorpe-Morgan

aus Huntingdon, United Kingdom

Tübingen

2024

Gedruckt mit Genehmigung der Mathematisch-Naturwissenschaftlichen Fakultät der Eberhard Karls Universität Tübingen.

Tag der mündlichen Qualifikation:	18.10.2024
Dekan:	Prof. Dr. Thilo Stehle
1. Berichterstatter/-in:	Prof. Dott. Andrea Santangelo
2. Berichterstatter/-in:	Prof. Dr. Klaus Werner

Abstract

This thesis is divided into two parts reflecting the two different fields of work presented within. The first half is dedicated to studies relating to indirect dark matter detection, while the second half details work undertaken in the very-high-energy astronomy domain, specifically on the observations of gamma-ray binaries.

The phenomenon of unseen mass in the Universe is as all-pervading as it is mysterious. The plethora of evidence in support of this conclusion spans both the baryonic and non-baryonic sectors, and the fingerprints of this unseen anomaly are detected through both direct and indirect methods making it a fundamental and ubiquitous part of the Universe. This "dark matter" remains one of the greatest challenges to modern cosmological models and to our understanding of the Universe. While many theories regarding its nature exist, it is as yet undetected and the identification of dark matter (composing 85% of the visible Universe) remains a very active field of research. Indirect detection of dark matter is a method that aims to infer the presence and properties of dark matter through the observation of secondary particles (mostly photons) resulting from dark matter interactions. In many dark matter models, secondary particles are produced through dark matter's decay, annihilation, or other interactions with standard model particles. In dark matter-dominated astrophysical objects, these secondary particles would form an excess on top of the known astrophysical populations. This excess can be probed for using modern X-ray and gamma-ray telescopes, allowing for their distinction and association with dark matter. In most cases, the flux of these secondary particles would allow for the inference of dark matter and for the derivation of its properties. A lack of dark matter-associated flux detected by an instrument allows one to place limits on a given dark matter candidate particle's properties. This work, in part, focuses on the field of indirect dark matter detection, specifically on the search for dark matter in astrophysical objects and the capacity of upcoming missions to fulfil this task. As part of this, the results of an annihilating dark matter search with Fermi-LAT in nearby galaxy clusters are presented. Moreover, studies into the potential of the upcoming THESEUS and eXTP missions in the detection of well-motivated decaying dark matter models are detailed.
Gamma-ray Emitting Binary (GREB) systems are a category of high-mass binaries with unique and variable non-thermal emission, even between objects within the class. They are categorised as systems containing a massive young star and a compact object, whose energy spectra peak at above 1 MeV (but typically at $E \gtrsim 100$

MeV). These spectra, however, often extend to extremely high energies ($E \gtrsim 10$ TeV). The physical mechanisms for the production of this emission are not well established, making GREBs exciting and novel objects for study. The second part of this thesis focuses on the study of GREBs and, specifically, on the system of PSR B1259-63. This system is comprised of a pulsar in a highly eccentric 3.4 year orbit around the O9.5Ve star LS 2883 and is known to emit a range of non-thermal radiation from radio to Very-high-energy (VHE) gamma rays. The bulk of this non-thermal emission occurs around the periastron and is thought to be connected to the orientation of the star's decretion disc of gas and dust to the orbital plane of the pulsar. This orientation means the pulsar crosses the disc ~ 16 days before and after the periastron. With the exception of the GeV energy band, in which intra-periastron variability has been observed, the emission from the source across the wavelengths follows a similar form between periastron passages. However, the 2021 periastron saw a plethora of previously unseen and interesting behaviours in the system across different wavelengths. This thesis will detail the work undertaken to analyse and the results of the VHE data taken on the system, by the H.E.S.S. array during the 2021 periastron.

Zusammenfassung

Diese Arbeit ist in zwei Teile gegliedert, welche die beiden unterschiedlichen Arbeitsbereiche widerspiegeln, die darin vorgestellt werden. Die erste Hälfte ist Studien zum indirekten Nachweis dunkler Materie gewidmet während die zweite Hälfte die Arbeit im Bereich der Hochenergieastronomie, insbesondere die Beobachtung von Gammastrahlen-Doppelsternen, beschreibt.

Das Phänomen der unsichtbaren Masse im Universum ist ebenso allgegenwärtig wie mysteriös. Die Fülle der Beweise, die diese Schlussfolgerung stützen, erstreckt sich sowohl über den baryonischen als auch nicht-baryonischen Bereich und die Signaturen dieser unsichtbaren Anomalie werden sowohl durch direkte als auch indirekte Methoden nachgewiesen, was sie zu einem fundamentalen und allgegenwärtigen Teil des Universums macht. Diese ”dunkle Materie” bleibt eine der größten Herausforderungen für moderne kosmologische Modelle und für unser Verständnis des Universums. Obwohl viele Theorien über die Natur dunkler Materie existieren wurde sie noch nicht entdeckt, und die Identifizierung der dunklen Materie (die 85 % des sichtbaren Universums ausmacht) bleibt ein sehr aktives Forschungsgebiet. Der indirekte Nachweis dunkler Materie ist eine Methode, die darauf abzielt, auf die Existenz und die Eigenschaften dunkler Materie durch die Beobachtung von Sekundärteilchen (meist Photonen), die aus Wechselwirkungen mit dunkler Materie resultieren zu schließen. In vielen Modellen dunkler Materie werden Sekundärteilchen durch Zerfall, Annihilation oder andere Wechselwirkungen der dunklen Materie mit Teilchen des Standardmodells erzeugt. In von dunkler Materie dominierten astrophysikalischen Objekten würden diese Sekundärteilchen zu einem Überschuss führen zusätzlich zu den bekannten astrophysikalischen Beiträgen bilden. Dieser Überschuss kann mit modernen Röntgen und Gammastrahlungsteleskopen untersuchen, was die Unterscheidung zu Beiträgen normaler Materie und die Verbindung mit dunkler Materie ermöglicht. In den meisten Fällen würde der Fluss dieser sekundären Teilchen einen Rückschluss auf dunkle Materie und ihre Eigenschaften liefern. Ein Mangel an dunkler Materie-assoziierten Flusses erlaubt es, die Eigenschaften der dunklen Materie Teilchen zu beschränken. Diese Arbeit konzentriert sich zum Teil auf den Bereich der indirekten Detektion dunkler Materie, insbesondere auf die Suche nach dunkler Materie in astrophysikalischen Objekten und die Fähigkeit künftiger Missionen, diese Aufgabe zu erfüllen. In diesem Zusammenhang präsentieren wir die Ergebnisse der Suche nach annihilierender dunkler Materie mit Fermi-LAT in nahen Galaxienhaufen. Darüber hinaus werden Studien über das Potenzial der kommenden Missionen THESEUS und eXTP bei der Entdeckung von zerfallender dunkler Materie ausführlich dargestellt.

GREB Systeme sind eine Kategorie von massereichen Doppelsternen mit einzigartiger und variabler nicht-thermischer Emission, sogar zwischen Objekten innerhalb der Klasse. Sie werden als Systeme kategorisiert, die einen massereichen jungen Stern und ein kompaktes Objekt enthalten und deren Maximum ihrer Energiespektren bei über 1 MeV, aber typischerweise bei $E \gtrsim 100$ MeV liegt. Diese Spektren reichen jedoch oft bis zu extrem hohen Energien von $E \gtrsim 10$ TeV. Die physikalischen Mechanismen für die Erzeugung dieser Emission sind nicht eindeutig geklärt, was GREBs zu spannenden und neuartigen Forschungsobjekten macht. Der zweite Teil dieser Arbeit konzentriert sich auf die Untersuchung solcher GREBs, insbesondere auf das System von PSR B1259-63. Dieses System besteht aus einem Pulsar, der auf einer stark exzentrischen 3.4-jährigen Um Laufbahn den Stern O9,5Ve-Stern LS 2883 befindet. Es ist bekannt, dass er dass der Pulsar nicht thermische Strahlung in einem Bereich, von Radiostrahlung bis hin zur sehr energiereichen (VHE) Gammastrahlung emittiert. Der Großteil dieser nicht-thermischen Emission tritt um das Periastron auf und hängt vermutlich mit der Ausrichtung der Gas- und Staubscheibe des Sterns zur Bahnebene des Pulsars zusammen. Diese Ausrichtung bedeutet, dass der Pulsar die Scheibe 16 Tage vor und nach dem Periastron durchquert. Mit Ausnahme des GeV-Energiebandes, in dem eine Intraperiastron-Variabilität beobachtet wurde, folgt die Emission der Quelle in allen Wellenlängenbereichen einer ähnlichen Form zwischen den Periastron-Durchgängen. Das Periastron 2021 zeigte jedoch eine Fülle von bisher nicht gesehenen und interessanten Verhaltensweisen des Systems in verschiedenen Wellenlängen. In dieser Arbeit werden die Arbeiten zur Analyse der VHE-Daten, die während des Periastrons 2021 mit dem H.E.S.S.-Array aufgenommen wurden und deren Ergebnisse ausführlich vorgestellt.

Acknowledgements

First and foremost I wish to thank Denys Malyshev for his role as my personal supervisor over the course of this PhD. Denys' extensive knowledge of physics and work ethic have inspired me throughout my PhD. His support throughout my time here, along with his patience and willingness to explain (no matter how trivial the question), have been greatly appreciated throughout. I would moreover like to thank Andrea Santangelo for acting as my supervisor during this PhD. His support has always been felt and I am grateful for the myriad opportunities he has afforded me throughout my time in Tübingen. Additionally, I would like to thank my secondary supervisor Josef Jochum, for taking me on board as his supervisee and for his diligence and help with several of the dark matter-related works. Though not formally a supervisor of mine, I wish to also express my gratitude to Gerd Pühlhofer, whose professionalism, attention to detail and knowledge of very-high-energy physics I aspire to one day achieve. Gerd has been beyond diligent in his assistance with the PSR B1259-63/LS 2883 project from start to finish and has gone to great lengths to help me, despite not being a student of his.

In the academic sphere, I have been extremely fortunate to have been afforded a number of opportunities through which I have (mostly) met many interesting people whom I am grateful to have crossed paths with. Although too numerous to name, each of you has made this experience what it has been. I would, however, be remiss to not personally mention Artur, Vadym, Dom, Alex (as well as Lillian and Oliver), Manali, Bastian, Heiko, Atul, Wilhelmina, Marvin, Leon and Moritz, who have each walked the lofty path from mitarbeiter to friend. Marvin and Moritz I would particularly like to thank for welcoming me into their office, and for the sense of fun they bring to work every day. I would like to thank all of you deeply, you've done more for me than you know.

I have been extremely fortunate during my time in Germany to have a number of friends from back home (and further afield) who, despite being separated by geographical and regulatory obstacles, have always managed to lift my spirits. Be it asking me to read their horoscope or diligently reminding me that I hadn't found dark matter yet, each hasn't let the distance get in the way of our friendship, and each has helped me along this journey. In particular, I would like to thank Wayne (whose simultaneous PhD journey has been a constant source of shared suffering

and inspiration), Sam, Christian, Robin, Andy, Ronnie and Sean. All of whom have that most admirable quality of being able to make light of even the toughest of situations. Of all the near-infinite combinations of (x, y, z, t), I consider myself very lucky to to have shared this narrow slice with you all.

The support of my family has been ever present during my PhD and I wish to take the opportunity to thank the wider members of my family for their encouragement and guidance. I'd particularly like to thank my uncle Ricky (and family) and my grandparents Dennis, Dee and Mary. Though some of whom may be gone, their support and example of a life well lived still inspire me. I'd especially like to thank my brother Alexander and my sister Francesca; both of whom I am deeply proud of for what they have, and continue, to achieve.

I have saved the last acknowledgement, by no accident, for my parents. Their unconditional love, support and guidance, not just through this process, but throughout my entire life have never been taken for granted; nor has the sacrifice they have made in raising me. I count myself among the luckiest to have landed with such a committed mother and father. I owe you a debt of gratitude I will never be able to pay. Thank you both.

Finally, I would like to dedicate this thesis to my late friend Ethan Alexander Peters who, as time goes on, I become evermore convinced embodied the very best in all of us.

"We are such stuff as dreams are made on."

Contents

Preface

This thesis is organised in the following manner:

- **Chapter 1** Introduces the phenomenon of dark matter, detailing its history, phenomenology and methods of detection. A special emphasis is placed on dark matter in an astrophysical context and, more specifically, its indirect detection. Several dark matter models are introduced that are particularly pertinent to the contents of this thesis.
- **Chapter 2** Gives an overview of X-ray astronomy and high-energy astronomy, including a brief history of both fields. The process of imaging X-rays is explained, including an introduction to X-ray optics as well as data collection and reduction. This explanation is also extended to high-energy astronomy, where particular emphasis is placed on the *Fermi* satellite and the reduction and analysis of its data. Additionally, this chapter provides an overview of the satellites that are used for dark matter studies later in the thesis.
- **Chapter 3** Details the results of an indirect search for dark matter undertaken with 12 years of data from the *Fermi-LAT* satellite. This search is specifically targeted at detecting signals from the annihilation of dark matter from nearby galaxy clusters. Limits on the velocity-averaged annihilation cross section derived from the non-detection of dark matter by this study are presented.
- **Chapter 4** Describes a recent study into the sensitivity of the proposed Transient High Energy Sky and Early Universe Surveyor (THESEUS) satellite to characteristic signals of decaying dark matter. In particular, this focuses on the capability of THESEUS' instruments to detect signals from the decay of sterile neutrinos, axion-like particles and dark photons. Simulated observations are used to determine the capability of the instruments as proposed at the time of writing. The resulting limits capable of being imposed on the interaction strength of the respective dark matter models are presented in the context of the available parameter space. **Chapter 4** additionally contains details of a study into the capacity of the forthcoming enhanced X-ray Timing and Polarimetry (eXTP) mission to detect the decay of the hypothetical sterile neutrino. This work is centred around simulated observations of nearby dwarf spheroidal galaxies in which a DM search is performed, and limits on the

mixing angle from the non-detection of characteristic sterile neutrino decay signals are derived.

- **Chapter 5** Summarises the topic of cosmic rays and describes the operational principles of imaging atmospheric Cherenkov telescopes due to their relevance to the work presented in **Chapter 7**. Firstly, the historical context of the field is introduced before the physical mechanisms behind cosmic rays, air showers and the formation of Cherenkov radiation are detailed. The aforementioned subjects are then linked to the working principles of imaging atmospheric Cherenkov telescopes. Due to its use as the primary instrument in **Chapter 7**, the observational methods, data acquisition and data analysis of the High Energy Stereoscopic System (H.E.S.S.) are outlined in detail.
- **Chapter 6** Introduces gamma-ray emitting binary systems as an astrophysical object class and details the major sub-categories within the group. Emphasis is placed upon gamma-ray binary systems due to the analysis of the gamma-ray binary PSR B1259-63/LS 2883 in the subsequent chapter. This chapter also introduces the different emission mechanisms and particle acceleration mechanisms present in high-energy/very-high-energy astrophysical systems. Several other gamma-ray binary systems are also introduced to give context to the field of work. Finally, the properties of PSR B1259-63/LS 2883 are detailed, as well as the characteristic non-thermal emission behaviour.
- **Chapter 7** Details a study into the TeV analysis of the 2021 periastron passage of PSR B1259-63/LS 2883 using H.E.S.S. data. This study probed the flux and spectral properties of the system during the 2021 periastron passage, as well as investigating potential correlations between contemporaneous X-ray – TeV data and GeV – TeV data.

Acknowledgement of Collaboration

The paper utilised as part of this thesis in **Chapter 3** has been published in [1]. **Chapter 4** is composed of the work published as [2], with the second paper within the chapter containing work published as [3] (of which C. Thorpe-Morgan is the second author). Finally, **Chapter 7** has been published as a H.E.S.S. Collaboration paper [4], of which C. Thorpe-Morgan is a corresponding author. The use of the pronoun "we" in these works and the wider thesis is meant to refer to all of the authors of the works referenced including myself. For the sake of clarity, however, my individual contributions to the papers are detailed below.

- **Chapter 3** *(Annihilating Dark Matter Search with 12 Years of Fermi-LAT Data in Nearby Galaxy Clusters, April 2021)*[1]: In this work, together with Denys Malyshev, I formulated the choice of targets by investigating the J-factors, galactic coordinates and caveats (nearby bright sources etc.) of each galaxy cluster. I then undertook the full process of the reduction and analysis of the data. I also coordinated with Denys on the choices of dark matter density profiles. I then ran extensive likelihood fitting to search for an annihilation signal from combinations of weakly interacting massive particle annihilation channels and masses, for different galaxy cluster dark matter density profiles. These results were compared to Denys' and a combination was used in the paper. I led the paper writing and revisions with assistance from co-authors.

- **Chapter 4** (*THESEUS insights into axion like particles, dark photon, and sterile neutrino dark matter, December 2020*), **[2]:** For this publication, I collaborated closely with Denys Malyshev, on the choice of observational strategy and the inclusion of systematics. Simultaneously with Denys, I undertook the simulations of blank sky observations with THESEUS' response files and calculated the subsequent sensitivity to the detection of various decaying dark matter models. I led the writing of the paper, with significant contributions from Denys in the introduction and discussion sections.

- **Chapter 4** (*eXTP perspectives for the ν MSM sterile neutrino dark matter model, Jun 2020*), **[3]:** My contributions to this publication were once again in the

discussion of observational strategy and choice of targets. Additionally, I undertook the analysis of the data simultaneously with the lead author Denys Malyshev. This included the simulation of observations of dwarf spheroidal galaxies, the calculation of eXTP's response to these, and the subsequent derivation of detectable limits on the mixing angle. I was heavily involved in writing the paper, and in places wrote drafts, making significant contributions throughout.

- **Chapter 7** (*H.E.S.S. observations of the 2021 periastron passage of PSR B1259-63/LS 2883*; H.E.S.S. Collaboration, Jul 2024) [4]: I performed all data analysis presented within this paper and led its writing. The writing was undertaken with contributions from the other corresponding authors (Gerd Pühlhofer, Denys Malyshev and Iurii Sushch). The task group and wider H.E.S.S. collaboration were instrumental in the review process of the paper. The discussion section of this paper was not written by me but instead by Iurii Sushch, Dmitry Khangulyan and Jonathan Mackey. I collaborated closely with Gerd and Denys in the analysis of the data set. The initial proposal for the observations of the 2021 periastron was led by Gerd Pühlhofer and Denys Malyshev resulting in over 100 hours of observation time on the H.E.S.S. array. As per H.E.S.S. collaboration rules, the analysis results were reproduced using an alternate H.E.S.S. analysis pipeline by Nukri Komin.

Personal Bibliography

This thesis contains several published works presented in the following list. For a breakdown of my individual contributions to these papers see the *preface* to this thesis.

- *Annihilating Dark Matter Search with 12 Years of Fermi-LAT Data in Nearby Galaxy Clusters*; **Charles Thorpe-Morgan**, Denys Malyshev, Christoph-Alexander Stegen, et al.; April 2021.
- *THESEUS insights into axion like particles, dark photon, and sterile neutrino dark matter.*; **Charles Thorpe-Morgan**, Denys Malyshev, Andrea Santangelo, et al.; Phys. Rev. D, 102(12):123003, December 2020.
- *eXTP perspectives for the ν MSM sterile neutrino dark matter model.*; Denys Malyshev, **Charles Thorpe-Morgan**, Andrea Santangelo, et al.; Phys. Rev. D, 101:123009, Jun 2020.
- *H.E.S.S. observations of the 2021 periastron passage of PSR B1259-63/LS 2883*; H.E.S.S. Collaboration (**corresponding author**); A&A, 2024

1 The Indirect Detection of Dark Matter

> *In the beginning the Universe was created.*
> *This has made a lot of people very angry and has been widely regarded as a bad move.*
>
> **— Douglas Adams**
> (The Hitchhiker's Guide to the Galaxy)

Our understanding of the Universe in the current age is defined more by its unknowns than by what is known. Seemingly small discrepancies in observations have revealed gargantuan holes in the patchwork of theories, old and new, that make up our physical understanding of the workings of the cosmos. Nowhere is this more true than in the case of Dark Matter (DM), where discrepancies in the rotation curves of galaxies have led the field cascading down to the conclusion that 85% [5] of the mass density in the Universe we cannot see and fundamentally do not understand. There is now an almost overwhelming amount of evidence for the existence of an all-pervading unseen mass, evidence present not only locally, but in all directions of the observable Universe. This evidence (as we understand it) largely points towards DM being a new fundamental particle. Staggeringly though, 90 years after its first postulation, we know nothing of its properties and are yet to observe anything more than its implied presence. Namely, assuming a particle nature of DM, its mass, self-interaction properties and the presence of interactions with the Standard Model (SM) beyond gravity continue to evade searches and are only bound by limits from non-detection. Moreover, given that the SM has long been known not to host a viable DM candidate particle any discovery would be, by its nature, beyond our current understanding of particle physics. The answer to these questions, and unveiling the existence of novel and fundamentally challenging physics, would therefore surely have groundbreaking implications on the field of physics as a whole and our understanding of the Universe.

1.1 Evidence For Dark Matter

The popularity and propagation of the DM hypothesis can be largely accredited to the scale and scope at which its effects can be seen. The overwhelming majority of evidence for DM is cosmological and astronomical, but it is the mass range over which these pieces of evidence are present, along with how well the hypothesis fits into the understanding of some of our most concrete theories, that really allow such an inherently contradictory hypothesis to merit the level of research present in the field today.

Gravitationally unseen mass can be inferred from the scale of mere galaxies, right up to galaxy clusters (which represent the largest virialsed objects within our Universe). Indeed, the presence of DM can even be seen within the Cosmic Microwave Background (CMB) itself, showing that this evidence also spans the non-baryonic sector. In fact, this mass range is merely defined by our sensitivity to gravitational effects and it is likely that the lower end of the mass scale of phenomena will only decrease with time.

The history of "dark matter" as a whole is extensive and multi-faceted and has seen the term bend and morph over the years into the modern definition, with all its appropriate connotations. However, its conception is (arguably) found somewhat humbly, in the appendices of a series of lectures given by Lord Kelvin entitled "Baltimore lectures on molecular dynamics and the wave theory of light" [6]. During these Kelvin, while postulating on velocity dispersion within the galaxy, proposed for the first time that there may exist a great number of "dark bodies". With these, Lord Kelvin was referring to stars which would in his own words be "extinct and dark" but would nonetheless exert a gravitational influence upon the galaxy. A definition eerily prodigious when compared to modern Massive Compact Halo Object theories.

Similarly, Jacobus Kapteyn took this concept further, using stellar velocities to place rough upper limits on the local amount of non-luminous matter [7]. Kapetyn's supervisee, and renowned radio astronomy pioneer, Jan Oort further advanced the field by continuing his supervisor's work. He published the results of a study on stellar motion in the solar neighbourhood [8]; improving upon Kapteyn's estimates.

Widely cited as taking the field from infancy to adolescence, was the work of Swiss astronomer Fritz Zwicky on observations of the Coma cluster. Zwicky, while performing redshift measurements of nearby galaxy clusters, noted large discrepancies between the individual galaxies comprising the Coma cluster (with velocity differences of up to 2000 kms^{-1})[9]. Interestingly, this scatter in the velocity dispersion

of the galaxies within the Coma cluster had been noted by Hubble and Humason in their original paper [10]. However, Zwicky was the first to apply the virial theorem to these results in order to estimate the mass of the cluster. By comparing the velocities of outlying galaxies in the cluster to the virial theorem, Zwicky was able to obtain an estimate of the mass. Famously, this result disagreed with the mass estimates based on the luminosity of the cluster's constituent parts, with Zwicky calculating a mass-to-light ratio of 500. Thus, the first observational evidence for dark matter was discovered. As an aside, the discrepancy between the observed and calculated mass at the time was greatly inflated by Zwicky's use of a now obsolete value of the Hubble constant [11]. Correcting for the modern Hubble constant value, a mass-to-light ratio of ~ 60 is obtained. However, this does not detract from the correct conclusion Zwicky drew that, in his own words, "If this would be confirmed, we would get the surprising result that dark matter is present in much greater amount than luminous matter" [9].

In the 1970's Vera Rubin and Kent Ford compounded the evidence for dark matter, but (critically) reduced its scale from that of galaxy clusters to singular galaxies. Rubin made detailed measurements of the rotational velocities of nearby spiral galaxies and, in particular, measured the velocity distribution as a function of galactic radii. Contrary to the standard Keplerian prediction, where galactic rotational velocities would decrease with increasing radius, Rubin and Ford found that the velocity remained almost constant as a function of radius [12]. Such a result can be explained by a large amount of non-luminous matter in the outer regions of the galaxy, where in fact Rubin et al. showed that the galaxy must contain around six times the amount of non-luminous matter as luminous matter. An example of a rotation curve demonstrating this trend is shown in Fig. 1.1. Similar studies repeated and expanded these results [13, 14, 15], cementing dark matter as both a measurable and major problem with our understanding of physics and astronomy.

In the years subsequent to the discovery of observational evidence for dark matter, the number of pieces of evidence and their variety has grown immensely. Yet, we still only infer its presence through gravitational effects, a fact that has led to the development of Modified Newtonian Dynamics (MOND) theories that call into question our current understanding of gravity as an alternative explanation to particle theories of DM. These theories attempt to explain dark matter through modifications or additions to the current gravitational paradigm [17]. Nonetheless, the presence of DM is near omnipresent in our observations of the Universe and this overwhelming evidence leaves little doubt today of the existence of dark matter in some form.

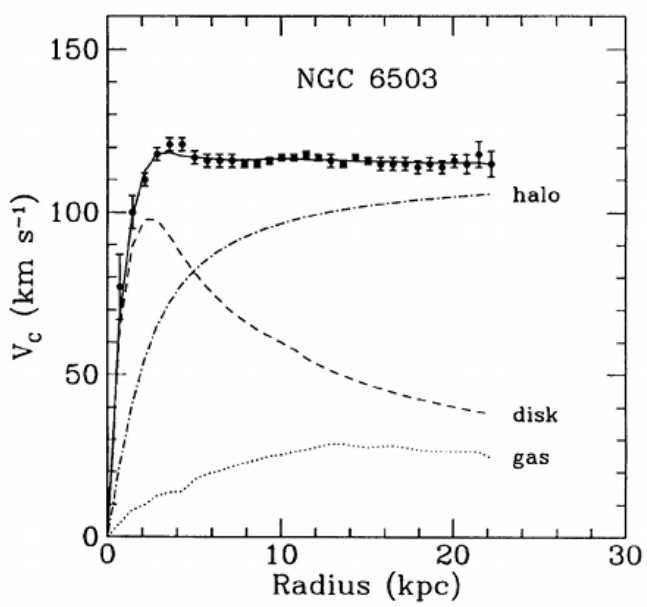

Fig. 1.1: The rotational velocity curve of the spiral galaxy NGC 6503, as a function of radial distance from the galaxy's centre. Observational data on the rotation are indicated by the black dots, while dashed lines represent the contributions to the rotational curve from galactic gas, stellar disc, and dark matter halo components. Figure taken from [16]

Further evidence for dark matter comes from gravitational lensing - the apparent bending of light around massive objects, as described by Einstein's theory of general relativity [18]. This effect is commonly witnessed astrophysically, whereby a background object's light (e.g. a galaxy) is lensed and distorted by the gravitational field of a massive object in the foreground. As laid out in general relativity, the angle by which a photon's path is bent is proportional to the mass of the foreground object, thereby making gravitational lensing an indirect method of mass measurement. Thus, by measuring the deflection angle of background sources, the mass of an intervening source can be measured. This method is typically utilised with galaxies and galaxy clusters, where the derived gravitational lensing mass of these objects can be compared to the observed luminosity, consistently producing high mass-to-light ratios [19].

The contemporary analysis of the Bullet Cluster (1E 0657-56), as well as similar analyses on MACS J0025.4-1222 [20] and other objects, provides monumental evidence in favour of dark matter [21, 22, 23]. This object (shown in Fig. 1.2) is actually comprised of two galaxy clusters undergoing a collision. Critically, this allows for the measurement of the behaviour of the cluster's constituent parts during this unique circumstance. In this collision, the majority of the baryonic matter of the two clusters is represented by hot gas emitting in the X-ray regime. Upon their

collision, the hot gas elements of both clusters were significantly impeded with respect to the constituent galaxies and putative dark matter components, due to their stronger electromagnetic interactions and abundance. On the other hand, since DM is characterised by a lack of interaction, the DM elements are not nearly as affected by the collision and were able to continue on their prior trajectory unimpeded. The result of this is that weak gravitational lensing surveys clearly show the concentrations of masses to be separate from the concentrations of baryonic matter, implying the majority of mass has passed uninhibited through the collision. Moreover, estimates of the luminous matter within the areas of mass concentration come up short of providing enough mass to account for the observed gravitational effects. The separation of the baryonic components and the concentrations of mass of the clusters provide very strong evidence for particle dark matter models and vice versa strong constraints against MOND theories.

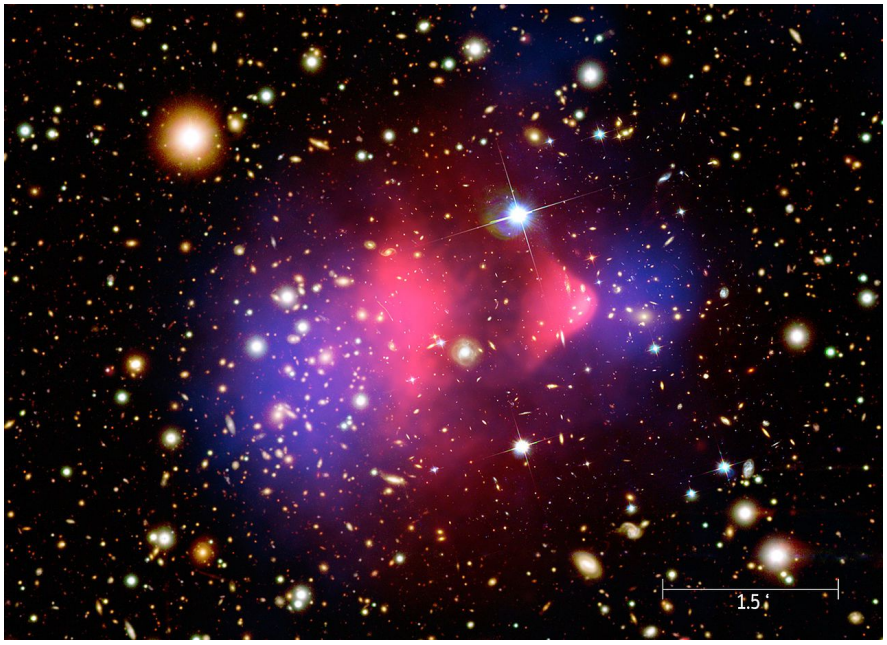

Fig. 1.2: Composite (Optical, infrared and X-rays, taken by the Hubble Space Telescope, the Magellan Telescope and the Chandra X-ray Observatory respectively) image of the Bullet cluster (1E 0657-56), the remnant collision of two galaxy clusters. Optical and infrared data are displayed in orange and white, X-ray data is shown in pink and the mass distribution (as inferred from weak gravitational lensing measurements of the cluster) is displayed in blue. Image credits X-ray: NASA/CXC/CfA/M.Markevitch et al.; Optical: NASA/STScI; Magellan/U.Arizona/D.Clowe et al.; Lensing Map: NASA/STScI; ESO WFI; Magellan/U.Arizona/D.Clowe et al.

Although all evidence for dark matter presented so far has been baryonic in nature, the CMB uniquely provides compelling evidence both on a cosmological scale and of a non-baryonic nature. Studies of anisotropies in the CMB, along with structure

formation in the early Universe, allow the derivation of robust constraints and abundances of dark matter in the present day.

The CMB itself is the remnant of photon radiation produced following the Big Bang. The recombination of electrons and protons into neutral hydrogen at around 380,000 years ($z \sim 1000$) [24] caused photons to decouple from the Universe, where they formed a high-energy photon bath. These photons formed the precursor of today's CMB, where the subsequent expansion of the Universe cooled them to the average temperature of the CMB we measure today: 2.73 K. First discovered by Penzias and Wilson in 1964[1] [25], we observe the CMB today as a sea of omnidirectional microwave photons. Although the CMB is a near-perfect black body, a fundamental and fascinating feature found by more sensitive contemporary surveys is its small-scale temperature fluctuations. These temperature anisotropies (at around the scale of 10^{-5} K [5]) represent the fingerprints of the conditions in the early Universe, mapping the density perturbations of matter at around the time of the Big Bang. These temperature anisotropies are mapped in Fig. 1.3. By using a multipole analysis

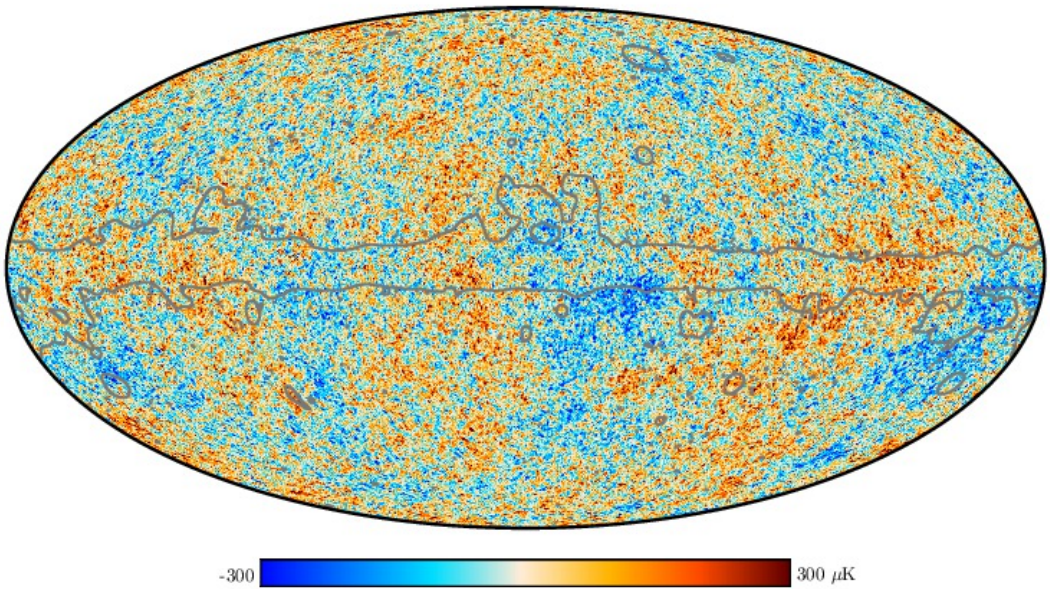

Fig. 1.3: Temperature fluctuations in the Cosmic Microwave Background as imaged by the Planck satellite. The image is coloured to indicate temperature fluctuations from the average, with blue representing negative fluctuations and red representing positive. Grey lines indicate regions that have been masked due to significant foreground emission. Dipoles created by orbital and solar effects have also been subtracted from the image. Image taken from [5]

(a Fourier analysis in two dimensions), the intensities of these fluctuations can be decomposed in terms of their angular dependence. Since these fluctuations are

[1] Somewhat by accident.

directly determined by the conditions of the early Universe, they represent a cosmic "fossil record" of the conditions under which the perturbations formed. These therefore correspond, in part, to the baryonic and dark matter densities at the surface of last scattering [26]. The result of this is that the power spectrum of the CMB provides a direct measurement of the density of dark matter in the early Universe[2] (see Fig. 1.4).

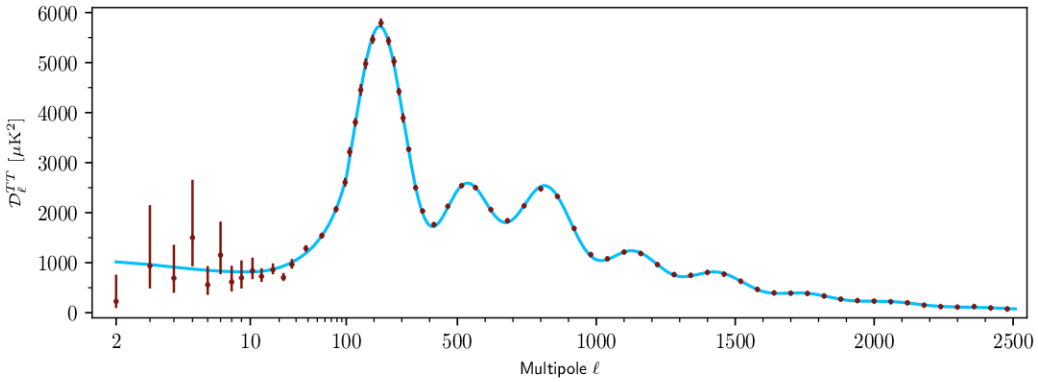

Fig. 1.4: Angular power spectrum of the CMB temperature, as imaged by the Planck satellite. The spectrum is both frequency-averaged and foreground-subtracted, where red points represent data and blue represents the best-fitting Planck model. Figure taken from [5].

The current cosmological paradigm is known as Λ Cold Dark Matter (ΛCDM) (with Λ being representative of dark energy and CDM as Cold Dark Matter (CDM)). This theory is extremely widespread and provides the current most successful and accurate metric by which cosmology can be understood. The proliferation of this theory is largely due to how accurately the CMB power spectrum can be reproduced from it. This model is a spatially flat 6-parameter model [28], where the energy present in the Universe is described as being of the form of 5% baryonic matter, ~ 26.5 % dark matter and ~ 68.5 % dark energy at the present day [5]. Moreover, the CDM element of the model implies a hierarchical structure formation whereby the formation of early structures in the Universe occurred in a bottom-up manner, driven by dark matter [29, 30]. Since baryonic matter is influenced by the radiation present in the early Universe, the density perturbations caused by baryonic matter alone would not have been sufficient to cause the observed structure formation. In fact, these perturbations would have been washed out by interactions with radiation without the gravitational driving force of dark matter, which does not suffer the problem of interacting with photons. This model and its physical implications lead to the extraordinarily good fit seen in the baryonic acoustic oscillations. It is additionally strongly supported by the results of N-body simulations such as the 2005

[2] See [26, 27] for further explanations and the history of CMB cosmology respectively.

Millennium simulations [31] or the ongoing EAGLE[3] [33] and Illustris TNG [34, 35] hydrodynamical N-body simulations. ΛCDM is, however, not without conjecture. The most recent, and perhaps challenging, case is the so-called Hubble tension (see [36] for a review of the subject), where differing measures of the Hubble parameter seemingly report different values.

1.2 Dark Matter Candidates and Models

The Standard Model is the best description of the known constituents of the Universe, and the forces that govern them, to date. Under one model, it comprises all known particles and three of the four fundamental forces that are known to govern them. Yet, despite its myriad successes, contemporary findings have placed increasing strain on the model. For example, the well-observed and understood phenomenon of neutrino oscillations implies that neutrinos are massive, a fact difficult and inelegant to reconcile within the framework. Moreover, the base model has no proposed explanation for gravity. One of the more intricate but compelling challenges to the SM though, is the hierarchy problem.

The hierarchy problem is in essence, the disparity between the energy regimes in which the weak force and gravity operate and why the former is so much stronger than the latter. Particles receive mass through their interaction with the Higgs field. The quantised excitement of the Higgs field, the Higgs boson (with a mass of ~ 125 GeV), mediates this interaction and the mass of the Higgs boson also determines the strength of the weak interaction. However, notably this mass is far smaller than the scale at which gravitational effects become significant ($\sim 10^{19}$ GeV, the Planck scale). The quantum corrections from virtual particles to the Higgs' mass[4] are of the order of this Planck scale, which by naive assumption would drive the Higgs mass to higher energies and subsequently weaken the strength of the weak force. The discrepancy arises in the fact we don't see the Higgs mass at this scale, and therefore lack an explanation as to why it should be at this level, which resultantly fine-tunes the weak force to be much larger than gravity. See [37] for an extensive breakdown of the topic. This problem strongly motivates the idea of physics beyond the standard model as an explanation for why the Higgs mass should appear to be so unnaturally fixed. Perhaps the most famous, and thought to be the strongest

[3] See [32] for an introduction to the project.

[4] Formally the quantum corrections are not applied to the mass itself but to the mass-squared parameter. This correction alters the potential of the Higgs field and thus its non-zero value. Thus the hierarchy problem arises from the discrepancy between the weak force's value and the non-zero Higgs field value. The term mass has however been used interchangeably here.

contender to solve this problem, is Supersymmetry which shared strong links to candidates for dark matter.

Ultimately, the greatest shortcoming of the SM is perhaps its inability to explain the extremely successful and well-justified ΛCDM model of cosmology. The standard model lacks any explanation for the observed effects of dark energy, for matter anti-matter asymmetry and of course for the observations of cold dark matter in both the modern Universe and the CMB. The contention between our understandings of the large and the smaller scales is perhaps the crux of the dark matter problem.

The observational evidence presented in 1.1 provides near unassailable proof of an unseen or unaccounted-for mass in the Universe. From these observations, we can furthermore infer key properties of dark matter. Dark matter must be

- Cosmologically stable - it must have a lifetime longer than the age of the Universe to explain its presence
- Gravitationally interacting - to explain the observed gravitational effects
- Vanishing interaction with SM particles - to explain the observed lack of interaction
- Cold (low kinetic energy compared to rest mass) - to explain observed structure formation
- Dark ($|Q| \ll 1$) - to explain the vanishing electromagnetic interaction

Additionally, while not a strict criterion, there is a strong chance that the problem of DM is linked to one of the myriad additional problems in the standard model. An ideal DM candidate would, therefore, have good motivation and solve an additional problem, though this is an idealised case. In the absence of any SM particle that fulfils these criteria many extensions, models, and theories have been proposed. Dark matter is defined by its currently undetectably small (and potentially non-existent) interaction with the SM. As such the only measurable quantity that has been derived from it is its relic abundance as inferred from gravitational measurements and probes of DM. The latest measurements of the relic abundance from [28], put this value at:

$$\Omega_{\mathrm{CDM}}\, h^2 = 0.1200 \pm 0.0011 \tag{1.1}$$

Where h is the reduced Hubble constant, and this value is given at 68% confidence interval (c.i.).

This elusive nature of dark matter, and its one measurable quantity, mean that the available parameter space for DM candidates is extremely large. This results in proposed models and particles ranging from masses of 10^{-15} eV, right up to DM candidates of several solar masses[5]. Though a plethora of candidates and theories spanning the available parameter space exist, in what follows, four of the most well-motivated, commonly cited, and most pertinent DM candidates to this thesis are introduced.

Thermal Freeze-Out Mechanisms

The presence of DM in measurements of the CMB confirms its presence in the early Universe and shows that its production must have occurred at times earlier than the decoupling of radiation ($z = 1100$, [39]). For particle dark matter the question then remains as to how such a large particle population was both produced and then survived to give rise to the relic density seen today.

A common explanation employed in many well-motivated DM theories explains this through a freeze-out mechanism. Freeze-out begins with the production of dark matter[6] in the early Universe. In this scenario, it is generally assumed that DM takes a form in which it self-annihilates, however, the process is applicable to a whole host of models encompassing both decaying and annihilating DM. DM particles are assumed to be produced alongside other particles in the early stages of the Universe (characterised by extremely high energies and densities). At this stage DM particles are assumed to be in thermal equilibrium with the primordial plasma and have not yet decoupled, interacting with the plasma through weak scale interactions [26]. At this point, the thermal bath of the early Universe produces DM particles, and these simultaneously self-annihilate back into energy, maintaining an equilibrium.

However, the expansion of the Universe causes a decrease in the temperature of the primordial plasma, reducing its energy density. As the temperature is driven lower, and the Universe larger, less energy is available to produce DM after its annihilation and the weak interactions that maintained equilibrium become less frequent. Moreover, the expansion of the Universe greatly reduces the probability of two particles annihilating, reducing the annihilation rate of DM. Eventually, the temperature reaches $T \sim m_{\mathrm{DM}}$ and dark matter particles decouple from the thermal

[5] Candidate particles that are produced thermally in the early Universe are however bound to be below $\mathcal{O}100$ TeV to preserve unitarity [38]. The value here refers to primordial black hole or Massive Compact Halo Object (MACHO) theories.

[6] Freeze-out mechanisms, while a common explanation for the production of dark matter, are not exclusive to dark matter and are more a general framework of particle production. In this context though it has been used as applied to the thermal production of dark matter in the early Universe.

bath of the early Universe entirely. The result of this is that the number density of DM particles is "frozen-out" at the value it held during the moment of decoupling [40]. This moment of freeze-out is defined by the moment in which the annihilation rate of DM becomes lesser than the expansion of the Universe:

$$\langle \sigma v \rangle \, n_{0,\mathrm{DM}} \approx H \tag{1.2}$$

where $\langle \sigma v \rangle$ (cm^3 s^{-1}) is the annihilation cross section of DM, $n_{0,\mathrm{DM}}$ (m^{-3}) the equilibrium number density and H ((km s^{-1})Mpc^{-1}) the Hubble parameter. This also implies that the mass of a DM particle defines the moment at which freeze-out occurs, with heavier particles decoupling earlier. Furthermore, Eq. 1.2 shows that the relic density is controlled by the strength of the annihilation cross section, with larger values of $\langle \sigma v \rangle$ leading to a higher relic density of DM [41]. Both of these effects are demonstrated in Fig. 1.5.

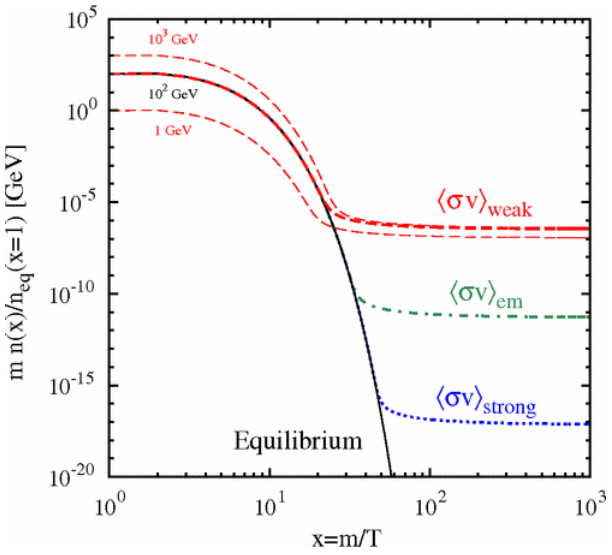

Fig. 1.5: The evolution of the number density of dark matter approaching, and after, the moment of freeze-out. The x-axis is given in terms of the mass-to-temperature ratio (a proxy for the quantity of time in the early Universe's expansion). Different line colours indicate the number density evolution of a $m_{\mathrm{DM}} = 100$ GeV DM particle, given different typical annihilation cross section scales: weak force scale(red), electromagnetic force scale (green) and strong force scale (blue). The number density evolution is shown for weak scale annihilations at differing DM masses. Figure taken from [42].

This freeze-out then leaves an entire population of DM present in the Universe but decoupled from the thermal bath, and with an annihilation rate so low that it is unable to annihilate in meaningful numbers. Thus, the dark matter population is

essentially fixed at the number density value present during freeze-out and has an evolution defined by the Boltzmann equation [26].

$$\frac{\mathrm{d}n_{\mathrm{DM}}}{\mathrm{d}t} + 3H\, n_{\mathrm{DM}} = -\langle\sigma v\rangle(n_{\mathrm{DM}}^2 - (n_{0,\mathrm{DM}})^2) \tag{1.3}$$

where H, $n_{0,\mathrm{DM}}$ and $\langle\sigma v\rangle$ have the same definitions as previously, and n_{DM} (m^{-3}) is the number density of DM at time t (s).

Freeze-out mechanisms are an effective explanation for the production of dark matter, given how definitively as well as naturally it explains the production of some of the more physically motivated dark matter candidates. However, an array of similar and complementary theories exist to explain the production of DM. The freeze-in mechanism, for example, posits the freeze-out of a particle-progenitor to dark matter which subsequently decayed to DM in the Universe today [43]. See [44] for an extensive review of dark matter production mechanisms.

1.2.1 Weakly Interacting Massive Particles

The Weakly Interacting Massive Particle (WIMP) paradigm is an overarching framework of hypothetical particles. These particles share the same basic properties and are strong contenders for DM. WIMPs interact with the Standard Model through gravitational interactions, the weak nuclear force and/or an undiscovered fifth force. WIMP candidates are most commonly thermally produced in the early Universe via a freeze-out mechanism, and constitute a CDM [11, 45] (See [46, 47]).

WIMPs are a popular DM candidate, in part, due to their compatibility with the Supersymmetric extension to the Standard Model (SUSY). In fact, SUSY suggests the existence of several particles that would make for strong DM candidates as a natural by-product of the theory's addition to the SM [48]. This, combined with the popularity of SUSY as an elegant solution to many of the SM's challenges (the previously discussed hierarchy problem for example), give WIMPs a strong theoretical backing as a DM candidate.

Perhaps the most compelling piece of evidence for WIMPs is the so-called "WIMP miracle". Particles operating under a freeze-out mechanism (as is a defining feature of WIMP candidates) have an observed relic abundance today resulting from the point when the expansion of the Universe became larger than their thermally-averaged self-annihilation cross section [44]. By measuring the relic abundance in the contemporary Universe one may therefore estimate the velocity averaged

annihilation cross section required for a WIMP-like particle to be responsible for DM. By undertaking this calculation, it was found that the observed relic abundance is naturally produced by a velocity-averaged annihilation cross section of

$$\langle \sigma v \rangle = 3 \times 10^{-26} \text{ cm}^3 \text{ s}^{-1} \tag{1.4}$$

For particles with a mass of several GeV [49, 50]. The correspondence of this value to the electro-weak scale (combined with proposed SUSY particles of GeV scale masses), earned this coincidence the pseudonym "the WIMP miracle" [48]. See [44, 51] for reviews.

Assuming an interaction strength of the weak scale, the abundance of DM observed today can only be reproduced by the mass range (m_{DM}, eV) [52]:

$$2 \text{ GeV} \lesssim m_{\text{DM}} \lesssim 100 \text{ TeV} \tag{1.5}$$

The WIMP's mass is strongly bound by the Lee-Weinberg limit, imposing that the mass must be above ~ 2 GeV. Particles with a mass less than 2 GeV would have a decreased thermally-averaged self-annihilation cross section causing freeze-out to occur at earlier times (see Sec. 1.2). This would cause a lower overall abundance than the observed value today, placing hard limits on the lower mass bound [49]. The upper mass limit is derived from unitarity bounds (see [53] for a review). A point like WIMP undergoing s-wave annihilation will be bounded by unitarity as:

$$\langle \sigma v \rangle \lesssim \frac{4\pi}{m_{\text{DM}}^2} \tag{1.6}$$

Comparing this bound once again to the relic density of dark matter, one finds that an upper bound of $m_{\text{DM}} \lesssim 100$ TeV. Values greater than 100 TeV have an insufficiently small annihilation cross section to deplete dark matter to relic abundance values [52].

R-parity conserving SUSY models predict WIMPs as a natural by-product of their extensions to the SM (see [54] for an introduction to SUSY theories). Additionally, little Higgs theories [55] and theories of universal extra dimensions [56] all similarly contain WIMP candidates. For SUSY the most likely candidate is the Lightest Supersymmetric Particle (LSP), which constitutes the lightest additional particle in supersymmetric models. As a result of their R-parity conservation, LSPs are unable to decay into SM particles, making them stable on cosmological timescales and good dark matter candidates.

Given the necessity for DM candidates to be electrically neutral, the strongest contenders for the LSP DM candidate are the neutralino and the gravitino. The neutralino is the favoured candidate for the WIMP and is an admixture of the bino[7] and a smaller amount of the wino[8] (as well as potentially the neutral Higgsino). See [57, 58, 59] for a review of SUSY DM.

The majority of WIMP candidates undergo self-annihilation of the form

$$\chi + \chi \rightarrow N_{\mathrm{SM}} + N_{\mathrm{SM}} \tag{1.7}$$

where χ is the WIMP and N_{SM} represents an undefined standard model particle. The final states of this annihilation can be many-fold and are model-dependent. They are defined by the available energetics and the differential particle spectrum. WIMP annihilation is one of the primary targets of indirect DM searches, with the host of secondary particles cascading from the initial final state forming an irreducible excess of detectable SM particles.

1.2.2 Sterile Neutrinos

The sterile neutrino is a compelling and commonly cited DM candidate, due to the strong physical motivation for its existence and its testability. Though a host of theories spanning differing mass ranges exist, sterile neutrinos are most commonly considered to be in the mass range of < 1 eV - $\mathcal{O}$ keV [60] (though can reach up to $\sim 10^{15}$ GeV [61]).

Neutrinos, in general, are the umbrella term for 3 types of electrically neutral fermions found within the SM. The three flavours of neutrino (ν_e, ν_μ, ν_τ) interestingly all have an inherent left-handed chirality [62], and are the only fermions without (known) right-handed chiral partners.

Although predicted to be massless in the SM, the experimental discovery of neutrino oscillations[9] (the admixing of neutrino flavour and mass states [63]) showed that neutrinos must be inherently massive [64], proving yet another flaw in the theoretical framework of particle physics. The generation of this mass is postulated to be achieved through one of two mechanisms: the Dirac mechanism (if the neutrino is a Dirac fermion) or the see-saw mechanism (if the neutrino is a Majorana fermion). The Dirac mechanism employs a similar physical method to the manner in which

[7] The superpartner of the hypercharge gauge boson field B.
[8] The superpartner of the weak isospin gauge boson field W^0.
[9] Winning the 2015 Nobel prize in physics.

other SM fermions acquire mass, however, it assumes the neutrino to be a Dirac fermion and contains left and right-handed chirality components. Namely, it proposes the existence of a Yukawa interaction between left-handed neutrinos and the Higgs field which, through the vacuum expectation value (VEV) of the Higgs field, generates a neutrino mass term [65]. Alternatively, the see-saw mechanism explains the mass of neutrinos through the introduction of a heavy right-handed neutrino. The Lagrangian of the neutrino mass term is then a convolution of the left and right-handed neutrinos, where the mass of each neutrino is inversely proportional to its chiral partner [65]. This right-handed chiral partner in the see-saw mechanism is often referred to as the sterile neutrino.

The extremely light mass of the neutrino lends to a large free-streaming length in the early Universe. This is in contradiction with the scale of density fluctuations seen in the early Universe and rules out the SM neutrino as a possible DM candidate [66]. However, under the see-saw mechanism, the extremely light mass of the neutrino implies a heavy sterile neutrino, which in turn could undergo free-streaming lengths on compatible scales with CMB fluctuations. A more massive sterile neutrino could also easily be produced via a freeze-out mechanism in the early Universe. This, combined with the potential for the particle to provide right-handed chiral partners to the SM neutrinos (thus improving the naturalness of the SM), make the sterile neutrino a well-motivated candidate for DM.

The Sterile neutrino (ν) Minimal extension to the Standard Model (νMSM) is an extension to the standard model that posits the existence of sterile neutrinos to explain neutrino mass and its generation through the see-saw mechanism [67]. Specifically, this introduces 3 new sterile neutrinos (1 counterpart for each active neutrino) which only interact via gravity and through weak mixing with standard model neutrinos [68]. In order for sterile neutrino masses to be compatible with observed large-scale structure formation, the mass range would have to lie in the $\sim$keV range [61]. In most dark matter theories this is achieved with a single lighter sterile neutrino in the mass range $\sim$ keV and two heavier sterile neutrinos with masses $\gg$ MeV [61]. The lighter sterile neutrino would therefore be a viable and prime dark matter candidate through its freeze-out production in the early Universe. Sterile neutrinos, however, have relativistic primordial velocity dispersions due to their lighter mass, this means that they are considered warm dark matter candidates rather than cold.

Sterile Neutrino Decay

The mixing interaction between sterile and active neutrinos can lead to the decay of the former, most commonly via a process that would produce 3 active neutrinos [69]. This process has a decay width given by:

$$\Gamma_{\nu_0 \to \nu_a \nu_a \bar{\nu_a}} = \frac{\alpha G_{\mathrm{F}}^2}{96\pi^3} \sin^2(2\theta) m_{\nu_0}^5 \approx 1.76 \times 10^{-20} \sin^2(2\theta) \left(\frac{m_{\nu_0}}{1\mathrm{keV}}\right)^5 \mathrm{sec}^{-1}, \quad (1.8)$$

Where G_{F} is the Fermi constant (GeV^{-2}), α the fine structure constant and m_{ν_0} (keV) is the mass of the sterile neutrino. θ (°) represents the mixing angle between the sterile and active neutrinos. θ is effectively a measure of the strength of the interaction of sterile neutrinos with the SM, as well as their decay rate and expected signal [69].

Sterile neutrino decay can, with a much lower probability, lead to the emission of an active neutrino and a monochromatic photon, through a loop-suppressed process [68].

$$\nu_0 \to \nu_{\mathrm{a}} + \gamma, \quad (1.9)$$

The energy of the photon produced from this decay would be $\frac{m_{\nu_0}}{2}$. Figure 1.6 shows two possible sterile neutrino decays that result in the production of a photon, as in Eq. 1.9. The decay of a sterile neutrino to a photon has the decay width [70]:

$$\Gamma_{\nu_0 \to \nu_a \gamma} = \frac{9\alpha G_{\mathrm{F}}^2}{256\pi^4} \sin^2(2\theta) m_{\nu_0}^5 \approx 1.38 \times 10^{-22} \sin^2(2\theta) \left(\frac{m_{\nu_0}}{1\mathrm{keV}}\right)^5 \mathrm{sec}^{-1}, \quad (1.10)$$

Where all symbols have their previous meanings. The comparison of this decay width to that of the sterile neutrinos' main decay channel to active neutrinos reveals that the radiative decay is suppressed by a factor of ≈ 127.55 [69].

Although this process is highly suppressed, the quantities of sterile neutrinos that would be present should sterile neutrinos constitute astrophysical DM, mean that this decay line would make for a clear and distinct signal. The presence of an unexplained spectral line in astrophysical observations, therefore, would be a "smoking gun" signature of sterile neutrino DM.

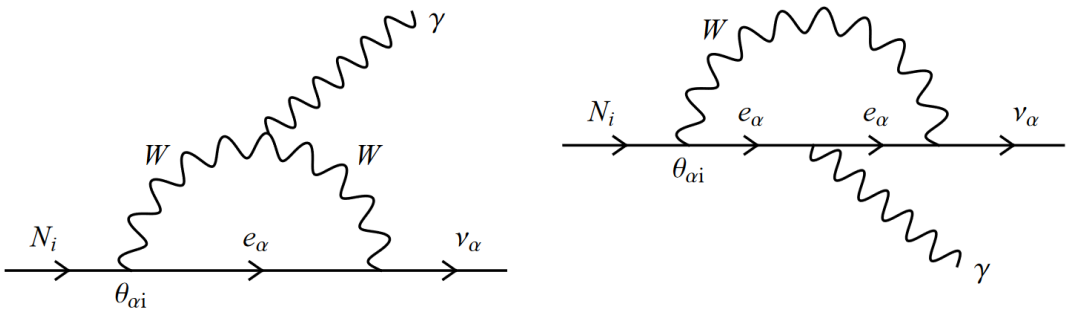

Fig. 1.6: Feynman diagrams of the sterile neutrino's (N_i) radiative decay through coupling to a W boson (*left*) and a charged lepton (e_α, *right*). ν_α represents a neutrino of the same flavour (α) as the charged lepton e_α, and $\theta_{\alpha,\mathrm{i}}$ is the mixing angle; a parameter proportional to the interaction strength of the sterile neutrino with the SM. γ indicates the photon, of energy $\frac{m_{N_\mathrm{i}}}{2}$, produced by the decay. Figure taken from [61].

1.2.3 Axions and Axion-like Particles

Quantum Chromodynamics (QCD) axions and other Axion-like Particles (ALPs) are another strongly theoretically motivated DM candidate. Much like WIMPs, they arise naturally as a result of an extension designed to solve one of the issues of the SM: the strong CP problem. In essence, the strong CP problem arises from the fact that under the current mathematics of QCD, it is possible for Charge-conjugation symmetry (C) and Parity symmetry (P) to be broken under certain conditions during the strong interaction. Experimental searches for this violation, however, have consistently found nothing. This leads to the question of why QCD seems to be fine-tuned in order to prevent CP violation.

Under the proposed Peccei-Quinn (PQ) mechanism (see [71, 72]), the PQ global symmetry spontaneously breaks (either pre or post-inflation in differing theories) resulting in the axion[10] field to "roll down" into an excited state [71, 73]. As shown by both Wilczek [74] and Weinberg [75], this field excitation has the effect of producing the axion particle[11] - formally a pseudo Nambu-Goldstone boson [73]. At this value, the axion field suppresses the QCD term responsible for allowing CP violation, providing a mechanism to explain its lack of observation. The QCD axion has the inherent mass range $10^{-5} < m_\mathrm{a} < 10^{-3}$ eV, as outlined in the PQ mechanism [71, 72, 76], typical ALP models are therefore bound by similar constraints with masses rarely exceeding ~ 1 eV. Because of their extremely low masses, axions are

[10] Here and ongoing, the term axion is used interchangeably with ALPs, since the statements made are interchangeable for either.

[11] The physicist Wilczek coined this new particle the axion after a brand of washing powder, citing that it "cleaned up" the problem.

not expected to be produced at colliders[12] and novel search techniques relying on axion-SM couplings must be exploited.

The axion particle produced from the excitation of this field is a prime candidate for CDM as discovered by three groups [78, 79, 80] simultaneously and independently [73]. It has vanishing interactions with the SM, a non-existent charge, interacts gravitationally and would be universally pervading. The production of axions is closely linked to the PQ mechanism. It is often described as the axion misalignment mechanism[13], describing the misalignment of the axion potential, which occurs when the Universe cools to QCD scales.

Under the PQ mechanism, the axion is naturally produced during the epoch of the PQ phase transition, where the axion potential takes on a new value and the axion materialises initially as a degree of freedom in the potential [79]. Models of axion production are most commonly split into two categories depending on whether this phase transition occurs before or after inflation (the pre and post-inflation scenarios respectively). The point at which the phase transition occurs, broadly speaking, affects the evolution of the axion field and the potential, for a full review of axions in cosmology see [81]. However, the generalised mechanism remains largely similar between models.

Regardless of the timing of the PQ phase transition, the axion field potential ($V(\phi)$) prior to the PQ phase transition is simply a zero value. However, as the temperature of the Universe decreases, the phase transition causes $V(\phi)$ to transform into a characteristic Higgs-like (often called a "Mexican hat") potential [78]. Due to the sudden change in the form of the potential, the axion field takes on a random non-zero phase value ($\theta_{\rm i}$), as it shifts to the newly formed circular area, minimising its $V(\phi)$ value. As the Universe cools further the QCD critical temperature is reached, and QCD effects cause a slight tilting of the potential in the angular direction [80]. What follows is that a preferred value of θ ($\theta_{\rm min}$) is created as the PQ symmetry is spontaneously broken. This $\theta_{\rm min}$ value is, therefore, the nominal value required to conserve CP in the strong interaction, solving the strong CP problem as outlined by [71, 72]. The misalignment between $\theta_{\rm min}$ (the value of θ with the lowest potential) and $\theta_{\rm i}$ (the random value of θ the axion field took on at the PQ phase transition) is both what causes the production of the axion field excitations, and gives the name to the mechanism [80]. The axion field potential then rolls down towards the new potential minimum, subsequently undergoing dampened oscillations around this

[12] Formally, high mass (GeV scale) axion models are possible in the framework and therefore can be searched for at detectors (see [77] for a review), though these models depart strongly from traditional axion models in their phenomenology.

[13] Sometimes this is referred to as the vacuum realignment mechanism in literature.

minimum value [78]. The oscillations of the potential therefore manifest as massive axion particles, behaving as CDM.

In pre-inflation models, the density of DM produced depends explicitly on the initial misalignment angle θ_{i}. Given that the PQ phase transition occurs during an epoch where the Universe is causally connected, this value is assumed for the whole Universe. This value can then be fine-tuned for a very large range of axion masses, in order to achieve the accurate relic density of DM. In pre-inflation scenarios, therefore any Topological Defects (TD) in the θ value of axions do not contribute.

However, the situation is somewhat different in post-inflationary-scenarios where (given the lack of causal connection of the Universe at the moment of PQ phase transition) θ_{i} takes on a range of different and random values between $-\pi$ and π. These values will therefore vary between various causally-disconnected patches across the Universe and smoothly vary between adjacent patches. These patches (after accounting for inflation) would be smaller than cosmological probes of DM therefore an effective average value of θ_{i} can be calculated using $\theta_{\mathrm{i}} = \langle\theta_{\mathrm{i}}^2\rangle^{0.5}$ which, for the possible range of θ_{i}, takes the value $\frac{\pi}{\sqrt{3}}$. However, this itself would form a population of axions with a mass $m_a \sim 26\ \mu\mathrm{eV}$. The situation is somewhat complicated by the formation of topological defects in this model. TDs have the ability to decay and, as such, produce a new population of axions, negating this simplistic estimate of the mass. The production of TDs (as laid out in the Kibble mechanism [82]) occurs in post-inflationary theories at the point that the axion field starts rolling down to the potential minimum. At this point, it is possible that one of the causally disconnected patches of axions is topologically isolated from the minimum value of θ and is contained by a surrounding axion field potential. These patches, trapping the axion field from the universal minimum value, therefore store large amounts of potential energy [82]. This leads to the formation of domain walls between regions, acting as potential barriers between the minima of different domains. These domain walls are, in any case, not static and are subject to the expansion of the Universe leading to them shrinking in size, and colliding with other domains. This process will lead to domains releasing their potential energy, as the θ_{i}, again, rolls down to a new local minimum, causing the production of a new population of axions [82]. The formation of domain walls throughout the patchwork of different axion populations at different potentials in the Universe leads to a cascade of differing axion populations.

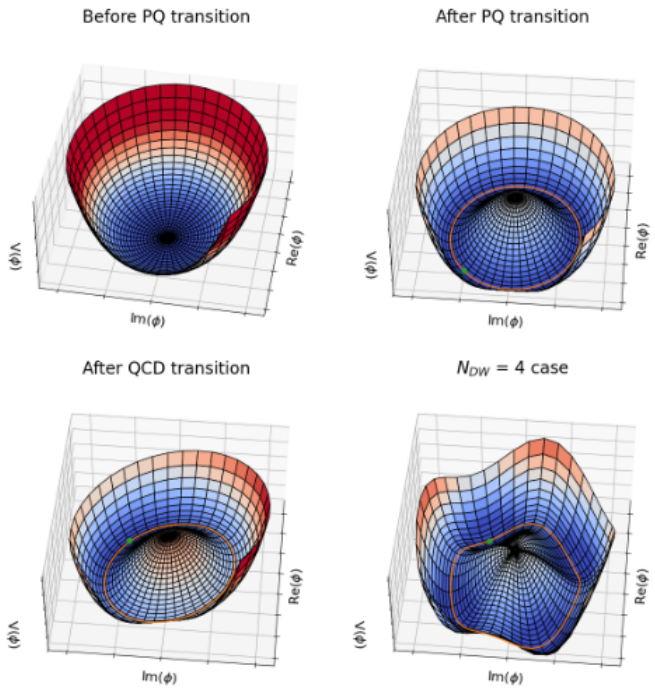

Fig. 1.7: Figure detailing the evolution of the axion field through its critical stages. The upper left panel indicates the form of the potential before PQ-symmetry is spontaneously broken. The potential following this (the PQ phase transition) is shown in the upper right. Here the potential takes the classic "Mexican hat" shape and the value θ of the axion field assumes a new, random, value at the new lowest potential point θi. The bottom left panel represents the effects of QCD interactions on the potential, which occurs when the temperature of the Universe falls below the QCD scale. This causes a tilt in the potential, resulting in a new favoured value of θ for the field. This value of θ is the value required to conserve C and P symmetry, thus solving the strong-CP problem. The final, bottom right, image shows an example of the form of the potential when the PQ phase transition occurs after inflation. This has led to the formation of domains of differing local minima of the potential, separated by domain walls (4 in this case). Figure taken from [73].

Axion-photon coupling

Within the PQ mechanism, there exists a model-independent coupling of photons to axions, resulting from the mixing of the axion field to the gluon field. This coupling is a necessary consequence of the PQ mechanism and exists in all axion models (since they rely on the PQ mechanism). This usually manifests as either the decay of an axion into two photons, or axion-photon oscillation in the presence of a background magnetic field. The coupling of the axion to the photon is expressed with the effective Lagrangian term:

$$\mathcal{L}_{\mathrm{A}\gamma} = -\frac{g_{\mathrm{A}\gamma}}{4}\mathrm{A}F_{\mu\nu}\widetilde{F}^{\mu\nu} = g_{\mathrm{A}\gamma}\mathrm{A}\mathbf{E}\cdot\mathbf{B} \tag{1.11}$$

where A is the QCD axion field, $g_{A\gamma}$ (GeV^{-1}) is the axion-photon coupling and $F_{\mu\nu}\widetilde{F}^{\mu\nu}$ represent the electromagnetic tensor and it's dual respectively. Additionally, **E** and **B** represent the interaction terms of the electric and magnetic fields. Thus, the most important term in this Lagrangian, with respect to the detection of axions as DM through their coupling to photons, is the coupling strength $g_{\mathrm{a}\gamma}$[14]. This term determines the production rate of photons from axions in the presence of strong magnetic fields, as well as the decay rate of axions as:

$$a \rightarrow \gamma + \gamma \tag{1.12}$$

Leading to the production of two photons at $E_\gamma = \frac{m_\mathrm{a}}{2}$, see the lower panel of Fig. 1.8. This decay is naturally advantageous for the detection of axions, providing a distinct and monochromatic decay line with no astrophysical origin in DM dominated objects. As such, this forms one of the major methods through which axions are searched for. In addition to their interactions with photons, axions can also undergo interactions with electrons and nucleons.

The rarity of their interactions makes axions an important sink of energy in astrophysical (particularly stellar) systems, where they can be produced in the interior of massive bodies and escape the system, removing energy from the object in the process. This additional source of energy loss for stellar systems would have tangible impacts on the evolution and lifetime of stars [83]. The non-detection of these effects, therefore, is used to place limits on the axion and its couplings. See [83] for an overview of this topic.

The additional coupling of axions to electromagnetic fields occurs through the Primakoff process [84] whereby, with an interaction strength controlled by $g_{\mathrm{a}\gamma}$, axions may convert to photons in the presence of an electromagnetic field and vice versa (see Fig. 1.8). This effect has led to a number of novel search methods utilising magnetic fields. For example, the aptly named "light shining through walls" experiments exploit this effect by using two matched Fabry-Perot cavities on either side of an opaque barrier. A strong magnetic field is then applied to both cavities, with a laser in one cavity injecting photons into one of the cavities, the secondary cavity is then equipped with photon detectors. Thus, a photon converting

[14] Where $g_{\mathrm{a}\gamma}$ is distinct from $g_{\mathrm{A}\gamma}$ in that the former is the coupling to the axion particle and the latter the coupling to the axion field.

to an axion in the B-field of the first cavity will then cross through the barrier unhindered as an axion, to convert into a photon in the secondary chamber's B-field and be subsequently detected. See [85] for a review of this subject and [86, 87] for experimental results. Light shining through wall experiments are just one of a number of axion detection experiments, such as haloscopes and helioscopes (see [88] for a description of these and other axion search techniques), that aim to search for axion dark matter.

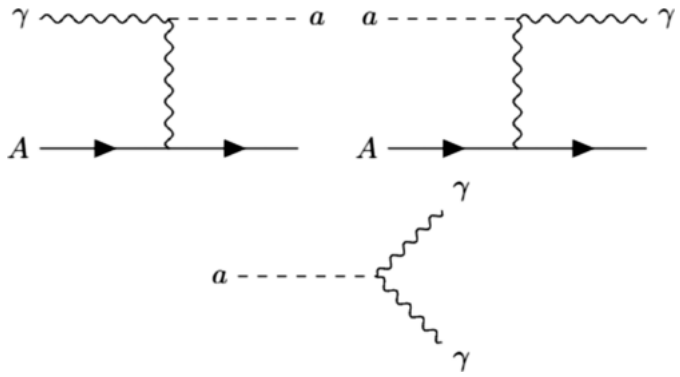

Fig. 1.8: Feynman diagrams of axion couplings to the photon. Shown in the top two diagrams is the axion-photon coupling through the Primakoff process. This shows the conversion of an axion to a photon (or vice-versa) in the presence of an electromagnetic field (here denoted as A). The lower diagram shows the decay of an axion into two photons. The strength and frequency of all of these processes are controlled by the axion-photon coupling constant $g_{a\gamma}$. Figure taken from [89]

.

1.2.4 Dark Photons

Dark photons are an example DM candidate from the wider vector DM (integer spin) particle framework, and operate as a hidden sector particle, specifically as a spin-1 gauge boson [90]. This means the dark photon is one constituent particle of a hypothetical extension to the standard model known as the hidden sector, and is proposed to act as a force carrier, in a comparable role to the photon of the standard model's Electromagnetic (EM) force. This hidden or dark sector posits an entire sector of undiscovered particles (and self-contained interactions of particles) within the sector. Dark photons can constitute dark matter in sufficient quantities via the misalignment mechanism (as described in Sec. 1.2.3), and fulfil the properties of a good dark matter candidate. Additionally, dark photons are also motivated by the ability of many hidden sector extensions to the SM (within which dark photons are naturally present) to account for the discrepancy between the measured and calculated magnetic moment of the muon.

Under a proposed new abelian U(1) gauge symmetry characteristic of vector DM models, the dark photon has the potential to undergo kinetic mixing with the SM photon, causing non-vanishing interactions with charged particles [90]. These interactions would be extremely weak but may lead to the detectability of the dark photon. This mixing, under most vector DM models, can lead to the decay of the dark photon into photons

$$V \rightarrow 3\gamma \tag{1.13}$$

for the case of $m_{\mathrm{V}} < m_e$ [91]. In this decay, V is the vector dark matter particle and γ a SM photon. This, in turn, allows for the indirect detection of dark photons, through the search for these characteristic SM photons. These searches enable limits to be placed on the strength of their interactions with the SM, from the non-detection of these decay photons.

1.2.5 Other Dark Matter Candidates

The list of dark matter candidates introduced above is by no means complete but does represent some of the strongest particle dark matter candidates, as well as the most relevant candidates in the context of this thesis and the work performed within. As previously discussed, dark matter theoreticians have extraordinary room to manoeuvre when positing new DM theories due to the size of the available parameter space. This leads to a host of particle dark matter theories such as WIMP-zilla (heavy WIMP particles), fuzzy cold dark matter and Kaluza-Klein particles (particles resulting from models with extra spatial dimensions [92, 93]) to name but a few. It is important to note however, that not all DM theories are particle in nature and compelling theories exist as alternatives to additions to the Standard Model (SM) such as modified theories of gravity (e.g. MOND [17]), and primordial black holes [94]. This thesis, however, focuses on particle dark matter and will detail studies into the attempted detection of several candidates. It is for this reason alone that non-particle dark matter is not introduced here, and is not a reflection of the merit of these theories. The reader is strongly encouraged to investigate these innovative and intriguing DM candidates.

1.3 Dark Matter Search Techniques

The prospect of revolutionising contemporary physics has naturally led to a coordinated global effort in the search for dark matter, spanning multiple disciplines of

the field. Generally, these searches can be divided into three categories based on the DM interaction they attempt to detect and their search technique (see Fig. 1.9, for a visualisation of the principles of these techniques.). These are direct detection, collider production and indirect detection. Variations in detection techniques allow for complementary limits to be placed on the nature of dark matter. As well as this, due to the nature of dealing with an unknown interaction, having alternate search techniques relying on different assumptions allows for both the falsification of results and ensures that, should one of the three techniques not be feasible through some unknown quirk of DM interaction, the other two techniques should circumvent this. It should be noted that the three main techniques are (mostly) more general in nature and are required to make assumptions about DM and its interactions with the SM. Alternatively, there are specific searches for individual DM candidates, which are more tailored to specific models. An example of this is the debatably separate category of axion detection experiments e.g. light-shining-through-walls experiments (see Sec. 1.2.3) and haloscopes/helioscopes [73]. However, the three aforementioned conventional techniques provide a more model-independent approach to DM detection and parameter space exclusion.

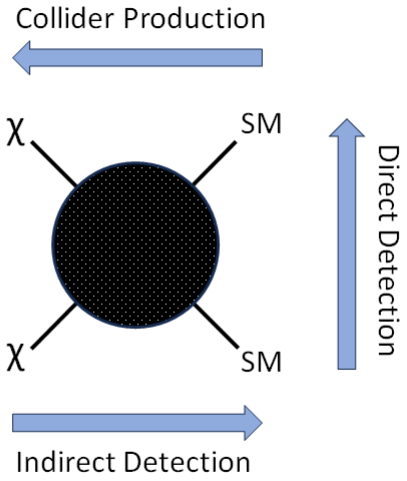

Fig. 1.9: Schematic diagram of possible dark matter interactions, in a highly generalised scenario, illustrating the interactions behind the 3 major branches of DM search. Dark Matter particles are represented by χ and SM indicates Standard Model particles. The central cross section contains the as-yet-unknown interaction of DM and SM particles and therefore encompasses new physics. The arrows surrounding the diagram indicate the interaction each of the labelled search techniques probes for. For example, the arrow labelling the indirect detection interaction represents the interaction $\chi + \chi \rightarrow N_{\mathrm{SM}} + N_{\mathrm{SM}}$.

1.3.1 Direct Detection

The fundamental principle around which direct detection revolves is the elastic or inelastic scattering of DM off of the nuclei or electrons of detector material. Critically, such an experiment relies on the assumption that dark matter interacts with SM particles beyond just gravitational interaction. Typically this interaction is taken to be of a weak-interaction-like nature, or in some cases a fifth undiscovered force. Formally though, the manner of the interaction does not matter for the experiment's operation, only that its strength is larger than gravitational interactions [95]. The interaction of DM passing through Earth (due to the planet's velocity through the local DM distribution) with the nuclei of the detector material, would, therefore, produce a recoil in the target particle with measurable energy.

The putative detection of dark matter interactions is made extremely challenging by the levels of background present in detectors. Most background is either a result of cosmic rays (muons and their secondary particles) or from radio-impurities of the materials in the experiment and its immediate vicinity. For this reason, extraordinary efforts are taken in direct detection experiments to minimise background. These include situating experiments deep underground to provide cosmic ray shielding and sourcing experimental apparatus and parts from extremely radio-pure materials [96]. To account for background most operational direct detection experiments measure both electron and nuclei recoil. This acts as a veto as dark matter is expected to predominantly scatter off of the target nucleus due to its weak interaction properties. These experiments can therefore utilise electron recoils to identify and discard background events since DM interactions are unlikely to produce significant electron recoils [97].

Given the strong motivation of the theory, most direct detection experiments aim to detect WIMP like particles in the GeV to TeV mass range. The manifold of modern techniques allows current direct detection experiments to search in the approximate mass range of a few eV to $\mathcal{O}$ TeV [95].

Time-dependent annual dark matter modulation experiments are a subcategory of direct detection experiments. These focus on detecting an annual modulation in the number of recoil events, reflecting the change in local dark matter density during different sections of Earth's solar orbit. Examples of such experiments are DAMA/LIBRA, COSINE and ANAIS (See [98] for the status and perspectives of DAMA/LIBRA as an example).

Liquid noble detectors such as XENON, LZ and PandaX (See [99, 100, 101] respectively for recent experimental reports), aim to detect dark matter through the

scintillation of noble elements in the liquid phase. The working principles of a liquid noble time projection chamber are shown in Fig. 1.10. The collision of a particle with a detector nucleus will produce an excitation and ionisation of the detector atom. Upon such a scattering event, the de-excitation of the target nucleus releases a prompt scintillation photon which, when detected by the Photomultiplier Tubes (PMTs), gives the initial time of the interaction as well as properties of the energy deposited and spatial information (S1). An applied electric field drifts the liberated electrons through the liquid noble gas towards a liquid/gas interface. In most modern detectors this interface hosts an even stronger electric field, which extracts the electrons. The acceleration of the electrons through the gaseous phase produces an additional (and secondary) signal from scintillation (S2). Measurements of the time difference between S1 and S2, allow full 3-dimensional spatial information about the interaction to be derived [95].

The comparison of the prompt S1 and scintillation S2 signals allows for distinction between electron and nuclear recoils and therefore also acts as a background discrimination technique [97]. The vast majority of background events are from gamma and beta particles, both of which have insufficient energetics to scatter off of the nucleus and thus recoil off of the electronic shell of the atom known as Electron Recoil (ER). Heavier particles such as incident neutrons or WIMPs interact with the noble atom's nucleus directly. These Nuclear Recoils (NRs) have a vastly different signal to their electron recoil counterparts. The difference between the two event types lies in the relative amplitudes of the two signal types. By comparing the ratios of the two signals one can differentiate between them:

$$\left(\frac{\mathrm{S2}}{\mathrm{S1}}\right)_{\mathrm{ER}} > \left(\frac{\mathrm{S2}}{\mathrm{S1}}\right)_{\mathrm{NR}} \tag{1.14}$$

Liquid noble detectors, therefore, must separate NRs resulting from neutrons (which constitute a background) and WIMPs. Several novel methods are employed to achieve this, including the comparison of quenching factors, contrasting the structures of the two scintillation signals (pulse shape discrimination), comparison of the energy spectra and the directionality of the recoil (neutrons are expected to scatter isotropically, whereas due to their weak interaction WIMPs may not).

Finally, one other category of direct detection experiments is cryogenic solid-state detectors. Cryogenic solid-state detectors operate using super-cooled solid-state material to detect excitations or phonons resulting from DM interactions. This method is advantageous due to its very low noise floor, and therefore, its ability to

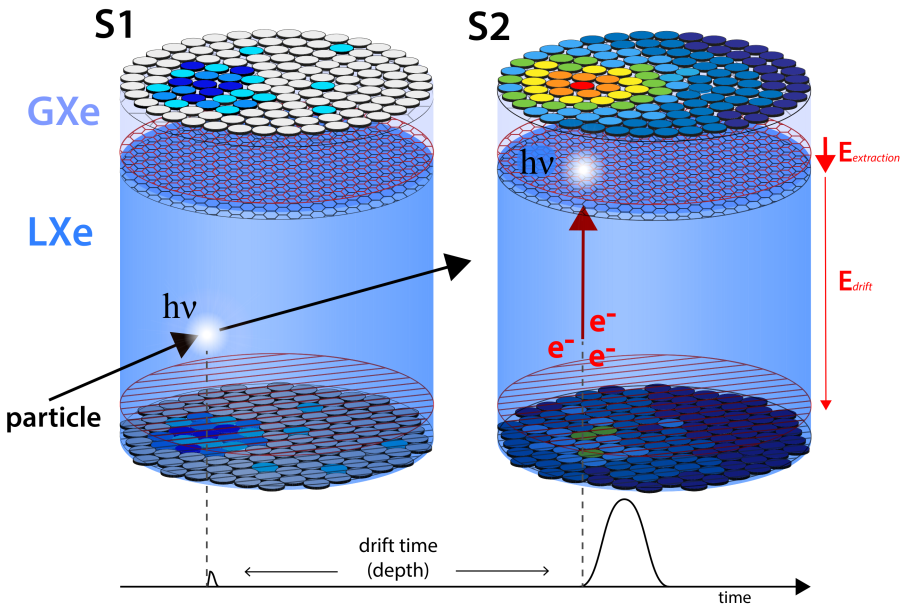

Fig. 1.10: Diagram of the working process of a dual phase time projection chamber operating on the principle of liquid noble gas scintillation, with time progressing from left to right. The initial scintillation light (S1) is released upon the impact of the target particle on the chamber. The liberated electrons then drift due to the electric field applied across the detector creating a secondary signal through ionisation (S2). The position of these two events, and the relative time between them, allow accurate 3D reconstruction of any scattering events. Moreover, a comparison of the amplitude of both signals allows for the rejection of background events from true DM events. Figure taken from [102].

probe to lower energies. Examples of these experiments include CRESST [103] and SuperCDMS [104].

These are only a handful of the many novel methods of direct detection dark matter searches, and with detector sensitivities approaching the neutrino fog[15], it is only likely that this number will increase as search strategies have to adapt to circumvent this problem.

A comparison of various limits on spin-independent elastic WIMP-nucleus scattering is shown in Fig .1.11, where the scattering cross section[16] is given as a function of WIMP mass. Due to their excellent sensitivity, control of systematics, shielding through deep underground operation, and cumulative search times direct detection experiments are currently the imposers of the most stringent limits upon dark matter. Despite this, it is important to stress that direct detection (as well as the other two

[15] Formerly "the neutrino floor", this is the point at which detectors will become sensitive enough for solar pp neutrinos to constitute a major and problematic background.

[16] Note, the scattering cross section is a different quantity to the annihilation cross section, which is itself the subject and goal of indirect detection studies.

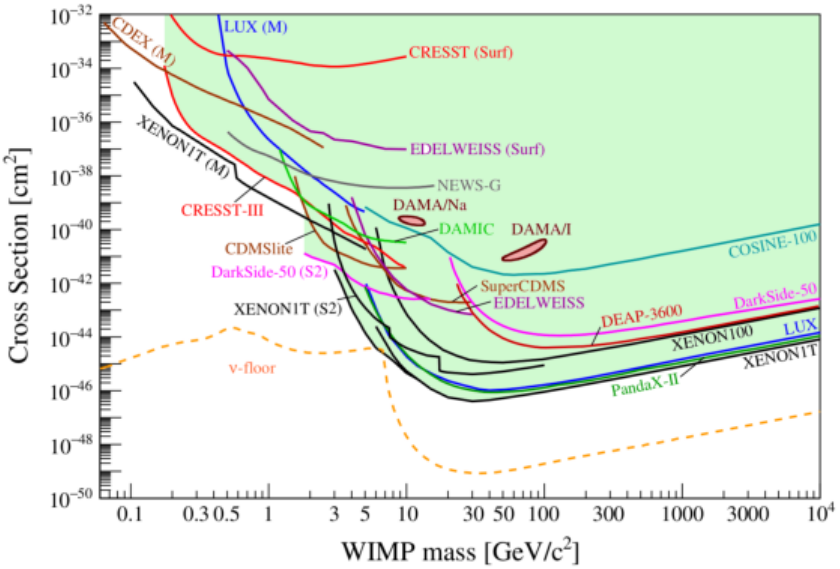

Fig. 1.11: A comparison of the current best limits on the spin-independent elastic scattering of WIMP-nuclei, where the limits on the scattering cross section are given as a function of WIMP mass. Limits are imposed assuming a standard isothermal WIMP halo with parameters: $\rho_0 = 0.3$ GeV cm^{-3} (DM density at Earth), $v_0 = 220$ km s^{-1} (DM velocity at Earth) and $v_{esc} = 544$ km s^{-1} (DM escape velocity). On the diagram, the green shaded area marks the currently probed parameter space with lines of varying colours indicating the limits imposed by different experiments. The neutrino floor is indicated by the yellow dashed line and is calculated as the cross section (σ_d) at which a given experiment has a 90% probability of detecting a WIMP with a scattering cross section $\sigma > \sigma_d$ at greater than 3 sigma. Figure and values taken from [105].

search methods presented) is not a perfect solution to detecting DM. The number of unknowns surrounding DM means each search method has the potential to have a hidden flaw, and no technique can claim a meaningful detection without corroboration from its counterpart methods.

1.3.2 Collider Production

A second dark matter search method centres around investigating signals of its production in particle colliders. Colliders utilise the assumption that dark matter can be made in pp collisions and that there exists characteristic weak or vanishing interactions of DM with the SM. The production of dark matter in this scenario would constitute missing energy or momentum in a particle collision, where the produced dark matter is expected to have exited the detector without interacting [106]. Such an approach has the disadvantage that, it is inherently limited by the collider's energy and can only probe dark matter particle production in the

available energy range. Secondly, the results produced (and their respective ability to exclude parameter space) are strongly dependent on the manner and strength of coupling between DM and SM particles in a given model. The latter of these makes the exclusions produced by collider searches difficult to compare to the more model-independent results of direct and indirect detection. Considerably though, collider production does not rely on any underlying astrophysical or cosmological factors such as local DM distribution, and therefore any detections would have an advantage in their refutability.

The majority of these searches have naturally been performed by the Large Hadron Collider (LHC) at CERN. The ATLAS and CMS collaborations are both heavily involved in the search for dark matter but have reported no detection as of yet [107]. However, LHC constraints, along with the detection of the Higgs boson, have enabled a large tightening/exclusion of the available parameter space for minimal Kaluza Klein models [108].

1.3.3 Indirect Detection

Indirect detection aims to search for evidence of dark matter through its annihilation, decay, oscillation or other transformative mechanism into detectable particles[17]. The detection of these particles (or their secondary effects) forms the foundation of indirect detection techniques. In principle, particles produced by dark matter interactions (e.g. annihilation or decay events) will form an anomalous excess of SM particles (i.e. photons) on top of known astrophysical foregrounds (an illustration of this is shown in Fig. 1.12). This excess of particles would be a distinct component, separate from known astrophysical populations or emissions, making it recognisable and detectable [41]. Of equal importance for the clarification of a signal's origin, is that these events will naturally be centred around areas of high dark matter density, and the emission will correspond directly to the dark matter distribution.

Indirect detection has the benefit of utilising the extremely large population of existing DM in the Universe for study. Moreover, indirect detection has the fortuitous advantage of an array of current astrophysical missions/telescopes, as well as a host of archival data from previous missions, all of which can be employed in the effort to search for the indirect effects of dark matter. The availability of telescopes and their data is very advantageous, with existing observatories spanning almost

[17] Most commonly these are standard model particles. However, there are cases whereby SM particles are not produced in the primary interaction and occur through interactions of a secondary exotic particle that is produced in an initial process.

the entire electromagnetic spectrum[18]. However, indirect detection comes with the significant disadvantage that any DM interaction that might result in visible products is, by the nature of the dark matter problem, extremely weak. This results in very low theoretical production rates for DM secondary particles. This characteristic low signal level is only complicated further by the smorgasbord of poorly understood astrophysical signals and foregrounds, mimicking signals of dark matter and making the distinction of a separate DM component much more difficult. For example, in the case of DM models searching for a sharp Gaussian line signal (e.g. the νMSM sterile neutrino), the many poorly understood emission and transition lines in astrophysical observations provide a significant background.

1.3.4 Dark Matter Signal

The exact nature of a dark matter signal in indirect searches is (in general) highly dependent on the model of DM one is attempting to search for. While it is true that most indirect detection methods search for an excess of SM particles, the type of particle and its origin can vary enormously between models. For example, models in which annihilation leads to gamma rays would expect an excess of gamma-ray events from DM dominated regions. On the other hand, for leptophillic DM models [109], one might expect both excesses of electrons or positrons from the Milky Way halo, coupled with an excess of secondary synchrotron from DM dominated regions with magnetic fields.

Annihilating Dark Matter

Due to both the popularity of models in which DM self-annihilates, and the detectability of signals of this origin, many indirect detection searches focus largely on attempting to discern signals from the annihilation of DM. Signals from DM annihilation follow the general form:

$$\frac{\mathrm{d}N_{\mathrm{ann}}}{\mathrm{d}A\,\mathrm{d}t\,\mathrm{d}\Omega\,\mathrm{d}E} = \frac{\langle\sigma v\rangle}{2m_{\chi}^{2}}\,\frac{\mathrm{d}N_{x}}{\mathrm{d}E}\,\frac{1}{4\pi} \times J_{\mathrm{ann}}(\psi), \tag{1.15}$$

This equation gives the number of particles in a given area, time, solid angle, and energy (differential intensity). Here $\langle\sigma v\rangle$ ($\mathrm{cm}^3\,\mathrm{s}^{-1}$) represents the thermally averaged annihilation cross section. m_{χ} (eV) in this equation is the DM particle's

[18] Moreover, there exist several telescopes and missions that are sensitive to the detection of cosmic rays which can also be utilised in the search for DM.

mass, and the differential spectrum of a particle x emitted per annihilation is represented by the term $\frac{\mathrm{d}N_x}{\mathrm{d}E}$. J_{ann} (GeV^2 cm^{-5}) represents the column density of DM in the instrument's Field of View (FoV). In this equation, the $2m_\chi^2$ term only applies to DM which is its own antiparticle and becomes $4m_\chi^2$ in cases where DM is not its own antiparticle [45]. Equation 1.15 describes the expected emission from a range of annihilating DM candidates. Foremost of these is the previously introduced WIMPs (see Sec. 1.2.1) which are expected to self-annihilate, producing a spectrum of final states.

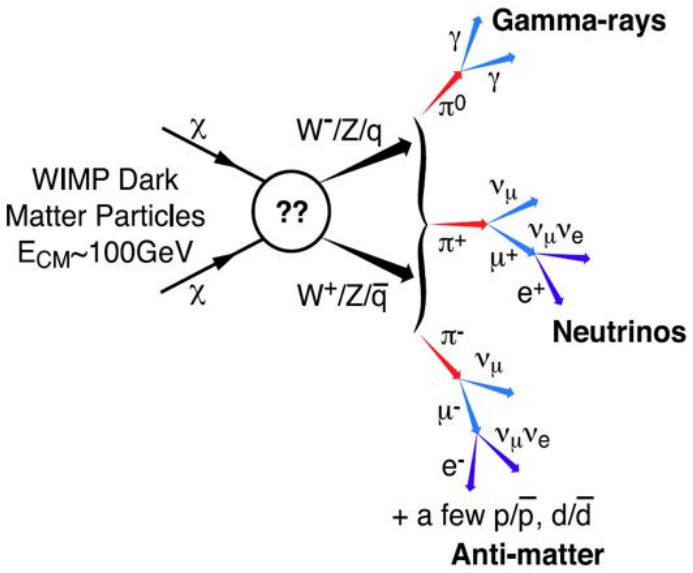

Fig. 1.12: An example of a DM particle cascade from the annihilation of two WIMP particles. Through some unknown process, the annihilation of the two particles may produce a variety of secondary SM particles. These particles, either primarily or through their decay to detectable particles, form a detectable excess particle population on top of astrophysical foregrounds. Annihilation is shown here as an example mechanism however the process is equally valid by DM decay or other transformative process. Figure taken from [110].

This equation can be divided into two terms, representing the particle physics and astrophysics contributions to a DM annihilation signal respectively. The particle physics term contains all the model-dependent information regarding the particle physics of the DM candidate and its annihilation into SM particles. The $\langle \sigma v \rangle$ parameter is indicative of a model's annihilation rate/interaction strength with visible matter [45]. As such, this quantity is used to place limits upon dark matter's non-detection. This involves taking flux upper limits from indirect searches and converting them into exclusions on the $\langle \sigma v \rangle$ parameter space as a function of DM particles mass.

The differential particle spectrum can be generalised in the following form:

$$\frac{\mathrm{d}N_x}{\mathrm{d}E} = \sum_f B_f \frac{\mathrm{d}N_{x,f}}{\mathrm{d}E}, \tag{1.16}$$

Distinctly, this does not assume a 100% branching ratio (B_f) to a single final state (f) but instead sums across all possible final states weighted by their branching ratios. This term therefore encapsulates the possible emission spectrum of a DM annihilation or decay event, as shown in Fig. 1.13. To ensure model independence, it is common for indirect searches to display limits to annihilation or decay to a particular final state, allowing comparison between objects and searches [45].

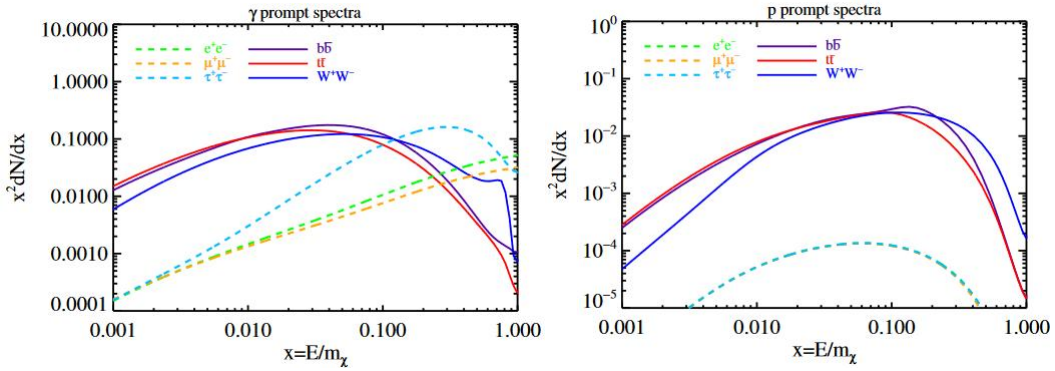

Fig. 1.13: The spectra resulting from the annihilation of two DM particles (of 500 GeV in mass) to given final states. In these spectra $x = \frac{E}{m_{\mathrm{DM}}}$. The left figure shows the individual spectra of γ particles emitted in secondary processes, given an initial DM annihilation to the varying final states shown. The right-hand figure displays the same final states but for the expected spectra of protons. Figures taken from [45].

Possible final states for DM particles are broad, where theoretically any SM particle pair that is energetically available can be formed [11]. The final states can however be divided into two particular categories based on their method of production of final state radiation. The "soft channels" are a category of final state particles that produce prompt photon emission through neutral pion decay formed as a result of their hadronisation [45]. Soft channels are typically gauge boson and quark final states e.g. W^+W^- bosons or $b\bar{b}$ / $t\bar{t}$ quarks [111]. On the other hand "hard channels" are typically leptonic final states (e.g. e^+e^-, $\mu^+\mu^-$ and $\tau^+\tau^-$[19]), which emit radiation through final state emission e.g. Bremsstrahlung or other astrophysical processes [109].

[19] $\tau^+\tau^-$ does not only produce radiation through final state emission but also decays through hadronisation to neutral pions similar to soft channels [111].

The resulting signal from both hard and soft channels, however, is similar and would be distinctive in the Spectral Energy Density (SED) of DM dominated objects. The production of prompt and final state radiation from these channels would result in a sloping feature on top of the astrophysical continuum [109]. This would have the characteristic shape of low flux at lower energies, sloping upward to higher flux at higher energies before an identifiable cutoff around the mass of the dark matter particle. This represents the emission resulting from kinematically available final products of an annihilation event.

The final states $\gamma\gamma$, $Z\gamma$ and $h\gamma$ would all result in the emission of a monochromatic spectral line of gamma-ray energy, which would be an extremely distinct signal of dark matter annihilation [45]. Since no astrophysical processes are known to produce a line signal at these energies, such a feature would be "smoking gun" evidence for dark matter. However, WIMPS do not couple directly to the photon meaning any final states producing a photon are loop-suppressed [109]. This loop-suppressed production rate, combined with the strong continuum emission of other final states would most likely result in this signal being drowned out and lost under the flux level of the continuum [45].

Decaying Dark Matter

The expected emission from decaying dark matter has several key differences when compared to that of annihilation. Emission from decay is given by the equation:

$$\frac{\mathrm{d}N_{\mathrm{dec}}}{\mathrm{d}A\,\mathrm{d}t\,\mathrm{d}\Omega\,\mathrm{d}E} = \frac{1}{m_\chi \tau}\frac{\mathrm{d}N_x}{\mathrm{d}E}\frac{1}{4\pi} \times J_{\mathrm{dec}}(\psi), \tag{1.17}$$

where m_χ and $\frac{\mathrm{d}N_x}{\mathrm{d}E}$ have the same definition as before, but τ (s) is the expected lifetime of the DM particle [45]. Notably, the astrophysical J-factor (J_{ann}) of equation 1.15 is different in the annihilating case to that of the decay (J_{dec}, GeV cm^{-2}).

Much like the case for annihilating DM, the differential particle spectrum, representing the available final states for a given DM particle, is given by Eq. 1.16. Similarly, this results in both soft and hard channels creating a continuum flux. In these cases, the signal would be similar to that of annihilating DM, with a sloping feature on top of astrophysical foregrounds, however, the cutoff in the case of decaying DM would be at half the DM particles mass. Alternatively, many decaying DM models couple directly to the photon, meaning that the expected signal from many DM decay models is a monochromatic line.

1.3.5 J-factor

Both Eq. 1.15 and Eq. 1.17 also contain a second term encompassing the astrophysical contribution to the expected DM flux. This J-factor[20] encompasses the sum of the dark matter column density in the field of view. For annihilating dark matter, this is given by the equation:

$$J_{\text{ann}} = \int_{\text{d}\Omega} \int_{\text{l.o.s}} \rho(r)^2 \, \text{d}l \, \text{d}\Omega, \tag{1.18}$$

and for decaying DM by:

$$J_{\text{dec}} = \int_{\text{d}\Omega} \int_{\text{l.o.s}} \rho(r) \, \text{d}l \, \text{d}\Omega, \tag{1.19}$$

In these equations, $\rho(r)$ (kg m^{-3}) is the dark matter density, where l (m) is the distance in the direction of the object and Ω (sr) is the solid angle subtended by the object on the sky. As can be seen, in both cases the J-factor is the summation of the amount of dark matter within the field of view of an observation. The differing dependence of each J-factor on the density is a product of annihilating DMs inherent requirement of 2 particles to annihilate[21], increasing the chance of an event and subsequently the signal in the field of view.

J-factors are therefore a useful tool to indicate the strength of a potential signal from a given object. Since the particle physics term can be held constant, the strength of a signal is inherently dependent on the J-factor, which is in turn maximised by objects with large angular extensions and high DM densities.

Dark Matter Distribution

As is evident from Eqs. 1.18 and 1.19, the distribution of dark matter within a target of observation is extremely influential on the expected DM signal emanating from the object. Since the J-factor is assumed as a constant factor in the calculation of DM interaction limits ($\langle \sigma v \rangle$, θ etc.) through Eqs. 1.18 and 1.19, the distribution and uncertainties of the dark matter profile have a direct effect on the limits imposed by any indirect search. As such a rigorous understanding of the dark matter distribution in an object is essential in calculating any J-factor.

[20] For decaying dark matter this is sometimes called the D-factor (or DM column density) to distinguish it from annihilating DM's J-factor which is of a different form.
[21] This is the case for self-annihilating DM.

Typically dark matter is clustered in halos centred on a massive astrophysical object. Within these objects, the spatial mass distribution most commonly follows the gravitational influence of the luminous matter. In the DM paradigm these halos are the result of bottom-up hierarchical formation, whereby smaller halos in the early Universe merged under gravitational influence to form the larger halos seen around astrophysical objects in contemporary observations [29, 30]. The formation of a larger halo in this manner unavoidably leads to a substructure, where un-merged small concentrations of dark matter are present throughout the halo. This scenario is confirmed in N-body simulations (see for example [112, 113, 114]), where the bottom-up structure formation of CDM particles displays significant clumping and structure due to merging timescales.

While there exists a body of evidence suggesting that the shape of dark matter profiles is triaxial [115, 112], the general shape of halos is still an actively researched topic between observations and N-body simulations. When modelling the profile it is common to assume a spherical symmetry as such an approximation is highly accurate close to the centre of a halo.

One of the most common profiles utilised in literature is the Navarro-Frenk-White profile, a 2-parameter relationship based on N-body simulations giving dark matter density as a function of radius [116, 117]. Given its versatility (the profile is accurate over 4 orders of magnitude in mass), alongside its accuracy in describing DM halos, it became prolifically used as a standard profile for objects. The profile is given by:

$$\rho_{\mathrm{NFW}}(r) = \frac{\rho_0}{\left(\frac{r}{r_{\mathrm{s}}}\right)\left[1+\left(\frac{r}{r_{\mathrm{s}}}\right)\right]^2}, \tag{1.20}$$

Where ρ_0 (kg m^{-3}) is the characteristic density, r_{s} (m) the scale radius and r (m) the radius from the cluster's centre. The former two of these three terms are individual to an object and can be measured from observations or derived from N-body simulations, allowing this profile to be applied to many different objects over a large mass range.

Though the NFW profile is versatile, simple, and accurate it is not without its shortcomings. Due to its development in an era where computational power was limited, most CDM simulations of the time only accounted for DM in their models without accounting for the baryonic component and its effects. With the advent of larger N-body simulations drawing from increasingly expanding computational power, it has become possible to model a greater number of elements in the production of these profiles.

N-body simulations subsequent to those performed by Navarro, Frenk, and White, have indicated that the presence of baryonic matter and its feedback effects can cause deviations in the inner regions of the halo profile. Processes such as adiabatic contraction cause a steepening of the inner profile, as the baryonic (and subsequently dark) matter is drawn closer to an object's centre [118, 119]. Moreover, astrophysical processes in the centre of a target, such as supernovae (known to occur more frequently towards the centres of objects) or the ejection of gas by Active Galactic Nuclei (AGN), can lead to significant flattening of the inner profile and affect the outer distributions of the profile [120, 121]. This led to the development of profiles that were more generalised iterations of the NFW, allowing for differing slope values as determined by the best fit of observations and N-body simulations. The Zhao profile [122] is an example of this:

$$\rho(r) = \frac{2^{\frac{(\beta-\gamma)}{\alpha}}\rho_0}{\left(\frac{r}{r_\mathrm{s}}\right)^{\gamma}\left(1+\left(\frac{r}{r_\mathrm{s}}\right)^{\alpha}\right)^{\frac{(\beta-\gamma)}{\alpha}}} \tag{1.21}$$

NFW returned at: $\alpha = 1, \beta = 3, \gamma = 1$

where the terms r, r_s and ρ_0 are, as before, the radius from the cluster's centre the scale radius and the characteristic density respectively. The α, β and γ parameters allow the slope of the density distribution to be fine-tuned through values reported by dedicated studies of objects. This feature of the profile makes it (and similar generalised profiles) popular among indirect searches due to the increased J-factor a fine-tuned profile can provide. As can be seen in the text below Eq. 1.21, certain values of α, β and γ return differing types of existing profiles such as cored profiles or the original NFW profile.

More recent simulations still have indicated that the NFW profile's assumed power law variation of density with radius is, in some cases, not a good approximation. To account for these discrepancies, models proposing a slope varying with radius (rather than a simple power law) were implemented. Perhaps the most utilised of these is the Einasto profile [22] [123], which follows the equation:

$$\rho_{\mathrm{Ein}}(r) = \rho_0 \exp\left\{-\left(\frac{2}{a}\right)\left[\left(\frac{r}{r_\mathrm{s}}\right)^{\alpha} - 1\right]\right\}, \tag{1.22}$$

[22] The Einasto profile was proposed significantly before the NFW. The profile itself was never specifically designed for the dark matter problem, but rather just described density profiles of spherical objects. It was later found to be an accurate general model to account for the variations in the slope of the profiles in the observations of astrophysical objects.

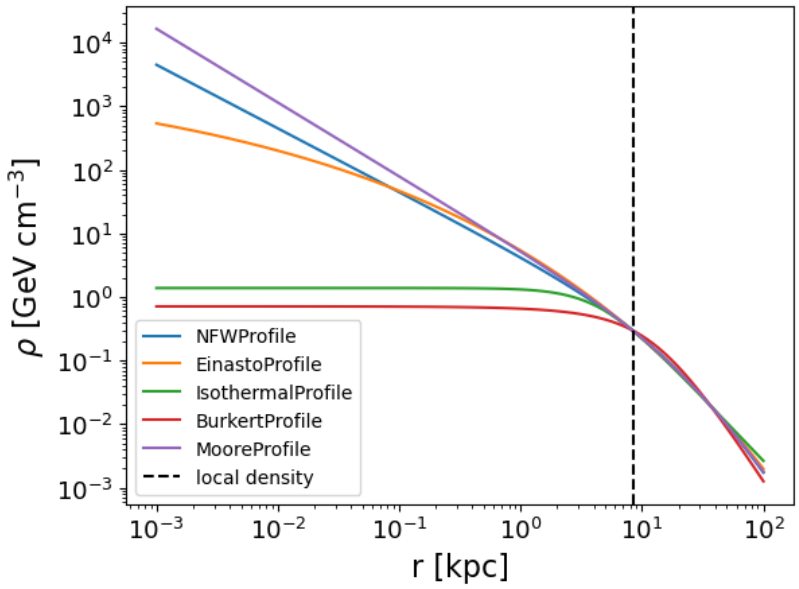

Fig. 1.14: Dark matter density profiles, displaying the change in dark matter density as a function of radius from an object's centre. Profiles are based on the Milky Way galaxy, with the distance of Earth from the galactic centre indicated by the dashed black line. Both cored (Burkert and Isothermal) and cuspy (NFW, Einasto and Moore) profiles are displayed for posterity. Figure created using `Gammapy-1.0`.

where the scale radius $r_{\rm s}$ and the characteristic density ρ_0 are defined as in the NFW. The additional α parameter is a measure of the change of the slope with respect to radius.

On top of this, it was subsequently discovered that the results of profiles from N-body simulations disagreed with the observed profiles for low-brightness galaxies and Dwarf Spheroidal (DSph) galaxies [124, 125]. In essence, N-body simulations showed a clear preference towards cuspy profiles (a large variation in density at small radii) as with larger objects, whereas observational evidence suggested a flattening at the centre of the profile or a core. This was coined the cusp–core problem [See 126, for an overview] and led to the development of mathematical descriptions of cored profiles, to better describe the density distributions of these smaller objects. A widely used example of such a profile is the Burkert profile [127]:

$$\rho_{\rm Burk}(r) = \frac{\rho_0}{\left(1+\frac{r}{r_{\rm s}}\right)\left(1+\frac{r^2}{r_{\rm s}^2}\right)} \tag{1.23}$$

ρ_0, $r_{\rm s}$ and r are all as defined in previous equations. Notably, the first term of the denominator in this equation ensures that the profile exhibits a constant density at smaller radii.

Profiles are often derived from dedicated N-body simulations of objects, or from gravitational probes [109] (see [115, 128] for examples of these two methods respectively), however, other techniques are also employed and are often tailored to specific objects. For example, in the case of objects that emit strongly in X-rays (like the hot Intra-cluster Medium (ICM) of galaxy clusters), X-ray probes can be used to infer the mass profile and subsequent DM density distribution [129]. On the other hand, for cooler less active dark matter-dominated objects, like dwarf spheroidal galaxies, profiles are often inferred from stellar kinematics [130] where the proper motion of gravitationally bound stars can be interpolated to reveal the mass profile.

The aforementioned profiles describe only the smooth component of the dark matter profile, however (as detailed earlier in this section) there is a non-negligible amount of substructure seen within most profiles. This substructure is extremely advantageous for observations of DM as it provides localised increases to the dark matter density within the profile which, when integrated over the entire profile, strongly increases the expected signal. To account for this, a "boost factor" is commonly employed. This is usually a simple multiplicative factor applied to the J-factor, which encapsulates the average boost to the signal the substructure within the profile would make. More rigorous treatment of the effects of substructure is usually performed by including the mass distribution function and the spatial distribution of the substructures. This results in a radially dependent boost to the DM profile, and a more accurate description of the underlying effects of the substructure. The `CLUMPY` code, is an example of a library that allows one to implement the radial dependant boost effect of substructure [131].

The utilisation of these profiles as applied to ΛCDM brings two distinct problems to the forefront. When comparing ΛCDM simulations to what is observed, it is clear that the CDM sub-halo stellar mass function is steeper than the observed satellite mass function. In essence, ΛCDM predicts that there should be a far greater number of satellites from substructure than we observe, both in terms of DM sub-halos in the Milky Way and in low luminosity galaxies in local galaxy groups. This is known as the so-called "missing satellite problem" [132, 133, 134].

This, in itself, creates an additional problem. The satellites predicted by ΛCDM are themselves large enough that they should host stellar populations and should thus be visible. This contradiction with the observed lack of satellites is known as the "too big to fail" problem [135, 136, 137].

With updated ΛCDM simulations though, there is evidence that these problems are lesser than originally thought, or are indeed non-existent. More recent simulations

(such as EAGLE and IllustrisTNG) show that there is no problem with the luminosity function as compared to modern codes, but that the gap between the first and second brightest systems is too big given this luminosity function [138]. This however could simply be the result of classical dynamical friction aiding gravitationally induced merging.

1.3.6 Indirect Search Targets

The importance of the J-factor on indirect searches and, in turn, on deriving limits on DM means it is imperative to ensure that it is maximised for the object of observation. As can be seen from Eq.1.18 and Eq.1.19, this equates to ensuring the maximum possible values of the dark matter density term ($\rho(r)$) and the solid angle subtended by the target ($\Delta\Omega$). The former of these is largely proportional to the mass of the object. Massive gravitationally bound structures, like galaxy clusters, host an abundance of dark matter due to their deep gravitational wells. In addition to this, the solid angle subtended by the object is naturally maximised by astrophysical targets that are large in the field of view. Therefore, mathematically speaking, the idealised situation for indirect searches is a target that is both extremely massive and either near enough or large enough (or a combination of the two) that it subtends a large solid angle on the sky.

A more experimental constraint on objects is the measurements of their profiles and the uncertainties involved. As mentioned in Sec.1.3.5 uncertainties in a dark matter profile can lead to their propagation into large uncertainties on derived dark matter limits [139].

Although mathematically the two previously mentioned conditions provide idealised targets for indirect dark matter searches, empirical targets with these attributes often prove challenging in dark matter searches. By their nature, most massive targets are sites of high astrophysical emission in the higher energy regimes. For example, though galaxy clusters are extremely massive, the potential well in their centre leads to strong X-ray emission through the in-fall of the ICM [24]. This foreground emission presents a challenge when looking for the faint signals expected from dark matter annihilation and decay. Astrophysical foregrounds provide irreducible backgrounds with which any potential signals from dark matter can become conflated [41]. On top of the terms that maximise the J-factor, it is therefore also important that the target object exhibits a low emission level in the energies the search is undertaken in.

The galactic centre has a huge concentration of mass, and more importantly, subtends one of the largest angles on the sky of any object. For these reasons, it is a highly favoured search target for DM studies. However, the situation is complicated by the myriad of high-energy processes and resulting emissions in the region. This strong astrophysical foreground emission introduces difficulties in any search and has the potential to dampen any claim of a DM detection.

Exemplary of this is the dark matter interpretation of an excess of high-energy gamma-ray emission emanating from the galactic centre region. The so-called "galactic centre excess" was first detected by the *Fermi Large Area Telescope (LAT)* in 2009, and seemed to indicate an excess of GeV emission from the galactic centre region in a manner consistent with the expected signal from annihilating dark matter [140]. However, due to the astrophysical foregrounds in the region, this situation is extremely complicated. Another interpretation of this signal, for example, is a population of undetected and unresolved millisecond pulsars in the region that could mimic an extended emission [141]. Alternatively, the diffuse emission in the region of the galactic bulge is extremely complex and it has been argued that this excess effect could be reproduced by insufficient modelling of this [142].

Alternatively, although they subtend a far smaller angle than other objects, Dwarf Spheroidal galaxies are characterised by extremely low emission in the high-energy regime. These objects are small, low-luminosity satellite galaxies of the Milky Way[23] that contains older stellar populations. Velocity dispersion studies of the stars within DSphs however, indicate that they are largely dark matter-dominated objects. This, in addition to their lack of foreground emission, makes them enticing targets for study and allows the derivation of competitive limits from indirect searches of them (see [144] for a review of indirect DM searches in DSphs).

In addition to the DM signal expected from the object itself, it is worth noting that the Milky Way's dark matter halo can often provide a significant addition to the expected J-factor from a target object. For this reason, the Milky Way's DM halo is often also utilised as a target for indirect studies ([145] is an example of a recent blank sky study). Such studies often make use of so-called "blank-sky" observations from instruments, where a telescope is pointed at a region of the Milky Way that is far from astrophysical sources and the galactic plane. This results in a very low astrophysical foreground, allowing an extremely clean search to be conducted, utilising just the Milky Way halo component.

[23] DSphs and have also been reported around other galaxies in the local group [143]. However, due to their distance, the J-factors of these objects are often too low to be considered for a meaningful DM study.

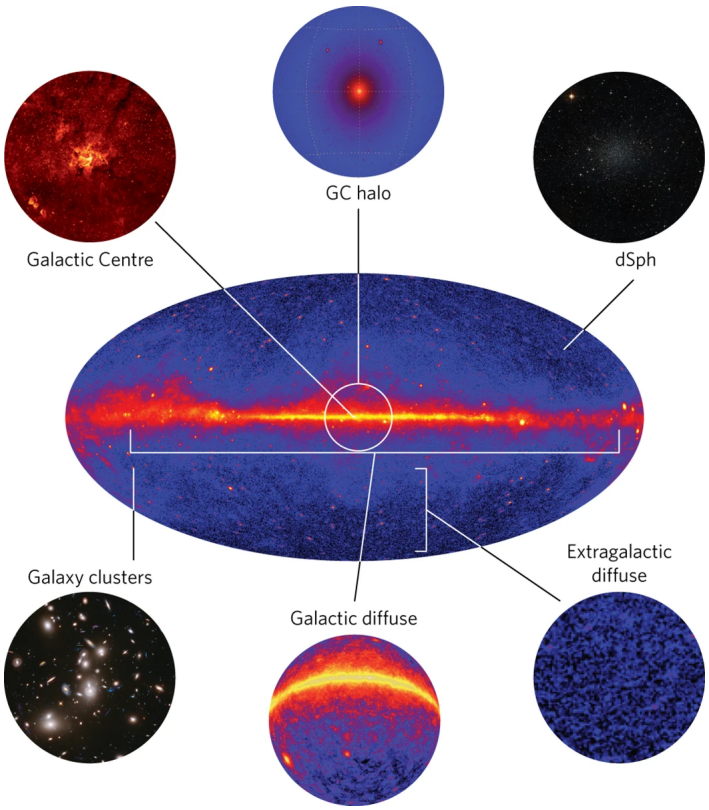

Fig. 1.15: A composite image displaying indirect DM detection search targets. Figure taken from [139].

Figure 1.15 shows a summary of well-motivated targets for indirect dark matter detection, and Tab.1.1 shows a summary of the J-factors for several object classes. Despite the sometimes competitive fashion in which target objects are listed, the observation of a wide range of astrophysical targets is quintessential for the identification and classification of a dark matter signal. Any tentative dark matter signal detected in a single category of object can only be confirmed with the supplication of its detection in all other dark matter-dominated objects. However, in lieu of first detection, the prioritisation of the most promising targets is a necessary step.

Target	$\log_{10}(J_{\text{ann}})$ [GeV^2 cm^{-5}]
Galactic Center	21.5
Dwarf Spheroidal Galaxies (best)	19.42
Galaxy Clusters (best)	18

Tab. 1.1: J-factors of three popular indirect dark matter search targets. Table adapted from [45], and references within. The quoted J-factors correspond to the best single J-factor of an object within that category at the largest reported angular extension within the work the value was taken from.

1.4 Indirect Dark Matter Searches

As described in previous chapters, the underpinning principle of indirect dark matter searches is the detection of SM particles resulting from some transformative process that a given dark matter candidate has undergone (e.g. decay or annihilation). The SM particles produced from this (or their secondary interactions with ambient matter) will thus form a detectable excess on top of the expected astrophysical foregrounds for any astrophysical object. Whilst the exact form of the signal in question depends strongly on the DM model being probed, the detection of an unexplainable excess of photons/particles, or a line signature that does not correspond to known atomic transitions would provide strong evidence for dark matter. It is for these reasons that models preferable for searches are those which have radiative final state emission, (or induce secondary radiative emission) making them testable as a hypothesis.

Observations are thus performed with various instruments to probe the levels of flux emanating from astrophysical objects, with the intent of attempting to detect an excess corresponding to a given model's signal. Depending on the model being probed, one can calculate the expected DM signal from an object using Eq. 1.15 or Eq. 1.17 for decaying and annihilating models respectively. This necessitates a good understanding of the underlying dark matter density distribution in the object (see Sec. 1.3.5), as this is the largest contribution to the uncertainty in most cases.

The instruments used in searches are inherently limited in their ability to detect an excess of DM induced signal by the minimum flux they can detect. For a given instrument this is given by

$$F_{\rm min} = \sigma \left(\sqrt{\frac{B\,\Delta E}{A_{\rm eff}\,T\,\Omega_{\rm FoV}}} + \alpha\,B\,\Delta E \right) \tag{1.24}$$

Where σ is the significance level of the detection, B (ph cm^{-2} s^{-1} keV^{-1} sr^{-1}) is the combined background contribution from astrophysical and instrumental backgrounds, and ΔE (keV) is the energy resolution. Additionally, $A_{\rm eff}$ (m^2) is the effective area, T (s) is the exposure of the observation, $\Omega_{\rm FoV}$ (sr) is the solid angle subtended by the instruments FoV, and α is the characteristic level of systematics expected for the instrument. Naturally, an improvement in these instrumental qualities improves the minimum level of flux an instrument is able to probe. Therefore, an ever-increasing control of systematics, increased effective areas and improved

energy resolutions in next-generation missions will prove instrumental[24] in future efforts to detect or place limits on dark matter's properties.

Given the non-detection of a DM signal, the comparison of Eq. 1.15/Eq. 1.17 to the minimum flux detected by an instrument can be used to place limits on the parameter which dictates the interaction of a given model with the SM. For example, searches that result in a non-detection of WIMP DM signals use the minimum detected flux in comparison with the expected flux (as derived from the J-factor for a given object) to place limits on the velocity averaged annihilation cross section of WIMPs $\langle \sigma v \rangle$. Similarly, non-detection of sterile neutrinos allows limits to be derived on the mixing angle (θ) and for axions limits on the axion-photon coupling constant can be derived ($g_{a\gamma}$) in the same manner.

The derivation of these limits allows studies to show how much of the available parameter space (interaction parameter as a function of mass) has been probed, allowing for comparison between studies. The available parameter space for each model is also bound by fundamental limits which are model dependent. These limits, in contrast to observational exclusions, are derived from theoretical arguments providing limits on mass ranges and interaction coupling strengths physically unfeasible for the model.

The following two subsections will provide a brief insight into a recent decaying dark matter search and a recent annihilating dark matter search. The context of these will be used to briefly explain fundamental limits as well as give an overview of the current state of indirect searches for some of the previously introduced DM candidates. However, this should not be taken as a comprehensive overview, especially in a field which evolves as rapidly as indirect DM searches.

1.4.1 Indirect Decaying Dark Matter Searches

Figure 1.16, shows a recent overview of the state of the parameter space of indirect searches for sterile neutrino dark matter. As well as the constrained parameter space derived from the non-observation of sterile neutrino decay, the figure displays a number of theoretical limits placed upon the parameter space which are calculated from theoretical arguments. Although applied to sterile neutrinos in this instance, many of the constraints shown are shared by other decaying DM models. Additionally, Fig. 1.17, shows a recent dedicated νMSM sterile neutrino search.

[24] Please pardon the pun.

Current X-ray constraints, as described in the previous section, are derived from a combination of studies probing different energy ranges and objects. The non-detection of a characteristic decay line in these observations allows limits to be derived on the mixing angle, as a function of DM mass. In addition to this, this study compares the current limits to two different estimations of the sensitivity of the upcoming ATHENA mission, at differing levels of systematics [146].

Phase space limits are commonplace among decaying dark matter models and denote a lower limit on the possible DM particle mass, as derived from phase space arguments from the Pauli exclusion principle. This so-called Tremaine-Gunn bound [147], and originates from the fact that the phase space density of DM cannot violate the Pauli exclusion principle and thus not form a degenerate Fermi gas. The smallest objects for which it is possible to reliably measure the DM content are DSphs, so in order to achieve the number densities of DM measured within these without creating degeneracy in these objects, a mass of greater than $\mathcal{O}100eV$ is required. The exact value of this bound, however, depends on the sample of DSphs utilised, and can, in fact, be shifted [148].

Thermal overpopulation denotes a limit that applies only to thermally produced sterile neutrino DM. This limit bounds the parameter space for which thermally produced sterile neutrinos would exceed the current relic DM density, negating such values of the interaction strength and mass as a possibility. It should be noted that this applies to any sterile neutrino that undergoes mixing with the SM neutrino. Exceptions to this bound can only be achieved by DM candidates that have a theoretical framework in which a different thermal history to the Universe is posited, or that suppress neutrino production at temperatures of several hundred MeV [69].

One possible mechanism for DM production, is resonantly enhanced thermal production requiring an enhanced lepton asymmetry (see [69], for a full description of this scenario). However, such a DM production mechanism is bound by the fact that this lepton asymmetry at a sufficient level will affect the values of Big Bang nucleosynthesis [149]. Thus resonantly produced keV scale DM is bound by a range of the parameter space that exceeds this value.

The Lyman-α forest refers to a cosmological tool, whereby measurements of the Lyman-α hydrogen transition line from extremely distant galaxies are utilised to map interposing gas clouds [150]. This is done by mapping the spectral changes to the line in a given direction and is used in dark matter studies as a means of measuring the free-streaming length of the early Universe. As has been covered in previous sections, dark matter candidates are bound by their free streaming scales,

as they must have streaming scales sufficiently low to allow for observed structure formation. In order to fulfil this, observations of the Lyman-α forest can be used to derive bounds on dark matter parameter spaces, showing values of the candidate's parameter space that would lead to free streaming lengths compatible with structure formation [151].

Finally, in some studies, the observation of the tentative 3.5 keV line is shown. This line was first detected from stacked XMM-Newton analysis of 73 galaxy clusters, in which an unexplained line was detected at a significance of greater than $> 3\,\sigma$ [152]. With no known explanation for this line, a dark matter hypothesis was posited. However, although confirmed in other galaxy clusters [153], this line was not seen in other astrophysical objects as is expected of a DM signal. The line remains a controversial topic among the community, and more recent studies perhaps indicate this line was an exotic transition line or the result of mismodelling [154].

1.4.2 Indirect Annihilating Dark Matter Searches

Annihilating dark matter searches, though generally model-independent, typically try to detect the products of WIMP annihilation given its testability and motivations as a theory. Importantly, the search itself is principally attempting to detect the secondary emission from a given annihilation's final state. Although perhaps the most well-motivated and broadest of such theories is the WIMP paradigm, indirect searches formally probe for any DM candidate that can annihilate into the final state channels being probed. Annihilating DM searches usually display limits on the velocity averaged annihilation cross section ($\langle \sigma v \rangle$) as a function of mass. This allows for an accurate and unified method of comparison between objects.

Given the many possible final states of DM annihilation, limits for indirect annihilating DM searches are calculated for individual final state channels (see Sec. 1.3.4, specifically Eq. 1.15). For simplicity and the purity of the limits, this almost always assumes a 100% branching ratio to a given channel (see Eq. 1.16), though this is unlikely to be the case in nature. As such the limits derived for indirect annihilating DM searches are individual to a given final state.

Figures 1.18 and 1.19, both show recent dark indirect annihilating dark matter studies. As can be seen in the latter figure, searches are now able to probe down to the value of $\langle \sigma v \rangle$ that one would expect a weak scale particle to have in order to fulfil the DM relic abundance.

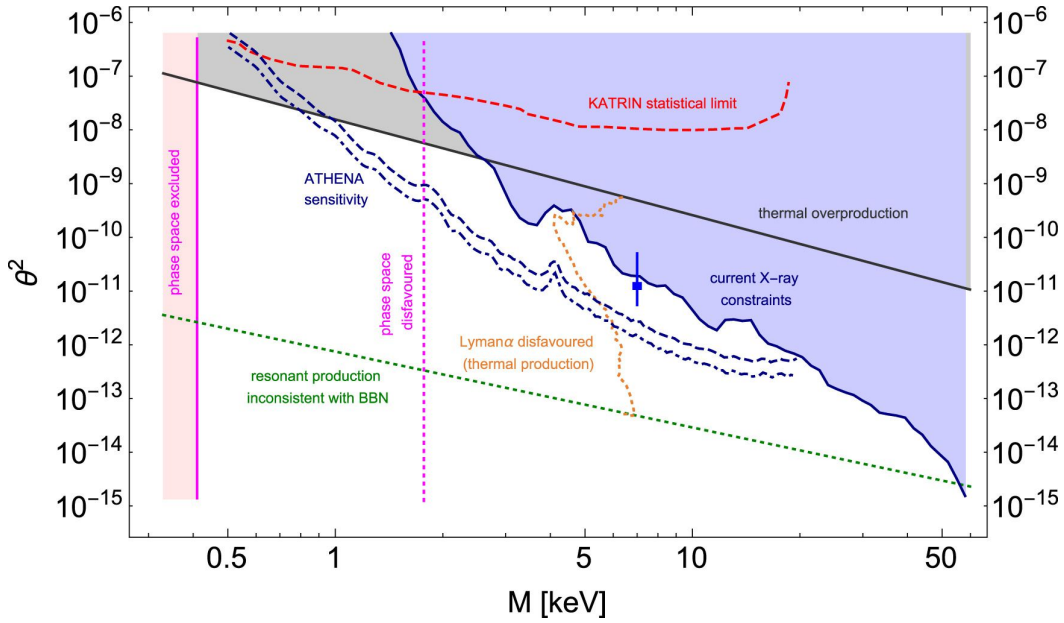

Fig. 1.16: The available parameter space for the mixing angle (θ) of the νMSM sterile neutrino as a function of mass. The figure displays a number of constraints including bounds derived from the non-observation of the characteristic decay line of the sterile neutrino, and further limits derived from theoretical interpretations. Among these, solid lines denote limits that are largely model-independent. The solid purple line represents the phase space-bound, a bound derived from the Pauli exclusion principle. The solid blue line that bounds the blue-shaded area denotes the previously probed parameter space. This corresponds to the range of masses and mixing angles that have already been excluded by the non-detection of the sterile neutrino's decay. The black line marks the thermal overpopulation bound. The denotes the parameter values which, for thermally produced sterile neutrinos, would lead to an overproduction of sterile neutrino DM as compared to the measured relic density. Below the dotted green line are the parameter values for which the required lepton asymmetries would lead to inconsistencies with Big Bang nucleosynthesis. Additionally, the dotted purple line shows the mass bound below which phase space arguments disfavour sterile neutrino DM. Blue dotted lines show two predicted sensitivities for the upcoming ATHENA mission. The yellow dotted line shows the lower limit value on the sterile neutrino mass as derived from Lyman-α forest measurements. Finally, the blue square represents the tentative 3.5 keV line measurement. See the text for further details on these limits. Figure taken from [69], see references within Fig.14 of this paper for further information on the derivation of these limits.

1.5 Summary

This chapter has introduced the phenomenon of dark matter and the methods used in the search for it. Particular emphasis has been given to the introduction of the dark matter problem and to outlining the numerous pieces of evidence for its existence. Following this, four well-motivated DM models were introduced including

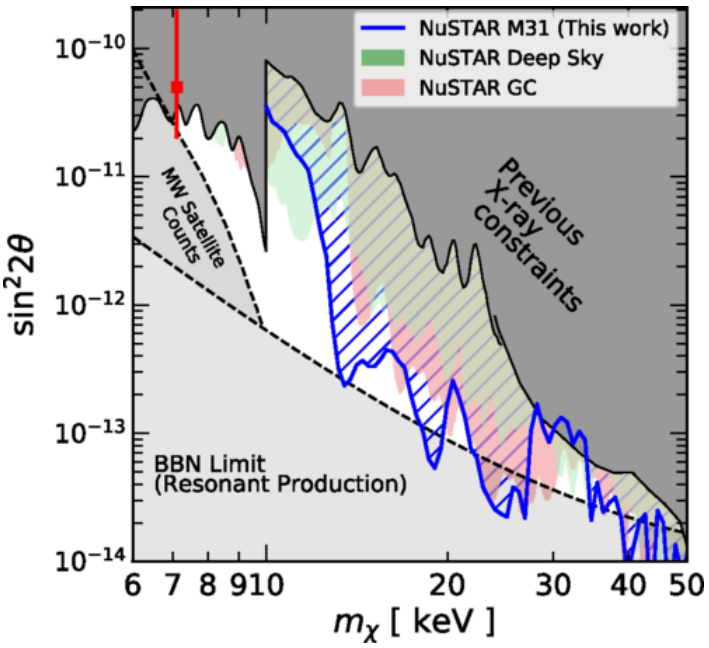

Fig. 1.17: Sterile neutrino limits from combined observations of M31 with NuSTAR. The blue region represents this work, whereas the grey regions indicate limits and constraints as marked in the figure. The red point corresponds to the position of the tentative 3.5 keV line detection. See the text of Sec. 1.4.1 for further details of these limits. Figure taken from [155].

WIMPs, sterile neutrinos and axions. The phenomenology of these models was explored, including their radiative emission mechanisms which would aid in the indirect search for them. The list of models introduced here is by far incomplete, and these particular models have been introduced due to their relevance in the works presented in subsequent chapters. The introduction in this thesis should not be considered an exhaustive list of models nor of their phenomenology.

Additionally, this chapter has introduced the three main methods of dark matter detection: direct detection, collider production, and indirect detection. Given the works presented later in the thesis, a special emphasis has been placed on the details of the indirect detection searches. This includes a discussion of the form of dark matter signals from different models, dark matter distribution (and a wider discussion of J-factors) and targets for indirect searches. Finally, the details of recent indirect decaying and annihilating dark matter searches were given, to provide the reader with an idea of the current state of the field.

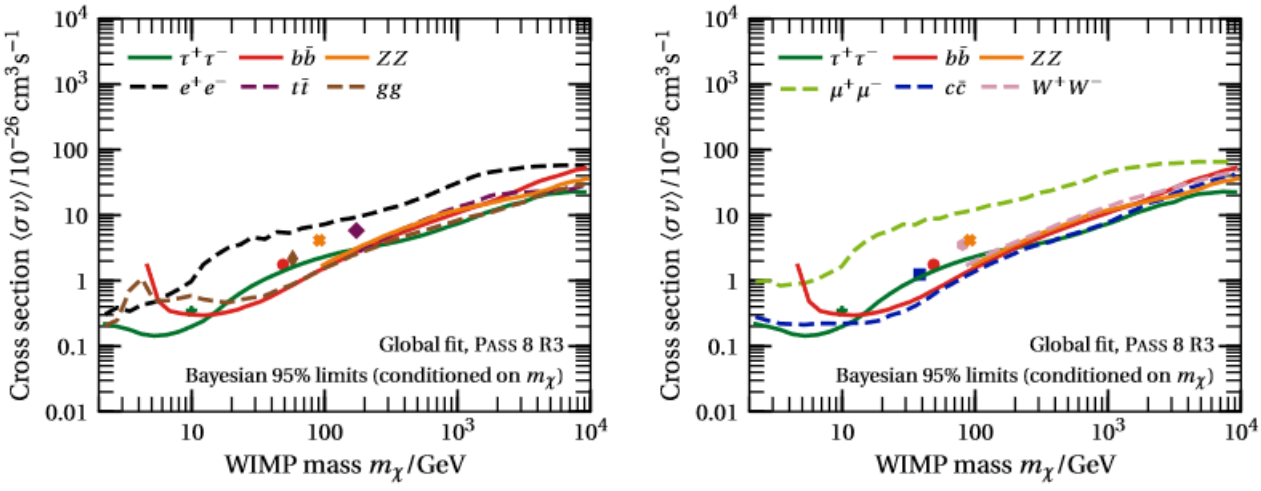

Fig. 1.18: Recent limits on annihilating DM, derived from the stacked analysis of 27 DSphs, from 11 years worth of *Fermi-LAT* data. The analysis was undertaken in nine different final state channels from a stacked analysis of all 27 DSphs. The data were further analysed under the *Fermi* Pass 8 configuration, and are presented at a 95% c.i. from Bayesian statistics. Figure taken from [156].

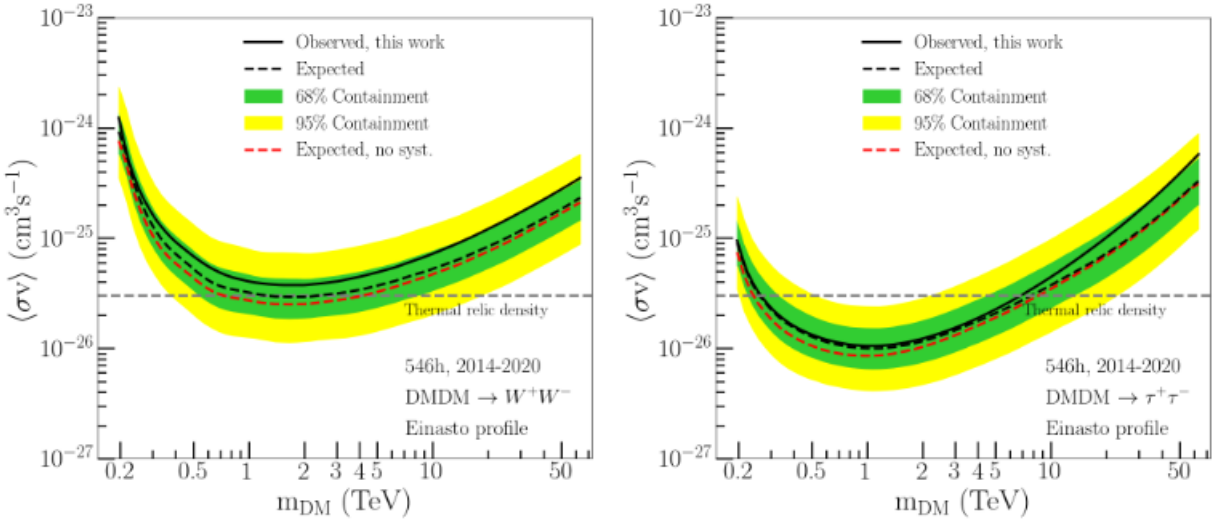

Fig. 1.19: Limits on the velocity averaged annihilation cross section of WIMP DM, calculated using an extensive VHE dataset of the galactic centre from the H.E.S.S. array. The figure shows the limits from the annihilation of DM into two final state channels. Also shown in the figure are the 95% and 68% c.i.. The dashed horizontal line marks the value of $\langle\sigma v\rangle$ that would correspond to the observed relic density of DM, as per the WIMP miracle (see Sec.1.2.1). Figure taken from [157], see paper for the limits on additional final state channels.

2 X-ray and High-energy Instrumentation

While there is no unified definition of when UV radiation becomes X-ray, typically X-rays are assumed to begin between the wavelengths of 8 nm to 0.008 nm, corresponding to an energy range of 100 eV to 100 keV respectively. The fundamental challenge of X-ray astronomy (and indeed High-energy (HE) astronomy in general) is the opacity of the Earth's atmosphere to high-energy radiation. This prevents astronomical observations of high-energy radiation, and must thus be circumvented. This requires (in the vast majority of cases) detectors to be taken to extremely high altitudes where the atmosphere is thinner, or to be taken outside the bounds of the atmosphere altogether. The requirements of lifting a detector outside of the upper atmosphere constitute a significant technological boundary that must be overcome before observations can be made. This meant that despite the discovery of X-rays in 1895, and predictions of its emission from astrophysical objects, observational X-ray astronomy did not start until the mid 20^{th} century.

2.1 The History of X-ray Astronomy

The field of experimental X-ray astronomy began in 1948 when U.S. researchers recorded solar X-rays for the first time after mounting X-ray detectors to a formerly German V2 rocket [158]. Launched at White Sands Proving Grounds (New Mexico), the advent of rocket technology allowed researchers to carry detectors far higher than balloons, thus escaping the atmosphere and its attenuating effects on X-ray radiation.

Throughout the 1950s and 60s rocket technology (as well as detector technology) increased dramatically, allowing increasing possibilities for further sustained X-ray astronomy. In 1962 the first extra-solar source of X-ray emission was detected from the constellation of Scorpius [159], cementing many theories that X-ray radiation was present and likely abundant in the cosmos. Moreover, this, and several subsequent missions, detected an almost uniform X-ray background, implying a population of astrophysical X-ray emitters responsible for the readings. The period of X-ray

astronomy following this discovery was marked by an extremely rapid generation of satellites such as Uhuru, SAS-3 and Ariel 5. This period was marked by the search and classifications of the brightest X-ray emitting objects, objects such as X-ray Binaries (XRBs) and Galaxy clusters.

In 1979, however, the launch of the Einstein Observatory (EO) marked the first dedicated X-ray telescope (making use of grazing incident optics) subsequently marking a new era in X-ray astronomy. The EO was able to provide thousands of images of a variety of astrophysical sources such as stars, XRBs and AGN.

The development of the Charge-coupled Device (CCD) and their use in X-ray astronomy throughout the 1990s further propelled the field forward. The advantages of increased spatial and energy resolution allowed a near-exponential increase in the discovery and cataloguing of X-ray sources. Additionally, several all-sky surveys were conducted allowing increasing knowledge and cataloguing of the X-ray sky. It was this era that laid the foundations of the understanding we have of the X-ray Universe in the present day.

2.2 Imaging Astrophysical X-rays

At the most basic level, detecting astrophysical X-rays concerns the acquisition of three properties of the incident photon: energy, direction and time. The methods utilised to obtain these over the history of X-ray astronomy have changed and generally improved, allowing for greater resolution of these parameters.

To attain these measurables X-ray telescopes usually collect photons from a large area and concentrate them onto a smaller detector (most commonly a CCD), this records the photon's attributes and is read out by onboard electronics. Additionally, the contribution of X-rays from unresolved sources (as well as local particle populations in the vicinity of the satellite) forms an irreducible background which must be accounted for and shielded against. X-ray instruments, therefore, often have shielding to prevent X-rays from outside the FoV from entering the collection area and contaminating the signal.

2.2.1 Mirrors and Optics

The reflection, absorption and transmission of light are all governed by the complex index of refraction

$$n = 1 - \delta - i\beta \tag{2.1}$$

where δ indicates the change of phase for the oncoming wave and β accounts for the absorption. These two parameters are a function of energy. At X-ray energies, this has the effect that the real part of Eq. 2.1 $(1 - \delta)$ is slightly less than one for matter, whereas it has the exact value of 1 in a vacuum [160]. The result of this is that traditional mirror and focusing techniques are ineffective when applied to X-rays. Given their high-energy and respective short wavelengths, X-rays have extremely low reflectivity at high incidence angles as are used in traditional optics. Incidence angles around the normal typically result in the near complete absorption/transmission of the incident X-ray, meaning the principles utilised at optical wavelengths are wholly ineffective. However, reflection becomes increasingly effective at smaller incidence angles (larger grazing angles). At small enough incidence angles, X-rays can undergo total external reflection, meaning an incident photon is completely reflected. This happens when an X-ray is incident at an angle below the critical grazing angle α_{t}

$$\cos(\alpha_{\mathrm{t}}) = 1 - \delta \tag{2.2}$$

where δ (having the same definition as before) is generally proportional to the atomic number of the reflecting material [160]. Thus by utilising total external reflection (ensuring X-rays are incident at angles less than the critical angle), it is possible to focus X-rays down to a far smaller angle.

This is typically achieved using grazing incidence optics. Grazing incidence optics focus on an incident X-ray using multiple reflections at very small grazing angles. By using a total hyperbolic or parabolic shape, each subsequent reflection can allow an increased change in the original direction of the photon, meaning large enough arrays of grazing mirrors can focus large X-ray collection areas down to a single focal point [160].

The most common design utilised in X-ray astronomy is the Wolter Type-1 (Wolter-1) telescope[1] [161], which utilises a series of parabolically and hyperbolically arranged mirrors to achieve low grazing angles thus focussing incident X-ray radiation. As shown in Fig. 2.1, Wolter-1 telescopes are typically produced in modules of concentrically nested mirrors. This design allows for the maximum collection of incident

[1] Named after its designer Hans Wolter.

X-rays, achieving large effective aperture areas with less complex alignment and manufacturing than other systems [160]. For these reasons, the Wolter-I telescope is used in almost every X-ray telescope and has been utilised on such pioneering missions as XMM-Newton, Chandra X-ray Observatory (CXO) and Nuclear Spectroscopic Telescope Array (NuSTAR), to name but a few.

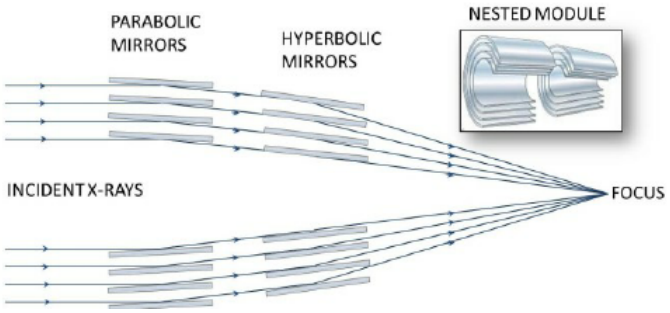

Fig. 2.1: Schematic diagram of the working principle of a Wolter I style X-ray telescope. Incident X-rays are reflected at very shallow angles by a combination of parabolic and hyperbolic mirrors focusing them down onto a point. The use of grazing angles minimises absorption and transmission of the X-ray. As shown in the figure, nested modules of concentric circular mirrors are used to maximise the collection area of the telescope. Figure taken from [162].

2.3 X-ray Data

In general, astrophysical fluxes of X-rays are significantly lower than fluxes at larger wavelengths. This means that individual events often correspond to a single X-ray photon recorded by a CCD. The goal of most standard X-ray telescopes is, therefore, to glean the aforementioned three pieces of information from the limited number of incident photons: the energy of the photon (or a proxy for this value), the direction from which it originated and the time at which it was incident. The energy of the photon is usually determined by the number of electrons that the incident photon has caused to be read out in the detector. A common occurrence is that incident X-rays will cause excitation in the depletion regions of multiple adjacent CCD pixels (as shown briefly in Fig. 2.2). A pattern recognition algorithm is therefore utilised to ensure that multiple excitations in adjacent pixels, occurring within the same frame, are combined into a singular event. Additionally, the location of the pixel (sometimes aided by auxiliary mechanisms like coded masks) determines the direction of origin for a given photon. Finally, the arrival time can be determined to a precision of the time taken for a single frame of readout (as an example, for XMM-Newton's EPIC-pn this is a readout time of 73.4 ms for the full frame [163]). For these reasons, unlike

optical counterparts which record the levels of integrated flux, X-ray telescopes measure the properties of these individual photons and store them in an event list.

2.3.1 Event Files

Raw X-ray data is comprised of an event list of putative photons. This list itself constitutes a 4-dimensional array of detector position (x and y), time and event energy. Commonly, photons will have additional information on top of these attributes stored in the file that will allow for further filtering. By choosing along which axis the data is binned, one can principally determine the output product. Images, for instance, are binned along the spatial axes but lose information on timing and energy. Thus, although end products represent the data in differing ways, the binning of such data loses information at some level.

The energy of an incident X-ray is measured as an instrumental energy estimate, falling into a discrete spectral channel (analogous to a bin). The energy value is therefore returned as an integer channel number known as the Pulse Height Amplitude (PHA)[2]. The value of the PHA is proportional to the reconstructed energy as related by the gain, a constant that varies with time and with the detector/pixel position. A schematic of this is shown in Fig. 2.2.

Commonly instruments correct the PHA channel for gain, creating what is known as a Pulse Invariant (PI) channel. This is a value representing PHA values that have been adjusted according to the gain, as well as to an instrument-specific and fixed constant proportional to the energy. This allows instruments with multiple detectors to create a common energy scale for their events, as well as produce a normalised event list for individual detectors alike. Each PI channel is then proportional to a range of reconstructed energy values (a PI channel in Neutron Star Interior Composition Explorer Mission (NICER), for example, corresponds to 10 eV [164]). However, these values are not convolved with the Redistribution Matrix File (RMF) and thus do not represent the true energy.

2.3.2 Instrument Response Files

The PHA list so far represents the detector's best estimate of the properties of incident photons. Biases in the detectors themselves as well as external factors that would

[2]The term PHA originates from the amplitudes of the pulses measured as part of older proportional counter technology, which is no longer widely utilised. The terminology has, however, stuck.

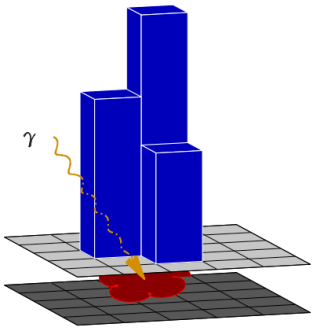

Fig. 2.2: Diagram of the principle of PHA generation. An incident photon (yellow) strikes the CCDs, creating a cloud of electron-hole pairs, shown in red. The charge cloud is read as a digital signal, forming the PHA in a given pixel. The height of a pulse here is determined by the incident energy and represents the channel in which it will be recorded. In this example, a single photon excites three pixels, which will be read out as a single photon by pattern recognition algorithms. Figure taken from [165]

introduce systematics are not, yet, accounted for, and must be correctly attributed to provide an accurate measure of a photon's quantities. This is done by convolving the events files with Instrument Response Functions (IRFs).

Ancillary Response File

The Ancillary Response File (ARF) contains the instrument's effective area as a function of energy, as shown in Fig. 2.3. This accounts for the sensitivity of the instrument at different energies resulting from the energy dependence of physical processes and different materials. This file accounts for the physical collection area of the instrument as a product of the energy-dependent efficiencies of the mirrors, filters, gratings (if present) and the detector itself.

As a result of detector defects, as well as vignetting, the ARF will differ between extraction regions (source position). Moreover, for telescopes that dither[3] the ARF will change during the observation, thus observation history and details are used to calculate an average ARF for the source.

[3]Dithering is a strategy employed by X-ray telescopes where the position of the optical axis on the sky is changed (according to a predetermined pattern) over the course of an observation. This allows greater angular resolution for some detectors, as well as negating the loss of photons to bad pixels, which would be completely lost for a static observation [166].

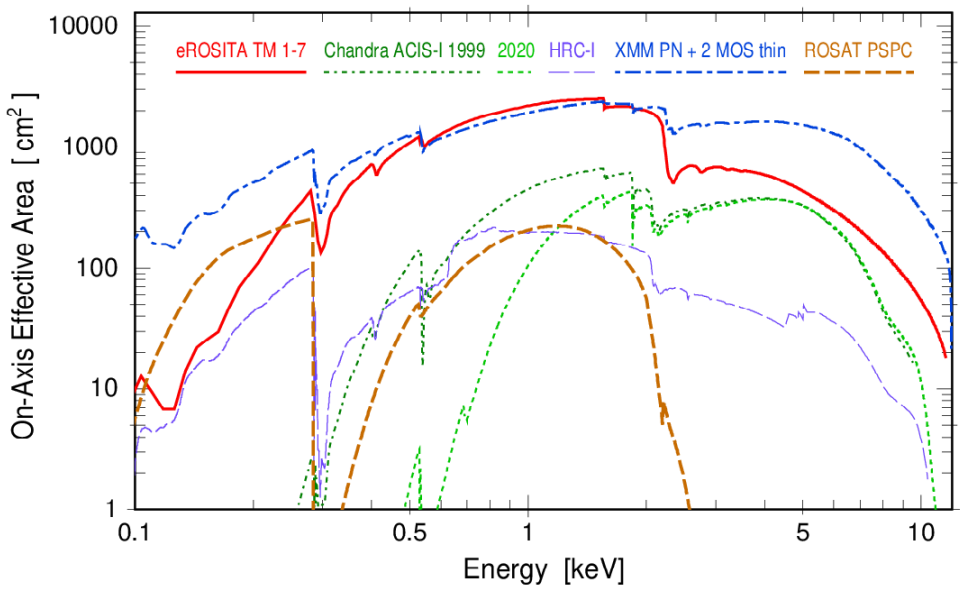

Fig. 2.3: Comparison of the effective areas of several X-ray missions. The effective area is a measure of the effective collection area an instrument has as a function of energy. The energy dependence of this value originates from the energy dependence of various physical processes and the energy-dependent properties of optics and detectors. Figure taken from [167]

Redistribution Matrix File

After accounting for the biases and non-uniformities in the optics and detectors, the RMF is used to convert the various pulse heights/channel values into reconstructed energy, reproducing the incident energy as accurately as possible. The RMF is a matrix that represents the relationship between the energy of an incident event, and its distribution over channels as recorded by the detector. The matrix therefore recounts the probability that a photon in a given channel had a given incident energy, as shown in Fig. 2.4.

Modern missions commonly combine the ARF and RMF into a single Response (RSP) file, presenting a matrix pre-convolved with the instrument's and observation's effective area.

Bad Pixel File

Bad pixel files contain lists of pixels that require correction or exclusion from the observation. For example, this can be for "hot" pixels, pixels which are temporarily compromised, as well as bad bias values or bias parity errors. Bad pixel files allow

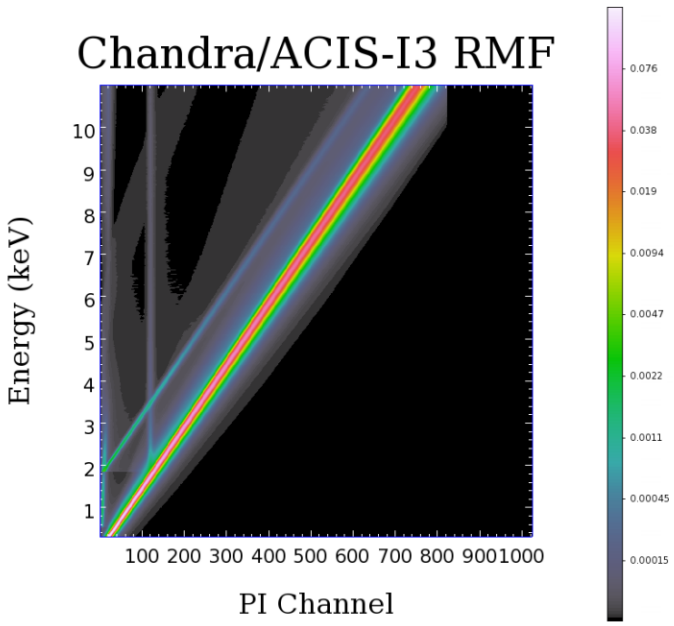

Fig. 2.4: An example RMF for Chandra's ACIS-13 detector, plotted to demonstrate the dependence of measured channels on reconstructed energy. The accompanying colour scale is logarithmic and represents the probability that a photon of a given incident energy will be recorded in a given channel. Figure taken from [165].

the exclusion of events reported from bad pixels, as well as the production of an exposure map.

Instrument and Exposure Maps

To correct for differing exposure, one must adjust for the differing quantum efficiency of the mirrors and detectors. An instrument map is an image of the instrument's sensitivity for a given observation. Convolving this with the aspect solution of the observation produces an exposure map, showing the different efficiencies across the detector. Creating this allows one to account for variations in exposure across the image.

2.4 The History of High-energy Astronomy

Before the first gamma-ray observatories were possible, it had long been theorised that high-energy processes in the Universe could lead to detectable emission. Proposed mechanisms by Primakoff and Morrison [168] (among others) led the way

in providing theory on mechanisms that could result in fluxes at gamma-ray energies. Such mechanisms included magnetic field interactions, supernovae and the interactions of cosmic rays with intermediate gas.

Fortunately for life on Earth, the planet's atmosphere is largely opaque to incoming gamma rays. On the contrary, this fact constitutes a significant barrier to gamma-ray astronomy requiring any potential instrument to have the prerequisite technology to reliably carry a detector outside of the atmosphere and return it (or return the data via telemetry). For these reasons, gamma-ray astronomy is one of the youngest branches of observational astronomy, with the first gamma-ray telescope launched aboard the Explorer 11 NASA satellite in 1961.

Explorer 11 returned with 9 hours of gamma-ray data resulting in 22 gamma-ray events and 22,000 cosmic ray events, noting an isotropic distribution of the former with no preference or clustering towards the galactic centre [169]. We now know that this asymmetric isotropic distribution is most likely originating from cosmic ray interactions with interstellar gas.

After a series of small space-bound gamma-ray experiments (such as OGO, OSO, Vela and Cosmos) the first dedicated gamma-ray satellite was the Small Astronomy Satellite - 2 (SAS-2) launched in 1972. Although only lasting seven months, this marked the beginning of long-term gamma-ray missions in space and the real beginning of dedicated gamma-ray astronomy. The results from SAS-2 confirmed the isotropic gamma-ray distribution that explorer 11 had detected, as well as detecting several point sources.

One of the first major discoveries in the field came as an unexpected detection by the Vela satellites. These satellites were a constellation of defence satellites pointed at Earth, designed to detect the characteristic double flash of a nuclear blast. To the surprise of the defence organisations operating them, the satellites would repeatedly report extremely bright gamma-ray emission from the direction of space rather than the Earth. These flashes would occur from random directions lasting seconds to minutes before disappearing entirely. Vela had of course made the first serendipitous detection of a Gamma-ray Burst (GRB), though these flashes remained a mystery for a considerable amount of time.

Throughout the 1980s and 1990s, gamma-ray astronomy benefited greatly from increased interest and advances in detector technologies. As well as satellites, this time period saw an increase in the use of high-altitude balloons as a method of transporting instruments outside of the atmosphere. Perhaps the most famous and

influential progenitor to modern missions, however, was the Compton Gamma Ray Observatory (CGRO).

The CGRO was the highest energy addition to NASA's "Great Observatories" initiative, designed to provide legacy observatories that would cover most of the electromagnetic spectrum. Launched in 1991, it hosted a series of 4 instruments allowing it to cover an energy range from 20 keV in X-rays to 30 GeV in gamma rays. The CGRO was able to make several key steps forward in the field including confirming an isotropic distribution of gamma-ray bursts, mapping the Milky Way in gamma rays[4] for the first time and identifying that the highest energy cosmic rays originated from blazars. Above all the CGRO was perhaps the first gamma-ray instrument with modern capabilities. Featuring a sensitivity and extension great enough to perform extensive analysis of the data, the CGRO paved the way for contemporary astrophysics and provided a glimpse into just how intriguing the gamma-ray Universe can be.

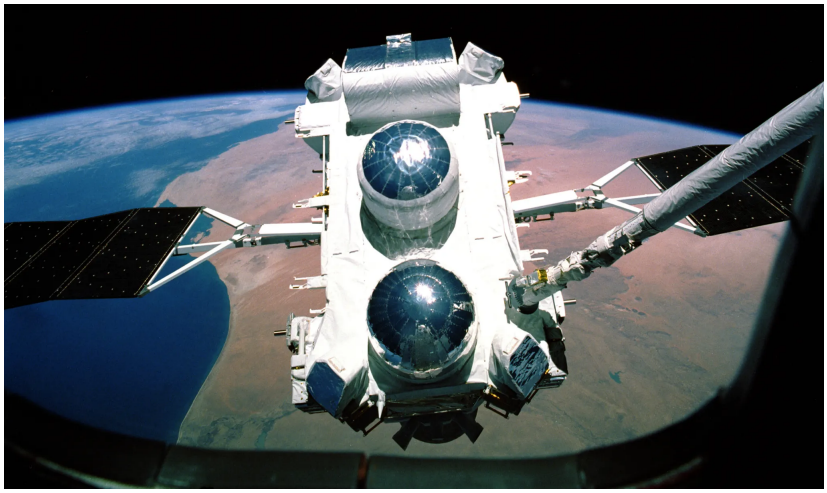

Fig. 2.5: The CGRO being released into orbit from the space shuttle Atlantis, on the 7th of April 1991. Image taken from [170].

2.5 Contemporary High-energy Astronomy

Following CGRO, modern-day gamma-ray astronomy (in the GeV band) is dominated by satellite missions. The technological advancements in the field of satellite deployment made in the 1990s and 2000s made space-based telescopes more accessible to space agencies, resulting in the launch of the current generation of telescopes

[4]This mapping was not strictly a gamma-ray survey as in modern instruments, but rather CGRO mapped the gamma-ray transition line from Aluminium 26 in the galactic plane.

covering a broad range of the electromagnetic spectrum. In the MeV-GeV energy range, some examples of missions are the *INTErnational Gamma-Ray Astrophysics Laboratory (INTEGRAL)*[5], *Astro-Rivelatore Gamma a Immagini Leggero (AGILE)* and *Fermi* satellites.

INTEGRAL is an ESA mission launched on October 17th 2002 which is still collecting data at the time of writing, it operates primarily in the energy range 15 kev to 8 MeV allowing it to perform observations and effectively identify high-energy transient sources [171]. Its main science goals revolve around the investigation of high-energy emitting phenomena and objects in the Universe, these include compact objects and GRBs. The mission also undertakes extragalactic astronomy and high-resolution spectroscopy studies. As one of the first gamma-ray instruments following CGRO, INTEGRAL has proved a cornerstone of modern gamma-ray investigations and has prolifically been involved in the discovery of new high-energy phenomena and sources, often abetting studies at other wavelengths by providing a high-energy window into the constituent physics [171]. Of particular note is that INTEGRAL was able to detect the counterpart gamma rays from the merger event responsible for the first gravitational wave signal detection GW150914.

Similarly, AGILE is a gamma-ray instrument dedicated to the study of the gamma-ray Universe launched by the Italian space agency on the 23rd of April 2007 [172]. Its gamma ray imaging detector is sensitive in the 30 MeV to 50 GeV range allowing it to probe to higher energies than INTEGRAL [172]. Much like INTEGRAL, it expanded upon the discoveries made by the CGRO by probing high-energy emission regions and objects. AGILE made key discoveries in the field, such as variable gamma-ray emission from the crab nebula, and the discovery of gamma-ray emission from the micro-quasar Cygnus X-3 [172].

Perhaps the most renowned gamma-ray observatory of the modern era, however, is the *Fermi* Gamma-ray space telescope mission, launched by NASA on June the 11th 2008 [173]. See Sec. 2.8 for full details of *Fermi*. Notably, *Fermi* is responsible for many key discoveries in the field such as the *Fermi* bubbles emanating from the galactic centre (that take their name from the mission), counterparts to gravitational wave discoveries and the discovery that the Crab Nebula is in fact a variable source in gamma rays [173]. Testament to the scientific rigour of the mission it continues to be operational 5 years after the initial planned mission ended and remains a cornerstone of high-energy observations to this day [173].

[5]Formally, *INTEGRAL* spans 4 keV - 10 MeV making it more of an X-ray instrument.

2.6 THESEUS Mission Summary

The Transient High Energy Sky and Early Universe Surveyor (THESEUS) (see Fig. 2.6) is a mission concept designed (originally) as a candidate for the medium-size mission category (M5) within the framework of the European Space Agency's cosmic vision program[6]. Broadly, THESEUS will be equipped to probe from the epoch of reionisation, up to the epoch in which the first stars formed ($z \sim 6$ to $z \sim 10$). THESEUS's primary scientific goal will be to investigate the first GRBs and produce a complete census of their primordial population. In its investigation into earlier universal epochs, THESEUS will also provide insight into the universal history of star formation, as well as study the first population of stars (population III stars) and their environments. Additionally, under its early Universe studies, THESEUS will investigate the conditions of the Interstellar Medium (ISM) and cosmic environments during the reionisation epoch, as well as measure star formation in the first galaxies. The secondary scientific goal of THESEUS is to perform extensive monitoring of the X-ray transient Universe. To accomplish this, the instrumental suite will act to locate and identify the EM counterparts of gravitational wave or neutrino triggers from other experiments. On top of this, THESEUS will provide real-time triggers and accurate positions of high-energy transient events such as GRBs.

To achieve these ambitious scientific goals, THESEUS will host a broad range of instruments monitoring large swathes of both X-ray and gamma-ray wavelengths. THESEUS will also host a near-infrared telescope, allowing it to further expand its scientific capabilities with transient phenomena identification and redshift determination. The suite of instruments planned to allow THESEUS to complete these goals is as follows:

- The Soft X-ray Imager (SXI) is an instrument comprising 4 identical lobster-eye telescope units, sensitive in an energy range of 0.34 to 6 keV. The four telescope modules will form a roughly square FoV, covering a solid angle of ~ 1 sr, and providing location accuracy of sources at $< 1''$ to $2''$. See [174] for a full breakdown of the planned instrument and its capabilities.

- The X and Gamma-ray Imager and Spectrometer (XGIS) is a detector array of monolithic X-gamma ray detectors, coupled with coded-mask cameras. These detectors are a coupling of silicon diodes with a CsI scintillator, allowing the instrument to be sensitive in the 2 keV to 20 MeV energy range. This broad range of energies will be probed by utilising two different styles of detector

[6] See the cosmic vision website for further details `https://www.esa.int/Science_Exploration/Space_Science/ESA_s_Cosmic_Vision`.

within the instrument. These two detectors are the XGIS-X and XGIS-S. XGIS-X will utilise Silicon Drift Detectors (SDDs) (covering the energy range 2 to 30 keV). The CsI scintillators on the other hand will allow the XGIS-S to operate in the energy range 20 keV to 2 MeV. For XGIS-X the effective area of the instrument at 10 keV is $A_{\rm eff} \approx 500$ cm^2, with an $\Delta E/E \approx 1.5\%$. The XGIS-S will have an effective area of $A_{\rm eff} \approx 1100$ cm^2 (at 300 keV). The $\Delta E/E$ of the XGIS-S will be $\sim 15\%$ below 100 keV and $\sim 2\%$ above this value. For further details and specification of the XGIS, see [175].

- The Infra-red Telescope (IRT) is an instrument aboard THESEUS that will be used to provide follow-up observations GRBs. The telescope will have a 0.7 m mirror diameter, covering an FoV of $15' \times 15'$, in the wavelength range 0.7 μm to 1.8 μm. For further information about the IRT, please see [176].

It is important to disclaim that, during the time between writing the accompanying paper (for which this section provides an introduction to THESEUS) and the writing of this thesis, the situation regarding the THESEUS mission became somewhat more complicated. Namely, in 2021 the Envision mission was chosen as the M5 mission for European Space Agency (ESA), rather than THESEUS. The reader should note that, should THESEUS be successfully proposed as a mission in future, its specification may be somewhat different to what is listed above.

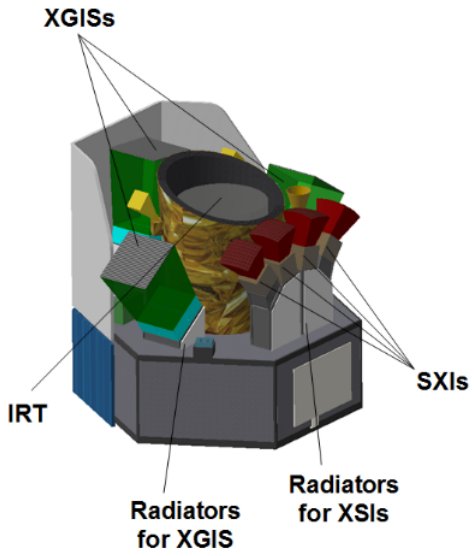

Fig. 2.6: A CAD model of the potential THESEUS mission and layout of instruments. Shown in the figure are the three main scientific instruments aboard THESEUS: the SXI, the XGIS and the IRT. Figure taken from [177].

2.7 eXTP Mission Summary

The Enhanced X-ray Timing and Polarimetry (eXTP) mission[7] [178, 179, 180] is an upcoming joint European-Chinese endeavour, primarily designed to study ultra-dense matter in neutron stars. Additionally, it will probe the equations of the state of neutron stars and exotic matter states resulting from extreme gravitational fields (such as in black holes or AGN). Further science goals include the study of QED effects in highly magnetised astrophysical objects and measurements of accretion onto X-ray pulsars and black holes. To achieve these science goals eXTP, will host a broad suite of both imaging and non-imaging X-ray instruments, these instruments are planned to cover a large section of the X-ray band from 0.5 to 50 keV. See Fig. 2.7 for an artist's impression of the mission. The planned instrumental payload of eXTP is as follows:

- The Spectroscopic Focusing Array (SFA) is an instrument comprising nine individual telescopes, covering an energy range of 0.5 to 10 keV. Each telescope module will have a FoV of $12'$ and a spatial resolution of $1'$, which will be achieved through the use of nested Wolter-I optics with coated glass focal elements. These optics, combined with SDDs (of < 180 eV spectral resolution), lead to a predicted effective area of ~ 0.8 m^2 at 2 keV and 0.5 m^2 at 6 keV for the SFA.

- The Large Area Detector (LAD) is a non-imaging X-ray instrument, sensitive between 2 to 30 keV (with a spectral resolution of < 250 eV), and is comprised of a series of 640 SDDs. The combination of these detectors will have an effective area of ~ 3.4 m^2 between 6 to 10 keV. Although for transient X-ray events of standard brightness, an upper energy range of 30 keV is expected, this may be as high as 80 keV for bright events such as magnetar flares and GRBs. The 40 modules of the LAD will be arranged in a 4×4 detector and collimator configuration, potentially achieving a FoV of $< 1^\circ$ at Full Width at Half Maximum (FWHM).

- The Wide Field Monitor (WFM) will provide eXTP with extensive sky coverage (a total FoV of 3.7 sr or $\sim 70^\circ \times 70^\circ$) in the 2 to 50 keV energy range. This will provide eXTP with an extended view of the X-ray sky, complete with on-board detection of bright events to trigger alerts. The instrument will consist of 3 pairs of coded mask wide-field units, each containing position-sensitive SDDs

[7] Please note, as eXTP is still in the planning phase, the details of the instrumentation and mission specifications may differ upon launch. For the purpose of this thesis eXTP has been introduced as per the specifications at the time of the publication of the related paper found later in this thesis (2020).

with a resolution of ~ 300 eV at 6 keV and a timing accuracy of 1 μs. Each constituent camera of a pair is only sensitive to the location of an arriving photon in one direction (there is a coarse sensitivity in the orthogonal direction however not accurate enough for pinpointing position). For this reason, each module in a pair is mounted at $90°$ to its counterpart, allowing for accurate 2D targeting for the pair. This mounting strategy will allow for an estimated positional accuracy of $1'$.

- The Polarimetry Focusing Array (PFA) is an instrument made up of 4 X-ray telescopes, operating in the 2 to 10 keV energy range. Each of these telescopes will be equipped with imaging gas pixel photoelectric polarimeters, allowing the measurement of the polarisations of incident photons. The instrument will have a total effective area of 900 cm^2 at 2 keV, as well as an FoV of $12'$ (with a projected angular resolution of $30''$).

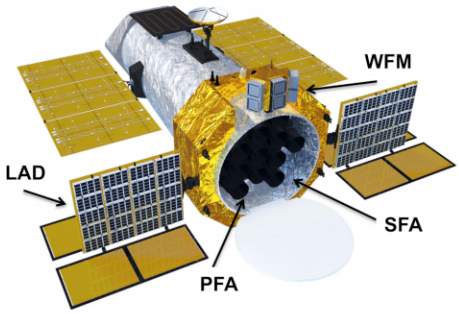

Fig. 2.7: An artist's impression of eXTP, with the major instruments highlighted. Figure taken from [180].

2.8 Fermi Gamma-ray Space Telescope Summary

The *Fermi* Gamma-ray Space Telescope[8] (*Fermi*) is a NASA mission launched on June 11th 2008 [173] (see Fig. 2.8 for an image of *Fermi*).

The *Fermi* satellite was placed in a low Earth orbit at an altitude of 565 km with an orbital inclination $28.5°$. This unique orbit enables *Fermi* to conduct observations in a survey mode, rather than capturing individual exposures of objects. In addition, *Fermi* alternates its pointing between orbits, with one orbit pointing $50°$ north and the following orbit pointing $50°$ south. Due to this orbital pattern, *Fermi* can scan the entire gamma-ray sky in just two of its 96-minute orbits.

[8]Initially this mission was named the Gamma-ray Large Area Space Telescope (GLAST) before the decision was made to change the name to something that would be more memorable.

Fermi is primarily a gamma-ray instrument, with a payload capable of detecting photons in the energy range 8 keV to 300 GeV. As an instrument capable of probing the higher energies of the EM spectrum, *Fermi's* science goals revolve around the exploration and observation of extreme environments in the Universe. While broadly this includes the study of all gamma-ray sources in the sky, more specifically *Fermi* is used to investigate the accretion and jets of black holes / AGN, GRBs, pulsar physics and the origin of cosmic rays and dark matter. *Fermi* is perhaps the most renowned gamma-ray observatory of the modern era due, in large part, to its versatility as an instrument and all-sky coverage. At the time of writing, *Fermi's* lifetime has been extended to 2025, with the possibility of further extensions to the mission.

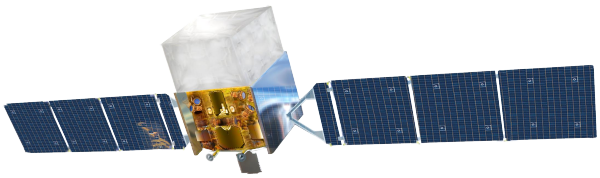

Fig. 2.8: An artist's impression of the *Fermi* satellite. Figure taken from [173]

2.8.1 Gamma-ray Burst Monitor

The Fermi Gamma-ray Burst Monitor (GBM) is the first of two instruments aboard *Fermi* primarily focussed on detecting GRBs and other high-energy transient events by providing burst triggers and locations. The instrument consists of two sets of detectors, which each contain twelve NaI scintillators, as well as two BGO scintillators. The NaI scintillators are advantageous in the range of a few keV to several MeV [173], where they provide the greatest sensitivity. The BGO detectors on the other hand provide coverage up to ~ 30 MeV, with a lower energy bound of ~ 150 keV providing good overlap with the NaI scintillators.

GRBs will be triggered following a significant change in the count rate of at least two NaI scintillators, which will then be communicated via telemetry, providing a trigger for other observatories. The instrument has an FoV of 9.5 sr as well as a time resolution of 2 μs [173].

2.8.2 Large Area Telescope

The LAT [181, 182, 183] is the second of two instruments aboard *Fermi* and provides the imaging capability for the mission in the energy range 20 MeV to 300 GeV.

Being sensitive to photons in the mid to VHE gamma-ray range means that the LAT can no longer take advantage of any focussing octics used at X-ray energies as, at these energies, photon absorption/transmission is near total at all incidence angles. Instead, the LAT utilises the pair production process in order to detect single incident gamma rays and reconstruct their energy and direction of origin.

To accomplish this, the LAT utilises techniques and detectors very similar to those used in terrestrial particle accelerators. A photon incident upon the LAT must first pass through a plastic anti-coincidence shield. This shield is made of a material designed to act as a scintillator for charged particles. A signal from this layer, therefore, allows the LAT to veto incident charged particles/cosmic rays, which greatly outnumber the incident gamma rays. After passing through the anti-coincidence shield, an incident photon will pass through layers of thin metal sheets, causing it to convert to an electron-positron pair via pair production. These metal sheets are vertically stacked layers of a high-Z material (tungsten), which provide a large nucleus to encourage pair production [181]. Additionally, these layers also contain stacked silicon microstrip detectors. The passage of a charged particle through these results in a charge signature. This can be recorded over various layers and is subsequently utilised to allow for the reconstruction and tracking of the electron-positron pair [181]. This will, in turn, allow the position of pair production to be determined and therefore provide information on the origin direction of the incident gamma ray.

Finally, the converted electron-positron pair enters a stack of CsI scintillators which form the LAT's calorimeter. By measuring the residual energy of the electron and positron, and combining this with the charge deposited in each layer of the microstrip detector and anti-coincidence detector, one can also reconstruct the energy of the incident photon.

Utilising these components, the LAT classifies a signal as a gamma-ray event on the following criteria

- The coincidence detector does not report a signal.
- Pair production is seen via the passage of two charged particles through the layers of microstrip detectors. These pathways must originate from the same point for this to indicate pair production.
- The calorimeter records an EM signal corresponding to the aforementioned charged particles.

- Simulations have provided additional parameters by which background events are rejected. More information on these simulations and their respective classification trees can be found in [184].

The LAT is a modular detector consisting of a 4×4 array of identical towers. Each of these towers contains the aforementioned tracking components (vertical layers of tungsten and microstrip detectors), an individual calorimeter and a data acquisition module. The calorimeter itself is comprised of eight layers of twelve CsI bars, arranged in a hodoscopic pattern, and is read out by photodiodes [181]. The LAT utilises dedicated simulations to account for the instrumental background. These simulations are important in the effort to reject background events as well as accurately reconstruct incident photons. The LAT has a FoV of 2.4 sr, a single photon angular resolution of $< 1^{\circ}$ (at 1 GeV) and a timing accuracy of 1 μs [183]. The survey mode operation of the LAT has allowed it to acquire a wealth of data and increasingly powerful simulations of the detector and photon reconstruction have, even recently[9], allowed for the improvement of the instrument's spatial and energy resolution capabilities.

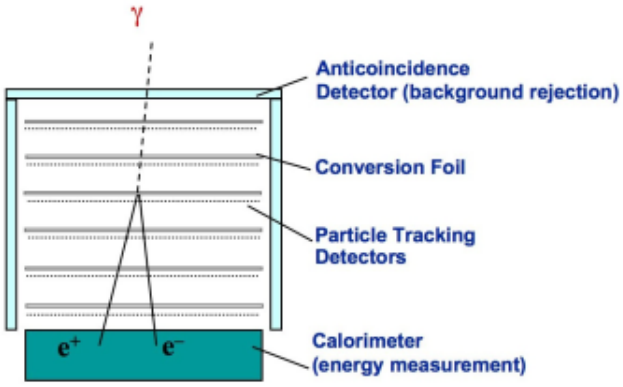

Fig. 2.9: A schematic diagram of the *Fermi-LAT*, displaying the various layers and the simplified path of an incident photon (and subsequent electron-positron pair). Figure taken from [185].

Fermi Analysis Pipeline

Here a brief overview of the *Fermi* data analysis pipeline will be given (see Fig.2.10 for a schematic overview of this process), for full details of the subject one should see [184, 186].

[9]Most recently was the Pass 8 update, improving *Fermi* data analysis greatly, see `https://fermi.gsfc.nasa.gov/ssc/data/analysis/documentation/Pass8_usage.html`.

Fermi's unique all-sky observation style results in a novel approach to calibration, reconstruction and background rejection. Incoming *Fermi* data is automatically reduced to create Data Level (DL) 3 products[10]. This is undertaken using *Fermi's* event-level analysis - a constantly updated series of event reconstruction algorithms that improve the accuracy of *Fermi's* data products. The most recent overhaul of this was the Pass 8 event reconstruction, and the P8R3_V3 is the most updated version of this at the time of writing.

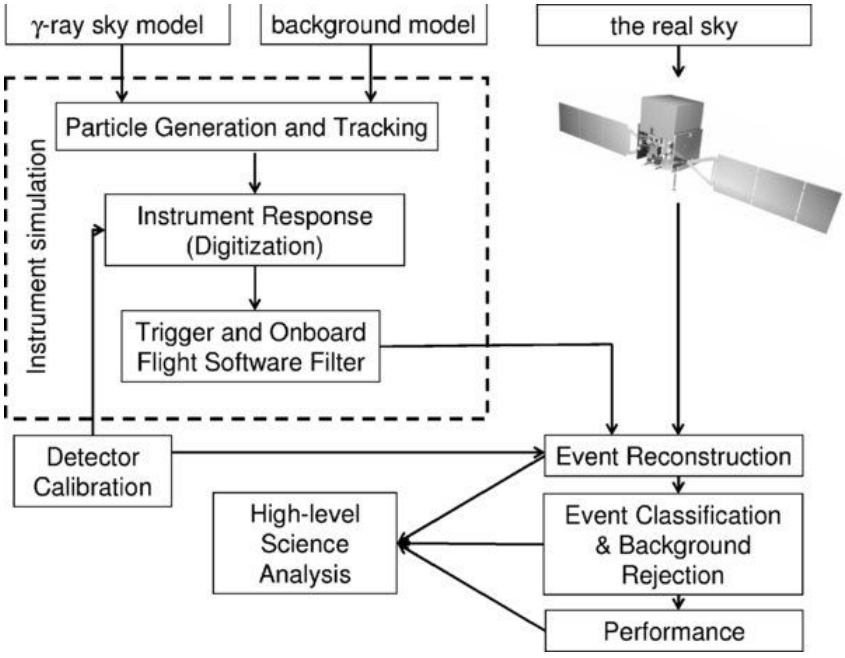

Fig. 2.10: An overview of the *Fermi* analysis pipeline, detailing the steps from particle tracking to reconstruction. Figure taken from [184].

Event Reconstruction

The task of event reconstruction within *Fermi* is a challenging one. One must take the extremely high levels of events and reject the background, before deriving measurable parameters on events with greater probabilities of being a true gamma ray. These measurables include energy, direction and the probability that the event is indeed a true gamma ray. An important part of this is having an accurate background model, which is derived from a combination of balloon and space-borne detectors. For example, the Alpha Magnetic Spectrometer (AMS) aboard the International Space Station measures the flux of cosmic rays in low earth orbit and has been used

[10]Events lists and IRFs, analogous to what is displayed in Fig. 5.9.

to develop background models of this radiation (See [187]). *Fermi* also utilises Monte Carlo simulations of detector response to the background as well as the response to gamma rays at all possible inclination angles and energies. Photons from various event classes then have their properties derived and compared to the input photons, allowing a derivation of the IRFs.

To derive events the data from the anti-coincidence shield, tracker and calorimeter must be combined and compared to the aforementioned Monte Carlo simulations. This comparison allows the reconstruction of astrophysical parameters from the response of these three sub-systems, such as the direction of origin and energy. Additionally, each event is given a likelihood of being the result of a true gamma ray, a parameter used to filter data quality in subsequent reduction stages.

To reconstruct the original direction of the event, the tracker utilises a global approach to particle tracking known as tree-based tracking. This method looks at the shower produced by the pair production of an electron and a positron. Crucially, this takes into account the hits on the tracker's layered detectors resulting from the energy radiated by the electron and positron moving through the tracker[11]. Thus the longest and straightest branches (subsequent detector hits) will be indicative of the primary electron-positron pair. Likewise, the radiation emitted from the primary pair's passage through the detector will result in sub-branches. By calculating the moments of inertia of all of these hits, the origin axis of the tree can be found. The axis of the tree then gives a photon's likely origin.

After calculating an axis, this can be used in combination with the data from the calorimeter to associate clusters of charge deposition with photons, thus associating an energy to a likely photon. As part of this process, a candidate photon is cross-checked with the anti-coincidence shield and is vetoed if it corresponds to a hit.

Event Selection

Events reconstructed by *Fermi-LAT* are divided into different quality levels depending on their likelihood of being a true gamma ray (a parameter defined in the previous step). At the user end, this allows control over the quality of the gamma-ray event used in the analysis, allowing varying levels of compromise between accuracy (the likelihood of an event being a true gamma ray) and statistics. This allows fine-tuning depending on the objective of the analysis.

[11] Previously only the primary electron-positron pair were tracked, however, this Pass 8 addition has greatly improved directional reconstruction of photons.

The 7 classes[12] range from the *TRANSIENT*, which maximises statistics over background, to *ULTRACLEANVETO* which imposes the strictest cuts on events available in standard *Fermi* analysis.

In addition to the overarching event classes, there are further sub-classes to enable a greater tailoring of the analysis. The first of these allows for the choice between selecting where photons convert. Starting from the top of the LAT and moving toward the calorimeter, the tracker is comprised of 12 layers of 3 % radiation length tungsten converters (the *FRONT* of the instrument) followed by 4 layers of tungsten at an 18% radiation length thickness (the *BACK* section). The thicker material found in the *BACK* section of the instrument is more prone to multiple scattering events, meaning that the *FRONT* section of the detector has an intrinsically better angular resolution. Since the pair production site is part of the analysis, one can choose to filter events from the *FRONT* or *BACK* only, depending on the goal of the analysis.

Additionally, events can be filtered according to the quality of the reconstructed direction and energy (though not simultaneously). Each of these quantities is subdivided into four quartiles depending on the quality of reconstruction. For directional reconstruction this amounts to the subdivisions *PSF0-PSF3* and for energy reconstruction, this is *EDISP0- EDISP3*, where 0 is the quartile with the worst quality and 3 the quartile with the best.

The selection of event class and subclass will ultimately decide on the IRFs used in the analysis, with each class and sub-class having an impact on the form of the IRF. Figure 2.11 shows an example of the impact of the different IRFs on the effective area.

High-level Data Analysis

To derive scientific results from the data, one must first download event data from the Region Of Interest (ROI) along with a spacecraft file for the observations in this area. Due to *Fermi's* survey operation, it is imperative that the position and orientation of the spacecraft are known so that they can be accounted for in the reconstruction of events. This information is stored in the spacecraft file.

The analysis of *Fermi* data is supported by the *Fermi* analysis software *Fermitools*[13], with the most recent version of *Fermitools* being 2.2.0. This package can be used to

[12] See `https://fermi.gsfc.nasa.gov/ssc/data/analysis/documentation/Cicerone/Cicerone_Data/LAT_DP.html` for a full list of the classes and their descriptions.
[13] `https://github.com/fermi-lat/Fermitools-conda/wiki`.

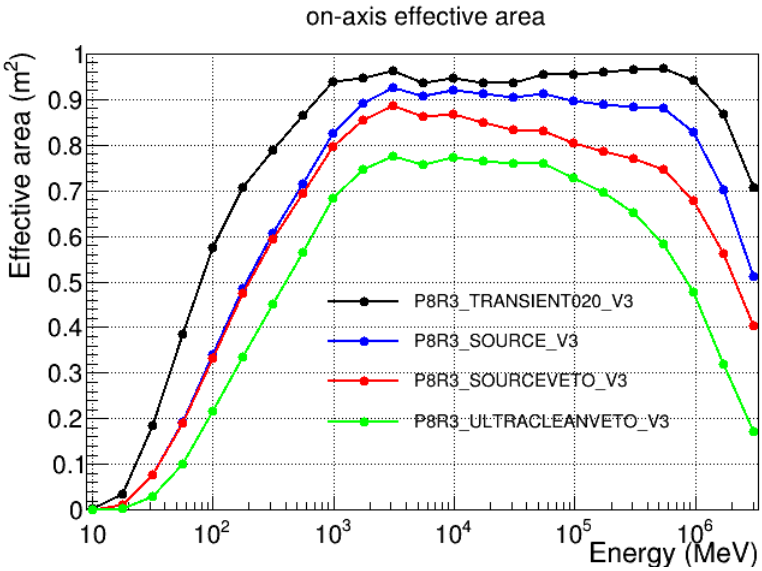

Fig. 2.11: A comparison of on-axis effective areas for the *Fermi-LAT* instrument. Different curves correspond to the effective areas of different classes within the *Fermi-LAT* analysis chain (see text for further details). Figure taken from [188].

undertake a full analysis of the data and perform the steps outlined in the following sections.

After file retrieval, one must make a cut on the zenith angle based on the analysis goal[14]. This avoids contamination of gamma rays from the Earth's albedo, but naturally a stricter cut reduces data. Following this one may specify time intervals, allowing the possibility to filter out periods that may have experienced instrumental issues or high background. Additional cuts can be made on the event class, filtering via the likelihood of being a photon to ensure a cleaner data set. The final step is to select the event class and the corresponding IRFs, as described in the previous section.

Likelihood Fitting

The goal of likelihood fitting is to generate a model of the gamma-ray sky and to iterate all the individual parameters of that model until it is as accurate a description of the true sky as possible. To achieve this, one must account for the models of individual sources as well as galactic interstellar emission (from the Milky Way and

[14]For further details of zenith cuts see `https://fermi.gsfc.nasa.gov/ssc/data/analysis/documentation/Cicerone/Cicerone_Data_Exploration/Data_preparation.html`.

extended sources) and isotropic[15] background (unresolved extra-galactic sources). In addition, it is possible to exclude sources or to add additional sources. For example, in order to search for dark matter, one may add an extended dark matter signal spatially following the DM density profile of an object, with emission defined by a set DM annihilation rate and channel (See Sec. 1.3.4). This model can be then iterated to find limits on the annihilation cross section of a given final state.

The models from individual sources are retrieved from a specified source catalogue of *Fermi-LAT* sources. The latest version of the *Fermi-LAT* catalogue is the 4FGL [189], which is currently in its fourth iteration (DR4) comprising 14 years of data [190].

With the model assembled, the spectral and spatial models of all the components are freed. Spatial models that best describe the source are used, thus accounting for extended or asymmetric sources. Spectral models can take a variety of forms such as a power law, Gaussian or log parabola[16].

The total model then undergoes likelihood fitting via a similar method outlined in 5.5.6. Through a number of iterations, differing values and combinations of model parameters are tested to find the combination that best reproduces the true gamma-ray sky. To do this the model must be convolved with the IRFs to compare the true gamma-ray sky, to the interpretation of *Fermi's* instruments to this.

2.9 Summary

This chapter has given an overview of the main methods of detection in both X-ray instruments and in the *Fermi* gamma-ray space telescope. This has included the methods by which X-ray instruments image astrophysical X-rays, including their unique mirror setups and detectors. An introduction to X-ray data was given along with its subsequent analysis to give context to later data analysis. Moreover, the THESEUS and eXTP mission profiles were introduced, due to the relevant papers presented in chapter 4.

Additionally, an overview of the *Fermi* mission was given. A particular emphasis was given to the introduction of the *Fermi-LAT*, along with an outline of the method of its data analysis pipeline. These instruments are only introduced to the level of

[15] For both isotropic and interstellar emission models see `https://fermi.gsfc.nasa.gov/ssc/data/access/lat/BackgroundModels.html`.

[16] For a full list of models supported by *Fermi* see `https://fermi.gsfc.nasa.gov/ssc/data/analysis/scitools/source_models.html`.

detail required for the understanding of subsequent chapters and full details should be sought out from the references within.

3 Annihilating Dark Matter Search

As outlined in Sec. 1.2.1 WIMPs, are a strongly motivated dark matter candidate and are detectable through their annihilation into Standard Model (SM) particles. Their presence in the Universe would therefore form a detectable excess of secondary SM particles in areas of high dark matter density, this signal would moreover follow the morphology of dark matter in that region. Galaxy clusters (being the largest virialised objects in the Universe) are a natural target for indirect searches, due to them hosting an abundance of dark matter as a result of their high mass. In the following paper, the analysis and results of an indirect DM search in five nearby galaxy clusters are presented. The choice of the specific clusters was motivated by maximising the potential DM annihilation signal, thus clusters with high J-factors and minimal foreground emission were chosen preferably. The search was conducted using 12 years of *Fermi-LAT* data, utilising a likelihood fitting method to fit the data to an artificially introduced dark matter signal. The dark matter templates introduced follow profiles reported in the literature. Additionally, the CLUMPY software was utilised to account for the effect of dark matter substructure and its subsequent boost to the expected annihilation signal. Using the results of the likelihood fitting, constraints are derived on the annihilation cross section for the $b\bar{b}$, W^+W^- and $\gamma\gamma$ annihilation channels. These results are then presented for differing DM density profiles both with and without the boost from the effects of substructure.

3.1 Annihilating Dark Matter Search With 12 Years of Fermi-LAT Data in Nearby Galaxy Clusters

Monthly Notices of the ROYAL ASTRONOMICAL SOCIETY

MNRAS **502,** 4039–4047 (2021) doi:10.1093/mnras/stab208
Advance Access publication 2021 January 25

Annihilating dark matter search with 12 yr of Fermi LAT data in nearby galaxy clusters

Charles Thorpe-Morgan ,★ Denys Malyshev, Christoph-Alexander Stegen, Andrea Santangelo and Josef Jochum

Institut für Astronomie und Astrophysik Tübingen, Universität Tübingen, Sand 1, D-72076 Tübingen, Germany

Accepted 2021 January 21. Received 2020 December 23; in original form 2020 October 26

ABSTRACT

Galaxy clusters are the largest virialized objects in the Universe and, as such, have high dark matter (DM) concentrations. This abundance of dark matter makes them promising targets for indirect DM searches. Here we report the details of a search, utilizing almost 12 yr of Fermi/LAT data, for gamma-ray signatures from the pair annihilation of WIMP dark matter in the GeV energy band. From this, we present the constraints on the annihilation cross-section for the $b\bar{b}$, W^+W^-, and $\gamma\gamma$ channels, derived from the non-detection of a characteristic signal from five nearby, high Galactic latitude, galaxy clusters (Centaurus, Coma, Virgo, Perseus, and Fornax). We discuss the potential of a boost to the signal due to the presence of substructures in the DM haloes of selected objects, as well as the impact of uncertainties in DM profiles on the presented results. We assert that the obtained limits are, within a small factor, comparable to the best available limits of those based on Fermi/LAT observations of dwarf spheroidal galaxies.

Key words: dark matter – galaxies: clusters: individual: Centaurus – galaxies: clusters: individual: Coma – galaxies: clusters: individual: Virgo – galaxies: clusters: individual: Perseus – galaxies: clusters: individual: Fornax.

1 INTRODUCTION

In contemporary astrophysics, dark matter (DM) continues to be one of the greatest unknowns in our understanding of the Universe. The dark matter phenomenon manifests itself seemingly universally, pervading a large range of mass scales and types of object – from dwarf spheroidal galaxies (dSphs) to, galaxies, clusters of galaxies, and features of the early Universe. The latest measurements of Planck suggest that dark matter is incredibly abundant and comprises approximately 26.4 per cent of the energy density of the Universe (Planck Collaboration VI 2018). However, despite being the second most abundant component in our Universe (after dark energy), very little is known about its physical properties. To attempt to explain this phenomenon, many differing theoretical frameworks exist, with a range of physical motivations and explanations (see e.g Peter 2012; Bauer & Plehn 2017; Baudis 2018, for a review). Within one broadly discussed paradigm of these, dark matter is composed of Weakly Interacting Massive Particles (WIMPs) with typical masses in the GeV–TeV range, and is characterized by weak-scale interactions with particles in the Standard Model (SM) (see e.g. Roszkowski, Sessolo & Trojanowski 2018, for a recent review).

WIMPs remain a favoured solution to DM for a number of reasons. First, the relic abundance of DM is naturally obtained through calculations utilizing WIMPs with the annihilation cross-section of a weak scale (DM-particles velocity averaged cross-section $\langle\sigma v\rangle_{th} \sim 3 \cdot 10^{-26}\,\mathrm{cm^3\,s^{-1}}$) and masses in 10 MeV–10 TeV range that have undergone a thermal freeze-out in the early Universe (the so-called WIMP miracle; Lee & Weinberg 1977; Feng & Kumar 2008), see Profumo (2013), Baer et al. (2015) for pedagogical reviews.

Furthermore, WIMP-like particles appear naturally in many SM extensions, including supersymmetric SM extensions (Jungman, Kamionkowski & Griest 1996; Catena & Covi 2014; Tanabashi et al. 2018) (as e.g. the lightest stable supersymmetric particles), compactified extra-dimensions theories (Cheng, Feng & Matchev 2002; Pérez-Lorenzana 2005; Kakizaki, Matsumoto & Senami 2006; Hooper & Profumo 2007) (as e.g. the lightest Kaluza-Klein states), GUT-inspired theories (Arcadi 2016; Berlin 2017; Arcadi et al. 2018), secluded WIMPs (Pospelov, Ritz & Voloshin 2008), and many others (see e.g. Arcadi et al. 2018; Roszkowski et al. 2018 for reviews).

Perhaps most importantly though, WIMPs remain viable candidates for both direct and indirect searches, and are thought to decay/annihilate into SM particles with a subsequent production of photons (Cirelli et al. 2011). In typical GeV-scale WIMP masses, this photon signal is expected to be of a similar energy to it's progenitor (within the GeV-energy band) which can lead to a detectable excess in the gamma-ray flux from DM-dominated astrophysical objects. Generally, this excess is characterized by non-trivial spatial (determined by the square of the DM-density profile) and spectral (dependent on the type(s) of SM particle(s) it mainly annihilates into the 'annihilation channels') profiles.

In this study, we focused on the detection of such an excess signal in the GeV band from annihilating WIMP dark matter, utilizing Fermi/LAT (Atwood et al. 2009) data on a number of nearby galaxy clusters. We focused on WIMPs that were predominantly annihilating either through the $b\bar{b}$ or W^+W^- channel, suggested to be dominant for a class of well-motivated Constrained Minimal Supersymmetric SM extensions (Jeltema & Profumo 2008). For the Virgo and Centaurus

★ E-mail: charles.thorpe-morgan@astro.uni-tuebingen.de

clusters, we also provide constraints for a direct annihilation of DM into photons ($\gamma\gamma$), expected to manifest itself via a narrow, line-like spectral feature.

Galaxy clusters (GC) are the largest virialized objects in the Universe, and as such represent attractive laboratories for the study of dark matter. Though located much further away than Dwarf Spheroidal galaxies (dSphs), their very large masses and hence large DM content maintain them as a competitive option for deriving limits on DM particle properties. Similar to dSphs, clusters of galaxies are characterized by low astrophysical background in the GeV band and have relatively well-measured properties via strong/weak lensing, X-ray observations, or cluster kinematics (see Bhattacharya et al. 2013, and references therein). These well measured properties allow for accurate definition of DM density distributions in each cluster, an essential feature for accurate astrophysical DM study. The location of galaxy clusters however can be problematic for their study. In particular, bright foreground Galactic diffuse gamma-ray emission can weaken the results and introduce uncertainties connected to the incompleteness or inaccuracies in the template of this emission. To minimize the effect of gamma-ray Galactic diffuse emission, we explicitly selected clusters located at high Galactic latitudes ($b > 10^{\circ}$) for the analysis.

Following this introduction the article will be structured as follows. In Section 2, we discuss the form of the signal from annihilating DM and its implication on the study. We furthermore outline the approach we took in selecting the clusters for study and highlight those selected. In this section, we also discuss the dark matter distribution in each cluster and the implications of uncertainties in this distribution for the expected DM annihilation signal. Section 3 is dedicated to the methodology and contains details of the data used and the associated processing of it. Finally, Section 4 discusses the obtained limits on the DM annihilation cross-section for all considered channels in the context of previous work, and their potential implications, before our concluding remarks.

2 SIGNAL AND GALAXY CLUSTERS SAMPLE

2.1 Dark matter signal

Pair annihilation of DM WIMPs (χ) into SM particles (f) follows the form: $\chi\bar{\chi} \rightarrow f\bar{f}$ (where the annihilation channel is named $f\bar{f}$ correspondingly). The subsequent gamma-ray radiation spectrum of this annihilation in any DM-dominated object, within the solid angle $d\Omega$, is given by (see e.g. Cirelli et al. 2011).

$$\frac{\mathrm{d}F(E)}{\mathrm{d}\Omega} \equiv \frac{\mathrm{d}N_{\gamma}}{\mathrm{d}E\mathrm{d}\Omega} = \frac{\mathrm{d}J/\mathrm{d}\Omega}{4\pi \cdot 2m_{DM}^2} \times \sum_f b_f \cdot \langle\sigma_f v\rangle \cdot \frac{\mathrm{d}N_{\gamma}^f}{\mathrm{d}E}(E). \quad (1)$$

Here m_{DM} is the mass of the DM particle χ, J is the object's J-factor, a term given by the integral of DM density ρ square over the line of sight:

$$\mathrm{d}J/\mathrm{d}\Omega = \int_{l.o.s} \rho^2(\ell)\mathrm{d}\ell. \quad (2)$$

Of the two parts that make up the product in equation (1), the first is proportional to the total number of DM-particle annihilations in the line of sight, while the second term represents the spectrum of one annihilation, averaged over all possible annihilation channels. To achieve this, the sum in the second term is performed over all possible annihilation channels (all possible f's in $\chi\bar{\chi} \rightarrow f\bar{f}$). Moreover, the b_f term (the branching ratio) corresponds to the probability of DM pair annihilation into certain SM particles (termed: the annihilation channel), such that $\sum_f b_f = 1$. $\langle\sigma_f v\rangle$ is the dark matter velocity averaged annihilation cross-section σ_f for channel $f\bar{f}$. We note that in the subsequent analysis, we have assumed a 100 per cent branching ratio to each annihilation product, thus making the values of b_f and $\langle\sigma_f v\rangle$ redundant. We have however displayed them for posterity, and to show their relevance for studies where multiple annihilation channels are considered. Finally, $\mathrm{d}N_{\gamma}^f/\mathrm{d}E$ represents the gamma-ray spectrum produced for one annihilation in its corresponding channel.

The expected dark matter annihilation signal from any astrophysical object is thus characterized by a specific spatial shape and spectrum. While the spectrum of the signal is completely determined by 'particle physics' factors (i.e. by $\mathrm{d}N_{\gamma}^f/\mathrm{d}E$ terms), its spatial shape is determined by elements of the equation with an astrophysical origin (i.e. dark matter density profile via the J-factor term). The overall strength of the signal is determined by the product $J\langle\sigma_f v\rangle$ i.e. is proportional (from equation 2) to the square of characteristic DM density in the astrophysical object and DM annihilation cross-section.

This strong, quadratic, dependence ensures objects with high DM densities have very large J-factors and therefore potentially have strong signals from DM annihilation. This makes large objects and those with the aforementioned high DM densities, primary targets for searches of DM-annihilation signals.

2.2 Cluster sample

As a result of the previously mentioned criteria for maximizing the DM annihilation signal, several types of DM dominated objects are usually presented as favourable targets for searches due to their maximization of these factors (see e.g. Bringmann & Weniger 2012; Funk 2015, for a discussion). Among these include nearby dwarf spheroidal galaxies (Archambault et al. 2017; Oakes 2019; Hoof, Geringer-Sameth & Trotta 2020; Linden 2020), the Galactic Centre (Ackermann et al. 2017; Rinchiuso & Moulin 2017) and clusters of galaxies (Huang, Vertongen & Weniger 2011; Zimmer 2015; Quincy Adams, Bergstrom & Spolyar 2016) to name but a few.

In the following, we focus our search for a DM annihilation signal on a sample of nearby galaxy clusters. For our studies, we selected a sample of nearby ($z \lesssim 0.02$), high Galactic latitude ($|b| > 10^{\circ}$) clusters; for each of these clusters, we also utilized dark matter profiles reported in the literature. The sample included five objects (The Centaurus, Coma, Virgo, Perseus, and Fornax clusters, see Table 1) and partially intersected with a sample used in a previous study (Huang et al. 2011). In comparison to this study, our work benefited from substantially better statistics in the data and improved Fermi/LAT calibration, see Section 3 for details.

2.3 Dark matter distribution

Given the quadratic dependence of the DM annihilation signal (equations 1–2) on the dark matter density distribution, it was imperative for our studies to ensure the dark matter profile was accurate and well described the distribution in the cluster being studied.

For each of the selected clusters, we adopted the smooth, spherically symmetric generalized NFW profile (also known as Zhao profile; Zhao 1996)

$$\rho(r) = \frac{2^{\frac{\beta-\gamma}{\alpha}}\rho_s}{(\frac{r}{r_s})^{\gamma}(1+(\frac{r}{r_s})^{\alpha})^{(\beta-\gamma)/\alpha}}$$
$$\text{with } \alpha = 1; \quad \beta = 3; \quad \gamma = 1 \quad (3)$$

Table 1. Details of the sample of nearby clusters analysed in this work. Coordinates are given in Galactic longitude and latitude (l and b, respectively). The characteristic radii r_s and densities ρ_s of NFW profile (see equation 3) are adopted from the corresponding references. Note, that ρ_s corresponds to $\rho_0/4$ for an NFW profile. The covariance matrices show the estimated level of correlation between DM profile parameters, see the text for further details.

Cluster	l (deg)	b (deg)	z	r_s (kpc)	ρ_s ($10^5 M_\odot$/kpc^{-3})	Covariance ($\log_{10} r_s$, $\log_{10}\rho_s$)	Reference
Centaurus	302.398	21.561	0.0114	470	2.13	$10^{-3}\times\begin{pmatrix}3.7 & -6.3\\ -6.3 & 13.65\end{pmatrix}$	Ettori, De Grandi & Molendi (2002)
Coma	283.807	74.437	0.0231	360	2.75	$10^{-2}\times\begin{pmatrix}31.8 & -47.9\\ -47.9 & 74.0\end{pmatrix}$	Gavazzi et al. (2009)
Virgo	187.697	12.337	0.0036	560	0.8	$10^{-3}\times\begin{pmatrix}22.5 & -39.7\\ -39.7 & 71.4\end{pmatrix}$	McLaughlin (1999)
Perseus	150.573	− 13.262	0.0179	369	2.73	–	Simionescu et al. (2011)
Perseus	150.573	− 13.262	0.0179	530	2.36	–	Ettori et al. (2002)
Fornax	236.712	− 53.640	0.0046	220	1.25	–	Drinkwater, Gregg & Colless (2001)(DW01)
Fornax	236.712	− 53.640	0.0046	98	14.5	–	Reiprich & Böhringer (2002)(RB02)
Fornax	236.712	− 53.640	0.0046	34	22.0	–	Schuberth et al. (2010)(SR10A10)

which gives the DM density ρ as a function of the radius r from the cluster's centre. We note that for the quoted α, β, γ parameters of this profile, equation (3) is equivalent to Navarro–Frenk–White (NFW Navarro, Frenk & White 1997) profile with characteristic DM density $\rho_0 = 4\rho_s$. The characteristic r_s, ρ_s parameters of this profile for the selected sample of clusters are summarized in Table 1 along with the references to the works from which these parameters were obtained.

For NFW profiles 3 the J-factor 2 is formally divergent at $r \to 0$ which corresponds to a rapid increase of the NFW DM-profile density at small radii. At radii $r \lesssim 10$ kpc, conversely to this, observations (Newman et al. 2013a,b) and simulations (Schaller et al. 2015; Tollet et al. 2016) of clusters of galaxies both show a flattening of DM density profiles. Such flattening effects can be connected to the effects of baryons/AGN feedback (Gnedin et al. 2004; Teyssier et al. 2011; Castro et al. 2020; Macciò et al. 2020). To account for the possible flattening of the DM profile, we explicitly set the DM column density to a constant value within the inner 10 kpc of each of the considered clusters thus avoiding a non-physical increase in density at small radii.

The radial dependence of the J-factor was derived according to equation (2) using the CLUMPY v.3 code (Charbonnier, Combet & Maurin 2012; Bonnivard et al. 2016; Hütten, Combet & Maurin 2019). Utilization of the CLUMPY code allowed us, in a method consistent over different clusters, to consider the impact of the presence of a large number of substructures in the cluster's DM density distributions, corresponding to the substructures seen in Cold Dark Matter cosmological N-body simulations (see e.g. Diemand, Kuhlen & Madau 2007; Springel et al. 2008).

The presence of such substructures can significantly boost the expected signal from the outer parts of haloes and thus should be properly taken into account. In order to adequately model the substructures, we assumed a mass distribution function of $\mathrm{d}N_{\rm sub}/\mathrm{d}M \propto M^{-1.9}$ with a 10 per cent mass fraction in substructures (Springel et al. 2008), for the minimal/maximal substructure mass to be $10^{-6}/10^{-2} M_{\rm clust}$ and utilized the same treatment as within Sánchez-Conde & Prada (2014) for the subclumps' mass–concentration relation. The substructures' spatial distribution $\mathrm{d}N_{\rm sub}/\mathrm{d}V$ was selected to follow the host halo's smooth profile.

Such a choice resulted in a more conservative estimation of the boosted signal (an order of magnitude increase of $J_{\rm tot} \equiv \int(\mathrm{d}J/\mathrm{d}\Omega)\,\mathrm{d}\Omega$) in comparison to one used by Huang et al. (2011) (factor of 10^3). For reference, we show J-factors for the Coma cluster with and without the presence of substructures in Fig. 1,

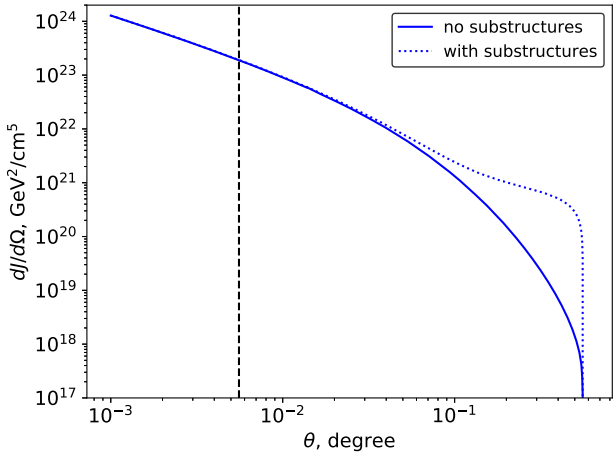

Figure 1. The J-factor profile for the Coma cluster is shown here both with and without the presence of substructures, denoted by solid and dotted blue lines in the figure, respectively. The vertical dashed line corresponds to a distance of 10 kpc from the cluster's centre; the DM density at radii closer to the centre than this point was assumed to be constant. The profile was assumed to continue to a distance of 1 Mpc from Coma's centre, at these greater distances the profile measurements were reported in Gavazzi et al. (2009).

with solid and dotted blue lines correspondingly. The vertical dashed line corresponds to a distance of 10 kpc from the cluster's centre – the point from which we assumed a constant DM density.

The density profiles of all clusters were assumed to continue up to the largest distances from the centre at which profile measurements were reported in the references in Table 1 (0.5 Mpc for Centaurus; 1 Mpc for the rest of the clusters). We note the possibility of the strong model dependence of the boosted signal thus present the results for both cases below – the halo with substructures ('boosted') and smooth halo only ('non-boosted') dark matter profiles.

2.4 Uncertainty propagation

The total uncertainty in the expected DM annihilation signal 1 arises from uncertainties in the J-factor value used for each cluster (see equation 2), which is in turn connected to the uncertainties in the cluster's dark matter distribution profile. We note that the r_s and ρ_s profile parameters are usually strongly correlated, see e.g. Fig. 2 (left-hand panel) showing 1σ and 2σ confidence contours

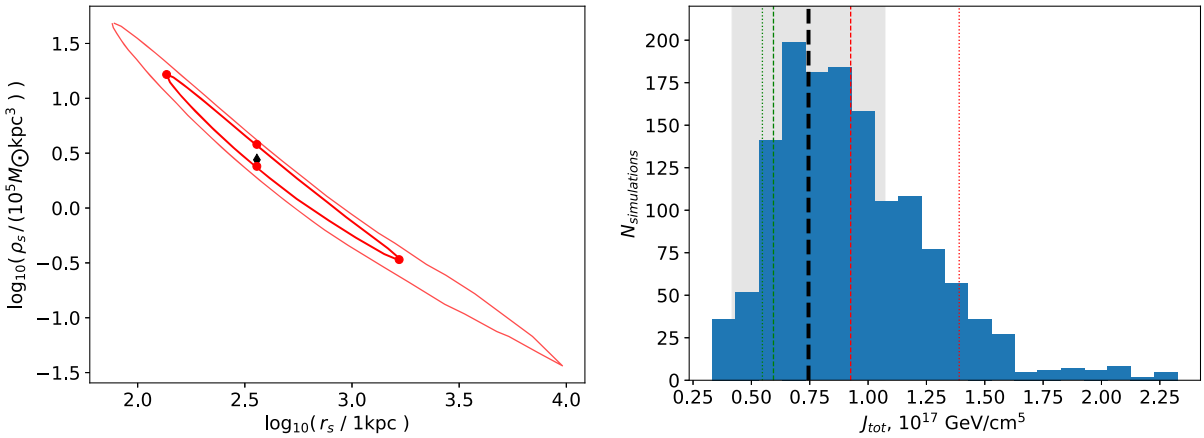

Figure 2. Left-hand panel: The red contour represents a 1σ confidence range for r_s, ρ_s parameters of DM profile 3 of the Coma cluster, adopted from the plot within Gavazzi et al. (2009). The central black diamond corresponds to Gavazzi et al. (2009) best-fitting values of r_s and ρ_s. The red square points show the characteristic parameters used for J-factor uncertainty estimations, see the text for the details. Right-hand panel: The J-factor distribution derived from 1400 points apportioned within the 1σ and 2σ contours shown in left-hand panel. The vertical black dashed line shows the mean J-factor value corresponding to Gavazzi et al. (2009) the best-fitting values of r_s and ρ_s. The grey shaded region indicates the formal dispersion of the derived distribution plotted around the mean J-factor value. Thin dotted lines correspond to red square points in the left-hand panel, see the text for the details.

(solid and thin red curves) adopted from Gavazzi et al. (2009). The black diamond symbol here corresponds to the best-fitting (r_s, ρ_s) parameters of Gavazzi et al. (2009).

The strong correlation of the (r_s, ρ_s) parameters reflects the fact that generally, the total masses of clusters are measured far more accurately and frequently (a value that is roughly proportional to the quantity $\rho_s r_s^3$) than the individual values of r_s and ρ_s. We note also that the explicit shape of the confidence contours for the DM-profile parameters is not available in the literature for most of the considered clusters. Typically quoted uncertainties for the r_s and ρ_s parameters are given without specification of the confidence contours and normally correspond to the projections of the confidence contour on to the r_s and ρ_s axes, see Fig. 2 (left-hand panel). Although these projections reflect the highest possible uncertainties for the r_s and ρ_s parameters, the direct propagation of these uncertainties on the J-factor, without accounting for the correlation of these parameters, can result in drastically overestimating the J-factor uncertainty.

Thus, the usual way of estimating J-factor uncertainty dJ is connected to the propagation of uncertainty from the total cluster mass estimation, see e.g. Huang et al. (2011). This is equivalent to the propagation of only the density uncertainty for the fixed (to its best-fitting value) r_s. In terms of Fig. 2 the $J - \mathrm{d}J$ and $J + \mathrm{d}J$ are achieved at red points below and above best-fitting black diamond point.

In Fig. 2 (right-hand panel) we show a J-factor ($J_{\rm tot} \equiv \int (\mathrm{d}J/\mathrm{d}\Omega)\,\mathrm{d}\Omega$) distribution from simulations based on confidence regions adopted from Gavazzi et al. (2009) for the Coma cluster. For the simulations, we considered 1000 (r_s, ρ_s) (log)uniformly distributed points within the 1σ contour and, 400 points (log)uniformly distributed between the 1σ and 2σ contours. The selected uniform distribution was chosen in absence of detailed information regarding the probability distribution within the aforementioned contours. For each considered pair (r_s, ρ_s) we calculated a J-factor in a method identical to that described above for the mean J-factor value. The obtained distribution is shown with blue histogram with a solid black dashed line illustrating the mean J-factor value (corresponding to the black diamond point in left-hand panel of this figure). The values of J-factors corresponding to the estimations based on 'total mass uncertainty' propagation are shown with dotted green and red lines. The light-grey shaded region depicts the dispersion of the J-factors distribution, plotted around the mean J-factor value.

While estimation based on the total mass uncertainty provides a reasonable estimation of J-factor uncertainty (comparable to the estimation based on the dispersion of the distribution), we note that the corresponding J-factors confidence range is somewhat biased to higher J-factors. This can consequently result in biased estimations of the uncertainties on the limits of dark matter's annihilation cross-section. Therefore, in what follows, we utilize the uncertainties on J-factors based on the dispersion of the J-factors distributions rather than 'total mass estimations'.

In addition to uncertainty connected to the J-factor value, we consider uncertainties in the dark matter annihilation cross-section, connected to an imperfect knowledge of the spatial shape of the expected signal. To estimate the level of this uncertainty, we utilize templates for the signal template based on (i) best-fitting values of r_s and ρ_s presented in the literature (see Table 1); (ii) templates based on (r_s; ρ_s) parameters at the edges of 1σ confidence region (i.e. the left-hand and right-most red points on the red contour in the left-hand panel of Fig. 2). We argue that these points correspond to the substantially different spatial shapes in the DM distribution and should be considered for the estimation of J-factor uncertainty connected to the possible spatial variations of the signal. The J-factors corresponding to these points are illustrated in right-hand panel with thin green and red dashed lines.

To be conservative, we used a maximum of two of the uncertainties described above to estimate the uncertainties for the presented limits on the dark matter annihilation cross-section, for each of the considered DM masses.

Among all the clusters listed in Table 1 the explicit information on the correlation of the (r_s, ρ_s) parameters is available only for the Coma cluster. To perform estimations for the Centaurus and Virgo clusters, we assume the 1σ confidence contours to be ellipses on the $\log r_s - \log \rho_s$ plane (similar to the Coma cluster). The major axes were estimated from the uncertainties of the r_s and ρ_s parameters (i.e. projections of major axes on $\log r_s$, $\log \rho_s$ axes) quoted in the literature. The minor axes and inclination angles of these ellipses were estimated from the total cluster mass uncertainty range presented in literature.

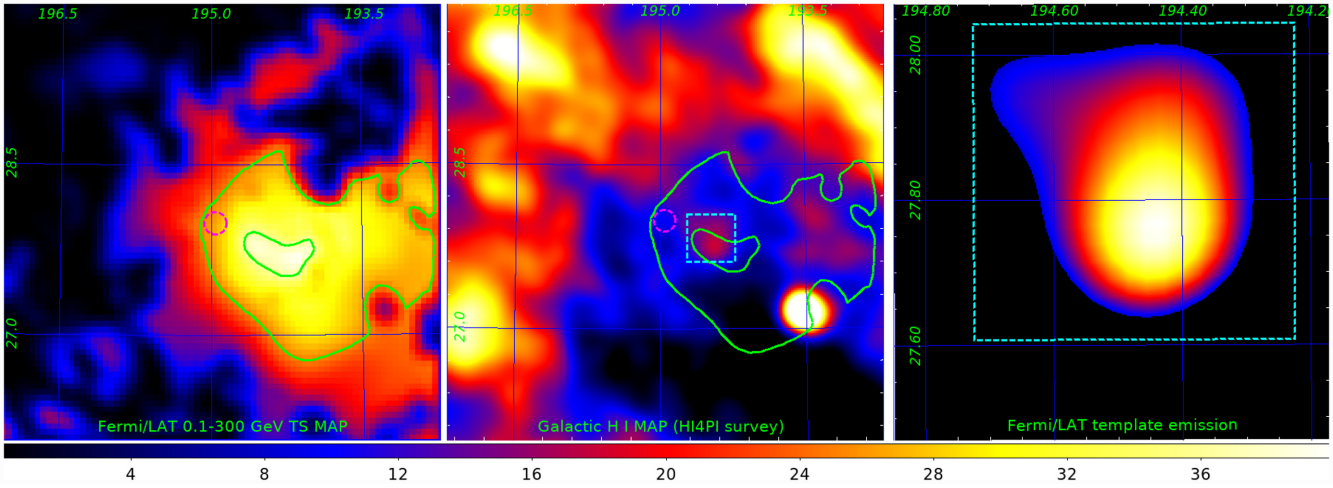

Figure 3. Left-hand panel: Fermi/LAT test statistics map of a $2^\circ \times 2^\circ$ region around the position of the Coma cluster, shown with a dashed magenta circle. The colour scale corresponds to the square of the significance of point-like source added at each point. The bright excess seen is consistent with the results of Xi et al. (2018). The green contours represent isobars of 6σ and 7σ detection significance (moving inwards, respectively). Middle panel: Galactic HI map of the region from HI4PI survey HI4PI Collaboration (2016). The green contours are overlayed and correspond to those of the left-hand panel. Right-hand panel: a template added to the model of the Coma cluster region used for Fermi/LAT data analysis. The cyan square corresponds to its counterpart in the middle panel, see the text for the details.

The aforementioned ellipse-like confidence regions can be described in terms of covariance matrices for $\log r_s - \log \rho_s$ parameters (see Table 1). The major and minor axes of each 1σ confidence ellipse is given by the square root of the eigenvalue of these matrices. The inclinations of ellipses are given by the angle between the eigenvector corresponding to the largest eigenvalue, and r_s axis. For completeness in Table 1 we present also the covariance matrix for the Coma cluster, corresponding to an ellipse approximately fitting the 1σ red contour from Fig. 2, left-hand panel.

For the Perseus and Fornax clusters, we noted several profiles independently derived in the literature (see Table 1). For these objects we estimated uncertainties on dark matter annihilation cross-section limit based on the corresponding quoted best-fitting profiles. Such an approach allows one to access the level of systematic uncertainty, known to be dominant at least for the Fornax cluster, see e.g. Abramowski et al. (2012).

In addition to the sources of systematic error discussed above, we would like to note several other possible sources of such errors. These include: the inner core radius of DM density profiles; minimal/maximal mass of the DM halo substructures; mass and spatial distribution of these objects and the mass–concentration model for subhaloes. Although the assumptions made in this study regarding the properties of these parameters are rather conservative, we further investigated the effect on the derived J-factors of parameter variations within a factor of 2 (typical for e.g. DM profile parameters). Variations of inner core radius result in a $\sim$10 per cent variation of the total J-factor $J_{\rm tot}$ and we find similar uncertainties applicable to all results presented below. We note however, that this systematic uncertainty is subordinate in comparison to the DM profiles uncertainties discussed above.

In the presence of substructures, the variations of minimal/maximal mass of subhaloes result in $\sim$5 per cent variations of $J_{\rm tot}$ (applicable to 'boosted' limits below). The largest uncertainties on $J_{\rm tot}$, reaching a factor of 100, arise from the uncertainties on the mass/spatial distribution and mass–concentration model of subhaloes (see Pinzke, Pfrommer & Bergström 2009; Ackermann et al. 2010; Pinzke, Pfrommer & Bergstr"om 2011; Sánchez-Conde et al. 2011). We stress, that in what follows we use a conservative estimations for $J_{\rm tot}$ boost due to the presence of subhaloes. Utilization of optimistic parameters can, however, substantially improve derived limits.

3 DATA ANALYSIS

This study utilized approximately 12 yr worth of Fermi/LAT survey mode data taken from the 2008 August 4 to the 2020 April 23. The presented analysis was performed with `FERMITOOLS` v.1.2.1 for `P8R3_CLEAN_V2` gamma-ray events[1] within energy range of 100 MeV to 300 GeV.

We applied the standard time cuts as described in Atwood et al. (2009) as well as a zenith angle cut at $\theta < 100^\circ$ to avoid contamination of the data from the Earth's albedo. The binned analysis (with enabled energy dispersion handling) was performed for the events within 15° around the position of each of the considered clusters. The model of the region included sources from the 4FGL catalogue (Abdollahi et al. 2020) as well as templates for Galactic and extragalactic diffuse emissions given by the `gll_iem_v07.fits` and `iso_P8R3_CLEAN_V2_v1.txt` templates correspondingly. The spectral parameters of these sources were initially assumed to be free. In addition, we included sources from the 4FGL catalogue up to 10° beyond the considered region of interest into the model, with all their parameters frozen to their catalogue values, in order to reduce bias connected to possible presence of bright sources outside of the considered region and effects to do with the LAT's poor PSF at low $\sim$0.1 GeV energies.

The spectral parameters of all free sources were determined from the broad-band fit of all the available data to the described model. At the second stage of our analysis, we fixed the spectral parameters of all sources, except normalizations, to their best-fitting values and added a template for a putative dark matter annihilation emission to the model.

This emission was modelled as a diffuse source with spatial emission distribution proportional to the J-factor described in previous

[1] See Fermi/LAT data analysis guidelines.

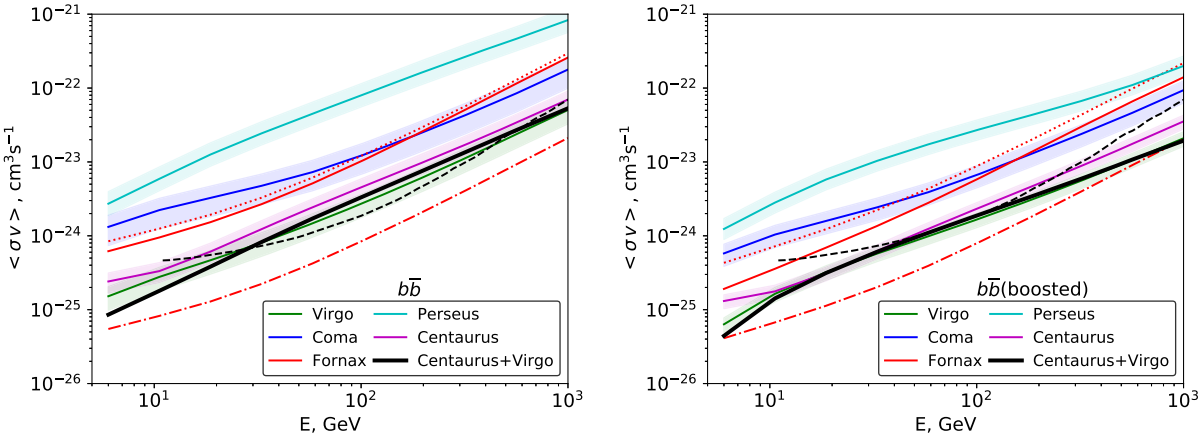

Figure 4. The 95 per cent CL limits on the annihilation cross-section of WIMP dark matter for the $b\bar{b}$ annihilation channel, with results shown for the sample of considered galaxy clusters. The left-hand panel shows the results for smooth DM haloes, while the right one shows the results when the presence of substructures is included. The shaded regions in both panels represent the expected 1σ uncertainties connected to uncertainties in DM profiles. For the Fornax cluster profiles from literature result in substantially different J-factors and consequently different limits on the annihilation cross-section. Results for DW01, RB02, and SR10A10 profiles (see Table 1) are shown with solid, dot-dashed, and dotted red lines, respectively. The solid black line corresponds to the limits from a stacked analysis of the Virgo and Centaurus clusters. The thin black dashed line in the left-hand panel represent results of a previous study by Huang et al. (2011).

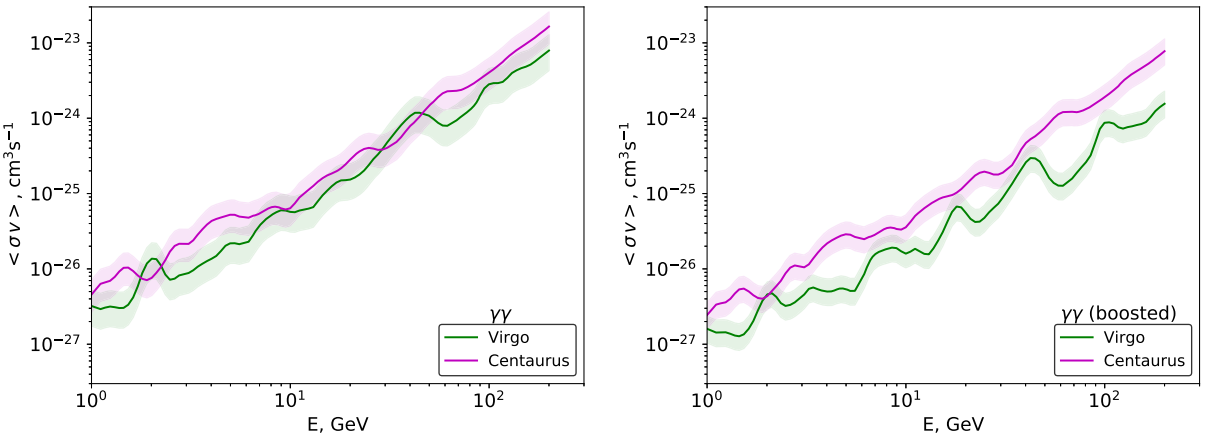

Figure 5. The 95 per cent CL limits on WIMP dark matter's annihilation cross-section for the $\gamma\gamma$ annihilation channel, in the Virgo and Centaurus clusters. These clusters were selected to show unique channel, given that they provided the best limits for the $b\bar{b}$ and W^+W^- channels. See Fig. 4 for detailed panel and lines description.

sections. The spectral component of the signal was given by the spectrum of annihilating dark matter for the considered ($b\bar{b}$ and W^+W^-) channel, provided within FERMITOOLS as `DMFitFunction` based on Jeltema & Profumo (2008). In the case of the $\gamma\gamma$ annihilation channel, we explicitly assumed the spectral part of the signal to be a narrow (5 per cent energy width) Gaussian line. To account for such a narrow feature, we performed the binned analysis with 50 log-equal energy bins per decade of energy (versus 10 bins per decade for other annihilation channels). For this case, we noted a significant increase in the required computational resources. Thus, we performed the search for the $\gamma\gamma$ annihilation signal only in the Virgo and Centaurus clusters given their superior constraints in other annihilation channels.

A note on the Coma cluster: Analysing the data on the Coma cluster, we note the presence of a weak signal close to the location of the cluster. The presence of a similar signal was reported in Xi et al. (2018). In Fig. 3 (left-hand panel) we show the test statistics (which corresponds to the square of the significance of an added point-like source) map of a $2^\circ \times 2^\circ$ region (0.05° pixel size) around the position of the Coma cluster (shown with dashed magenta circle) in the energy range of 0.1–300 GeV. This map is consistent with the results of Xi et al. (2018). The bright residuals represent an emission of a source(s) not included in the 4FGL catalogue. While generally the origin of this emission is not clear (Liang et al. 2018; Xi et al. 2018) we note the presence of spatially coincident excess in the Galactic hydrogen HI survey HI4PI (HI4PI Collaboration 2016), see middle panel of Fig. 3. Note also, that all intensity variations in the middle panel are within 10–15 per cent of its mean value. Green contours in the left-hand and middle panels correspond to the 6σ and 7σ levels of point-like source detection significance in the Fermi/LAT data.

Although detailed studies of the observed excess are beyond the scope of this paper, we argue on its potential association with a foreground Galactic HI cloud. In our studies, we modelled the excess with a spatial template based on HI map (see right-hand panel of Fig. 3; dashed cyan squares show identical regions on the right-hand and middle panels). The spectrum of this source was assumed to

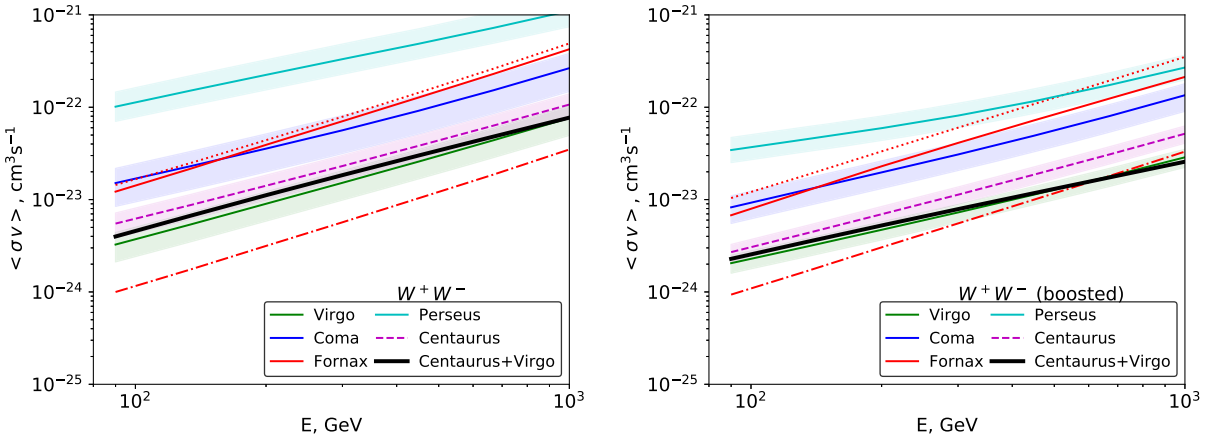

Figure 6. The 95 per cent CL limits on WIMP dark matter's annihilation cross-section for the W^+W^- annihilation channel, across the sample of considered galaxy clusters. See Fig. 4 for detailed panel and lines description.

be a power law (best-fitting index 2.65 ± 0.1; consistent with Liang et al. 2018). We note also that the obtained, relatively soft, best-fitting slope is consistent with the reported values for the average spectral slope of diffuse emission at corresponding Galactic latitudes, and in several nearby molecular clouds (see e.g. Neronov & Malyshev 2015; Yang, Aharonian & Evoli 2016; Neronov, Malyshev & Semikoz 2017; Aharonian et al. 2020). Such similarity marginally supports the proposed possible association of the observed emission.

4 RESULTS AND DISCUSSION

Galaxy clusters are the largest virialized objects in the Universe, hosting large amounts of dark matter which make them effective targets for indirect DM searches at all wavelengths. With their relatively well measured DM density profiles, low astrophysical background signal in the GeV–TeV energy range, galaxy clusters are one of the best targets for WIMP searches with current and future high-energy observational facilities (Bringmann & Weniger 2012; Funk 2015; Morselli & Consortium 2017; Yapici, Smith & HAWC Collaboration 2017).

This study carried out an analysis, using almost 12 yr of Fermi/LAT data, of five nearby clusters expected to be the strong sources of high energy photons originating from DM annihilation. We modelled the DM halo of each cluster by a spherically symmetric NFW profile with the parameters adopted from dedicated studies (see Table 1). A significant amount of attention was devoted to the accurate propagation of uncertainties on the DM profile parameters and on the uncertainties in the spatial shape and intensity of expected signal. For the Perseus and Fornax clusters, more than one measurement of DM profiles were reported in the literature; in these cases we used different available profiles to check the possible effects of systematic uncertainties on the obtained results.

This study, as well as its larger data set, also benefited from the utilization of the updated Pass 8 Fermi/LAT instrument response functions (IRFs), characterized by better non-photon background rejection than Pass 7 IRFs used in previous studies (Huang et al. 2011). Furthermore, as previously mentioned, this study has focused in great detail on the uncertainties in the DM profiles of the selected objects and their effect on the derived limits, where we have taken a more rigorous approach. Finally, our comparison of different profiles for the same object is a distinctive feature of this work in comparison to previous works. This comparison has allowed us to highlight potential anomalies in profiles and provide basis for further testing and comparison of these.

In absence of a significant detection ($>2.5\sigma$) of a DM annihilation signal in any of the considered clusters, we present 95 per cent C.L. constraints on the annihilation cross-section for the $b\bar{b}$ and W^+W^- channels; channels for which the highest branching ratios are expected within a certain class of (astro)physically motivated constrained minimal supersymmetric Standard Models (Jeltema & Profumo 2008). For the two clusters showing the best constraints in these channels we, in addition, present the limits on the flux and annihilation cross-section in the $\gamma\gamma$ channel, usually considered as a 'smoking-gun' signature of dark matter annihilation or decay in the Universe. Corresponding results are presented in Figs 4–5. Left-hand/right-hand panels of the figures show the results for DM annihilation cross-section in the corresponding channel, both with or without accounting for a presence of substructures in DM halo.

Formally the tightest constrains were provided by the Fornax cluster, assuming that the dark matter distribution follows an RB02 (Reiprich & Bohringer 2002) NFW profile (see red dot-dashed line in Figs 4–6). Similar conclusions were previously derived by Huang et al. (2011) for the data set covering first 3 yr of Fermi/LAT observations. Two other profiles reported in the literature – DW01 (Drinkwater et al. 2001) and SR10A10 (Schuberth et al. 2010) (solid and dotted red lines correspondingly) result in weaker constraints by a factor of ∼20. A substantial difference in the results of this profile to other considered profiles was also noticed within HESS TeV data analysis (Abramowski et al. 2012). Given the large discrepancy in the limits in the Fornax cluster, we do not draw the final limits based on this object.

After the Fornax (RB02 profile), the best constraints were provided by the Virgo and Centaurus clusters. The constraints from the Coma and Perseus clusters proved to be up to an order of magnitude higher than their counterpart limits from the Fornax RB02 profile or the limits from Virgo and Centaurus. The significant degradation of limits from these clusters follows from (i): somewhat lower J-factors in these objects; (ii) the presence of γ-ray sources close to the centre of the cluster (NGC 1275 for the Perseus cluster and a source in the Coma cluster potentially associated with HI cloud 3). The presence of bright sources implies partial confusion of the fluxes attributed by the analysis between the gamma-ray source and DM signal, which resulted in a higher level of flux uncertainties and consequently weaker limits on the DM annihilation cross-section.

The black solid lines in Figs 4–6 show the best results from stacked analyses of the Centaurus and Virgo clusters. To perform such stacking, we built the log-likelihood profile as a function of $\langle \sigma v \rangle$ for each of these clusters. The limits shown correspond to the $\langle \sigma v \rangle$ value at which the sum of log-likelihood profiles changes by 2.71/2 (Rolke, López & Conrad 2005).[2]

The dashed black lines in the left-hand panels of Figs 4–6 correspond to the Huang et al. (2011) limits (without accounting for substructures), for each of the channels.

Despite utilizing substantially larger amounts of data, the obtained limits are comparable to ones obtained by Huang et al. (2011) for smooth DM profiles and weaker by a few orders of magnitude for profiles accounting for the presence of substructures. We argue that such discrepancies arise from two main differences in the methods of analysis chosen by this study and Huang et al. (2011). The best limits within Huang et al. (2011) originate from the Fornax cluster. The dark matter profiles presented in the literature for this cluster (see Table 1) result in a difference of one order of magnitude on limits on DM annihilation cross-sections, see red solid, dashed and dot-dashed Figs 4–6 corresponding to the DW01, SR10A10, and RB02 profiles. The results presented in Huang et al. (2011) are based on the RB02 profile (dot-dashed curve) which formally provides the best limits in this work too. Given the large discrepancy between the results of differing profiles for the Fornax cluster, in contrast to Huang et al. (2011), we have opted not to draw any conclusions based on this cluster. For the profiles characterized by a presence of subhaloes, we assumed conservative values of boost-factors (total *J*-factor boost $\sim$10 versus $\sim$1000 considered by Huang et al. 2011). The combination of these two factors resulted in the correspondingly weaker upper limits.

Although the presented constraints are somewhat weaker, they are within an order of magnitude comparable to the recent limits based on a stacked analysis of a large number of dwarf spheroidal galaxies (Ackermann et al. 2015; Hoof et al. 2020). However, the potential uncertainty connected to stacking large numbers of dSphs with poorly known individual profiles can reach up to a factor of 2 (Linden 2020), which has the potential to make the presented results more competitive. We note, that systematic uncertainties in DM density profiles of clusters of galaxies can affect this study to a comparable extent (see e.g. Figs 4–5). At the same time we argue that the results derived in this work are based on a substantially different class of objects containing DM than dSphs. This make the results all the more important as they provide grounds for cross-check analyses.

We finally note the importance of accurate measurements of DM profiles in galaxy clusters. The accurate measurement of such profiles (including explicit quotation of correlation between the parameters) with currently available X-ray and/or optical data is key for the reliability in the estimation of *J*-factors, and consequently, the parameters of annihilating dark matter.

ACKNOWLEDGEMENTS

The authors acknowledge support by the state of Baden-Württemberg through Baden-Württemberg High Performance Computing (bwHPC). This work was supported by the Deutsche Forschungsgemeinschaft (DFG) through the grant MA 7807/2-1.

[2]See also discussion on Fermi/LAT upper limits calculation.

DATA AVAILABILITY

The data underlying this article are available at the Fermi LAT data server, https://fermi.gsfc.nasa.gov/cgi-bin/ssc/LAT/LATDataQuery.cgi. Other data used in the article will be shared on reasonable request to the corresponding author.

REFERENCES

Abdollahi S. et al., 2020, ApJS, 247, 33
Abramowski A. et al., 2012, ApJ, 750, 123
Ackermann M. et al., 2010, J. Cosmol. Astropart. Phys., 2010, 025
Ackermann M. et al., 2015, Phys. Rev. Lett., 115, 231301
Ackermann M. et al., 2017, ApJ, 840, 43
Aharonian F., Peron G., Yang R., Casanova S., Zanin R., 2020, Phys. Rev. D, 101, 083018
Arcadi G., 2016, J. Phys.: Conf. Ser., 718, 042003
Arcadi G., Dutra M., Ghosh P., Lindner M., Mambrini Y., Pierre M., Profumo S., Queiroz F. S., 2018, Eur. Phys. J. C, 78, 203
Archambault S. et al., 2017, Phys. Rev. D, 95, 082001
Atwood W. B. et al., 2009, ApJ, 697, 1071
Baer H., Choi K.-Y., Kim J. E., Roszkowski L., 2015, Phys. Rep., 555, 1
Baudis L., 2018, The Search for Dark Matter. Cambridge Univ. Press, Cambridge
Bauer M., Plehn T., 2018, preprint (arXiv:1705.01987v2)
Berlin A., 2017, Phys. Rev. Lett., 119, 121801
Bhattacharya S., Habib S., Heitmann K., Vikhlinin A., 2013, ApJ, 766, 32
Bonnivard V., Hütten M., Nezri E., Charbonnier A., Combet C., Maurin D., 2016, Comput. Phys. Commun., 200, 336
Bringmann T., Weniger C., 2012, Phys. Dark Universe, 1, 194
Castro T., Borgani S., Dolag K., Marra V., Quartin M., Saro A., Sefusatti E., 2021, MNRAS, 500, 2316
Catena R., Covi L., 2014, Eur. Phys. J. C, 74, 2703
Charbonnier A., Combet C., Maurin D., 2012, Comput. Phys. Commun., 183, 656
Cheng H.-C., Feng J. L., Matchev K. T., 2002, Phys. Rev. Lett., 89, 211301
Cirelli M. et al., 2011, J. Cosmol. Astropart. Phys., 2011, 051
Diemand J., Kuhlen M., Madau P., 2007, ApJ, 657, 262
Drinkwater M. J., Gregg M. D., Colless M., 2001, ApJ, 548, L139
Ettori S., De Grandi S., Molendi S., 2002, A&A, 391, 841
Feng J. L., Kumar J., 2008, Phys. Rev. Lett., 101, 231301
Funk S., 2015, Proc. Natl Acad. Sci., 112, 12264
Gavazzi R., Adami C., Durret F., Cuillandre J. C., Ilbert O., Mazure A., Pelló R., Ulmer M. P., 2009, A&A, 498, L33
Gnedin O. Y., Kravtsov A. V., Klypin A. A., Nagai D., 2004, ApJ, 616, 16
HI4PI Collaboration et al., 2016, A&A, 594, A116
Hoof S., Geringer-Sameth A., Trotta R., 2020, J. Cosmol. Astropart. Phys., 2020, 012
Hooper D., Profumo S., 2007, Phys. Rep., 453, 29
Huang X., Vertongen G., Weniger C., 2011, J. Cosmol. Astropart. Phys., 2012, 042
Hütten M., Combet C., Maurin D., 2019, Comput. Phys. Commun., 235, 336
Jeltema T. E., Profumo S., 2008, J. Cosmol. Astropart. Phys., 2008, 003
Jungman G., Kamionkowski M., Griest K., 1996, Phys. Rep., 267, 195
Kakizaki M., Matsumoto S., Senami M., 2006, Phys. Rev. D, 74, 023504
Lee B. W., Weinberg S., 1977, Phys. Rev. Lett., 39, 165
Liang Y.-F., Xia Z.-Q., Xi S.-Q., Li S., Shen Z.-Q., Fan Y.-Z., 2018, preprint (arXiv:1801.01645)
Linden T., 2020, Phys. Rev. D, 101, 043017
Macciò A. V., Crespi S., Blank M., Kang X., 2020, MNRAS, 495, L46 ,
McLaughlin D. E., 1999, ApJ, 512, L9
Morselli A., Consortium C., 2017, Proc. Sci., The Dark Matter Programme of the Cherenkov Telescope Array, SISSA, Trieste, PoS(ICRC2017)921
Navarro J. F., Frenk C. S., White S. D. M., 1997, ApJ, 490, 493
Neronov A., Malyshev D., 2015, preprint (arXiv:1505.07601)
Neronov A., Malyshev D., Semikoz D. V., 2017, A&A, 606, A22

Newman A. B., Treu T., Ellis R. S., Sand D. J., Nipoti C., Richard J., Jullo E., 2013a, ApJ, 765, 24
Newman A. B., Treu T., Ellis R. S., Sand D. J., 2013b, ApJ, 765, 25
Oakes L., 2019, PoS, 36th International Cosmic Ray Conference (ICRC2019), p. 539
Pérez-Lorenzana A., 2005, J. Phys. Conf. Ser., 18, 224
Peter A. H. G., 2012, preprint (arXiv:1201.3942)
Pinzke A., Pfrommer C., Bergström L., 2009, Phys. Rev. Lett., 103, 181302
Pinzke A., Pfrommer C., Bergstr"om L., 2011, Phys. Rev. D, 84, 123509
Planck Collaboration VI, 2018, A&A, 641, A6
Pospelov M., Ritz A., Voloshin M., 2008, Phys. Lett. B, 662, 53
Profumo S., 2013, preprint (arXiv:1301.0952)
Quincy Adams D., Bergstrom L., Spolyar D., 2016, preprint (arXiv:1606.09642)
Reiprich T. H., Böhringer H., 2002, ApJ, 567, 716
Rinchiuso L., Moulin E., 2017, preprint (arXiv:1711.08634)
Rolke W. A., López A. M., Conrad J., 2005, Nucl. Instrum. Methods Phys. Res. A, 551, 493
Roszkowski L., Sessolo E. M., Trojanowski S., 2018, Rep. Progr. Phys., 81, 066201
Sánchez-Conde M. A., Prada F., 2014, MNRAS, 442, 2271
Sánchez-Conde M. A., Cannoni M., Zandanel F., Gómez M. E., Prada F., 2011, J. Cosmol. Astropart. Phys., 2011, 011
Schaller M. et al., 2015, MNRAS, 451, 1247
Schuberth Y., Richtler T., Hilker M., Dirsch B., Bassino L. P., Romanowsky A. J., Infante L., 2010, A&A, 513, A52
Simionescu A. et al., 2011, Science, 331, 1576
Springel V. et al., 2008, MNRAS, 391, 1685
Tanabashi M. et al., 2018, Phys. Rev. D, 98, 030001
Teyssier R., Moore B., Martizzi D., Dubois Y., Mayer L., 2011, MNRAS, 414, 195
Tollet E. et al., 2016, MNRAS, 456, 3542
Xi S.-Q., Wang X.-Y., Liang Y.-F., Peng F.-K., Yang R.-Z., Liu R.-Y., 2018, Phys. Rev. D, 98, 063006
Yang R., Aharonian F., Evoli C., 2016, Phys. Rev. D, 93, 123007
Yapici T., Smith A., HAWC Collaboration, 2017, Proc. Sci., Dark Matter Searches with HAWC, SISSA, Trieste. PoS(ICRC2017)891
Zhao H., 1996, MNRAS, 278, 488
Zimmer S., 2015, preprint (arXiv:1502.02653)

This paper has been typeset from a TEX/LATEX file prepared by the author.

4 Sensitivity of Future Missions to Decaying Dark Matter

The next generation of X-ray instruments have the capacity to contribute significantly to the field of decaying dark matter. The increase in instrumental sensitivity will provide the potential to greatly reduce the available parameter space of some decaying DM models, or perhaps exclude them entirely.

In the following works, the potential of two upcoming X-ray missions in the field of indirect dark matter detection is outlined, and their potential impact on the parameter space of given models is quantified. In the first work, [2], the capability of the upcoming THESEUS mission in the detection of X-rays resulting from the decay of sterile neutrinos, ALPs and dark photons is investigated. This was achieved by simulating observations of the Milky Way and utilising so-called blank-sky observations, thus maximising the potential of THESEUS' wide field instruments. The findings are presented in the context of existing limits on the three DM models investigated, and it is found that the levels of systematics will play a large role in THESEUS' potential. The second work presented, [3], is a similar study performed for the forthcoming eXTP mission. Here observations of DSphs with eXTP are simulated and its capability to probe the parameter space of the νMSM sterile neutrino is investigated. Results are presented, once again, in the context of existing limits and projections of upcoming missions. The control of systematics will once again be a crucial factor in the ability of eXTP to probe decaying dark matter models.

4.1 THESEUS Insights into ALP, Dark Photon and Sterile Neutrino Dark Matter

THESEUS insights into axionlike particles, dark photon, and sterile neutrino dark matter

Charles Thorpe-Morgan,[1] Denys Malyshev,[1] Andrea Santangelo,[1] Josef Jochum,[2] Barbara Jäger,[2] Manami Sasaki,[3] and Sara Saeedi[3]

[1]*Institut für Astronomie und Astrophysik Tübingen, Universität Tübingen, Sand 1, D-72076 Tübingen, Germany*
[2]*Eberhard Karls Universität Tübingen, 72076 Tübingen, Germany*
[3]*Remeis Observatory and ECAP, Universität Erlangen-Nürnberg, Sternwartstrasse 7, 96049 Bamberg, Germany*

(Received 20 August 2020; accepted 28 October 2020; published 1 December 2020)

Through a series of simulated observations, we investigate the capability of the instruments aboard the forthcoming THESEUS mission for the detection of a characteristic signal from decaying dark matter (DM) in the keV-MeV energy range. We focus our studies on three well studied Standard Model extensions hosting axionlike particles, dark photon, and sterile neutrino DM candidates. We show that, due to the sensitivity of THESEUS' x and gamma imaging spectrometer instrument, existing constraints on dark matter parameters can be improved by a factor of up to ∼300, depending on the considered DM model and assuming a zero level of systematic uncertainty. We also show that even a minimal level of systematic uncertainty of 1% can impair potential constraints by one to two orders of magnitude. We argue that nonetheless, the constraints imposed by THESEUS will be substantially better than existing ones and will well complement the constraints of upcoming missions such as eXTP and Athena. Ultimately, the limits imposed by THESEUS and future missions will ensure a robust and thorough coverage of the parameter space for decaying DM models, enabling either a detection of dark matter or a significant improvement of relevant limits.

DOI: 10.1103/PhysRevD.102.123003

I. INTRODUCTION

Dark matter (DM) remains to be one of the greatest obstacles to our understanding of cosmology. The presence of a universally pervading extra mass is clear and has been precisely measured ($\Omega_{\rm DM} = 0.2641 \pm 0.0002$ [1]); however, apart from its presence in the Universe, the nature and properties of dark matter remain elusive. The Standard Model (SM) is now known not to host any viable dark matter candidate particles, which has led to the consideration of various extensions to the SM that host potential dark matter candidates, see [2–4] for recent reviews.

A very general low energy extension of the SM is comprised of a "dark sector," so called due to its extremely weak interaction with the SM. While such a sector can, in principle, host a variety of new particles providing natural DM candidates (see [5] for a review) and self-interactions, it can most easily be accessed via interactions between the dark and SM sectors. Such cross-sector interactions are often undertaken through a "mediator"—a particle with both, SM and dark sector, quantum numbers. Alternatively the SM particles can interact with the DM particles either directly (if they possess charge under the corresponding interaction) or through mixing. Some representative types of DM models are these [6,7]:

(1) models with (pseudo)scalar DM particles, e.g., axions and axionlike particles (ALPs);
(2) models with sterile neutrinos acting as DM particles;
(3) models with a vector DM particle [e.g., a dark photon (DP)].

In the following, we investigate three well-studied cases of these models with massive DM candidates, which have the potential to comprise the majority of the observed dark matter. Namely, we will consider ALPs, sterile neutrinos, and dark photons as dark matter candidates.

In these models a dark matter particle can decay, consequentially emitting photons. An axion or ALP a can decay into two photons $a \to \gamma + \gamma$. On the other hand, sterile neutrino dark matter N can manifest itself via a two body decay: $N \to \nu + \gamma$, while dark photons V are subject to three-photon decay $V \to 3\gamma$ (a preferable decay channel for $m_V < m_e$ [3]).

The foremost consequence of such radiative decay channels would be the potential for a detectable signal originating from DM dominated astrophysical objects. thesus

While, generally, any astrophysical object with a high DM concentration can be a target for such searches, one must consider additional astrophysical properties of the

object to analyze its feasibility as the focus of such a search. For example, the high DM density and a low level of astrophysical background makes dwarf spheroidal galaxies (dsphs) advantageous targets for dark matter searches across a considerable section of the electromagnetic spectrum. However, dsphs are at most degree-scale targets, and such a small angular size does not allow for the full utilization of the capabilities of broad field of view (FOV) instruments. Conversely, when considering wide FOV instruments, much wider objects with angular extensions of close to the whole sky (e.g., DM halo of the Milky Way) are preferable targets for these instruments.

Despite numerous searches, no clear evidence for any of the described dark matter candidates has been found so far. These searches have however allowed for parameters (mass and/or coupling strengths) to be significantly constrained for all candidates considered in this work.

The fundamental limit on the sterile neutrino mass $m_N \gtrsim 1$ keV arises from the requirement that the phase space density of DM particles in the halos of dsphs may not exceed the limits imposed by the uncertainty relation and the initial phase space density at the moment of production of DM in the early Universe [8–11]. The mixing with active neutrinos is also constrained from above and below by the nondetection of a decay line in astrophysical observations and the exclusion of values that would lead to a discrepancy between observed and predicted abundances of light elements produced during big bang nucleosynthesis [12–17].

The best limits on ALPs in different energy bands are based on observations of objects of a totally different nature. These include astrophysical observations (nondetection of a decay line in the γ-ray background) in the keV-MeV mass range, limits based on the evolution of horizontal branch stars (eV-keV masses), or direct detection experiment limits and astrophysical limits based on nondetection of ALP-photon conversion in certain magnetized astrophysical objects, see [3,18] for reviews.

The parameters of Dark photons are subject to constraints from the nonobservation of a characteristic feature in the spectrum of the galactic diffuse background (for masses $m_V \gtrsim 10$ keV); stellar-evolution constraints (including the Sun, horizontal branch, and red giant stars [19]) for masses $m_V \sim 10^{-6}$–10^4 eV; and cosmological and direct detection experiment limits at lower masses, see [3,20] for reviews.

In what follows we study the capabilities of the forthcoming Transient High Energy Sky and Early Universe Surveyor (THESEUS [21–24]) mission to constrain parameters of keV-MeV mass scale dark matter focusing on the candidates described above.

THESEUS is a European mission concept[1] designed in response to the European space agency call for medium-size mission (M5) within the Cosmic Vision Program.[2] The fundamental goals of the THESEUS mission are the study and detection of high energy transient phenomena, the study of the early Universe and the epoch of reionization, and "the hot and energetic Universe." These goals are planned to be achieved using the mission's unique combination of instruments.

The THESEUS mission will host a total of three telescope arrays, covering a section of the infrared regime as well as the energy range of soft and hard x-rays. The proposed instrumental payload for THESEUS is as follows:

(1) The soft x-ray imager (SXI), an array of four lobster-eye [26] telescope units with a quasisquare FOV covering the energy range of 0.3–5 keV with an effective area of $A_{\rm eff} \approx 1.9$ cm^2 at 1 keV and an energy resolution $\sim$4%. These will cover a total FOV of $\sim$1 sr with source location accuracy $<$1–2 arcminutes (for a full review of the instrument see [27]).

(2) The infrared telescope (IRT), a single large (0.7 m) telescope that will be used for follow-up observations of gamma-ray bursts. It will operate in the wavelength band 0.7–1.8 μm and have a $15' \times 15'$ FOV (for further specifications on the IRT see [28]).

(3) The x-gamma ray imaging spectrometer (XGIS) array, consisting of coded-mask cameras (with the total half-sensitive FOV comparable to that of the SXI) using monolithic x-gamma ray detectors based on bars of silicon diodes coupled with CsI crystal scintillator. XGIS will operate in the energy range of 2 keV–20 MeV, which will be achieved using the two different detectors, referenced hereafter as XGIS-X and XGIS-S. The silicon drift detector (SDD) will cover the energy range of 2–30 keV (XGIS-X), whereas the CsI scintillator will cover the range of 20 keV–2 MeV (XGIS-S[3]). The effective areas and energy resolutions of XGIS-S are $A_{\rm eff}(300\ {\rm keV}) \approx 1100$ cm^2 and energy resolution changing from $\Delta E/E \sim 15\%$ at below 100 keV to $\Delta E/E \sim 2\%$ at higher energies. The effective area and resolution of XGIS-X instrument are $A_{\rm eff}(10\ {\rm keV}) \approx 500$ cm^2 and $\Delta E/E \sim 1.5\%$, see [29] for the full technical proposal for the XGIS. We summarize these technical characteristics and compare them to current and next-generation missions in Table I.

Focusing on keV-MeV mass scale dark matter, we omitted the IRT from our further investigations. However, both the SXI and the XGIS have a large potential for the detection of DM decay given their very large FOVs (see, e.g., discussion in [31]), thus the sensitivity simulations run by this study were performed for both these instruments.

[1]Selected by European space agency on May 7, 2018, to enter an assessment phase study.

[2]See the Cosmic Vision Program website [25].

[3]Note, that due to the transparency of the XGIS coded mask at hard x-rays at $E \gtrsim 150$ keV XGIS-X operates as a collimator.

TABLE I. Technical characteristics of THESEUS compared to current and next generation missions. The table summarizes the peak effective area $A_{\rm eff}^{\rm peak}$, its corresponding energy $E^{\rm peak}$ and the energy resolution at this energy ($dE/E^{\rm peak}$) as well as the field of view of the instrument. The "Date" column summarizes either the planned launch date of future missions (as of 2021), or the launch and deorbit date of current generation missions. We note that the parameters of the Hitomi/SXS are similar to those of the XRISM mission, planned for 2022 [30].

Instrument	$A_{\rm eff}^{\rm peak}$ cm^2	$E^{\rm peak}$ keV	$dE/E^{\rm peak}$	FOV sr	Date
SXI	1.9	1	0.04	1	2032
XGIS-X	504	8.5	0.06	1	2032
XGIS-S	1060	350	0.024	1	2032
Athena/X-IFU	1.6×10^4	1.4	1.9×10^{-3}	3.3×10^{-6}	2031
eXTP/SFA	8600	1.5	0.1	9.6×10^{-6}	2027
eXTP/WFM	77	9	0.029	2.5	2027
Hitomi/SXS	84	6	9.4×10^{-4}	7.1×10^{-7}	2016–2016
XMM/PN	815	1.5	0.07	4.5×10^{-5}	1999-$**$

Following this introduction, we present the methodology of our study of the capabilities of the forthcoming THESEUS mission to probe the parameter space of DM models with ALPs, sterile neutrinos and dark photons.

II. SEARCH FOR DECAYING DM WITH THESEUS

The decay of massive ($m_{\rm DM}$) DM particles with an emission of μ photons in each decay will result in the photon spectrum (as a function of photon energy E)

$$\frac{d\mathcal{F}}{d\Omega} \equiv \frac{dN}{dEdtdAd\Omega} = \frac{1}{4\pi} \cdot \frac{\mu \mathbf{D}}{m_{\rm DM}} \cdot \frac{d\Gamma(E)}{dE} \tag{1}$$

and a corresponding spectrum in the total field of view of the observing instrument:

$$\mathcal{F}_{\rm FOV} = \int \frac{d\mathcal{F}}{d\Omega} d\Omega = \frac{\mu \mathbf{D}_{\rm FOV}}{4\pi m_{\rm DM}} \cdot \frac{d\Gamma(E)}{dE}. \tag{2}$$

The $\mathbf{D}_{\rm FOV}$ term in Eq. (2) is the total $\mathbf{D}$ factor (DM mass column density) within the field of view and represents the astrophysical component of the dark matter signal. This is defined as the integral of the DM density over the field of view of the instrument and the line of sight ($l.o.s.$), i.e.,

$$\mathbf{D}_{\rm FOV} \equiv \int \mathbf{D} d\Omega = \int_{\rm FOV} \int_{l.o.s.} \rho_{\rm DM} d\ell d\Omega. \tag{3}$$

The Γ term in Eqs. (1)–(2) represents the radiative decay width—a model-dependent term that for the three differing models considered in this study is described below. Γ for the νMSM (sterile neutrino) model, is given by [32,33]:

$$\left.\frac{d\Gamma}{dE}\right|_{\nu\rm MSM} = \frac{9\alpha G_F^2}{256 \cdot 4\pi^4} \sin^2(2\theta) m_N^5 \delta(E - m_N/2). \tag{4}$$

Here m_N is the mass of the sterile neutrino; θ is the mixing angle and $\alpha_{\rm QED}$ and G_F stand for fine structure and Fermi constants.

For ALPs, $d\Gamma/dE$ is of the form [3,34]

$$\left.\frac{d\Gamma}{dE}\right|_{\rm ALP} = \frac{g_{a\gamma\gamma}^2 m_a^3}{64\pi\hbar} \delta(E - m_a/2). \tag{5}$$

In this equation m_a denotes the mass of the ALP; whereas $g_{a\gamma\gamma}$ represents the ALP-photon coupling strength.

Finally the value of Γ for dark photons is given by the equation [3,35],

$$\begin{aligned} \left.\frac{d\Gamma}{dE}\right|_{\rm DP} &= \frac{2\kappa^2 \alpha_{\rm QED}^4}{2^7 3^7 5^3 \pi^3 \hbar} \left(\frac{m_V}{m_e}\right)^8 \cdot f(x); \\ f(x) &= x\left(1715 - 3105x + \frac{2919}{2}x^2\right); \\ x &\equiv \frac{2E}{m_V}; \qquad x \in [0;1], \end{aligned} \tag{6}$$

where again m_V is the mass of the dark photon, and κ is the DP kinetic mixing parameter.

Substituting the respective expressions of Eqs. (4)–(6) into Eq. (2) and utilizing values from [34], one obtains the form of expected signal for each model,

$$\begin{aligned} \mathcal{F}_{\nu\rm MSM}(E) &\approx 10^{-7} \left(\frac{\sin^2(2\theta)}{10^{-16}}\right) \left(\frac{m_N}{10\ \rm keV}\right)^4 \\ &\times \left(\frac{\mathbf{D}_{\rm FOV}}{10^{22}\ \rm GeV/cm^2}\right) \delta(E - m_N/2) \frac{\rm ph}{\rm cm^2\,s\,keV}; \\ \mathcal{F}_{\rm ALP}(E) &\approx 1.2 \times 10^{-7} \left(\frac{m_a}{10\ \rm keV}\right)^2 \left(\frac{g_{a\gamma\gamma}}{10^{-20}\ \rm GeV^{-1}}\right)^2 \\ &\times \left(\frac{\mathbf{D}_{\rm FOV}}{10^{22}\ \rm GeV/cm^2}\right) \delta(E - m_a/2) \frac{\rm ph}{\rm cm^2\,s\,keV}; \\ \mathcal{F}_{\rm DP}(E) &\approx 4.08 \times 10^{-7} \left(\frac{\kappa}{10^{-10}}\right)^2 \left(\frac{m_V}{10\ \rm keV}\right)^7 \\ &\times f\left(\frac{2E}{m_V}\right) \left(\frac{\mathbf{D}_{\rm FOV}}{10^{22}\ \rm GeV/cm^2}\right) \frac{\rm ph}{\rm cm^2\,s\,keV}; \end{aligned} \tag{7}$$

Here we adopted values of the known fundamental constants (e.g., α, G_F, etc.) from [34]; we also scaled parameters for some characteristic values and finally accounted for the production of $\mu = 1$ photon in sterile neutrino decays, $\mu = 2$ photons for ALP decays and $\mu = 3$ for three-photon dark photon decay.

The DM-decay signal for each model respectively will be comprised of the spectrum given by Eq. (7), and this signal is expected to be present in the real data on top of astrophysical and instrumental backgrounds. Such a signal can be distinguished from the background due to its characteristic shape (a narrow line for νMSM or ALPs; a relatively broad spectral feature in the case of dark photons). The minimal detectable flux for a given instrument depends on several factors and may be estimated as

$$F_{\rm min} = \sigma\left(\sqrt{\frac{B\Delta E}{A_{\rm eff}T\Omega_{\rm FOV}}} + \alpha B\Delta E\right)\frac{\rm ph}{\rm cm^2\ s\ sr}. \quad (8)$$

Here, T is the exposure of the observation (time duration for which data are taken), the instrument's effective area and energy resolution are denoted by $A_{\rm eff}(E)$ and $\Delta E(E)$, respectively, and the observed background (instrumental and astrophysical) is $B(E)\,{\rm ph}/({\rm cm^2\,s\,keV\,sr})$. The parameter σ stands for the significance level of the detection (e.g., $\sigma = 2$ for 2σ or ~95% C.L. detection) and α for the level of characteristic systematic uncertainty of the instrument. We note that for DM candidates producing a signal that is broader than the instrument's energy resolution, one must utilize the characteristic width of the signal, instead of ΔE.

Using Eq. (8), the minimal detectable flux $F_{\rm min}(E)$ derived from the data can be compared to the expected dark matter decay signal $F_{\rm DM}(E)$ given by Eq. (7) for each of the considered DM candidates. This allows for the derivation of the range of dark matter parameters which the instrument is capable of probing.

A. Observational strategy

Any astrophysical object hosting a significant amount of dark matter can serve as a candidate for indirect searches for decaying dark matter. However, in order to maximize the potential of any instrument used, the object must have an angular size in the sky comparable to the instrument's FOV. Conversely, the observation of an object with a much smaller angular size than an instrument's FOV will suffer from a deterioration of the **D** factor (and thus resulting DM decay flux), as the integral $\mathbf{D}_{\rm FOV} = \int \mathbf{D} d\Omega$ vanishes beyond the characteristic size of the object. Therefore, neglecting to consider the relative size of an instrument's FOV can lead to the instrument's potential not fully being utilized. It is thus imperative to consider targets of a comparable angular size to the instrument's FOV.

In the context of indirect DM detection, the suite of x-ray instruments aboard THESEUS possess uniquely broad fields of view (~1 sr) which pose the issue of being larger than the angular size of any extragalactic dark matter dominated object. Thus, with reference to the previous discussion of fields of view and object sizes, to fully utilize the capabilities of THESEUS, we propose to focus on indirect DM searches of local, Milky Way concentrations of dark matter with THESEUS' instruments. Additionally, in order to minimize the level of astrophysical background (e.g., galactic ridge x-ray emission) we propose that the observations should be located away from the galactic plane. Namely, we propose the observations to be located at latitudes $|b| > 20$ where galactic ridge x-ray emission contributions are minimal [36]. We note, that a similar strategy was proposed for the eXTP and several other broad-FOV missions [31,37].

To estimate the **D** factor in the FOV of THESEUS' instruments, and, consequently, the strengths of the expected decaying DM signals [see Eq. (7)], we assume that the density of the dark matter in the Milky Way follows a Navarro-Frenk-White [38,39] profile:

$$\rho_{\rm DM}(r) = \frac{\rho_0 r_0^3}{r(r+r_0)^2}, \quad (9)$$

with $r_0 \approx 17.2$ kpc and $\rho_0 \approx 7.9 \times 10^6\ M_\odot/{\rm kpc}^3$ [40].

The dark matter column density given by integrals in Eq. (3) was calculated numerically and the derived values of the **D** factors for proposed for observations regions are summarized in Table II. We would like to note that the results presented below do not depend directly on the considered DM profile, but rather on the **D** factor (dark matter column density) value. These results can be rescaled according to the $\mathbf{D}_{\rm FOV}$ if another DM distribution model in the Milky Way is considered. We, however, expect the effect of rescaling due to the variations in the dark matter profile to be relatively small. For example, an alternative profile considered in [40] gives a **D** factor of ~10% lower

TABLE II. Parameters of the simulated observations from blank sky readings. The FOV is assumed to be parallel to the galactic plane and roughly corresponds to the sky area at the border of which the effective area is 50% of the on axis one, see [29]. Galactic coordinates show the coordinates of the FOV center in which the **D** factor was calculated and the observation simulated (see text for details).

Observation	FOV deg^2	Galactic coordinate center	$\mathbf{D}_{\rm FOV}$ GeV/cm^2
SXI	$\sim 104° \times 31°$	(110, 50)	1×10^{22}
Blank Sky			
XGIS	$\sim 104° \times 31°$	ON (0, 50)	2×10^{22}
Blank Sky		OFF (110, 50)	1×10^{22}

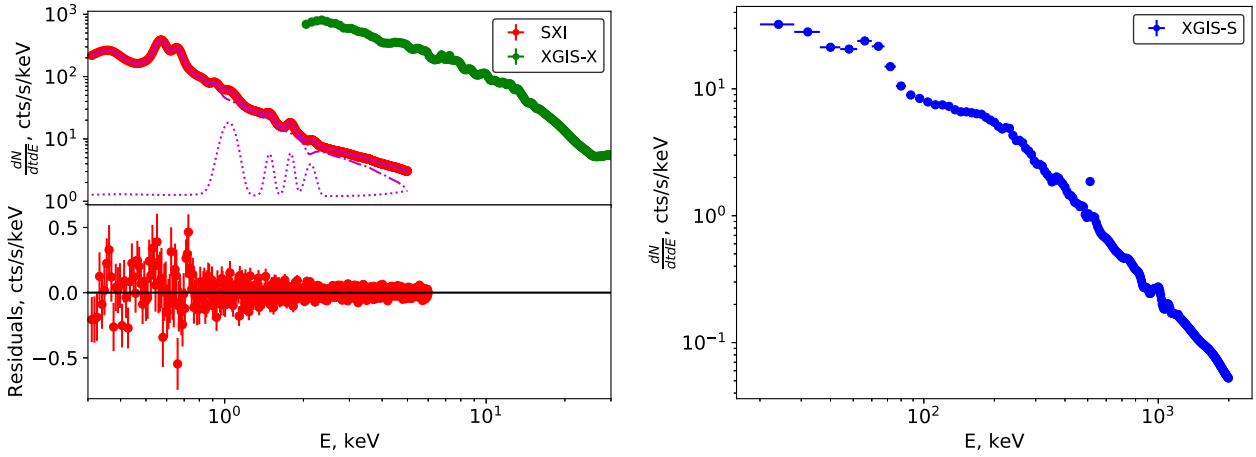

FIG. 1. Spectra of blank sky observations from THESEUS' instruments: the SXI, XGIS-X (left panel), and XGIS-S (right panel). The lower subpanel illustrates the residuals (model subtracted from data) of the SXI instrument according to the best-fit model (solid magenta line). Dotted and dot-dashed magenta lines represent the instrumental and sky components of the model, see text for more details.

than the best fit considered model, consequently resulting in a marginally weaker signal.

To access the minimal detectable flux level [see Eq. (8)] within THESEUS' observations, we estimated the expected background flux level from simulated 1 Msec exposure blank sky observations with the THESEUS/SXI and XGIS instruments. The simulated data were obtained with the *fakeit* XSPEC (version: 12.10.1f) command, based on templates of blank sky observations provided by the THESEUS collaboration[4] (`sxi_bkg.pha`,[5] `XGIS-X_0deg_v7.bkg`, and `XGIS-S_0deg_v7.bkg`) and corresponding response files, see Fig. 1. We note, that the provided templates are based on the estimations of both, instrumental and astrophysical backgrounds and thus any additional component(s) to model the background were not included.

The instrumental component of the backgrounds were simulated by the THESEUS collaboration utilizing the GEANT4 toolkit. These backgrounds were based on known low Earth orbit characteristic spectra and on the intensities of the particle background. The astrophysical background was adapted from the ROSAT all sky survey x-ray background, specifically from an area of sky of a 10° radius, centered on the north ecliptic pole [41].

We acknowledge that variations in the flux level between the simulations and observations will have an impact on the results of our simulations and therefore on our estimates of THESEUS' capabilities. We argue that, a recent report on the background in the HXMT satellite has shown minimal variation between simulated (performed in the same manor as in THESEUS) and observed backgrounds in an energy range similar to the SXI's [42]. Namely, only a 5%–15% increase is reported in the observed background, when compared to its counterpart in silico [42]. We argue that given the similar low Earth orbits and energy ranges of HXMT and THESEUS, the simulations provide an accurate estimation of THESEUS' background level.

Our simulations revealed that the spectral shapes of the background differ vastly between the SXI and XGIS-S/X instruments. The background of the SXI can be adequately modeled by the sum of two models representing both the astrophysical and instrumental backgrounds. The model of the astrophysical background was selected to be the sum of a power law and a hot thermal plasma with the temperature ∼0.2 keV, constituting contributions from cosmic x-ray background and galactic x-ray emission [43,44]. The instrumental background was best modeled by the sum of a power-law (not convolved with the effective area) and a set of four narrow Gaussian lines (see dot-dashed and dotted magenta lines in the left panel of Fig. 1 for corresponding model components). For this instrument we therefore propose the use of the common observational strategy whereby one searches for a decaying-DM spectral feature on top of an adequately modelled background. This method is widely used in decaying dark matter searches in various astrophysical objects, see [4] for a review.

On the other hand, the backgrounds of the two XGIS detectors are characterized by a large number of linelike and broad spectral features (dominating the instrumental part of the background due to the coded-mask optics and SDD/CsI detectors in the instruments). We conclude that the XGIS' background is significantly more complicated than SXI's, and cannot be adequately modeled with any simple model. We thus propose the use of a different method for the XGIS, the "ON-OFF" observational strategy. This strategy requires the use of pairs of observations of a comparable duration, both "ON" and "OFF" the target.

[4]V7 templates dated May–July 2020; see THESEUS website.
[5]Scaled by 17508, to account for template's FOV (675 arcmin^2).

We propose to locate the "ON" observations closer to the Galactic Center than "OFF" ones, so $\mathbf{D}^{\mathrm{ON}}_{\mathrm{FOV}} - \mathbf{D}^{\mathrm{OFF}}_{\mathrm{FOV}} > 0$. The estimations for $\mathbf{D}^{\mathrm{ON}}_{\mathrm{FOV}}$ and $\mathbf{D}^{\mathrm{OFF}}_{\mathrm{FOV}}$ for the sample "ON" and "OFF" observations are summarized in Table II.

We acknowledge several possible variations in the shape and intensities of the astrophysical and instrumental backgrounds including energy, spatial, and temporal fluctuations. These include variations in the instrumental/astrophysical background across the FOV of the instrument; variations in the instrumental background along the orbital path due to particle background variations, as well as variations in the astrophysical background between "ON" and "OFF" observation regions. To minimize the impact of orbital variations of the background we propose to perform "ON" and "OFF" observations in series of short consecutive observations, minimizing the change in the above factors. Additional sources of background uncertainty include an imperfect modeling of the instrumental background and an imperfect knowledge of the instrument's response and effective area.

In the absence of detailed studies characterizing the level of possible background variations for THESEUS' instruments, we propose to estimate the impact of the previously described effects by introducing a systematic uncertainty in THESEUS' spectra. Below, we present all results for the case of an absence of systematic uncertainty, and compare them to the results in which a 1% systematic uncertainty was introduced. Such a value of systematic uncertainty is characteristic for XMM-Newton.[6] In order to replicate the effects of systematic uncertainty, we introduced a new STAT_ERR column to the simulated spectral files which, in addition to the standard Gaussian error, included a value proportional to the total counts in each channel.

We note that the systematics applied operate at small energy scales. Such systematics effectively prevent uncertainties in each energy channel from being smaller than some fraction of the flux independently of the observation's duration. Contrary to this, large scale systematics (applied to the whole spectrum or to its broad intervals) can change the overall normalization of the spectrum (or its normalization over broad intervals), without preventing the uncertainties in each interval becoming arbitrarily small. The characteristic level of large-scale systematics can be as large as ∼20%–30% due to mismodeling of the instrumental background (as in HXMT's case [42]), variability of the instrumental background along the orbital path due to particle background variations (see [46] for a discussion on XMM-Newton background, and, for spatial variations of cosmic x-ray background, see [47]).

For localized spectral feature searches, large scale systematics, up to some level of accuracy, can be eliminated by the modification of certain features. First one may alter the model considered for a fit (e.g., increase/decrease overall model normalization in the simplest case); second, one may also modify the instrument's responses (see, e.g., discussion in [48]) or remedy this by splitting the data on a set of broad energy intervals and analyzing each interval independently. Given otherwise arbitrarily small flux uncertainties (with increased observational time), these approaches can allow for the estimation of the impact of large-scale systematics on the flux of narrow features to be of the same order as the systematics, i.e., ∼20%. In what below we show that the 1% small-scale systematic can imply a substantially larger impact.

B. Results

Following the previously outlined methodology for simulating observations in both of THESEUS' instruments, we conducted a search for a dark matter decay signal with a spectral shape (for each respective model) given by Eq. (7), originating from the whole FOV.

We calculated 2σ upper limits on the normalization of the signal, following Eq. (8). For both the considered approaches (background modeling for the SXI and the ON-OFF technique for the XGIS) we adopted identical methods for the limit calculation. We note only that the only significant difference between the two approaches was that in terms of Eq. (8) the background B within the characteristic signal width ΔE was estimated either from the model or from the "OFF"-observation spectrum at the corresponding energy. The obtained limits allow us to derive the sensitivities of each of THESEUS' instruments to the parameters of the DM particle in the corresponding model according to Eq. (7).

The 2σ (∼95% confidence level) limits on flux[7] from 1 Msec long observation of Milky Way halo are shown with solid red, green and blue curves, for the SXI, XGIS-S, and XGIS-X instruments respectively, in Fig. 2. The left and right panels show the results for a narrow Gaussian line signal (sterile neutrino and ALP decay cases) and a broader spectral feature expected from a dark photon decay. Limits from observations where a 1% systematic uncertainty was introduced to each instrument are shown with dashed lines.

The displayed limits illustrate that the sensitivity of each of THESEUS' instruments to a DM decay signal is detrimentally affected by the effect of poorly controlled systematics for all of the types of DM particles considered. For a narrow line signal (sterile neutrino or ALP dark matter candidates) the SXI will suffer from worsening of its limits by a factor of ∼10, whereas the XGIS is significantly more affected, seeing a reduction by a factor of ∼100 in its sensitivity in both detectors. We therefore conclude that, despite the promising sensitivities of each instrument, instrumental systematics can be a significant obstacle

[6]See EPIC Calibration Status document [45].

[7]Corresponding upper limits on the normalization were calculated with Error 4.0 XSPEC command.

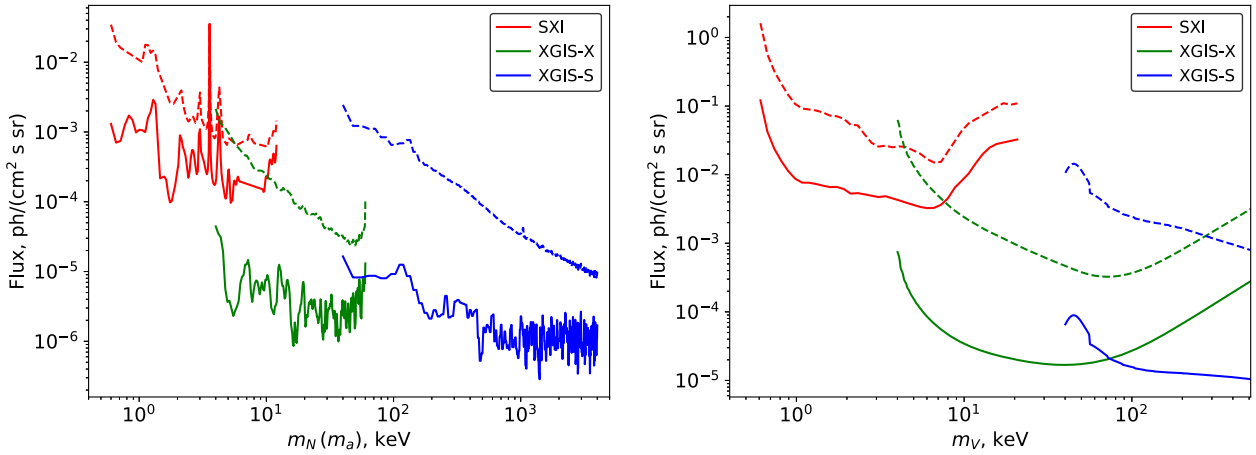

FIG. 2. The 2σ limits on the sensitivity of THESEUS' instruments to a narrow Gaussian line (left panel) and a spectral feature expected for a dark photon decay (right panel) [see Eq. (7) for a 1 Msec long observation]. The signal is assumed to be present in the whole FOV of the instrument. Dashed lines show the sensitivity of the instruments assuming a 1% systematic error in each respectively. Results are presented as functions of the mass of the DM particle.

and severely impair the ability of each instrument if not controlled.

For each of the considered DM models (ALPs, sterile neutrino and dark photons), we converted the obtained flux limits into limits on the parameters of the DM particles, see Eq. (7) and Figs. 3 and 4, and compared the obtained limits to other limits presented in the literature.

For the sterile neutrino we compared limits derived by this study to existing observational x-ray and γ-ray constraints (see [4] for a review). We also display, for comparison, the expected limits from 1 Msec-long Segue I dsph observations by the forthcoming Athena mission [50], given a zero level of systematic uncertainty. The limits based on the phase space density arguments for the DM in dsphs [8–11] and otherwise incorrect abundance of sterile neutrinos produced in the early Universe [53,54] are shown as gray shaded regions. Model dependent limits based on parameter values that are inconsistent with the observed

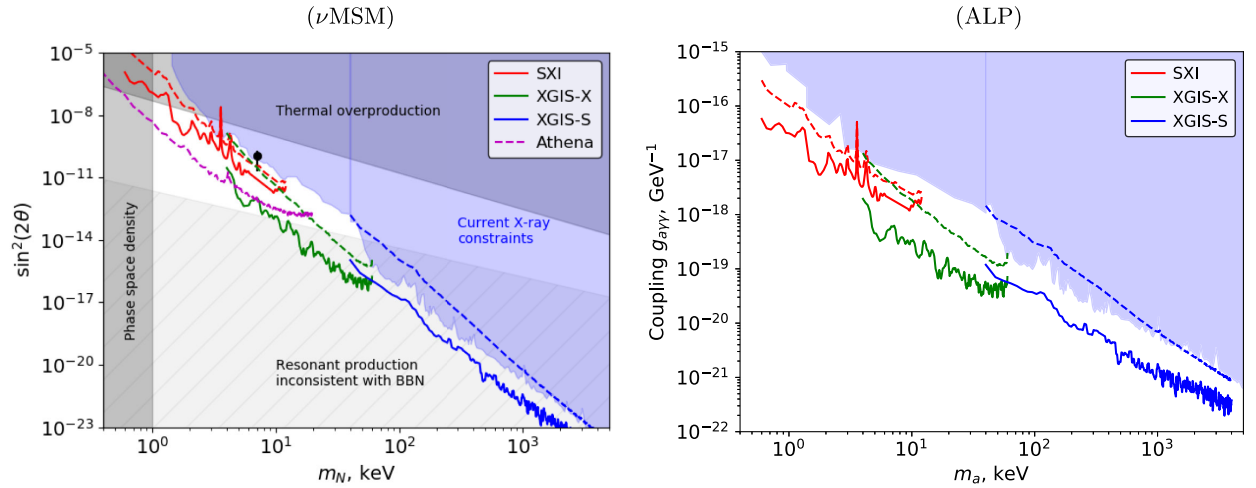

FIG. 3. The sensitivity of the instruments aboard THESEUS to the parameters of sterile neutrino and ALP dark matter. All limits correspond to the 2σ values of the flux obtained from 1 Msec simulated observations of the Milky Way's DM halo, see Table II for the details. On all panels red, green and blue solid curves represent sensitivity limits for the SXI, XGIS-X, and XGIS-S instruments, respectively, for a 0% systematic uncertainty. Dashed curves illustrate similar limits for 1% systematics present in the data. Shaded regions denote current exclusions adopted from [3,4,8–16,18–20,49]. Left panel: THESEUS' sensitivity for the sterile neutrino (νMSM) DM. The Magenta curve illustrates limits reachable for Athena [50]. The black point represents the parameter point corresponding to the tentative detection of an ~3.55 keV line in certain DM-dominated objects (see [4,51,52] for recent reviews). Right panel: sensitivity limits for ALP dark matter, see text for details.

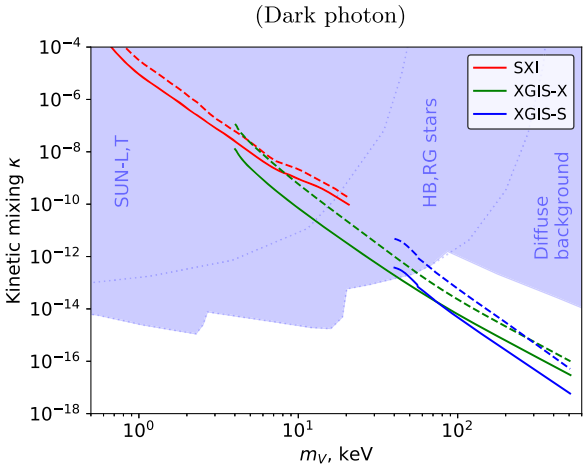

FIG. 4. The sensitivity of the instruments aboard THESEUS to the parameters of dark photon dark matter, see caption of Fig. 3 for designations and text for details.

abundances of light elements produced during big bang nucleosynthesis [12–16] (see, however, [17]) are shown as a gray hatched region.

The limits on ALPs were compared to the existing limits in the keV band based on the nondetection of a linelike feature in the spectrum of diffuse gamma-ray background in the keV-MeV band [18,49]. The limits on dark photons, on the other hand, are compared to stellar evolution-based limits (the Sun limits in longitudinal and transverse channels; the limits from horizontal branch and red giant stars' evolution [19]) and the limits from the diffuse gamma-ray background, see [3,20] for a review.

III. DISCUSSION AND CONCLUSIONS

This study has investigated the sensitivity of the proposed x-ray telescope arrays aboard the upcoming THESEUS mission to decaying dark matter signals from DM models with ALPs, sterile neutrinos and dark photons. Our results demonstrate that THESEUS has the potential to impose significantly better limits than the current generation of instruments. The use of 1 Msec long THESEUS observations of blank sky regions has the potential to improve existing x-ray constraints on the parameters of dark matter, by a factor of up to ∼300, within the keV-MeV dark matter particle mass range, see Figs. 3 and 4.

The regions proposed for observations are located at significant angular distance from the Galactic Center. This allows the minimization of uncertainties connected to the knowledge of the exact shape of the dark matter profile and excludes the presence of strong astrophysical backgrounds. In case the THESEUS mission is approved with reduced specifications,[8] the relocation of observational regions closer to the Galactic Center can compensate (within a factor of ∼2) the subsequent decrease in the expected dark matter signal.

We also show that the XGIS has the potential to completely explore the sterile neutrino parameter space in the mass range $m_N \sim 15$–150 keV (see Fig. 3, left panel), assuming a marginally possible 0% level of systematic uncertainty.

We assert that the effect of systematics on THESEUS' instruments will be severely detrimental to their sensitivity to all types of decaying DM. We have shown a level of systematics at 1% can considerably worsen the constraints that can be achieved by both instruments, with the limits imposed by the SXI and XGIS falling by up to factors of ∼10 and ∼100, respectively, for all considered DM models. At these levels of systematic uncertainty, while the XGIS will remain able to probe new areas of the parameter space, the SXI's limits may, in certain ranges, be worse than the existing limits in this energy band. To summarize, only full control of the systematics in these instruments would make them a formidable addition in the search for DM.

The tentative detection of a 3.55 keV line in some DM-dominated objects [51,52] is still actively being discussed in the field (see [4] for a recent review). Such a signal was originally proposed to originate from the decay of a sterile neutrino with the mass $m_N \sim 7$ keV and a mixing angle of $(\sin^2(2\theta) \sim 2 \times 10^{-11})$. The corresponding range of mixing angles discussed in the literature is denoted by the black point with error bars in Fig. 3. We mention that the constraints displayed in Fig. 3 for a 0% systematic uncertainty (left panel) indicate also that THESEUS will be sensitive enough to exclude or detect this line, at a $\gtrsim 7\sigma$ level ($\sim 3\sigma$ level if 1% systematics is present). The strength of such a line could be compared to other DM-dominated objects or along the sky in order to correlate its intensity with the known $\mathbf{D}_{\mathrm{FOV}}$ value, and thus draw conclusions on its possible DM-decay origin.

We would further like to note that several other models were proposed to explain the observed 3.55 keV signal. These models include scalar [56] and pseudoscalar, ALP [57,58] dark matter. We argue that the (non)detection of such a line or feature by THESEUS can provide significant constraints on the parameters of these models.

The THESEUS mission, as well as its numerous scientific objectives, will play an essential part in high energy studies over the next decade. Its overlap with other planned missions such as eXTP and Athena provides prime potential for the complementary study of the decaying DM's parameter space using the above mentioned next generation satellites, among many others. The use of these instruments in conjunction with one another has the potential to impose tighter limits on DM candidates than ever before and significantly decrease their unexplored parameter space.

[8]See recent updates on THESEUS mission website [55].

We conclude that THESEUS, alongside well controlled systematics, has the potential to either detect decaying dark matter, or to impose some of the strongest constraints on its properties among its generation of satellites.

ACKNOWLEDGMENTS

The authors acknowledge support by the state of Baden-Württemberg through bwHPC. This work was supported by DFG through Grant No. MA 7807/2-1.

[1] N. Aghanim, Y. Akrami, M. Ashdown, J. Aumont, C. Baccigalupi, M. Ballardini, A. J. Banday, R. B. Barreiro, N. Bartolo *et al.* (Planck Collaboration), Astron. Astrophys. **641**, A6 (2020).
[2] A. Boyarsky, D. Iakubovskyi, and O. Ruchayskiy, Phys. Dark Universe **1**, 136 (2012).
[3] M. Pospelov, A. Ritz, and M. Voloshin, Phys. Rev. D **78**, 115012 (2008).
[4] A. Boyarsky, M. Drewes, T. Lasserre, S. Mertens, and O. Ruchayskiy, Prog. Part. Nucl. Phys. **104**, 1 (2019).
[5] M. Battaglieri, A. Belloni, A. Chou, P. Cushman, B. Echenard, R. Essig, J. Estrada, J. L. Feng, B. Flaugher, P. J. Fox *et al.*, arXiv:1707.04591.
[6] R. Essig, J. A. Jaros, W. Wester, P. Hansson Adrian, S. Andreas, T. Averett, O. Baker, B. Batell, M. Battaglieri, J. Beacham *et al.*, arXiv:1311.0029.
[7] M. Raggi and V. Kozhuharov, Nuovo Cimento Riv. Ser. **38**, 449 (2015).
[8] S. Tremaine and J. E. Gunn, Phys. Rev. Lett. **42**, 407 (1979).
[9] A. Boyarsky, O. Ruchayskiy, and D. Iakubovskyi, J. Cosmol. Astropart. Phys. 03 (2009) 005.
[10] D. Gorbunov, A. Khmelnitsky, and V. Rubakov, J. Cosmol. Astropart. Phys. 10 (2008) 041.
[11] D. Savchenko and A. Rudakovskyi, Mon. Not. R. Astron. Soc. **487**, 5711 (2019).
[12] X. Shi and G. M. Fuller, Phys. Rev. Lett. **82**, 2832 (1999).
[13] P. D. Serpico and G. G. Raffelt, Phys. Rev. D **71**, 127301 (2005).
[14] M. Shaposhnikov, J. High Energy Phys. 08 (2008) 008.
[15] M. Laine and M. Shaposhnikov, J. Cosmol. Astropart. Phys. 06 (2008) 031.
[16] L. Canetti, M. Drewes, T. Frossard, and M. Shaposhnikov, Phys. Rev. D **87**, 093006 (2013).
[17] A. Kusenko, Phys. Rev. Lett. **97**, 241301 (2006).
[18] P. W. Graham and S. Rajendran, Phys. Rev. D **88**, 035023 (2013).
[19] J. Redondo and G. Raffelt, J. Cosmol. Astropart. Phys. 08 (2013) 034.
[20] M. Fabbrichesi, E. Gabrielli, and G. Lanfranchi, arXiv:2005.01515.
[21] L. Amati, P. OBrien, D. Gtz, E. Bozzo, C. Tenzer, F. Frontera, G. Ghirlanda, C. Labanti, J. Osborne, G. Stratta *et al.*, Adv. Space Res. **62**, 191 (2018).
[22] G. Stratta, R. Ciolfi, L. Amati, E. Bozzo, G. Ghirlanda, E. Maiorano, L. Nicastro, A. Rossi, S. Vinciguerra, F. Frontera *et al.*, Adv. Space Res. **62**, 662 (2018).
[23] G. Stratta, L. Amati, R. Ciolfi, and S. Vinciguerra, Mem. Soc. Astron. Ital. **89**, 205 (2018).
[24] N. R. Tanvir, Mem. Soc. Aston. Ital. **89**, 163 (2018).
[25] https://www.esa.int/Science_Exploration/Space_Science/ESA_s_Cosmic_Vision.
[26] J. R. P. Angel, Astrophys. J. **233**, 364 (1979).
[27] P. O'Brien, E. Bozzo, R. Willingale, I. Hutchinson, J. Osborne, L. Amati, and D. Götz, Mem. Soc. Astron. Ital. **89**, 130 (2018).
[28] D. Götz, O. Boulade, B. Cordier, E. Le Floc'h, F. Pinsard, J. Amiaux, T. Tourrette, S. Basa, S. Vergani, J. L. Atteia *et al.*, Mem. Soc. Astron. Ital. **89**, 148 (2018).
[29] R. Campana, F. Fuschino, C. Labanti, L. Amati, S. Mereghetti, M. Fiorini, F. Frontera, G. Baldazzi, P. Bellutti, G. Borghi *et al.*, Mem. Soc. Astron. Ital. **89**, 137 (2018).
[30] XRISM Science Team, arXiv:2003.04962.
[31] D. Zhong, M. Valli, and K. N. Abazajian, Phys. Rev. D **102**, 083008 (2020).
[32] P. B. Pal and L. Wolfenstein, Phys. Rev. D **25**, 766 (1982).
[33] V. Barger, R. J. N. Phillips, and S. Sarkar, Phys. Lett. B **352**, 365 (1995).
[34] M. Tanabashi *et al.* (Particle Data Group), Phys. Rev. D **98**, 030001 (2018).
[35] H. An, M. Pospelov, J. Pradler, and A. Ritz, Phys. Lett. B **747**, 331 (2015).
[36] R. Krivonos, M. Revnivtsev, E. Churazov, S. Sazonov, S. Grebenev, and R. Sunyaev, Astron. Astrophys. **463**, 957 (2007).
[37] D. Malyshev, C. Thorpe-Morgan, A. Santangelo, J. Jochum, and S.-N. Zhang, Phys. Rev. D **101**, 123009 (2020).
[38] J. F. Navarro, C. S. Frenk, and S. D. M. White, Astrophys. J. **462**, 563 (1996).
[39] J. F. Navarro, C. S. Frenk, and S. D. M. White, Astrophys. J. **490**, 493 (1997).
[40] M. Cautun, A. Benitez-Llambay, A. J. Deason, C. S. Frenk, A. Fattahi, F. A. Gmez, R. J. J. Grand, K. A. Oman, J. F. Navarro, and C. M. Simpson, Mon. Not. R. Astron. Soc. **494**, 4291 (2020).
[41] S. Snowden, R. Egger, D. Finkbeiner, J. Freyberg, and P. Plucinsky, Astrophys. J. **493**, 715 (1998).
[42] J. Zhang, X. Li, M. Ge, H. Zhao, Y. Tuo, F. Xie, G. Li, S. Zheng, J. Nie, L. Song *et al.*, Astrophys. Space Sci. **365**, 158 (2020).
[43] D. McCammon, R. Almy, E. Apodaca, W. Bergmann Tiest, W. Cui, S. Deiker, M. Galeazzi, M. Juda, A. Lesser, T. Mihara *et al.*, Astrophys. J. **576**, 188 (2002).
[44] A. De Luca and S. Molendi, Astron. Astrophys. **419**, 837 (2004).
[45] https://xmmweb.esac.esa.int/docs/documents/CAL-TN-0018.pdf.

[46] F. Gastaldello, S. Ghizzardi, M. Marelli, D. Salvetti, S. Molendi, A. De Luca, A. Moretti, M. Rossetti, and A. Tiengo, Exp. Astron. **44**, 321 (2017).
[47] S. L. Snowden, R. Egger, M. J. Freyberg, D. McCammon, P. P. Plucinsky, W. T. Sanders, J. H. M. M. Schmitt, J. Trümper, and W. Voges, Astrophys. J. **485**, 125 (1997).
[48] A. Acharyya, R. Adam, C. Adams, I. Agudo, A. Aguirre-Santaella, R. Alfaro, J. Alfaro, C. Alispach *et al.* (T. Cherenkov Telescope Array Consortium), arXiv:2007.16129.
[49] A. Boyarsky, D. Malyshev, A. Neronov, and O. Ruchayskiy, Mon. Not. R. Astron. Soc. **387**, 1345 (2008).
[50] A. Neronov and D. Malyshev, Phys. Rev. D **93**, 063518 (2016).
[51] A. Boyarsky, O. Ruchayskiy, D. Iakubovskyi, and J. Franse, Phys. Rev. Lett. **113**, 251301 (2014).
[52] E. Bulbul, M. Markevitch, A. Foster, R. K. Smith, M. Loewenstein, and S. W. Randall, Astrophys. J. **789**, 13 (2014).
[53] S. Dodelson and L. M. Widrow, Phys. Rev. Lett. **72**, 17 (1994).
[54] T. Asaka, M. Shaposhnikov, and M. Laine, J. High Energy Phys. 01 (2007) 091.
[55] https://www.isdc.unige.ch/theseus/mission-payload-and-profile.html.
[56] K. S. Babu and R. N. Mohapatra, Phys. Rev. D **89**, 115011 (2014).
[57] M. Cicoli, J. P. Conlon, M. C. D. Marsh, and M. Rummel, Phys. Rev. D **90**, 023540 (2014).
[58] J. P. Conlon and F. V. Day, J. Cosmol. Astropart. Phys. 11 (2014) 033.

4.2 eXTP Perspectives for the ν MSM Sterile Neutrino Dark Matter Model

eXTP perspectives for the νMSM sterile neutrino dark matter model

Denys Malyshev,[1] Charles Thorpe-Morgan,[1] Andrea Santangelo,[1] Josef Jochum,[1] and Shuang-Nan Zhang[2,3,4]

[1]*Institut für Astronomie und Astrophysik Tübingen, Universität Tübingen, Sand 1, D-72076 Tübingen, Germany*

[2]*Key Laboratory of Particle Astrophysics, Institute of High Energy Physics, Chinese Academy of Sciences, Beijing 100049, China*

[3]*University of Chinese Academy of Sciences, Beijing 100049, China*

[4]*National Astronomical Observatories of China, Chinese Academy of Sciences, Beijing 100012, China*

(Received 22 January 2020; accepted 19 May 2020; published 9 June 2020)

We discuss the potential of the *eXTP* x-ray telescope, in particular its Spectroscopic Focusing Array, Large Area Detector and Wide Field Monitor for the detection of a signal from keV-scale decaying dark matter. We show that the sensitivity of the *eXTP* is sufficient to improve existing constraints on the mixing angle of the neutrino minimal extension of the Standard Model (νMSM) by a factor of 5–10 within the dark matter mass range 2–50 keV, assuming 1% level of systematic uncertainty. We assert that the *eXTP* will be able to probe previously inaccessible range of νMSM parameters and serve as a precursor for the *Athena* mission in decaying dark matter searches.

DOI: 10.1103/PhysRevD.101.123009

I. INTRODUCTION

Astrophysical sources offer attractive laboratories for testing and constraining the properties of dark matter (DM) through indirect detection of its annihilation or decay products (e.g., photons, neutrinos, charged particles). With the lack of any firm detection so far, the search remains ongoing and will be aided by the next generation of satellites. These future missions will allow access to previously unavailable sensitivities in search of DM, enabling better constraints of DM properties or, finally, measurements of its parameters.

The lowest mass range for fermionic dark matter is known to be located in the keV band [1–4]. Several extensions of the Standard Model (SM) of particle physics incorporate dark matter candidate particles which can produce radiative signatures in this band, including gravitinos [5], pseudo-Nambu-Goldstone bosons [6], axions and axionlike particles [7,8]. In what is below, we focus on one of the most well explored of such theories—the minimal sterile neutrino extension of the SM (νMSM) [9–13].

A sterile neutrino of mass $m_{\rm DM}$ can decay producing a Standard Model neutrino and a monochromatic keV photon with an energy of $E = m_{\rm DM}/2$ [13–16]. This decay signal can appear as a narrow linelike feature in x-ray spectra of astrophysical DM-dominated objects [14], e.g., clusters of galaxies or dwarf spheroidal galaxies (dSphs). The strength of the signal is determined by the active-sterile neutrino mixing angle θ.

The parameters of the νMSM model (the mass of sterile neutrino $m_{\rm DM}$ and mixing angle θ) are constrained from below and above and only a narrow window of the parameter space remains unexcluded so far, see e.g., Fig. 2 and [13] for a recent review.

The lower bound on the mass of fermionic dark matter particles $m_{\rm DM} \gtrsim 1$ keV arises from limits imposed by the uncertainty relation. Specifically, the phase space density of the DM particles in the halos of dwarf spheroidal galaxies cannot exceed the fundamental limits imposed by the uncertainty relation and the initial phase space density at the moment of production of the DM in the early Universe [1,3,4,17].

High values of mixing angle θ are forbidden because the abundance of sterile neutrinos produced in the early Universe with such mixing angles would exceed the observed DM density in the present day (see e.g., [2,11] and [13] for a recent review). Additional upper limits originate from nondetection of the described linelike feature in multiple DM-dominated objects with the current generation of instruments [13].

The lower bound on the mixing angle indicates the region where the lepton asymmetries required for resonantly enhanced thermal sterile neutrino production to work are ruled out. Mixing angles lower than this bound would result in the abundances of light elements produced during big bang nucleosynthesis (BBN) to be in disagreement with the current measured values [18–22]. Note however that these limits can be substantially relaxed in other production models, including e.g., Higgs decay [23].

In the following, we study the capabilities of the forthcoming *eXTP* mission to probe the remaining "island" of the allowed parameter range of the νMSM model, which is unexplored by the current-generation x-ray instruments.

TABLE I. The technical characteristics of the considered *eXTP* instruments compared to the characteristics of the *XMM-Newton* (PN camera) and the *Athena*/*X*-IFU. The table summarizes the approximate effective area $A_{\rm eff}$ of each instrument, its FoV $\Omega_{\rm FoV}$, energy resolution ΔE (FWHM), the total (instrumental and CXB) expected flux B and the minimal flux detected at infinite exposure assuming 1% systematic uncertainty [$\alpha = 0.01$, see Eq. (5)]. Where applicable, the quantities are given at energies 3 keV/5 keV/10 keV and for the *eXTP* 's instruments, derived from the templates/models described in the text. For *XMM-Newton* and *Athena* missions the quoted parameters were taken from the data used in [28,29].

Instrument	$A_{\rm eff}$, cm^2	$\Omega_{\rm FoV}$, sr	ΔE, keV	B, ph/(cm^2 s keV sr)	$F^{\infty}_{\rm min}$, 10^{-2} ph/(cm^2 s sr)
eXTP/LAD	$(23/31/33)\times 10^3$	2.4×10^{-4}	0.29/0.31/0.33	8.0/5.1/3.4	4.6/3.2/2.2
eXTP/SFA	$(7.8/5.6/0.9)\times 10^3$	9.6×10^{-6}	0.16/0.16/0.21	4.5/2.6/5.1	1.4/0.8/2.1
eXTP/WFM	42/68/76	2.5	0.24/0.24/0.26	4.8/2.4/0.9	2.4/1.2/0.6
XMM-Newton/PN	$(0.6/0.6/0.1)\times 10^3$	4.5×10^{-5}	0.16/0.20/0.28	6.7/5.2/22.2	2.1/2.1/12.4
Athena/*X*-IFU	$(6.4/3.5/0.4)\times 10^3$	3.3×10^{-6}	$(2.6/2.6/3.5)\times 10^{-3}$	2.8/3.5/26.5	$(1.5/1.8/18)\times 10^{-2}$

Namely, we propose deep observations of a DM-dominated object (dwarf spheroidal galaxy) and blank sky regions aiming either to detect the line from decaying dark matter, or to constrain $(m_{\rm DM}, \theta)$ sterile neutrino parameters.

The enhanced X-ray Timing and Polarimetry mission (*eXTP* [24–26]) is a forthcoming[1] Chinese-European mission primarily designed for the study of the equation of state of matter within neutron stars, measurements of QED effects in highly magnetized stars and studies of accretion in the strong-field gravity regime.

The mission will host a set of state of the art scientific instruments operating in the soft to hard x-ray band (0.5–50 keV). The main instruments on board the *eXTP* are

(1) The Spectroscopic Focusing Array (SFA), consisting of nine x-ray modules operating in the 0.5–10 keV band with a field of view (FoV) of 12′ [full width half-maximum (FWHM)], total effective area of $\sim$0.8 m^2 at 2 keV and an energy resolution of better than 10%;
(2) The Large Area Detector (LAD), nonimaging instrument operating at 2–30 keV energies, with a FoV of 60′ (FWHM), an effective area of $\sim$3.4 m^2 and an energy resolution better than 250 eV;
(3) The Wide Field Monitor (WFM), a wide, steradian-scale, FoV instrument operating in the 2–50 keV energy band with an effective area of $\sim$80 cm^2 and an energy resolution similar to that of the LAD. The capabilities of this instrument for indirect dark matter searches were recently discussed by [27].

In addition to the instruments described above, the *eXTP* will host another module—the Polarimetry Focusing Array (PFA). This instrument has a moderate effective area and an energy resolution comparable to current-generation instruments. Thus, in our work, we will only focus on the prospectives of the SFA, LAD and the WFM for indirect decaying dark matter searches in the keV mass scale. Additional relevant characteristics of these instruments are summarized in Table I.

[1]As of 2019 the launch is planned to 2027.

II. SEARCH FOR DECAYING DM WITH *EXTP*

The flux of a DM-decay line at energy $E = m_{\rm DM}/2$ from an object covering the entire FoV of an instrument is given by

$$F = \frac{\Gamma}{4\pi m_{\rm DM}} \cdot J_{\rm FoV}$$
$$J_{\rm FoV} = \int_{\rm FoV}\int_{l.o.s.} \rho_{\rm DM} d\ell\, d\Omega \qquad (1)$$

where Γ is the radiative decay width [15,30] which, for a sterile neutrino, is given by

$$\Gamma = \frac{9\alpha G_F^2}{256\cdot 4\pi^4}\sin^2(2\theta) m_{\rm DM}^5; \qquad (2)$$

$J_{\rm FoV}$ is the total J factor of decaying DM within the field of view; the corresponding integrations are performed over the field of view of the instrument (FoV) and the line of sight distance ($l.o.s.$) to the object. Substituting the expression for Γ into Eq. (1) one obtains

$$F_{\rm DM} \approx 10^{-7}\left(\frac{\sin^2(2\theta)}{10^{-11}}\right)\left(\frac{m_{\rm DM}}{10\ {\rm keV}}\right)^4 \times \left(\frac{J_{\rm FoV}}{10^{17}\ {\rm GeV/cm^2}}\right)\frac{\rm ph}{\rm cm^2\ s}. \qquad (3)$$

The J factor in the direction of a distant object (and consequently its DM-decay signal) is composed of foreground emission from DM present in the Milky Way (MW) galaxy and the signal from DM residing in the source.

As a matter of fact, within regions of $\sim$10′ (an angular size comparable to FoVs of modern instruments), the DM-decay signal is comparable for a variety of DM-dominated objects with masses ranging from dSphs to clusters of galaxies [31]. Thus, additional considerations such as low levels of astrophysical background, well-measured J-factor, etc., should be taken into account when selecting targets for a deep DM-search observation. On larger scales

(specifically ∼steradian) the contribution of individual DM-dominated objects becomes negligible in comparison to the expected foreground MW signal.

Given this, in this study we consider dSphs (for a narrow, 10′-scale FoV instruments) and MW blank sky regions (for broad, steradian-scale FoV instruments) as the main targets for decaying DM search in the keV band. Contrary to other objects, e.g., clusters of galaxies, in this energy range dSphs and blank sky regions are characterized by low astrophysical backgrounds and can provide a "clean" decay-line signal.

The dark matter density profiles for dwarf spheroidal galaxies have been intensively studied in literature (see e.g., [32–35]). In our work we rely on numerical J-factor values reported in [34] as a function of the distance from the dSph's center.

We estimated the MW contribution to the expected signal of a decaying dark matter assuming Navarro-Frenk-White (NFW) [36] profile for dark matter density:

$$\rho_{\rm DM}(r) = \frac{\rho_0 r_0^3}{r(r+r_0)^2} \tag{4}$$

with the $\rho_0 = 7.8 \times 10^6\ M_\odot/{\rm kpc}^3$, $r_0 = 17.2$ kpc parameters adapted from the best-fit NFW model of the recent MW-mass distribution study [37]; the integration in Eq. (1) was performed numerically.

Corresponding values (for both MW and dSph contributions) for the SFA and LAD instruments for a sample of dwarf spheroidal galaxies are summarized in Table II. The uncertainties on J factors for dSphs illustrate the differences between minimal and maximal J-factor profiles reported in [34].

Statistics of the DM-decay signal collected within the exposure time T are determined by the line flux [Eq. (3)] as well as the intrinsic properties of the instrument. These include effective area $A_{\rm eff}(E)$, energy resolution ΔE, the level of background B [instrumental and astrophysical, in ph/(cm^2 s keV sr)], FoV of the instrument $\Omega_{\rm FoV}$ and the level of systematics α. The minimal detectable flux of a line scaled to the FoV of the instrument can be estimated as

$$F_{\rm min} = 2\left(\sqrt{\frac{B\Delta E}{A_{\rm eff}T\Omega_{\rm FoV}}} + \alpha B\Delta E\right)\frac{\rm ph}{\rm cm^2\ s\ sr} \tag{5}$$

where the factor of 2 stands for a 2σ (or ∼95% C.L.) detection or upper limit significance. Table I summarizes the basic characteristics of *eXTP* 's instruments at 3, 5 and 10 keV energies, compared to the characteristics of *XMM-Newton* and *Athena* missions. The minimal detectable flux in the case of the presence of a 1% systematic (given by $F^{\infty}_{\rm min}$ column) allows a rough estimation of the relative sensitivity of the instruments to the narrow-line signal.

TABLE II. Parameters of a sample of dSph galaxies. J factor in the field of view of SFA [$J_{\rm FoV}(6')$] is given as a sum of Milky Way [37] and dSph [34] contributions. J factors for the field of view of the LAD [$J_{\rm FoV}(30')$] correspond only to contributions from dSphs, see text for further details. Uncertainties on dSph contributions illustrate the values for minimal and maximal expected J factor within the selected radius.

dSph	Galactic coordinates	$J_{\rm FoV}(6')$ 10^{17} GeV/cm^2	$J_{\rm FoV}(30')$ 10^{17} GeV/cm^2
Segue 1	(220.5; 50.4)	$0.84 + 2.0^{+2.1}_{-1.2}$	$9.8^{+14.8}_{-8.4}$
Draco	(86.4; 34.7)	$1.1 + 2.2^{+0.6}_{-0.5}$	$33.4^{+17.8}_{-16.0}$
Carina	(260.1; -22.2)	$1.0 + 0.9^{+0.2}_{-0.1}$	$7.9^{+7.4}_{-4.1}$
Fornax	(237.1; -65.7)	$0.95 + 1.0^{+0.3}_{-0.2}$	$7.2^{+1.7}_{-1.4}$
Sextans	(243.5; 42.3)	$0.90 + 0.5^{+1.0}_{-0.2}$	$7.8^{+6.3}_{-5.3}$
Sculptor	(287.5; -83.2)	$1.1 + 1.7^{+0.3}_{-0.3}$	$15.5^{+5.9}_{-3.9}$
Ursa minor	(105.0; 44.8)	$1.0 + 2.4^{+0.9}_{-0.8}$	$10.7^{+14.2}_{-4.4}$
Ursa major I	(159.4; 54.4)	$0.8 + 0.7^{+1.0}_{-0.4}$	$4.1^{+7.3}_{-3.2}$
Ursa major II	(152.5; 37.4)	$0.75 + 2.3^{+3.7}_{-1.5}$	$23.9^{+48.3}_{-18.1}$
Bootes I	(358.0; 69.6)	$1.4 + 0.9^{+0.9}_{-0.5}$	$8.0^{+13.7}_{-6.3}$
Coma Ber	(241.9; 83.6)	$1.1 + 1.8^{+2.1}_{-1.0}$	$9.2^{+13.9}_{-6.8}$

Detailed comparison of $F_{\rm min}(E)$ derived from the data to the expected $F_{\rm DM}(E)$ allows one to derive the range of $(\theta, m_{\rm DM})$ values to which the instrument is sensitive.

To perform such a comparison we simulated 1 Msec long observations of a dwarf spheroidal galaxy with both the *eXTP*/SFA and the *eXTP*/LAD instruments. The simulated spectra were assumed to originate from contributions over the whole FoV and to be composed of instrumental and astrophysical background components.

The instrumental background components were given by the XTP_sfa_v6.bkg,[2] LAD_40mod_300 eV.bkg and WFM_M4_full.bkg templates for SFA, LAD and WFM respectively, which were provided by the *eXTP* Collaboration.[3] We adopt the FoV size of LAD and SFA instruments from [24–26]. For the FoV of WFM instrument we adapt a $\Omega_{\rm FoV} = 2.5$ sr basing on WFM-EXTP_1OBS_AREA.fits spatial template presenting the effective area of a pointing observation. Namely we defined $\Omega_{\rm FoV} \equiv (\sum A_i\Omega_i)/\max(A_i)$, where the sum goes over all pixels of the template and A_i, Ω_i are effective area and the size of ith pixel. The adapted value is within the range (0.3–4 sr) quoted in [24–26] for fully coded and 20% bounce FoV values.

For the astrophysical cosmic x-ray background (CXB) for the *eXTP*/LAD and *eXTP*/WFM we adopted a cutoff power-law model [38–41]

[2]Note, that the provided template corresponds to the background in ∼3′ and has to be rescaled by a factor of 16 to match 12′ FoV of SFA. The WFM background template was provided for one module and had to be upscaled by a factor of 3.

[3]See *eXTP* website, https://www.isdc.unige.ch/extp/.

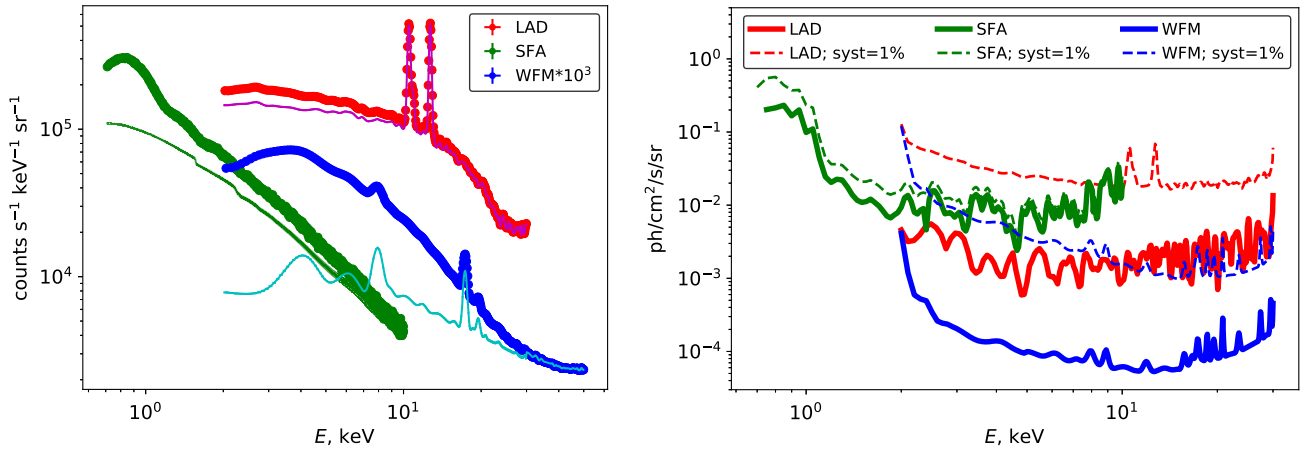

FIG. 1. Left: *eXTP*/LAD, SFA and WFM simulated spectra of 1 Msec observations of a region of blank sky (red and blue points). Cyan, magenta and light green curves illustrate the levels of instrumental background in these instruments. Right: Sensitivity of the SFA, LAD and WFM to a narrow Gaussian line present in the whole FoV of the instrument. Dashed lines show the change in the sensitivity of the instrument to the flux, assuming 1% value of systematic uncertainty.

$$F_{CXB} = 7.877E^{-0.29}e^{-E/41.13\ \mathrm{keV}}\frac{\mathrm{keV}}{\mathrm{keV\,cm^2\,s\,sr}} \quad (6)$$

which well describes the existing data in the 3–60 keV range. For the *eXTP*/SFA, which has an energy range extending significantly below 3 keV, we instead adopted the model of CXB derived from *XMM-Newton* observations of a set of dwarf spheroidal galaxies [28]. We verified explicitly that at intersecting energy ranges both models agree within an accuracy of ∼10%–15%.

The observations described above were performed with the *fakeit* XSPEC (version: 12.10.1f) command. The resulting spectra (normalized per FoV of corresponding instrument) are shown in the left panel of Fig. 1. Red, green and blue points illustrate the total expected flux seen by LAD, SFA and WFM correspondingly, while magenta, light-green and cyan lines present the level of the instrumental background.

We would like to note that the instrumental background of *eXTP* strongly varies between the instruments. The SFA's background is featureless and can be adequately modeled by a sum of two power-law models (convolved and not convolved with the effective area). The background of WFM below 30 keV can be modeled with a broken power-law model, containing a break at $E_{br} \sim 16$ keV, and hosts multiple instrumental lines. To avoid further complications with the background model of this instrument hereafter, we limit the considered energy range for this instrument to 2–30 keV. Finally, the instrumental background of the LAD is even more complicated and cannot be modeled accurately with any simple model.

A. Observational strategy

Given these points, we propose somewhat different observational strategies of a dSph by the SFA and LAD instruments. For the SFA we propose that the observation should be centered on the dSph and accompanied with subsequent modeling of instrumental and astrophysical background. Thus, a DM-decay line can be searched for on top of the modeled background. This strategy is similar to one widely used in decaying dark matter searches in astrophysical objects, see e.g., [13] for a review.

For the LAD, we propose performing a set of "ON-OFF" observations, where "ON" observations are centered on the dSph and "OFF" on an empty sky region close to the object, but for which the contribution from dSph DM-decay signal is minimal. In this case we propose that rather than modeling astrophysical/instrumental backgrounds, to instead use OFF observations as a background for ON observations. The DM-decay line in this case is searched for in the obtained, background subtracted, (consistent with 0) spectrum. Such a strategy allows one to avoid modeling the complex LAD background and/or potential systematic effects connected with our poor knowledge of it.

The extremely large FoV (∼2.5 sr) of the WFM instrument unavoidably covers a region much broader than the angular size any known dSph, and therefore the contribution to the expected signal of any dSph in this FoV will be negligible. To fully utilize the capacity of the WFM in dark matter searches, we propose instead use it to observe blank sky regions characterized by low astrophysical background.

We note that in case of blank sky observations with WFM the ON-OFF strategy is only marginally possible since the expected dark matter signal is by an order of magnitude comparable in any direction on the sky similarly to possible variations of the astrophysical background. Yet, to maximize the expected signal within ON-OFF strategy one may locate the ON region as close as possible to the Galactic Center (as was proposed e.g., by [27]). We note, however that in this case an additional astrophysical

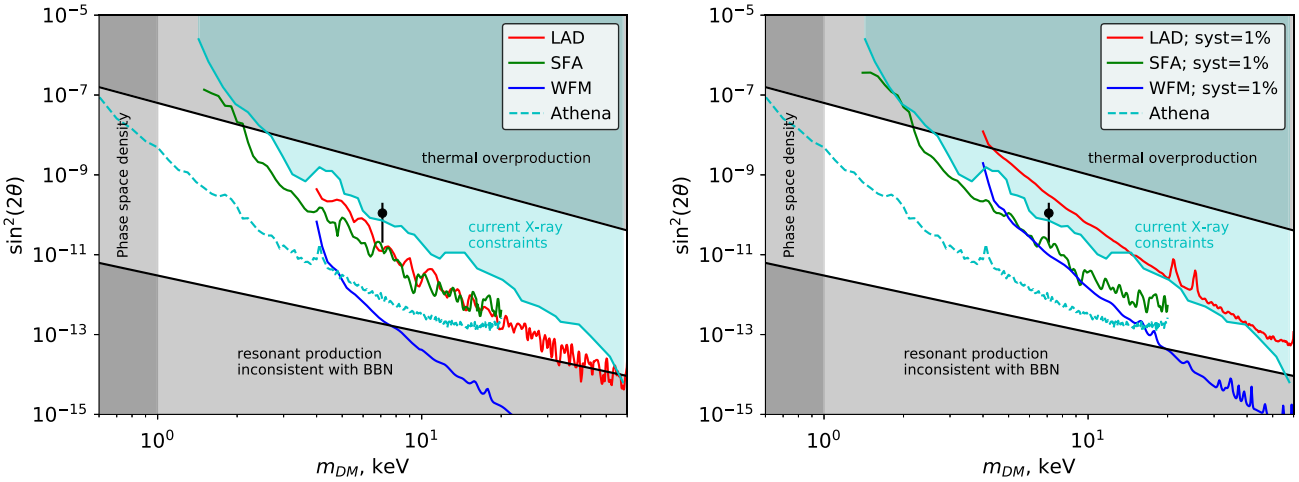

FIG. 2. 2σ sensitivity reach of the *eXTP* to the parameters of the sterile neutrino from 1 Msec observations of Seg I dSph (by LAD and SFA) and same duration blank sky observations (WFM). Left and right panels assume a zero and 1% level of systematic uncertainty for all instruments correspondingly. Used J factors correspond to mean values reported in Table II and in the text. The cyan dashed curve illustrates 2σ *Athena* constraints from 1 Msec observations of the same target [29]. The light blue region shows the existing constraints (adapted from [13]). Phase space density [1,3,4,17], thermal overproduction (see [2] and [13,42] for the review) and the bounds originating from the abundances of light elements produced during BBN [19] are shown as grey regions. The black point represents the sterile neutrino parameters from the tentative detection of an unidentified ~3.55 keV line in certain DM-dominated objects (see [43,44] and [13] for a recent review).

component—galactic bulge/ridge x-ray emission (GRXE) should be taken into account. The GRXE emission is present at low galactic latitudes and is believed to originate from a population of unresolved x-ray binaries [45]. At these latitudes, GRXE flux can exceed the flux of cosmic x-ray background by an order of magnitude [45,46]. Its spectrum is not featureless and hosts multiple astrophysical lines at least at energies $\lesssim$3 keV [47] which can lead to additional confusion between astrophysical and DM-decay signals.

To minimize potential GRXE contribution we propose to observe relatively high galactic latitudes ($|b| > 20$) with the WFM, where the GRXE contribution is minimal [45]. We propose also to locate the quasirectangular FoV of the WFM parallel to the galactic plane to minimize the average distance to the Galactic Center and thus maximize the expected DM-decay signal.

B. Results

Following the proposed strategy for the SFA and WFM, we perform a search for a narrow Gaussian line originating from the whole FoV, on top of the modeled backgrounds (specifically, the sum of the instrumental and astrophysical background models as described above). For the LAD we performed an additional 1 Msec long simulation of an OFF region characterized by the same astrophysical/instrumental backgrounds as an ON observation of a dSph. In this case we performed the search for a narrow Gaussian line in the background subtracted spectrum. Upper limits of 2σ (~95% confidence level) on the normalization of such line[4] are shown with solid blue (SFA) and red (LAD) curves in the right panel of Fig. 1. These limits are exact equivalents of the minimal detectable flux in Eq. (5).

We would like to stress the significance of the potential effects of systematic uncertainties on the limits which can be derived by the LAD and WFM instruments. To simulate this effect we modified STAT_ERR column of simulated spectral files by adding a value proportional to the total number of counts observed each channel. Dashed curves in the right panel of Fig. 1 present limits on the line normalization which can be obtained in the presence of a 1% systematic uncertainty. We conclude that in the case where *eXTP* systematic is not well controlled, the subsequent limits for decaying DM by the LAD and WFM will worsen by a factor of $\gtrsim$10. On the contrary, the low instrumental background and relatively small FoV of the SFA do not allow statistical uncertainty to substantially overcome systematic uncertainty in within a 1 Msec observation. Consequently presented limits are only weakly dependent on any added systematics.

Using the derived results for the *eXTP* 's sensitivity to a narrow Gaussian line, we obtain the corresponding minimal value of the mixing angle θ at which a DM-decay line can be detected at a given energy $E = m_{\rm DM}/2$. Corresponding limits for 1 Msec long Segue 1 dSph observations (assumed

[4]The upper limits were calculated with the error 4.0 XSPEC command.

$J_{\mathrm{FoV}} = 2.84 \times 10^{17}$ GeV/cm^2 for the SFA; $J_{\mathrm{FoV}} = 9.8 \times 10^{17}$ GeV/cm^2 for the LAD and $J_{\mathrm{FoV}} = 2 \times 10^{22}$ GeV/cm^2 for the WFM observations of a blank sky region centered at Segue 1 and parallel to the galactic plane) are shown in Fig. 2 along with current theoretical and observational constraints of sterile neutrino parameters (see e.g., [13] for the review). Also displayed for comparison are the expected limits on observations by the forthcoming *Athena* mission [29], given the same exposure and target. Note that here, the presented limits correspond to a zero level of systematic uncertainty. The expected limits from observations of other low astrophysical background DM-dominated objects can be obtained by rescaling presented limits according to the J_{FoV} of the target, see e.g., Table II.

III. DISCUSSION AND CONCLUSIONS

This study has demonstrated the capability of the upcoming *eXTP* satellite in searching for decaying dark matter and found it can impose significantly better limits than current observational means. Observations with *eXTP* of DM-dominated objects with exposures of 1 Msec e.g., Segue 1 (by SFA and LAD), or blank sky regions (by WFM), have the potential to improve existing 2σ x-ray observational constraints by a factor of ∼5–10 within the 2–50 keV dark matter particle mass range (see Fig. 2, right panel), assuming 1% level of systematic uncertainty. The same constraints for the unlikely case of much smaller, consistent with zero, level of systematic are significantly better and are shown in the left panel of Fig. 2.

We assert that the systematic uncertainty will play a significant role in constraining decaying DM parameters from LAD and WFM data. Uncontrolled systematics at a level of $\gtrsim$1% can detrimentally affect obtained constraints by an order of magnitude in comparison to zero-systematic case. In the case of the LAD this could produce constraints comparable to, or even worse than, those of current x-ray instruments. When considering the proposed 1 Msec observation, the low instrumental background and relatively narrow FoV of the SFA makes the effects of systematics less significant in this instrument. The systematic at a level of 1% (comparable to the estimated flux systematic uncertainty of *XMM-Newton*[5]) will lead to a deterioration of zero-systematic constraints by only a factor of ∼1.5.

We note that a 1% systematic uncertainty can be a reasonable estimation for *XMM-Newton* -like instruments such as SFA and LAD. However, for a broad-FoV instrument not designed specifically for spectral studies such as WFM, we recognize that this uncertainty could be rather optimistic.

The constraints presented in Fig. 2 indicate also that the *eXTP* will be sensitive enough to exclude or detect, at 3σ level, a sterile neutrino with the mass of $m_{\mathrm{DM}} \sim 7$ keV and a mixing angle of $[\sin^2(2\theta) \sim 2 \times 10^{-11}]$. This angle roughly corresponds to the minimal mixing angle of a sterile neutrino producing a ∼3.55 keV line, as discussed in literature. This line has been tentatively detected in some DM-dominated objects and is still actively being discussed in the field (see [43,44] and [13] for a recent review). The corresponding range of mixing angles discussed is denoted by the black point with error bars in Fig. 2.

With the optimistic assumptions on the mixing angle $\sin^2(2\theta) \sim 8 \times 10^{-11}$ (corresponding to 2σ limits on mixing angle from current X-ray observations), the DM-decay line can be detected with a significance of $\gtrsim 10\sigma$, given a 1% systematic with *eXTP*/SFA or WFM (in line with estimations of [27]) instruments. The strength of such a significant line could be compared across the sample of other DM-dominated objects and/or along the sky in order to correlate its intensity with the known J_{FoV} value and thus draw conclusions on its DM-decay origin.

Alongside its numerous other scientific objectives, *eXTP* will be a precursor to the forthcoming *Athena* mission's decaying dark matter searches. The improved sensitivity of *eXTP* in comparison to the current generation of instruments will lead to a significant reduction of the sterile neutrinos unobserved parameter space. We assert that with well-controlled systematic uncertainties, the *eXTP* has the potential to discover decaying dark matter and make the first estimations of its parameters which can be further verified with *Athena*.

ACKNOWLEDGMENTS

The authors acknowledge support by the state of Baden-Württemberg through bwHPC. This work was supported by DFG through Grant No. MA 7807/2-1.

[5]See e.g., EPIC Calibration Status document, http://xmm2.esac.esa.int/docs/documents/CAL-TN-0018.pdf.

[1] S. Tremaine and J. E. Gunn, Phys. Rev. Lett. **42**, 407 (1979).
[2] S. Dodelson and L. M. Widrow, Phys. Rev. Lett. **72**, 17 (1994).
[3] A. Boyarsky, O. Ruchayskiy, and D. Iakubovskyi, J. Cosmol. Astropart. Phys. 03 (2009) 005.
[4] D. Savchenko and A. Rudakovskyi, Mon. Not. R. Astron. Soc. **487**, 5711 (2019).
[5] K. Hamaguchi, M. Ibe, T. T. Yanagida, and N. Yokozaki, Phys. Rev. D **90**, 015027 (2014).
[6] K. Nakayama, F. Takahashi, and T. T. Yanagida, Phys. Lett. B **734**, 178 (2014).
[7] P. Arias, D. Cadamuro, M. Goodsell, J. Jaeckel, J. Redondo, and A. Ringwald, J. Cosmol. Astropart. Phys. 06 (2012) 013.
[8] B. Henning, J. Kehayias, H. Murayama, D. Pinner, and T. T. Yanagida, Phys. Rev. D **91**, 045036 (2015).
[9] T. Asaka, S. Blanchet, and M. Shaposhnikov, Phys. Lett. B **631**, 151 (2005).
[10] A. Boyarsky, A. Neronov, O. Ruchayskiy, and M. Shaposhnikov, Sov. J. Exp. Theor. Phys. Lett. **83**, 133 (2006).
[11] T. Asaka, M. Shaposhnikov, and M. Laine, J. High Energy Phys. 01 (2007) 091.
[12] A. Boyarsky, D. Iakubovskyi, and O. Ruchayskiy, Phys. Dark Universe **1**, 136 (2012).
[13] A. Boyarsky, M. Drewes, T. Lasserre, S. Mertens, and O. Ruchayskiy, Prog. Part. Nucl. Phys. **104**, 1 (2019).
[14] K. Abazajian, G. M. Fuller, and W. H. Tucker, Astrophys. J. **562**, 593 (2001).
[15] P. B. Pal and L. Wolfenstein, Phys. Rev. D **25**, 766 (1982).
[16] R. Adhikari, M. Agostini, N. A. Ky, T. Araki, M. Archidiacono, M. Bahr, J. Baur, J. Behrens, F. Bezrukov, P. S. Bhupal Dev *et al.*, J. Cosmol. Astropart. Phys. 01 (2017) 025.
[17] D. Gorbunov, A. Khmelnitsky, and V. Rubakov, J. Cosmol. Astropart. Phys. 10 (2008) 041.
[18] X. Shi and G. M. Fuller, Phys. Rev. Lett. **82**, 2832 (1999).
[19] P. D. Serpico and G. G. Raffelt, Phys. Rev. D **71**, 127301 (2005).
[20] M. Shaposhnikov, J. High Energy Phys. 08 (2008) 008.
[21] M. Laine and M. Shaposhnikov, J. Cosmol. Astropart. Phys. 06 (2008) 031.
[22] L. Canetti, M. Drewes, T. Frossard, and M. Shaposhnikov, Phys. Rev. D **87**, 093006 (2013).
[23] A. Kusenko, Phys. Rev. Lett. **97**, 241301 (2006).
[24] S. N. Zhang, M. Feroci, A. Santangelo, Y. W. Dong, H. Feng, F. J. Lu, K. Nandra, Z. S. Wang, S. Zhang, E. Bozzo *et al.*, *eXTP: Enhanced X-ray Timing and Polarization mission*, Society of Photo-Optical Instrumentation Engineers (SPIE) Conference Series Vol. 9905 (Science China Physics, Mechanics & Astronomy, 2016), p. 99051Q, https://ui.adsabs.harvard.edu/abs/2019SCPMA..6229502Z/abstract.
[25] J. J. M. in't Zand, E. Bozzo, J. Qu, X.-D. Li, L. Amati, Y. Chen, I. Donnarumma, V. Doroshenko, S. A. Drake, M. Hernanz *et al.*, Sci. Chin. Phys. Mech. Astron. **62**, 29506 (2019).
[26] S. Zhang, A. Santangelo, M. Feroci, Y. Xu, F. Lu, Y. Chen, H. Feng, S. Zhang, S. Brandt, M. Hernanz *et al.*, Sci. Chin. Phys. Mech. Astron. **62**, 29502 (2019).
[27] D. Zhong, M. Valli, and K. N. Abazajian, arXiv:2003.00148.
[28] D. Malyshev, A. Neronov, and D. Eckert, Phys. Rev. D **90** (2014).
[29] A. Neronov and D. Malyshev, Phys. Rev. D **93**, 063518 (2016).
[30] V. Barger, R. J. N. Phillips, and S. Sarkar, Phys. Lett. B **352**, 365 (1995).
[31] A. Boyarsky, O. Ruchayskiy, D. Iakubovskyi, A. V. Maccio', and D. Malyshev, arXiv:0911.1774.
[32] M. G. Walker, M. Mateo, E. W. Olszewski, J. Peñarrubia, N. W. Evans, and G. Gilmore, Astrophys. J. **704**, 1274 (2009).
[33] J. Wolf, G. D. Martinez, J. S. Bullock, M. Kaplinghat, M. Geha, R. R. Muñoz, J. D. Simon, and F. F. Avedo, Mon. Not. R. Astron. Soc. **406**, 1220 (2010).
[34] A. Geringer-Sameth, S. M. Koushiappas, and M. Walker, Astrophys. J. **801**, 74 (2015).
[35] L. E. Strigari, Rep. Prog. Phys. **81**, 056901 (2018).
[36] J. F. Navarro, C. S. Frenk, and S. D. M. White, Astrophys. J. **490**, 493 (1997).
[37] M. Cautun, A. Benitez-Llambay, A. J. Deason, C. S. Frenk, A. Fattahi, F. A. Gómez, R. J. J. Grand, K. A. Oman, J. F. Navarro, and C. M. Simpson, Mon. Not. R. Astron. Soc. **494**, 4291 (2020).
[38] D. E. Gruber, J. L. Matteson, L. E. Peterson, and G. V. Jung, Astrophys. J. **520**, 124 (1999).
[39] M. Revnivtsev, M. Gilfanov, R. Sunyaev, K. Jahoda, and C. Markwardt, Astron. Astrophys. **411**, 329 (2003).
[40] E. Churazov, R. Sunyaev, M. Revnivtsev, S. Sazonov, S. Molkov, S. Grebenev, C. Winkler, A. Parmar, A. Bazzano, M. Falanga *et al.*, Astron. Astrophys. **467**, 529 (2007).
[41] M. Türler, M. Chernyakova, T. J. L. Courvoisier, P. Lubiński, A. Neronov, N. Produit, and R. Walter, Astron. Astrophys. **512**, A49 (2010).
[42] G. Bertone, D. Hooper, and J. Silk, Phys. Rep. **405**, 279 (2005).
[43] A. Boyarsky, O. Ruchayskiy, D. Iakubovskyi, and J. Franse, Phys. Rev. Lett. **113**, 251301 (2014).
[44] E. Bulbul, M. Markevitch, A. Foster, R. K. Smith, M. Loewenstein, and S. W. Randall, Astrophys. J. **789**, 13 (2014).
[45] R. Krivonos, M. Revnivtsev, E. Churazov, S. Sazonov, S. Grebenev, and R. Sunyaev, Astron. Astrophys. **463**, 957 (2007).
[46] K. Perez, R. Krivonos, and D. R. Wik, Astrophys. J. **884**, 153 (2019).
[47] K. Ebisawa, S. Yamauchi, Y. Tanaka, K. Koyama, Y. Ezoe, A. Bamba, M. Kokubun, Y. Hyodo, M. Tsujimoto, and H. Takahashi, Publ. Astron. Soc. Jpn. **60**, S223 (2008).

5 The Principles of Very-high-energy Gamma-ray Astronomy

5.1 Gamma-ray Astronomy

The advent of satellite-based observations and Cherenkov telescopes has led to the discovery of increasingly complex and high-energy astrophysical emission. As our vision of the cosmos has stretched further up the electromagnetic spectrum, it has revealed that we are surrounded on all sides by a violent and energetic Universe. The tranquil scenes of a gentle dark reported by ground-based telescopes were suddenly juxtaposed by a myriad of explosions, collisions and accelerations.

At increasing energies, many novel and interesting astrophysical objects have been detected. The expectations of these high-energy emissions long predate their detection, yet the range and scope of astrophysical objects (and the circumstances of their production) are unprecedented. This has led to a plethora of categories and sub-categories of high-energy astrophysical objects. For an overview of the history of gamma-ray astronomy and contemporary missions see Sec. 2.4 and Sec. 2.5.

The observation, analysis and modelling of these objects form the cornerstone of our understanding of the high-energy Universe, as well as the physical processes that underpin high-energy emission as a whole. As such, high-energy ($\sim$ GeV) and VHE astronomical objects ($\sim$ TeV) provide ideal laboratories for testing extremely high-energy physics and the limits of nature. Moreover, the study of these objects and processes allows for a more complete picture of the nature of the objects and environments that cause such emissions to be built.

5.2 Cosmic Rays

The discovery of what is contemporarily understood as cosmic radiation was made in 1912 by a man, his hot air balloon, and an electroscope. Victor Franz Hess sought to

investigate the (then-assumed) hypothesis that the Earth was the source of ionising radiation. Through a series of daring balloon flights (made at great risk to himself, see Fig. 5.1) Hess personally used an electroscope to measure the levels of ionising radiation at varying altitudes. His efforts proved that the levels of ionising radiation increased greatly above an altitude of 1 kilometre, a discovery that won him the Nobel prize in 1936.

Fig. 5.1: Victor Hess (centre) aboard his hot air balloon. By riding the balloon into the upper atmosphere Victor Hess took measurements of the ionising radiation at varying altitudes. Image taken from [191]

What Hess had detected were of course Cosmic Rays (CR), a spectrum of astrophysical protons, electrons and nuclear fragments incident on the Earth. The discovery of these, moreover, birthed the thriving field of astroparticle physics. The detection, analysis, and understanding of CRs is now the focus of a plethora of instruments from satellite missions to (now unmanned) balloons.

These CRs must inherently possess very high energies to travel the vast distances from their origin to Earth. This naturally implies the existence of extremely high-energy acceleration mechanisms and sites, an extremely interesting concept for high-energy particle and astrophysicists alike. Intermediary EM fields, however, interact with cosmic rays, deflecting their original direction. It is for this reason their distribution is near isotropic on Earth. This fact also makes the association of CRs with sources extremely difficult. The complicated nature of galactic and interstellar magnetic fields makes the reconstruction of long-range particle trajectories a non-trivial task.

The flux of CRs at Earth has since been measured to extremely sensitive degrees across the energy range of ~ 1 GeV to ~ 100 EeV. The observed spectrum at Earth

is displayed in Fig. 5.2. Of the many incident particles, the largest contribution to the flux originates from both protons and heavier nuclei fragments, with electrons constituting a negligible component of the flux. The form of the spectral energy density displayed in Fig. 5.2 follows a rough power-law shape with two notable points where the spectrum appears to change index considerably. These two points are known as "the knee" (occurring at around ~ 1 PeV), around which the spectrum softens, and "the ankle" (seen at around ~ 5 EeV) where the spectrum hardens considerably.

The spectrum noticeably begins with a sharp rise in flux from lower energies up to energies of several GeV. This feature is a result of the shielding effect of the solar magnetic field and the heliosphere, which is (generally) more effective at lower energies. Beyond this, the spectrum appears to follow a power law of the form $\frac{\mathrm{d}N}{\mathrm{d}E} \propto E^{-\Gamma}$, with an index of $\Gamma \approx 2.7$ up to the knee. Incident CRs up to this point are largely believed to be of galactic origin. However, the region beyond the knee is of particular interest, since this represents the highest energy particles that originate from within the galaxy. Research into galactic sites capable of accelerating particles to PeV energies (so-called PeVatrons) is ongoing and PeVatrons are an expansive field of research. The region from the knee down to the ankle shows a spectral softening ($\Gamma \approx 3.1$), which is widely believed to be indicative of a transition in the spectrum between galactically and extra-galactically produced CRs. At higher energies than the ankle, the spectrum hardens once again to roughly its previous value of $\Gamma \approx 2.6$ and is largely believed to be almost exclusively comprised of extra-galactic contributions. Finally, at energies of ~ 100 EeV, the spectrum undergoes a cutoff. The cause of this is still inconclusive and in some theories is postulated to be the result of an intrinsic cutoff of extragalactic sources at this energy. Alternatively, the Greisen–Zatsepin–Kuzmin limit/cutoff [192, 193] places a theoretical upper bound on the energies of extragalactic CR protons and could thus provide an alternative explanation. This effect occurs as a result of extremely high-energy protons interacting with photons of the CMB through the Δ resonance. The result of this would be that protons exceeding an energy of 50 EeV would interact with the CMB producing pions and reducing their energy considerably.

5.3 The Detection of Very-high-energy Gamma Rays

Gamma rays are the most energetic subdivision of photons in the electromagnetic spectrum and are defined as having energies of greater than 0.2 MeV. The opacity of Earth's atmosphere to short-wavelength radiation requires that any instrument

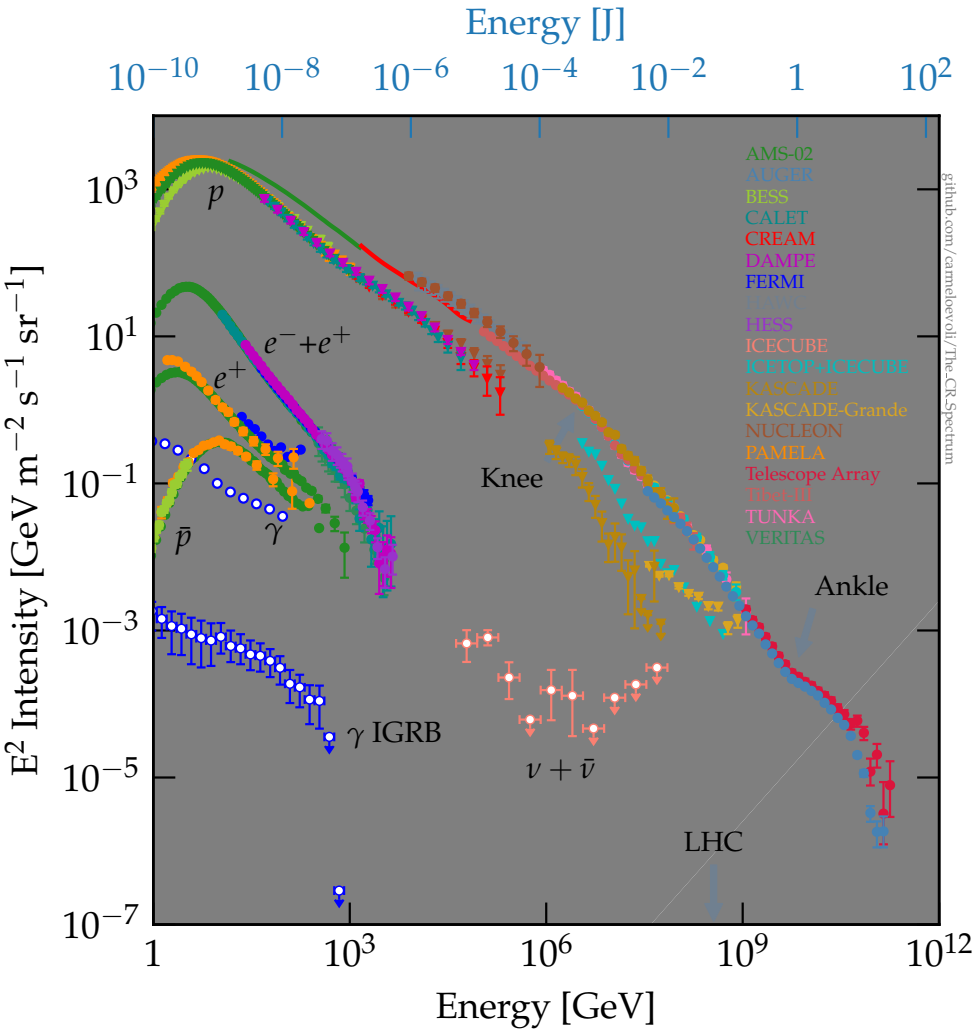

Fig. 5.2: The spectral energy density of cosmic rays as recorded at Earth. The figure is complete with markings indicating the individual particle components in the all-particle spectrum. Moreover, the "knee" and "ankle" (the strong break in the power law indicating, perhaps, a change in acceleration physics at these energies) are labelled in the figure. Shaded regions indicate the rough frequency of incident particles. Figure taken from [194].

designed to detect gamma rays must either be deployed outside of the atmosphere (see 5.1 for an overview and history of this subject) or utilise a method of indirectly detecting incident photons.

Satellite-borne gamma-ray detectors are effectively utilised in the energy range of several MeV to several hundreds of GeV (HE gamma rays). However, at energies greater than a few hundred GeV (VHE gamma rays), the expected flux of astrophysical sources drops dramatically. This necessitates a photon collection area larger than is technologically possible and monetarily efficient for satellite detectors, to

detect sufficient levels of VHE gamma-ray flux. Therefore, astronomy in the VHE gamma-ray regime (for now) must be conducted at ground level, utilising indirect methods to enable adequately large photon collection areas.

5.4 Imaging Atmospheric Cherenkov Telescopes

Imaging Atmospheric Cherenkov Telescopes (IACTs) are ground-based telescopes that operate in the VHE gamma-ray regime. VHE gamma rays incident to the Earth interact with particles in the upper atmosphere forming a shower of secondary particles. IACTs operate around the detection of this shower, and the subsequent reconstruction of the properties of the progenitor photon.

5.4.1 Air Showers

In addition to astrophysical gamma rays, very high numbers of Cosmic Rays accelerated from galactic and extra-galactic sources also enter the upper atmosphere. The majority of cosmic rays are protons but can also be electrons, alpha particles, and heavier nuclei.

Regardless of the nature of the incident particle, a primary particle incident to Earth will induce a cascade of secondary particles through interactions with atoms in the upper atmosphere. This cascade of relativistic secondary particles is known as an Extensive Air Shower (EAS). The nature of the incident particle dictates the interactions the EAS will undergo, with hadronic primaries inducing hadronic interactions in their showers, and EM primaries inducing EM interactions. These two categories of shower are unique in their structure and evolution, a fact capitalised on by IACTs to distinguish between gamma-ray events and events from cosmic rays.

For a primary particle, the distance it is able to penetrate into the atmosphere is defined as the slant depth X (g cm^{-2}):

$$X(h) = \int_{\mathrm{h}}^{\infty} \rho(z)\,\mathrm{d}z \tag{5.1}$$

Where ρ(z) (g cm^{-3}) is the density profile of the target material. For the NASA defined standard Earth atmosphere [195], this is given as a function of height, h (km) as:

$$\rho(h) = \rho_0 \exp(\frac{-h}{h_0}) \tag{5.2}$$

where $\rho_0 \approx 1.2$ kg m^{-3} and $h_0 \approx 8.4$ km [195].

From Eq. 5.1, the value of $X_{\max}$ can be obtained and is defined as the depth at which a shower contains its maximum number of particles. This value is characterised by both the density of the target material (in this case air, as defined in Eq.5.2) and the cross section of available interactions σ (cm^2). Thus, the development of a shower and its maximum height is closely related to the interaction length λ (g cm^{-2}):

$$\lambda = \frac{\rho}{n\sigma} \tag{5.3}$$

where n (cm^{-3}) is the number density of target particles.

It is important to note that for different primary particles different interactions will be accessible to the secondary particles that are produced. This in turn will have dramatic effects on the height and evolution of the EAS.

Electromagnetic Showers

Electromagnetic showers occur when the primary particle of an EAS is a photon or a lepton. The evolution of electromagnetic showers is dominated by pair-production and bremsstrahlung processes [196]. Interestingly, these processes result in the fact that each interaction length will double the number of particles. This is due to the fact that incident photons will form an electron-positron pair ($e^{\pm}$) upon interaction with an ambient target nucleus, which will produce photons via bremsstrahlung. Similarly, bremsstrahlung photons produced from primary or secondary events will undergo pair production while it is kinematically available, perpetuating and expanding the EAS. At the critical energy ($E_{\rm c} \approx 86$ MeV) ionisation becomes the dominant energy loss mechanism over bremsstrahlung and the shower's growth halts. Following this, further energy losses are exclusively through ionisation of the surrounding air particles [197].

The process of electromagnetic shower development is described (to a first approximation) by the Heitler model [198], which dictates the general properties of a shower and its evolution from the primary particle (shown in Fig. 5.3). The model assumes a fixed interaction length of $d = \ln(2)\lambda_{\rm e}$ (where $\lambda_{\rm e} = 37$ g cm^{-2} for air), and that an incident particle of energy E_0 will produce two particles of energy $E_0/2$. This assumption is continued for every interaction length, such that after k interactions there are 2^k particles each with an energy of $E = \frac{E_0}{2^k}$. At the critical energy the shower will reach its largest size, allowing the calculation of the maximum number

of particles under this model as $N_{\max} = \frac{E_0}{E_c}$. This leads to a maximum shower depth of $X_{\max} = \lambda_e \ln \frac{E_0}{E_c}$.

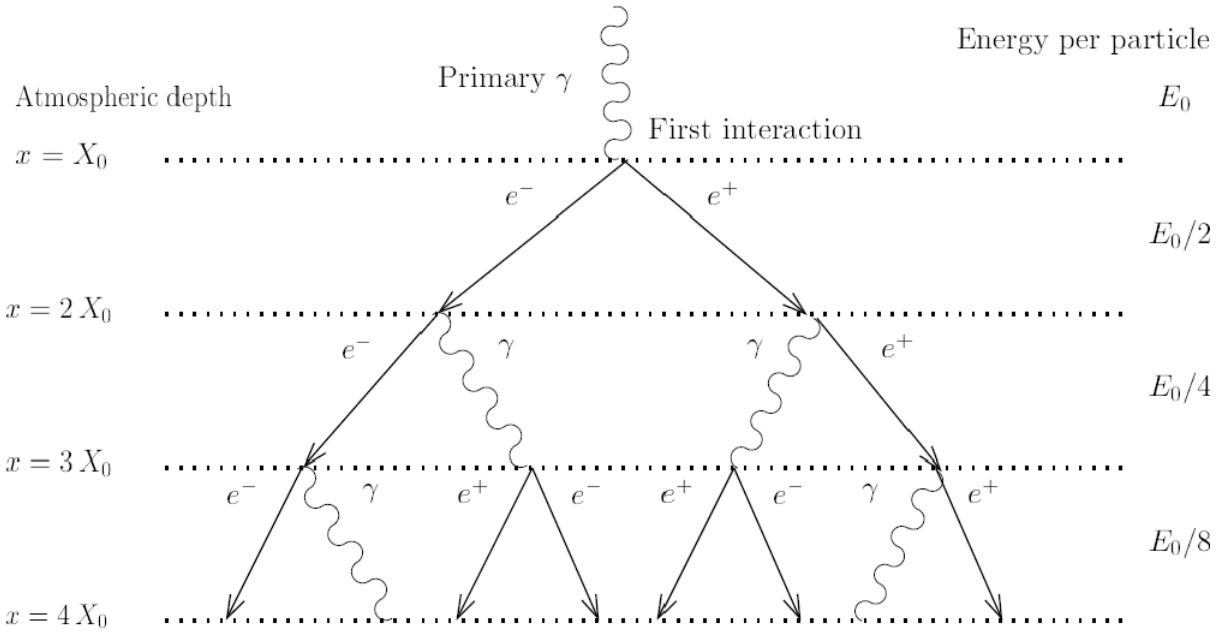

Fig. 5.3: A schematic diagram of the development of an EM air shower, following the simplified Bethe and Heitler model of a cascade. As shown in the figure, a gamma ray (γ) incident upon a nucleus in the upper atmosphere begins an EM cascade, where the number of particles is doubled after each step k. In this model, the total energy decreases accordingly with particle production until, at the critical energy, it is no longer energetically possible to produce more particles and the shower will reach its maximum number of particles. Figure taken from [199].

Hadronic Showers

For incident hadronic cosmic rays, the dominant physical process is the inelastic scattering of the hadron off a target nucleus via the strong interaction. This interaction results mainly in the production of charged ($\pi^{\pm}$) and neutral pions (π^0), but in smaller quantities also produces protons (p), neutrons (n), nuclear fragments and other more exotic particles. Typically, charged pions constitute approximately $\frac{2}{3}^{\text{rds}}$ of the particles produced, the highest branching ratio for their subsequent decay is to muons ($\mu^{\pm}$) and muon neutrinos (ν_μ), but at smaller probabilities charged pions can decay into electrons (e^-) and electron neutrinos (ν_e). The remaining third of the particles is made up of neutral pions, which will decay almost immediately after production into two gamma rays. These gamma rays will, in turn, produce an electromagnetic EAS as described previously in Sec.5.4.1. An example of a hadronic air shower cascade is shown in 5.4. The physical description of the propagation

of hadronic showers is described by an extension to the Heitler model in [200]. Unlike in EM showers, hadronic showers are not limited by ionisation losses, but rather by the energy dependence of the decay length of pion decay. As the shower dissipates in energy, the decay length becomes smaller than the average spacing between atmospheric nuclei rendering the production of further pions impossible.

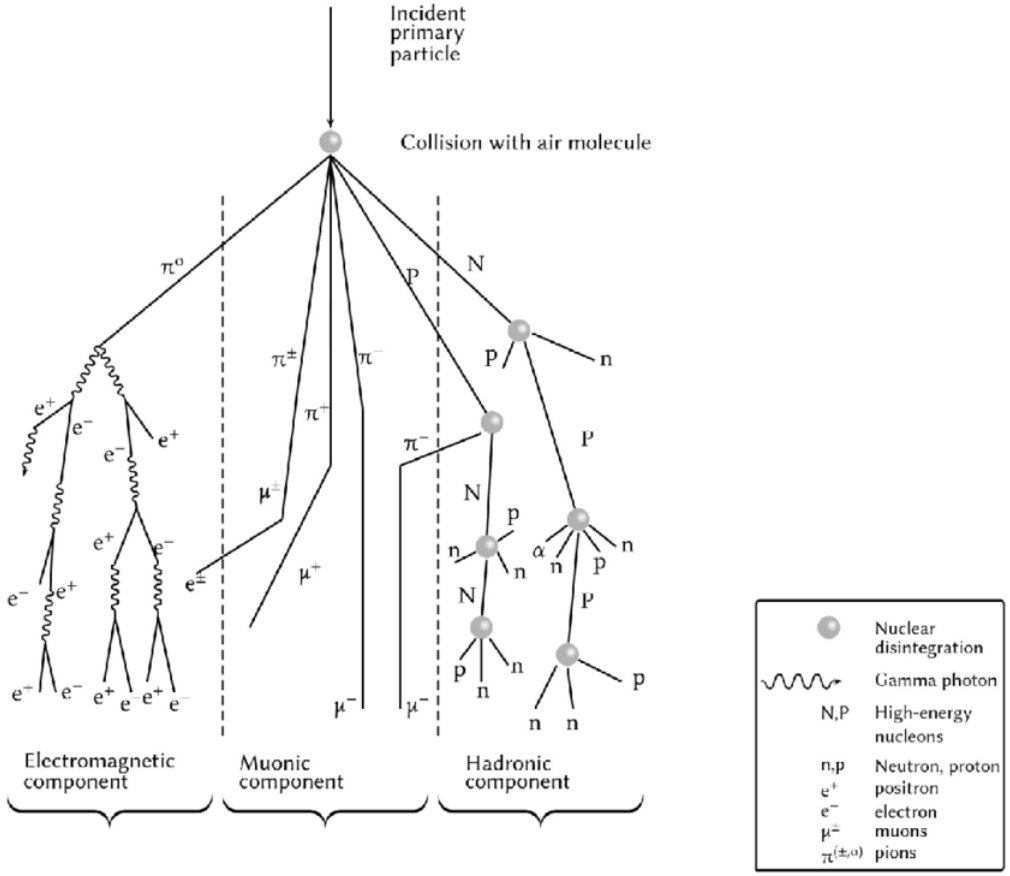

Fig. 5.4: A schematic diagram of the development of a hadronic air shower. The cascade begins following the inelastic scattering of a hadron off of an ambient nucleus. The shower itself can be split into several sub-shower components following the different interactions that take place. Given the states and interactions kinematically accessible to the particles, the secondary particles, sub-shower structures and energetics can vary significantly. Figure taken from [201].

Discrimination Between EM and Hadronic Showers

In order to reconstruct incident photons with precision, IACTs must accurately and consistently discriminate between EM showers (constituting signals) and hadronic showers (constituting background). In order to achieve this, IACT arrays exploit the physical differences between the structures and evolution of the EASs resulting

from the two progenitors. Recognising these different shower properties allows IACTs to veto showers originating from primaries that are considered background. A comparison of the shower structure and Cherenkov light pools between EM and hadronic showers is shown in 5.5. Showers are distinguished via the following properties.

- **Lateral spread** The transverse momentum transferred in the lateral direction (with respect to the shower's evolution) is typically far lower in EM showers. This results in smaller and tighter showers. Conversely, the inelastic scattering of hadronic primary particles often results in a large spread of transverse momentum leading to wider, larger and more diffuse showers.

- **EAS structure** The combination of EM and strong force interactions within hadronic showers lead to a more diffuse shower with greater clustering of the sub-structure. The development of EM showers within hadronic showers (as a result of neutral pion decay, see Sec.5.4.1) plays a major role in this and results in the large shower-to-shower variability. Alternatively, due to the homogeneous nature of the physical processes governing EM shower development, EM EASs tend to be more ordered and less variable between showers. The difference in shower structure can be evidently seen in Fig. 5.5.

- **Muons** Charged pions are the particle product with the greatest abundance in hadronic EASs. The subsequent decay of these charged pions into muons means that hadronic showers are unavoidably characterised by high numbers of muons. On the contrary, interactions producing muons in EM showers have an extremely low probability, resulting in negligible numbers of muons. Thus, the detection of muons is highly indicative of a hadronic shower. Moreover, the Cherenkov radiation produced from muons has a unique ring-like structure in the cameras of IACTs, a fact exploited by IACTs to discern between hadronic and EM showers.

- $\mathbf{X}_{\max}$ EM processes (generally) undergo interactions at shorter interaction lengths than hadronic interactions. This difference in interaction length over the length of an entire EAS results in hadronic showers penetrating deeper into the Earth's atmosphere and having larger $X_{\max}$ values.

Cherenkov Radiation

The Cherenkov effect is a phenomenon that results in the emission of electromagnetic radiation from relativistic charged particles. It is named after Pavel Cherenkov who

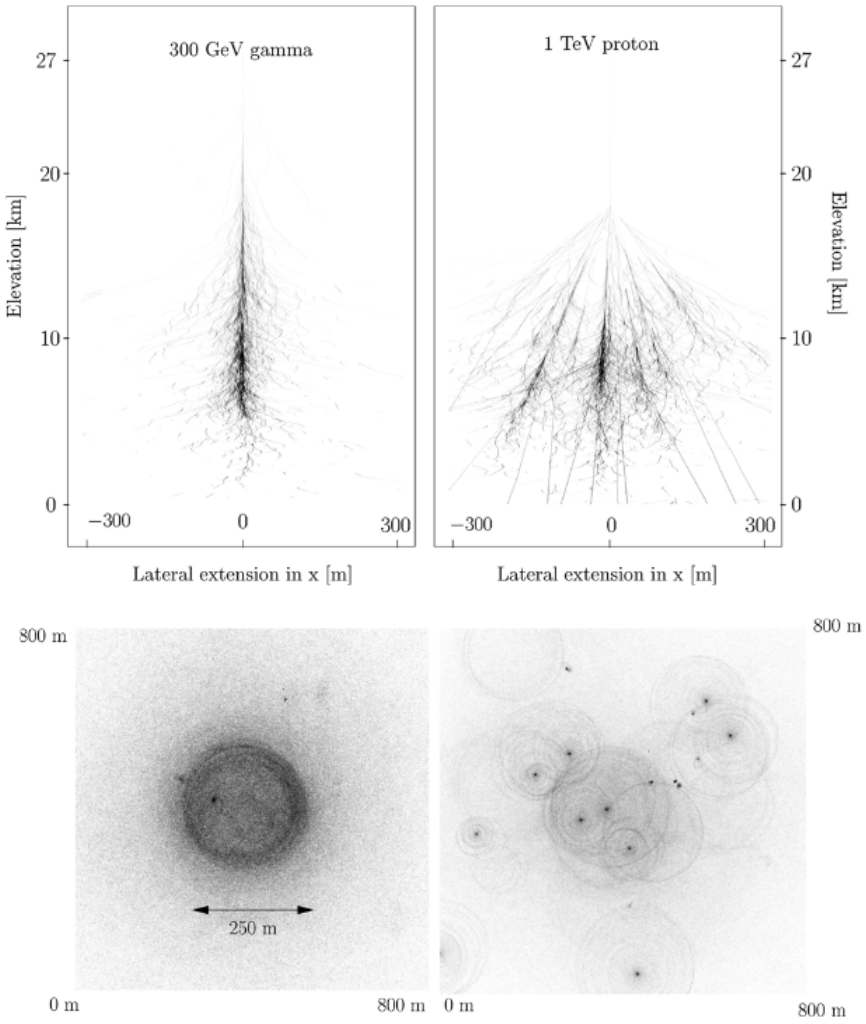

Fig. 5.5: *Top:* A comparison of the shower structure and development of a simulated EAS initiated by a 300 GeV gamma ray (left) and a 1 TeV proton (right). *Bottom:* The simulated Cherenkov light pool for the two aforementioned showers as seen from an upward-facing perspective. In both these figures, the structure of the hadronic shower and its light pool is inhomogeneous allowing for the discrimination between the two types of shower. Figures taken from [202].

first explained the blue light observed emanating from submerged nuclear reactors in 1934 [203]. The Cherenkov effect is observed following the passage of a relativistic charged particle of velocity v (ms^{-1}) through a dielectric medium of refractive index n. The incident charged particle will cause polarisation in the medium resulting in the induction of a dipole state in the atoms of the medium, the subsequent de-excitation of these atoms results in the emission of EM radiation. For particles at less than the phase velocity of light in the medium ($v < v_{\mathrm{p}}$ where $v_{\mathrm{p}} = \frac{c}{n}$) these spherical wavefronts interfere destructively resulting in no emission. However, in

the case where $v > v_{\mathrm{p}}$ these wave-fronts interfere constructively within an emission angle of θ_{c} (°), resulting in the emission of Cherenkov light in a conical beam. The angular extension of this cone is given by:

$$\cos(\theta_{\mathrm{c}}) = \frac{1}{n\beta} \qquad \text{where: } \beta = \frac{v}{c} \tag{5.4}$$

Thus, a cone of Cherenkov light is emitted by all elements of an EAS exceeding v_{p}, as shown in Fig. 5.6. Using $n = 1.00029$ [195], the value of the refractive index of air at sea level, energies of ~ 21 MeV, ~ 4.4 GeV and ~ 39 GeV are required for electrons muons and protons respectively to induce Cherenkov emission. The subsequent production of these particles in EM and hadronic showers therefore requires the incident particle to exceed these energies for a detectable signal to be produced. For average EAS energies, the resulting Cherenkov light has an $\theta_c \sim 1°$ to $2°$, which for standard X_{max} values results in the Cherenkov light cone forming a ring of ~ 100 m at ground level, lasting on the order of several nanoseconds.

The spectrum of Cherenkov light emanating from a particle of charge q (C), can be expressed in terms of the photons produced (N_γ) per distance (x, m):

$$\frac{\mathrm{d}N_\gamma}{\mathrm{d}x} = 2\pi\alpha Z^2 \int_{\lambda_1}^{\lambda_2} \left(1 - (n\beta)^{-2}\right) \frac{1}{\lambda^2}\,\mathrm{d}\lambda \tag{5.5}$$

where α is the fine structure constant and λ (m^{-1}) the wavelength of emitted light [204]. The combination of the λ^{-1} dependence of the Cherenkov photons produced, the preferential Rayleigh and Mie scattering of short wavelength light, and the atmospheric absorption of low wavelength light, results in the spectrum of Cherenkov light at ground level peaking at wavelengths corresponding to blue optical light.

5.4.2 IACT Operational Principles

IACTs function around the core principle of reconstructing the properties of a photon incident to the Earth's atmosphere, by measuring the flash of Cherenkov light from the resultant EAS. The use of the atmosphere as a calorimeter in this manner allows IACTs to circumvent the issue of small detection areas satellite-borne detectors face. This method, in fact, enables the (indirect) detection of VHE photons from an area of several km^2.

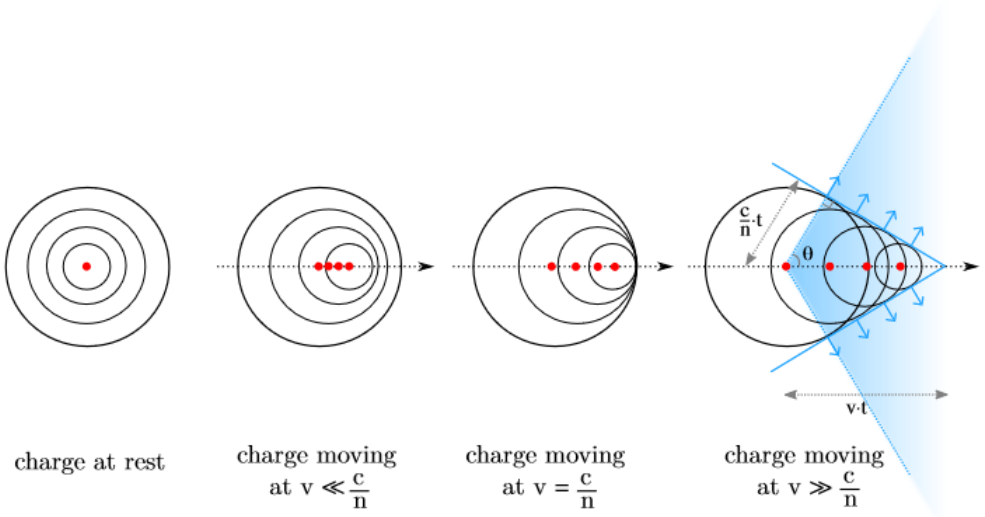

Fig. 5.6: A diagram showing the mechanism by which Cherenkov radiation is produced. From left to right, a charged particle passes through a dielectric medium with increasing speed. On the far right the charged particle achieves a velocity (v) greater than $\frac{c}{n}$ thus inducing constructive interference in the produced wavefronts and, therefore, Cherenkov radiation. As can be seen, this Cherenkov radiation is produced in a narrow cone in the direction of travel. Figure taken from [205].

The extremely short-lived nature ($\sim$ns) of Cherenkov flashes provides the major challenge in the imaging of the events, however, the use of PMTs allows most modern arrays to capture these events on such short timescales. Fortunately, the large extension of these Cherenkov flashes negates the need for cameras with high resolution. Additionally, the need to detect faint light in the optical band means that IACTs are extremely sensitive to background light. This means IACTs can only be operated during the night and during periods of low moon illumination. Moreover, due to their use of the atmosphere as a calorimeter, IACTs are extremely sensitive to weather conditions.

As EAS showers develop, the Cherenkov light cone (which can be modelled roughly as a prolate spheroid) will be detected as an ellipsoid by the IACT camera. The physical dimensions and properties of the image of this ellipsoidal shower are the primary variables in reconstructing the properties of the EAS, and therefore the incident particle. Properties such as the length and width of the ellipsoid allow for the reconstruction of the shower size, whereas the major and minor axes allow the reconstruction of the shower direction and thus the direction of the original photon. Commonly IACTs will operate in stereoscopic arrays where the ellipsoids of gamma-

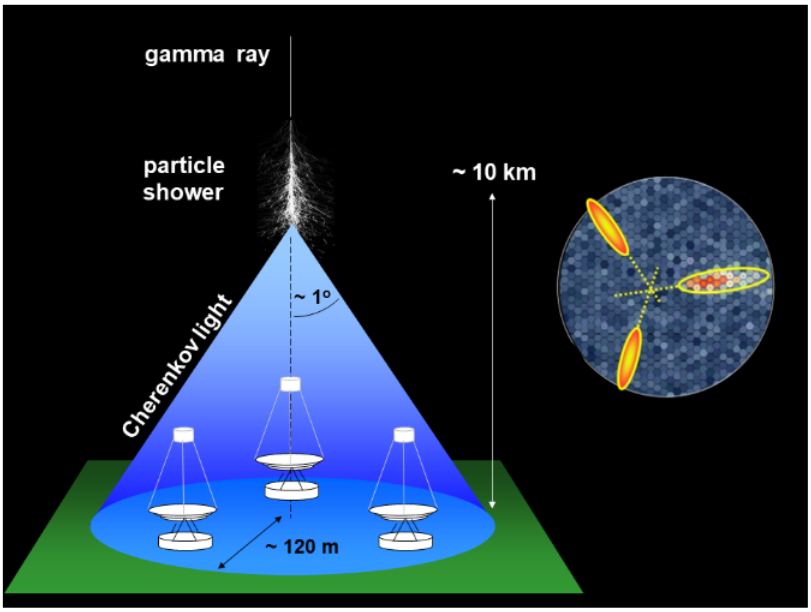

Fig. 5.7: Image showing the working principle of an IACT array. Each telescope individually images the EAS developing in the atmosphere. The geometries and details of this image are used in combination with those from the entire array to discern the properties of the shower. Figure taken from [206].

ray events are combined between multiple telescopes improving the accuracy of the directional reconstruction (see Fig.5.7).

The Fred Lawrence Whipple Observatory (completed in 1968) was the first IACT to demonstrate the viability of detecting Cherenkov light from high-energy gamma rays and, claimed the discovery of the first TeV emission from the Crab Nebula in 1988 [207]. Subsequently, the High-energy Gamma Ray Astronomy (HEGRA) array was completed in 1987 and pioneered the technique of stereoscopic observation in IACTs by simultaneously observing with 5 smaller telescopes and combining the data stereoscopically.

At the time of writing four IACT arrays are operational: the High Energy Stereoscopic System (H.E.S.S.) [1] (coincidentally the only current IACT located in the southern hemisphere), the Major Atmospheric Gamma Imaging Cherenkov Telescopes (MAGIC), the First G-APD Cherenkov Telescope (FACT), and the Very Energetic Radiation Imaging Telescope Array System (VERITAS). Moreover, the highly anticipated Cherenkov Telescope Array (CTA) is under construction and is likely to be active in the near future. By combining the knowledge learned so far from all IACTs, with the

[1] Named as a homage to the founder of astroparticle physics Victor Hess.

advances in detector technology, it is expected to have an unparalleled sensitivity which will propel the field forward.

5.4.3 The High Energy Stereoscopic System (H.E.S.S)

H.E.S.S. is an array of five imaging atmospheric Cherenkov telescopes located in the Khomas Highlands of Namibia (23°16'18"S, 16°30'0"E) at an altitude of 1800m above sea level [208]. H.E.S.S. is sensitive in the energy range ~ 20 GeV to several tens of TeV[2] [208], and is currently the only IACT operating in the southern hemisphere. The array itself consists of four identical IACTs (CT1-4) arranged at the corners of a square of side length 120m, with a fifth larger telescope (CT5) at the centre, as shown in Fig. 5.8.

Fig. 5.8: The H.E.S.S. array in the Khomas highlands of Namibia. At the centre is the larger telescope unit CT5, surrounding this the smaller telescope units CT1-4 form the vertices of a square. Image credit: H.E.S.S. Collaboration.

CT1-4 each hosts a segmented mirror of 382 circular mirror segments arranged in a hexagonal pattern with a total diameter of 12m. These mirrors are mounted according to the Davies-Cotton configuration [209]. Each of the telescope modules also contains a camera with 960 high-efficiency PMTs, each of which forms a pixel in the camera with an angular coverage of $0.16°$. This leads to a total FoV for the four telescopes of $\sim 5°$ and an energy resolution of ~ 100 GeV at zenith [208, 210].

CT5 is the largest and newest of the telescopes and hosts a 28m parabolic dish mirror which is made up of 875 smaller hexagonal mirrors. Although the style of the camera within CT5 has been changed in its history, the current iteration contains

[2]The maximum available energy is highly dependent on the conditions of observation.

1764 pixels, leading to an FoV for CT5 $3.2°$. The larger mirror of CT5 allows the collection of more diffuse Cherenkov light than the smaller telescopes in the array. Subsequently, CT5 has a lower energy threshold of ~ 20 GeV [211].

CT3 was the first telescope in the H.E.S.S. array and began operation in the Summer of 2002. It was then joined by CT1,2 and 4 in December of 2003. Prior to the installation of the fifth telescope, the H.E.S.S. array was made up of only these four telescopes. In the H.E.S.S. nomenclature this period is referred to as the H.E.S.S. I era. After the installation of the fifth telescope in 2012, the H.E.S.S. II phase began. The array was then further improved in 2016 after the upgrading of the cameras in CT1-4, reducing dead time in each camera and bolstering the performance of the array as a whole.

H.E.S.S. operates by pointing at target regions, in an order pre-determined by a schedule. It operates on a run-wise data acquisition basis with each full run taking 30 minutes (28 mins of observation, and 2 mins of calibration). In order to detect Cherenkov light, H.E.S.S. may only be operated in dark conditions restricting its operational time to be at night. Additionally, due to its sensitivity to high optical light levels, H.E.S.S. cannot be operated during periods of high moonlight (defined as a moon illumination of greater than 40%). This results in period-wise data taking, with each 28-day period of observation being punctuated by approximately 4 days of non-observations, during which calibration runs are performed.

Under usual conditions, the H.E.S.S. array operates in a stereoscopic mode, whereby two of the 5 telescopes must be triggered in order for an event to be recorded [210]. This criterion allows for improvements in the instrument's ability to reject background (both muon and hadronic), as well as improving the angular energy resolution and the accuracy of shower reconstruction [208]. Sometimes it is necessary to either split the array or isolate a telescope from observation; for this reason, the constituent telescopes of the array can observe independently of one another. This gives rise to several modes of operation in H.E.S.S. namely: *stereo* mode where at least two telescopes of CT1-4 are in simultaneous observation of a source, *mono* mode where data from only CT5 is considered, or *hybrid* mode where two telescopes of the array, which must include CT5, are in simultaneous observation.

5.5 H.E.S.S. Data Reduction and Analysis Pipeline

To enable the translation of raw recorded Cherenkov light to astrophysical data, an extensive process of calibration, reconstruction, event selection and background

modelling (among many other steps) must be undertaken. Conventionally this is described in terms of Data Levels (DLs), as shown in Fig. 5.9. DLs are a descriptor of the form of the data at a given stage of the reduction and analysis process. The eventual intent is to produce scientific products (DL4). To achieve this the raw Data Acquisition System (DAQ) output (DL0) must be translated first into image parameters in the camera (DL1), from which shower parameters can be derived (DL2), before the inclusion of IRFs and the formation of an event list at DL3. At this stage, the data is then ready for scientific analysis.

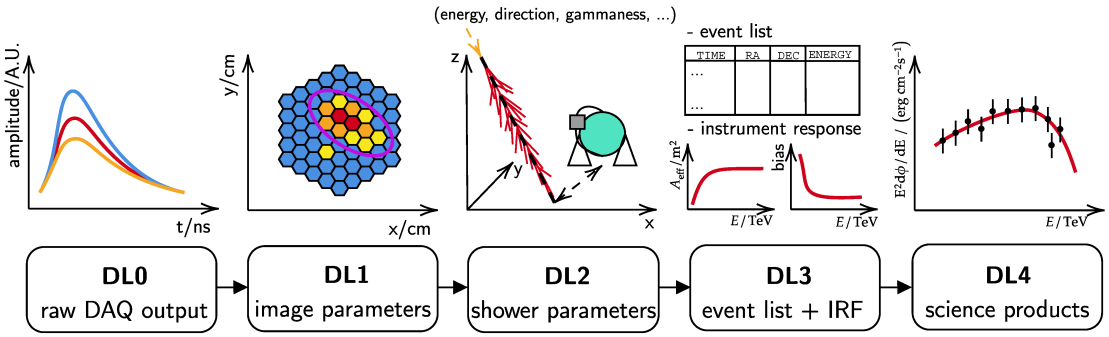

Fig. 5.9: The pipeline of data reduction and analysis from IACTs. Raw data is recorded by the DAQ forming DL0, this is in turn translated to image properties (DL1) and subsequently the properties of the shower (DL2). From DL2, candidate events can be taken to form an events list, these events are folded with the instruments IRFs (DL3) to create the final scientific data products used for analysis (DL4). Figure taken from [212].

5.5.1 Calibration and Image Cleaning

The operational principle of each camera within H.E.S.S. is the translation of Cherenkov light into charge in a given pixel. It is therefore essential to ensure that the response of each pixel to a signal is well understood and that instrumental factors affecting this process are accounted for. This is achieved in H.E.S.S. through the following dedicated calibration procedures.

- **Pedestals** This calibration categorises the background noise in the electronics. This provides the baseline readout of the electronics, ensuring this background charge is not conflated as a signal. The baseline electronic noise is recorded as the pedestal position variable $P_{\rm i}$ and is derived from the data of each run. While this calibration is required in CT1-4, it is performed automatically within CT5 and stored as $C_{\rm red}$.

- **Photomultiplier Gains** Enables the calibration of the amount of charge produced for a given light signal. During a dedicated run, a low illumination Light Emitting Diode (LED) emits a specified amount of light in front of the camera. Since the illumination is known, the amount of charge this produces in the PMTs allows the calibration of their gain (G_{i}).

- **High/Low Ratio** The cameras of CT1-4 utilise an Analogue Digital Converter (ADC) recording charge in both a High Gain (HG) and a Low Gain (LG) channel. Using two distinct channels, it is therefore important to account for the relative electronic gains and any changes in these via the ratio of the two (R_{i}). This value is derived from the data of each run individually, therefore does not require dedicated runs. CT5's camera only has one gain channel, negating the need for this step.

- **Broken Pixel Fraction** Is a value that denotes the number of pixels that are disabled for a given run. Pixels are disabled on a single-run basis to account for high levels of background light e.g. a bright star or satellite, or for multiple runs due to a long-term issue in the given pixel. This fraction is recorded in the value B_{i}.

- **Flat Fielding** Measures the quantum efficiency of the PMTs in each camera. This is achieved by illuminating the camera with pulsed laser light passed through a diffuser during a dedicated run. This produces a uniform signal at the PMTs, allowing for the relative quantum efficiency differences between PMTs to be calculated. The average of these for a camera is the flat fielding coefficient (FF_{i})

From these calibration runs, the baseline number of photoelectrons recorded by the DAQ can be adjusted to account for instrumental effects for both the high gain and the low gain channel.

$$C_{\mathrm{i}}^{\mathrm{HG}} = \frac{ADC_{\mathrm{i}}^{\mathrm{HG}} - P_{\mathrm{i}}^{\mathrm{HG}}}{G_{\mathrm{i}}^{\mathrm{HG}}} FF_{\mathrm{i}}\, B_{\mathrm{i}}^{\mathrm{HG}} C_{\mathrm{i}}^{\mathrm{LG}} = \frac{ADC_{\mathrm{i}}^{\mathrm{LG}} - P_{\mathrm{i}}^{\mathrm{LG}}}{G_{\mathrm{i}}^{\mathrm{HG}}} FF_{\mathrm{i}}\, B_{\mathrm{i}}^{\mathrm{LG}}\, R_{\mathrm{i}} \tag{5.6}$$

Where C_{i} is the calibration of the number of photoelectrons obtained. A more detailed breakdown of the calibration process in H.E.S.S. for CT1-4 can be found within [213].

For CT5 this calibration takes the form

$$C_{\mathrm{i}} = (C_{\mathrm{red}} - P_{\mathrm{i}}) FF_{\mathrm{i}} B_{\mathrm{i}} \tag{5.7}$$

Where each of the terms has the same meaning as in Eq.5.6 but are dedicated values taken from CT5 calibration runs. Further details of CT5 calibration can be found within [214]

Additionally, the optical efficiency of the system is measured on a run-by-run basis, allowing for corrections to be applied for the degradation/change of the optical efficiencies of the telescope components over time (e.g loss of reflectivity in the mirrors and Winston cones resulting in an overall dimming of the image). This step is extremely important as the intensity of pixels in the camera are the measurable quantity by which the energy of the progenitor photon is determined. Thus, corrections to the optical efficiency will have a direct impact on the accuracy of the energy calculation. To this end, the well-defined ring-like shape resulting from muonic Cherenkov emission is utilised. The Cherenkov rings seen from these muons can be used to calculate the properties of the progenitor muon and thus, in turn, the expected brightness of the Cherenkov emission that should be present. The comparison of this expected brightness to the image intensity in the camera is what allows for the calculation of the optical efficiency. For this however, near-perfect muon rings are required and thus strict cuts are placed upon the muons observed on a run-by-run basis to ensure an accurate reconstruction of the optical efficiency. Further details of this method can be found in [215].

Following calibration, images are subjected to cleaning to remove noise. For H.E.S.S. the majority of this background usually originates from Night Sky Background (NSB) light. The standard method of image cleaning for H.E.S.S. data is the two-step tailcuts method. Firstly, only pixels with an intensity greater than 3 times the pedestal width (baseline electronic value) are considered, and all pixels that do not satisfy this criterion are discarded. Secondly, pixels must fulfil the criteria of having a greater intensity than 4 times their pedestal width, but also neighbour a pixel with an intensity above 7 times its own pedestal width. In this way, only large-scale structures in the image remain and individual bright pixels are removed. Variations on these steps can be implemented for analyses requiring stringent conditions, e.g. a lower or higher threshold for intensities, or requiring at least 2 neighbours in the second step.

5.5.2 Event Reconstruction

Following calibration and cleaning, images are used to reconstruct the EAS and its properties. Chief among these are the direction and energy of the primary.

The geometry of a shower's image in the camera (typically an ellipsoid) provides direct information regarding the properties and directionality of the EAS, and therefore of the primary particle. These image geometries are thus utilised to constrain a shower's properties, by measuring the so-called Hillas parameters[3]. The Hillas parameters are the most elementary approach to shower reconstruction and refer to a series of empirical values of the image's geometry such as length, angle of the image from the normal and the width [216]. These parameters, in turn, can be used to reconstruct the initial shower properties as shown in Fig. 5.10. The Hillas parameter approach is most effective when stereoscopic observations are employed, allowing for a more precise reconstruction of the initial direction. Stereoscopic observations also help to alleviate directional degeneracies, an error this technique is prone to. In this technique, the energy is reconstructed from a combination of the charge and the shower's approximate penetration depth. An increase in primary particle energy results in an increase of secondary particles and shower development, and therefore a greater Cherenkov light yield. By comparing the charge measured to the shower's distance the energy of the primary can be calculated.

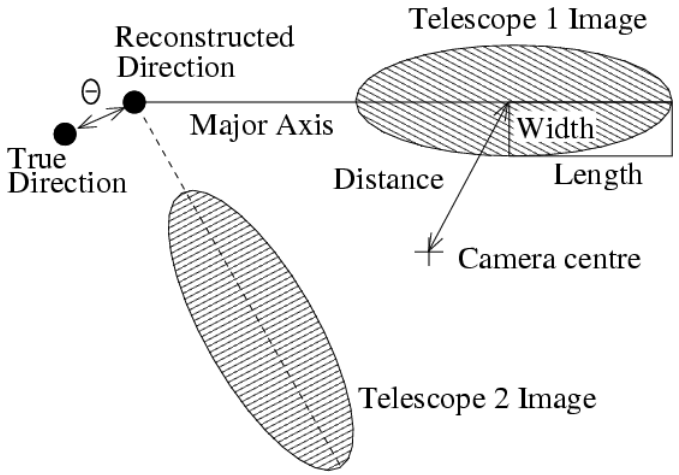

Fig. 5.10: Figure detailing the characterisation of shower images via their Hillas parameters. Cleaned images of showers usually form an ellipsoidal shape, as shown in the figure. The characteristic, width, length and other measurables are used to determine the properties and geometry of the shower. The major axis is indicative of the incident direction of the shower, as shown in the figure. The use of multiple telescopes to image a shower can significantly increase the accuracy in deriving the shower's initial direction (as well as its other properties). Figure taken from [217].

A more contemporary reconstruction technique employed by many current IACTs, is the likelihood comparison of shower images to a library of simulated gamma-ray shower events. The Image Pixel-wise fit for Atmospheric Cherenkov Telescopes (Im-

[3]Named after the author who pioneered the technique.

PACT) [218] is one such method implemented in the H.E.S.S. array. This technique calls upon a library of template images produced by Monte Carlo simulations of gamma-ray induced EASs. These images are produced by utilising a ray tracing technique to construct an accurate image of how showers of varying initial properties would appear to each telescope module. In this technique, event images from each telescope are first fit with Hillas parameters to find like-templates in the library. After finding a set of similar templates, the image is fit in a pixel-wise manner using a maximum likelihood approach. The result of this fit provides the template with the highest likelihood. From this template, the initial properties of the simulated gamma-ray event (which best matches the real data) can be extracted.

In addition to Hillas parameter reconstruction, the increased availability of computational power has allowed the development of the 3D modelling of showers from camera images [219]. This method creates a 3-dimensional image of the shower from the available parameters to more accurately determine the direction and energy of the progenitor particle. More recently, deep learning techniques are also being applied to the reconstruction of showers with the intention of using machine learning to more easily and accurately identify the parameters of particle showers from their images [220].

5.5.3 Gamma Ray – Hadron Discrimination

Following reconstruction, it is essential to ensure only events from gamma rays are considered. This ensures that hadrons (that constitute a background) are not conflated with gamma-ray signals from an astrophysical target. Broadly, this is achieved by implementing techniques that discriminate using the variation in the resulting shower image between EM and hadron-induced showers due to their differing shower evolution and properties (see Sec. 5.4.1).

Originally so-called "box cuts" were implemented to achieve this task. These simply defined values of the Hillas parameters as bounds for an event to be considered gamma-like, with images containing values outside of these bounds considered as hadronic and discarded. The parameters utilised in these cases were the mean reduced scale width and the mean reduced scale length, as defined in [217]. Further details on the implementation of this can be found in [221].

The categorisation of events into gamma rays or hadrons represents a classification problem with two distinct categories, an area in which machine learning algorithms can provide significant advantages. Thus, contemporary discrimination of the

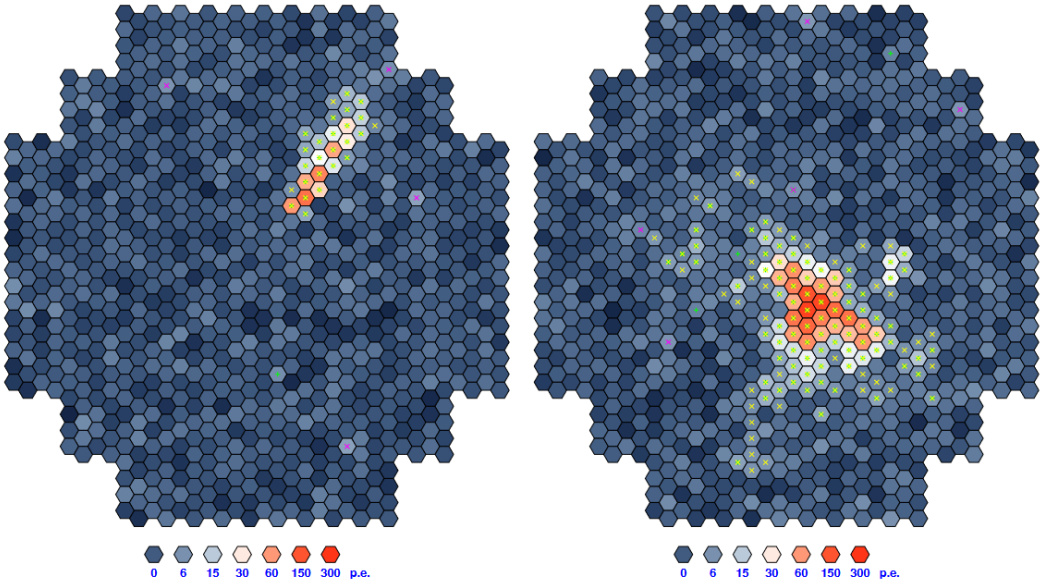

Fig. 5.11: Image comparing the appearance of a gamma ray and hadron-induced EAS, in the camera of an IACT. Gamma-induced EASs (left) notably appear as a somewhat regular ellipse (depending on their orientation), whereas a hadron-induced shower is imaged as a far less regular shape due to the asymmetry and more diffuse shower structure of hadronic showers. Figure taken from [222]

primary particle is more often performed using machine learning techniques, specifically Boosted Decision Trees (BDTs). A BDT implements a multivariate analysis of event classification by running image parameters through a series of nodes. Each of these nodes evaluates a criterion of the image and results in a binary choice between two outcomes [223]. Most commonly, the mean reduced scale width and the mean reduced scale length are both used as inputs for these decisions. Once an image has parsed all the nodes of the tree it is assigned a value representing its likelihood of being a gamma-ray-induced event (ζ_{BDT}). This value is later used to implement cuts on the data. For a detailed breakdown of this technique see [223].

5.5.4 Instrument Response Functions

The IRFs are the mathematical description of a telescope's response to an astrophysical flux. The list of gamma-ray events produced after reconstruction and gamma-hadron discrimination contains only a minimal amount of information about each event. Thus, in order to derive meaningful astrophysical quantities from each event, these events must be convolved with the IRFs. These functions provide a

means to translate reconstructed event parameters into a close approximation of the true parameters of the actual photon and are typically derived through Monte Carlo simulations.

Effective Area

The effective area (see Fig. 5.12), A_{eff} (m^2), is the description of the effective photon collection area of a telescope at a given energy. More specifically, it is the product of the detector collection area and the detection efficiency of the array. The latter of these two terms is highly sensitive to observational conditions and therefore the effective area fluctuates with the zenith angle, telescope optical efficiency, event energy and the offset of the EAS from the telescope's pointing position.

Energy Dispersion

The energy dispersion (see Fig. 5.12), E_{disp} (TeV^{-1}) is the probability that an event with energy E_{true} will be reconstructed with an energy E_{recon}. This is affected by several systematics effects including the atmospheric conditions and the response of the mirrors and camera.

Point Spread Function

The Point Spread Function (PSF) similarly represents the probability that an event at position p_{true} will be reconstructed with a position p_{recon}. The PSF is ultimately a measure of the accuracy of an event's reconstruction and is typically derived from Monte Carlo simulations. The PSF is expressed as an angular separation $\theta_{\text{PSF}} = p_{\text{true}} - p_{\text{recon}}$, where $\text{PSF}(\theta_{\text{recon}}|p_{\text{true}}, E_{\text{true}})$ and is commonly defined as the function's 68% containment radius. The value is affected by: zenith angle, optical efficiency, as well as event energy and offset. See Fig. 5.12, for an example PSF.

Background Model

The background model (see Fig. 5.12) is used to account for residual background from misclassified hadronic events and fluctuates with event energy and offset. A background model is constructed for use in likelihood fitting, as is commonly used

in source modelling within `Gammapy`[4]. Sec 5.5.5 provides detail on the ON-OFF background method[5].

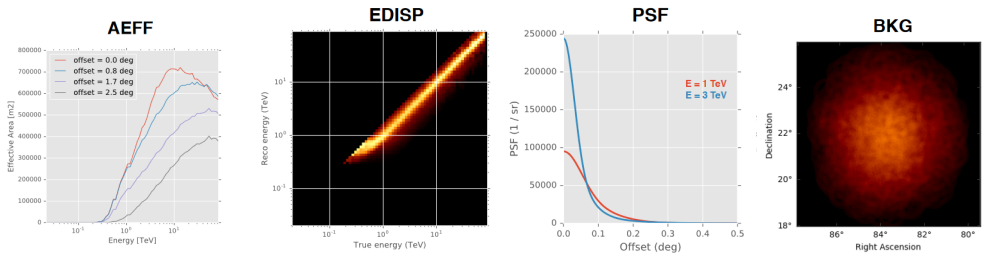

Fig. 5.12: Example IRF components (left to right: effective area, energy dispersion, point spread function and background model) derived from H.E.S.S. I observations of the Crab Nebula. Figure adapted from [224].

5.5.5 Background

Background estimation is essential for any IACT observation in order to correctly characterise and remove erroneously categorised hadronic events, and thus accurately derive excess gamma-ray counts of a source. The process can be understood as an array's acceptance of residual hadronic events after cuts. This acceptance is a function of the reconstructed energy, the reconstructed position as well as the zenith and azimuthal angles.

The residual background elements in IACTs, at this stage of analysis, form an isotropic background. Typically within observations, there are regions around the source from which no VHE emission is expected. These regions are, therefore, used to determine the background counts in the observation and are designated the "OFF" region. Broadly speaking, the counts from the OFF region can then be subtracted from those of the ROI (the "ON" region) to remove these background counts from the source. Cases where emission is detected in designated OFF regions are usually treated by excluding that specific region to ensure emission is not falsely subtracted as background.

Within the ROI, the number of events is given by:

$$N_{\mathrm{ON}} = N_{\mathrm{source,ROI}} + N_{\mathrm{bkg,ROI}} \tag{5.8}$$

[4]An open source python package designed for use in gamma-ray astronomy. See `https://gammapy.org/` for full details of the package.
[5]The latter of these methods was utilised in the analysis of PSR B1259-63/LS 2883 and, is thus, more pertinent to this thesis.

where N_{ON} (counts) is the total number of events in the ON region, $N_{\mathrm{source,ROI}}$ (counts) is the number of those events from the source in question and $N_{\mathrm{bkg,ROI}}$ (counts) is the number of the total events that constitute a background.

By its nature, an uncontaminated OFF region will principally contain isotropic background events, since these are isotropic

$$N_{\mathrm{bkg,ROI}} = \alpha N_{\mathrm{bkg,OFF}} \tag{5.9}$$

where $N_{\mathrm{bkg,OFF}}$ (counts) is the number of counts in the OFF region and α is the acceptance ratio between the two (commonly the ratio of the area and exposure between the ON and OFF regions) given by

$$\alpha = \frac{A_{\mathrm{on}} t_{\mathrm{on}}}{A_{\mathrm{off}} t_{\mathrm{off}}} \tag{5.10}$$

where A (m^2) is the area and t (s) the exposure times of the ON and OFF regions respectively.

This fact leads allows one to derive the excess (Ex, counts) as

$$Ex = N_{\mathrm{source,ROI}} = N_{\mathrm{ON}} - \alpha N_{\mathrm{bkg,OFF}} \tag{5.11}$$

where the subtraction of the acceptance corrected counts in an OFF region from an ON region determines the number of events from the source [225].

By this reasoning, the observational strategies of IACTs generally revolve around obtaining data simultaneously from an ON and an OFF region. Given the highly run-specific and variable nature of the background observation counts, backgrounds must be individually accounted for with each run. However, a number of different observational strategies are employed by IACTs to achieve this goal.

Reflected Background

One of the most commonly utilised and simplistic background methods employed by IACTs is the reflected background. In this method, the observation is purposefully offset from the ROI by $\sim 0.7°$ (this value is the default wobble offset for H.E.S.S. but can vary depending on the source and situation). As shown in Fig. 5.13, the ROI forms one of many regions arranged in a ring of constant radius around the observation's centre. Counts are measured in the single ON region containing the source, as well as all other regions constituting the ring, forming the OFF regions [226]. By applying the acceptance factor to the counts in the background regions

(which as the ON region and a single OFF region share the same size is simply the number of OFF regions) the excess can be calculated via Eq.5.11. Typically this technique is performed using a "wobble observation" where data is taken at one offset from the source before pointing the array to the same offset on the alternate side of the source. This approach is highly utilised among IACTs and is a robust method of determining 1D energy spectra, however, collating counts in the ON region loses information on the geometry of the source. Despite its advantages, the reflected background method relies on radial symmetry of the camera's acceptance and is strongly affected by a gradient in zenith angle [226].

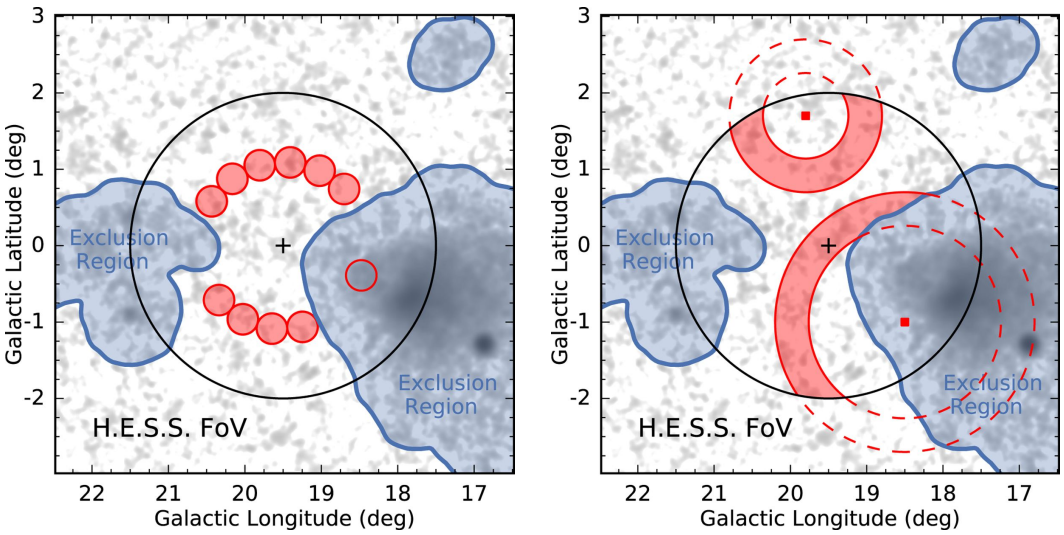

(a) Reflected Background **(b)** Ring Background

Fig. 5.13: *Left:* A depiction of the reflected background method utilised by IACTs (in this case, specifically H.E.S.S.). Here the central cross denotes the centre of the observation, where additionally the ON region is marked by an empty red circle. The OFF regions in the figure are denoted by the filled red circles and are regions of the same area as the ON region, from which the background is taken. Background regions are taken at a constant radius from the observation's centre and must be outside of excluded regions (blue) and have an offset smaller than the safe offset from the pointing position (black circle). *Right:* An example of the ring background method, here showing an analysis of two positions. The central point of each ring marks the ON region, whereas the red-shaded rings denote the area from which the background is taken. Ring radii can be adaptively sized (as shown by the difference in size between the two rings) to obtain a sufficient background estimate. Figures taken from [227].

Ring Background

The ring background method is a technique in which the observation is centred on the ROI, and the background is taken from a ringed OFF region around the central

ON region (see Fig. 5.13). This method has the advantage of negating the effects of gradients and large-scale fluctuations [226]. However, is not as effective in energy spectrum determination, and is typically used for the construction of maps of a region and morphological studies [226].

ON-OFF Background

The ON-OFF background method is utilised by taking a larger ON region in a run and performing a second run with similar conditions as an OFF region. This method is advantageous in the analysis of extended sources for which OFF regions cannot be obtained in the same FoV. It is extremely important to the final background subtraction that the OFF observations are undertaken under similar weather conditions and zenith angles, given the dependencies of counts on these factors. This method is auspicious given that no assumptions are made on the acceptance.

5.5.6 Data Analysis

Significance and Maps

Observations in IACTs principally aim to detect significant emission of VHE gamma rays from a source region. To establish the significance of an observation, the Test Statistic (TS) is applied

$$\mathrm{TS} = -2\log\left(\frac{\mathcal{L}(\mathcal{H}_0)}{\mathcal{L}(\mathcal{H}_1)}\right) \tag{5.12}$$

This equality tests the preference of a hypothesis in which there is a source ($\mathcal{H}_1$) against a null hypothesis ($\mathcal{H}_0$) [228]. The preference between these two outcomes is measured using the likelihood ($\mathcal{L}$) of each hypothesis (see [229] for an introduction to the concept of likelihood).

For one degree of freedom, the significance can be calculated from the test statistic using

$$\sigma = \sqrt{\mathrm{TS}} \tag{5.13}$$

where a significance of 5σ denotes a detection in VHE gamma-ray astronomy, following the standard of detection at almost all wavelengths. It can occur that the excess counts from a source region are negative. In this case, the significance is (by convention) denoted as a negative significance such that $\sigma = -\sqrt{\mathrm{TS}}$.

The hypothesis that a source is present ($\mathcal{H}_1$ of Eq. 5.12) can be tested via two distinct techniques.

- **Excess Significance** Describes the process in which the significance is obtained using the computed excess of the source described in Sec.5.5.5. This is calculated via the convention pioneered by Li and Ma [225].

$$\sigma = \sqrt{2}\left\{N_{\rm on}\ln\left[\frac{1+\alpha}{\alpha}\left(\frac{N_{\rm on}}{N_{\rm on}+N_{\rm off}}\right)\right] + N_{\rm off}\ln\left[(1+\alpha)\left(\frac{N_{\rm on}}{N_{\rm on}+N_{\rm off}}\right)\right]\right\}^{\frac{1}{2}} \tag{5.14}$$

- **Model Significance** Is the significance calculated when comparing a source's excess to the predicted excess of a physically motivated model of the source and background. This method relies heavily on the existence of an adequate background model of the region, as well as the correct modelling of the source's spectral behaviour and morphology.

Given that not all calculated excesses are significant, mapping the significance is advantageous compared to a map of just the excess counts. Therefore, an important analysis tool for any source is the production of the significance map. For both the methods described above, the significance is calculated in each pixel of the map and displayed. While model-based significances are prone to mismodelling, significances calculated from excesses are calculated by grouping pixels within a given radius. This in turn impacts the scales at which structures appear in the resultant map. For both methods, the excess counts are (by convention) smoothed using a top-hat function applied in a given radius. The radius at which this function operates can also impact structural scales.

Flux Points and Light Curves

In order to calculate the flux of a source, many IACTs utilise an aperture photometry method. In HE and VHE astronomy, simply utilising the excess counts alone is often not a feasible measure of the flux due to the low statistics associated with higher energies and the energy-dependent exposure of high-energy photons. For H.E.S.S., aperture photometry is implemented under the H.E.S.S. Analysis Program (HAP).

The aperture photometry technique utilises a reference spectrum of the source given by

$$\Phi_{\rm Ref} = \Phi_0(E_0)\left(\frac{E}{E_0}\right)^{-\Gamma} \tag{5.15}$$

where Φ_{Ref} (TeV^{-1} cm^{-2} s^{-1}) is the reference spectrum, Φ_0 (TeV^{-1} cm^{-2} s^{-1}) is the normalisation flux (flux of the spectrum at the decorrelation energy E_0, TeV) and Γ is the spectral index of the reference spectrum (the slope of the spectrum).

Given that by definition

$$\Phi(E) = \frac{\mathrm{d}N}{\mathrm{d}E\,\mathrm{d}A\,\mathrm{d}T} \tag{5.16}$$

and

$$F = \frac{\mathrm{d}N}{\mathrm{d}A\,\mathrm{d}T} \tag{5.17}$$

where F is the flux (cm^{-2} s^{-1}), N is the number of counts, E (TeV) the energy, A (m^2) the effective area and T (t) the time. Combining these two equations we obtain

$$F = \int \Phi(E)\,\mathrm{d}E \tag{5.18}$$

which for the reference spectrum would be

$$F_{\mathrm{Ref}} = \int_{E_{\mathrm{min}}}^{E_{\mathrm{max}}} \Phi_{\mathrm{Ref}}(E)\,\mathrm{d}E \tag{5.19}$$

As well as measuring the Excess of the source (Ex_{Meas}), one may calculate the expected excess of the source from the reference spectrum, which would follow the form

$$Ex_{\mathrm{Exp}} = \int_{\Delta E} \Phi_{\mathrm{Ref}}(E)\,A_{\mathrm{eff}}(E)\,\Delta t\,\mathrm{d}E \tag{5.20}$$

Thus by combining Eq.5.18, Eq. 5.20 and Eq.5.19 one can obtain the true flux of the source from the following equality

$$F = \frac{Ex_{\mathrm{Meas}}}{Ex_{\mathrm{Exp}}} \cdot F_{\mathrm{Ref}} \tag{5.21}$$

This value, also referred to as the aperture flux, provides an energy-dependent and exposure-corrected value of the flux of a source. It should be noted that the value of the reference spectrum is often iterated to the best-fitting value where possible. This is the main method utilised by HAP in the calculation of flux in an observation.

In order to investigate flux trends and system behaviours, it is often beneficial to investigate the variation of flux over time by plotting a light curve. This is achieved through the integration of the differential energy flux in a given energy and time interval. To attain the flux in differing time periods, the reference spectrum is often refit and new flux points are attained. For light curves covering short time periods, it

is often necessary to fix the reference spectrum, as opposed to fitting it to each point. Fitting to individual points suffers from the low statistics individual points have; this causes the fit parameters to become highly variable, introducing systematic errors.

Spectra

The spectrum of an astrophysical object provides key insights into the physics and particle acceleration responsible for its emission. Its derivation is therefore quintessential for the thorough analysis and subsequent modelling of any source. Spectra are calculated through an assumption on the form of the differential flux

$$\phi(E) = \frac{\mathrm{d}N}{\mathrm{d}E} \tag{5.22}$$

where N is the number of photons arriving in a given area and time, and E (TeV) is the energy. The assumed model often depends on the nature of the source and the expected acceleration mechanisms. Commonly in VHE astronomy, this is a power law or exponential cut-off power law. A power-law model follows the form

$$\phi(E) = \phi_0 \left(\frac{E}{E_0}\right)^{-\Gamma} \tag{5.23}$$

where ϕ_0 (TeV^{-1}cm^{-2}s^{-1}) is the flux normalisation, E_0 (TeV) the reference energy and Γ the spectral index (slope of the power law). Another common model is the exponential cut-off power law

$$\phi(E) = \phi_0 \left(\frac{E}{E_0}\right)^{-\Gamma} \exp(-(\lambda E)^{\alpha}) \tag{5.24}$$

Here α is the cut-off index and $\lambda = \frac{1}{E_{\mathrm{cut}}}$, dictating the sharpness of the cutoff and the energy at which it occurs.

To derive the spectral points, a process of forward-folding the spectrum is applied. This takes the assumed model of the source and forward-folds (convolves) it with the IRFs of the instruments, whilst also accounting for observational conditions. Doing this results in the expected gamma-ray excess for that model assumption, which can then be compared to the measured excess through a series of energy bins. Bin sizes or definitions are frequently tailored to a particular analysis, but a common standard is utilising a bin where the data within are a minimum of 2σ significance. The measured excess is then compared to the expected excess via a maximum likelihood fit, allowing the optimisation of the model parameters to best fit the observed data. The derivation of the best-fitting spectral model then allows

the computation of the spectrum in each energy bin. Flux points in each energy bin are therefore the normalisation of the model best fitting the gamma-ray signal in that specific bin, at an energy corresponding to the logarithmic centre of that bin. An example of a comparison between excess and model-derived counts, as well as the resulting spectrum, are shown in Fig. 5.14.

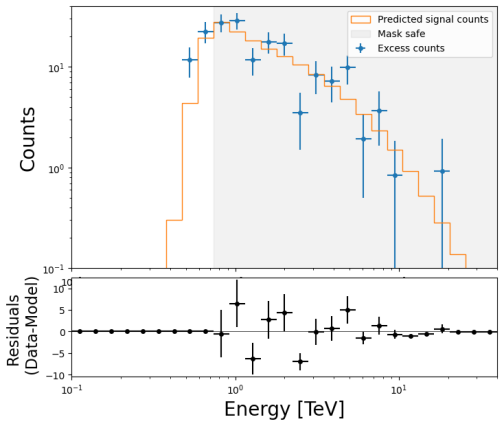

(a) Model Counts

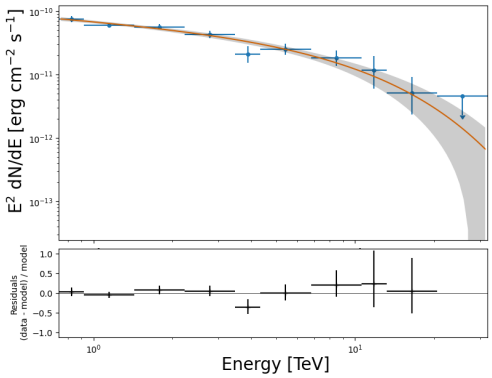

(b) Spectral Energy Density

Fig. 5.14: *Left:* A comparison of the excess counts derived from observations, and the predicted counts in each energy bin derived from the fitting of a power-law model to the data. The grey region indicates the safe mask and is derived from the value of 10% of the effective area. The bottom panel shows the residuals between the excess counts and the model counts. *Right:* Displays the resultant spectral model and flux points, where the bottom panel depicts the residuals between these. Figures created from four H.E.S.S. observations of the Crab Nebula released in public data release 1, where the counts are derived in an aperture of $0.11\,\mathrm{deg}$. Spectra made using Gammapy.

5.6 Summary

This chapter has provided an overview of the subject of very-high-energy gamma-ray astronomy and the principles by which very-high-energy photons are detected. In particular, the main focus of the overview has been on introducing the principles by which IACTs operate, due to their relevance in the work presented in chapter 7. This has been undertaken by explaining the principles behind cosmic rays and photons incident on the Earth, as well as the EASs caused by their interaction with particles in the atmosphere. This principle, along with the production of Cherenkov light, is used in the context of IACTs to explain how the indirect imaging of VHE gamma rays is possible. The second half of this chapter has detailed the H.E.S.S. array and its data analysis pipeline. To achieve this, a step-by-step guide has been undertaken to show how the array detects the resultant EAS's of gamma rays and then cleans,

reconstructs and rejects background to form event lists. Finally, the process of data analysis within H.E.S.S. (and the underlying mathematics and principles of these) is also detailed.

6 Gamma-ray Binary Systems

Gamma-ray binary systems are a relatively newly discovered subclass of high and intermediate-mass binary systems. They are defined by their energy spectra peaking at > 100 MeV; where these spectra also often extend beyond 10 TeV. Historically, Gamma-ray binaries were expected to be far more numerous, the abundance of X-ray Binariess (XRBss) provided solid evidence that binaries were strong non-thermal emitters up to X-ray energies. It was expected, therefore, that this emission would continue to HE and VHE regimes. To date over 500 XRBs have been tentatively discovered [230, 231], yet only ~ 10 of these have been detected as gamma-ray emitters.

6.1 Binary Systems

Binary systems, in the context of high-energy astrophysics, are typically formed of a massive star (of spectral type O or B) with a compact object (either a neutron star or a black hole) in orbit around it. The mass of the companion star is most commonly used to categorise systems, with $M_{\rm comp} \geq 5M_{\odot}$ denoting high mass systems, $M_{\rm comp} \leq 1M_{\odot}$ denoting low mass systems. The handful of currently discovered systems that fall between these mass ranges are classified as intermediate-mass systems [231].

The majority of binary systems fall under the category of either Low-mass X-ray Binaries (LMXBs) or High-mass X-ray Binaries (HMXBs). These systems are categorised by strong non-thermal emission in the X-ray regime. The mechanisms for this emission are thought to mainly arise from particle acceleration occurring in the process of mass accretion from the donor star to the compact object [232]. Alternatively, a scenario in which particle acceleration occurs due to the resultant shock formed from pulsar wind and stellar outflow is favoured for higher mass systems [232]. See [232] and [233] for reviews of XRBs and their emission mechanisms.

6.2 Gamma-ray Emitting Binaries

The umbrella term for any binary system with an energy spectrum peaking at above 1 MeV (but typically at $E \gtrsim 100$ MeV) is a Gamma-ray Emitting Binary (GREB). Though each is a high-energy binary system, there are currently three distinct categories of GREB corresponding to the three emission mechanisms thought to occur in these systems.

6.2.1 Microquasars

Microquasars are so named for their similarity (albeit on a smaller scale) to the jetted physics observed in AGN and quasars. These objects are a category of binary sources that display jetted structures powered by the accretion of matter onto a compact object. In all systems in which the companion can be identified, the compact object has been confirmed as a roughly solar-mass black hole. In this accretion process, the donor star's matter is transferred to an accretion disc around the compact object. This matter subsequently falls into the black hole; here it is accelerated and a small fraction is ejected along relativistic jets perpendicular to the compact object's axis of rotation. These jets are known to be sites of ultra-relativistic particle acceleration and as such are the sites of TeV gamma-ray emission. This can be seen in the left-hand panel of Fig. 6.1. Examples of microquasar systems include Cyg X-1, Cyg X-3 and SS 433. For a review of jetted sources in the galaxy see [234].

6.2.2 Colliding Wind Binaries

Another category of binaries that can produce emission in the gamma-ray regime are Colliding Wind Binarys (CWBs). These systems (unlike any category previously mentioned) do not contain compact objects, and are instead typically two massive stars with powerful stellar outflows. The resultant shock formed from the confluence of the two stellar winds provides a site for high-energy particle acceleration, allowing some systems to emit up to HE ($0.1 < E < 100$ GeV) gamma rays. VHE emission from these systems is also expected, such as in the case of Eta Carinae [235, 236]. To date three CWBs have been detected making them a somewhat unique object for study, these include: Eta Carinae, γ^2 Velorum and HD93129A.

6.2.3 Gamma-ray Binaries

The final category of binaries emitting in the HE and VHE regime, and the category most important in the context of this thesis, are simply known as gamma-ray binaries. VHE emission in these systems is widely accepted to occur from the shock front formed between the stellar wind of the optical companion and the pulsar wind. Typically in these systems, the optical companion is a very large star of (most often) B stellar classification. The termination zone where these two outflows collide is a prime site for HE and VHE particle acceleration. This situation is predicted to occur in systems that host a highly energetic pulsar capable of producing pulsar winds that are sufficiently energetic to prevent accretion. Due to the central role of the pulsar wind, these systems are often referred to as plerionic binaries (see the right-hand panel of Fig. 6.1). Plerionic binaries are usually characterised by fast rotation and strong magnetic fields. In fact, in these systems only a small percentage of a pulsar's spin-down luminosity (around 1%) is necessary to drive a pulsar wind capable of preventing accretion [237].

To date $\sim$ 10 gamma-ray binaries or gamma-ray binary candidates have been discovered, however, determining the nature of the companion remains a difficult task. Moreover, it is often difficult to discern between gamma-ray binaries and microquasars due to the fact that one must resolve the jets to classify a system as the latter, which in turn requires significant observational data. Therefore, it is common that binaries emitting in the HE and VHE regimes will be first classified as gamma-ray binaries before later being reclassified. To date, only three systems have well-identified companions, namely PSR B1259-63 [238], PSR J2032+4127 [239] and LS I+61 303 [240]

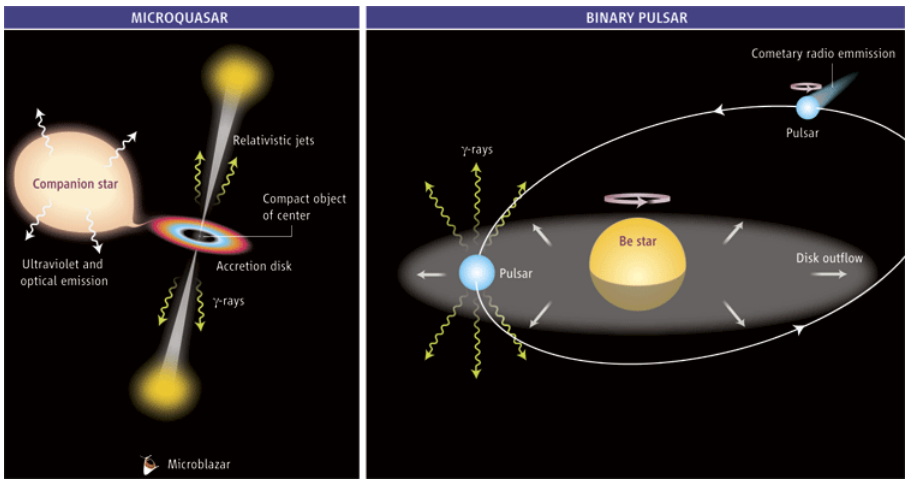

Fig. 6.1: Diagram depicting an overview of the layout and processes in both microquasar and plerionic binary systems. Figure taken from [241].

6.3 Oe and Be Stars

Oe and Be type stars have been confirmed as the optical companions to all three gamma-ray binary systems in which the compact object has also been identified. As a common stellar companion in gamma-ray binary systems, and in particular the companion to PSR B1259-63, they are of particular pertinence to this thesis. Oe and Be type stars share very similar properties, so much so that Oe stars are often referred to as Be stars in literature. Most information on Oe-type stars in the following is thus also applicable to Be-type stars.

The O of Oe stars denotes their spectral class on the Hertzsprung-Russell diagram. Objects in the O spectral class are the largest and hottest stars in the Universe, making them extremely luminous blue stars with masses of $\geq 16 M_{\odot}$. Oe stars are, therefore, stars within this spectral class that additionally have emission lines within their spectra, denoted by the spectral peculiarity code "e" (typically hydrogen).

One of the features of Oe and Be stars with more interesting ramifications, is their rapid rotation. Oe and Be stars have a rapid mass loss rate, losing 10^{-7} to 10^{-5} $M_{\odot}$ year^{-1}. The combination of this mass loss and fast rotation commonly causes the formation of a low-velocity, but dense, equatorial wind forming an equatorial disc of gas and dust. The presence of this disc can be inferred by the linear polarisation of optical light, and the detection of extended IR emission resulting from the scattering of optical starlight [242]. In addition to these features, the circumstellar disc exhibits evidence of free-free/free-bound emission as well as Hα lines. These lines are often the emission via which the systems are denoted as having the spectral peculiarity "e", thus, this is often seen as indicative of the system hosting a circumstellar disc.

In addition to the equatorial winds, Oe and Be stars are known to host high-velocity polar winds. These polar winds are typically of lower density than the equatorial winds and can be detected via resonance lines in the ultraviolet band. Wind from these two sources is also not typically uniform, and evidence of clumps of matter is present in observations of Oe and Be-type stars.

6.4 Pulsars

Pulsars are a type of neutron star, which themselves represent the stellar endpoint of stars with a total mass of $10 - 20$ $M_{\odot}$. Many types of pulsars exist with different properties attributed to them; these include magnetars, radio pulsars and millisecond pulsars. Though commonly found with a companion, pulsar formation is not

predicated upon being in a binary system and there exist a large number of isolated pulsars.

The supernova explosion of a massive supergiant star is preceded by the rapid compression of the star's matter, as radiation pressure becomes insufficient to halt gravitational collapse. This collapse causes a shock wave which compresses matter into the core of the star before bouncing off this core and ejecting material in the supernova. This then leaves the remnant core of compressed star matter behind. To become a neutron star, the mass of this core must exceed the Chandrasekhar limit, but not the Tolman-Oppenheimer-Volkoff limit ($1.44\ \mathrm{M}_\odot < \mathrm{M} < (2.2 - 2.9)\ \mathrm{M}_\odot$).

In a physical sense, these limits represent the force of gravity being so strong as to overcome electron degeneracy pressure, but not sufficient to exceed fermionic Pauli exclusion principles. Neutron stars are, therefore, supported from further collapse by neutron degeneracy pressure and repulsive nuclear forces. In most basic models these ultra-dense objects are constituted mainly of neutrons since the intense gravitational pressure forces the combination of protons and electrons into neutrons. The collapse of a massive supergiant star from a size of $< 30\ \mathrm{R}_\odot$ (often greatly exceeding this value at up to $500\ \mathrm{R}_\odot$) down to 10 km causes the neutron star to exhibit extreme properties. The slow rotation rate of the progenitor star is greatly increased when this collapse happens via the conservation of angular momentum. This results in an extremely rapidly spinning neutron star, with periods of $\sim$ms to s. A similar effect occurs with the magnetic field which, due to Alfvén's theorem (the conservation of magnetic flux), grows rapidly with its diminishing size.

The extreme environments embodied in neutron stars are known to accelerate particles to relativistic energies, causing neutron stars to be sites of high-energy emission. The extremely strong magnetic fields, combined with the fast rotation, result in the acceleration of particles to relativistic energies. The cascade of these particles along the magnetic field lines leads to synchrotron radiation, which is highly polarised towards the magnetic poles. This leads to strongly beamed relativistic emission from the neutron star's magnetic poles. Most often, the magnetic poles are not aligned with the rotational axis of the neutron star, thus the rapid rotation creates a lighthouse effect. Neutron stars which have beams aligning with the Earth are known as pulsars[1].

By the nature of the extreme physics that underpins them, pulsars are very enigmatic objects that are difficult to study. As such there is little total consensus on the mechanisms that underpin emission from pulsars, nor on the structure. The following section will outline a simple pulsar model along with a brief explanation of emission

[1]For the rest of this section pulsars and neutron stars will be referred to interchangeably.

and pulsar winds. The introduction given will follow sections of the theoretical overview given in [243].

6.4.1 Simple Pulsar Model

During the supernova of a massive supergiant, the sudden contraction of the star (leaving behind the core that will become the pulsar) is accompanied by a shrinking of the star's magnetic field. Accompanying this shrinking, the conservation of magnetic flux causes the magnetic field density to increase and therefore the magnetic field strength to also increase. Consequently, pulsars host among the strongest magnetic fields of any astrophysical object, with typical field strengths of $10^8 - 10^{12}$ G.

To introduce the underlying physical processes of a pulsar, the following methodology is undertaken on the assumption of a simple idealised pulsar model. In this idealised model, the pulsar behaves like a dipole that radiates as a result of the rotating magnetic field, and energy is radiated away at its magnetic poles. The main source of energy from which the pulsar generates its emission is through its rotational kinetic energy E_{rot}. The loss of this energy over time is the main engine that drives other processes, this is measured in terms of the spin-down luminosity

$$\dot{E} = \frac{\mathrm{d}E_{\text{rot}}}{\mathrm{d}T} = 4\pi^2 I \frac{\dot{P}}{P^3} \tag{6.1}$$

where

$$\dot{P} = \frac{\mathrm{d}P}{\mathrm{d}t} \tag{6.2}$$

In this equation, I (kg m^2) represents the moment of inertia of the pulsar, P (s) the rotational period and $\dot{P}$ (s^{-2}) the rate of change of the rotational period. Typically $\dot{E}$ (erg s^{-1}) has a value with an order of magnitude of $10^{35} - 10^{39}$ erg s^{-1}.

The loss of rotational energy will unavoidably cause a slowing in the rotation rate of the pulsar. Thus, at its conception, a pulsar would have had a smaller rotational period of P_0. The slowing of this rate is represented in a slowing of the angular frequency $\Omega = \frac{2\pi}{P}$. This diminution of the angular frequency is governed by a constant k and a value is known as the braking index (n) such that

$$\dot{\Omega} = -k\Omega^n \tag{6.3}$$

The value of the braking index n is assumed to be 3 in an idealised case, whereby energy is lost through magnetic dipole radiation.

The characteristic pulsar age is an estimate of the age of a pulsar; this can be derived from observables of the system (assuming a constant spin-down rate). It further allows one to relate the expressions introduced so far to measurable quantities of a system. With the assumptions of magnetic dipole radiation ($n = 3$) and that $P_0 \ll P$, the characteristic pulsar age can be derived as

$$\tau_{\mathrm{c}} = \frac{P}{(n-1)\dot{P}} \tag{6.4}$$

Using equation 6.3, the age of the pulsar can be calculated using

$$\tau = \frac{P}{(n-1)\dot{P}} \left[1 - \left(\frac{P_0}{P} \right)^{n-1} \right] \tag{6.5}$$

where τ_{c} and τ are both measured in seconds. With this expression, one can then derive the time dependency of key values of the system.

Much like the spin period, a pulsar would have started its life with a spin-down luminosity which had an initial value of $\dot{E}_0$. One can, therefore, similarly express the time evolution of the spin-down luminosity as a function of the initial spin-down time scale of the pulsar (τ_0).

$$\dot{E}(t) = \dot{E}_0 \left(1 + \frac{t}{\tau_0} \right)^{-\frac{(n+1)}{(n-1)}} \tag{6.6}$$

where

$$\tau_0 = \frac{P_0}{(n-1)\dot{P}_0} = \frac{2\tau_{\mathrm{c}}}{(n-1)} - t \tag{6.7}$$

This equation shows that the energy output of the pulsar is mathematically constant until it reaches the age τ_0. After this time the energy radiates as $\dot{E} \propto t^{-\frac{n+1}{n-1}}$. The period of the pulsar also undergoes similar evolution as

$$P = P_0 \left(1 + \frac{t}{\tau_0} \right)^{\frac{1}{n-1}} \tag{6.8}$$

which at $t \approx \tau_0$ becomes $P \propto t^{\frac{1}{n-1}}$.

Pulsar Wind

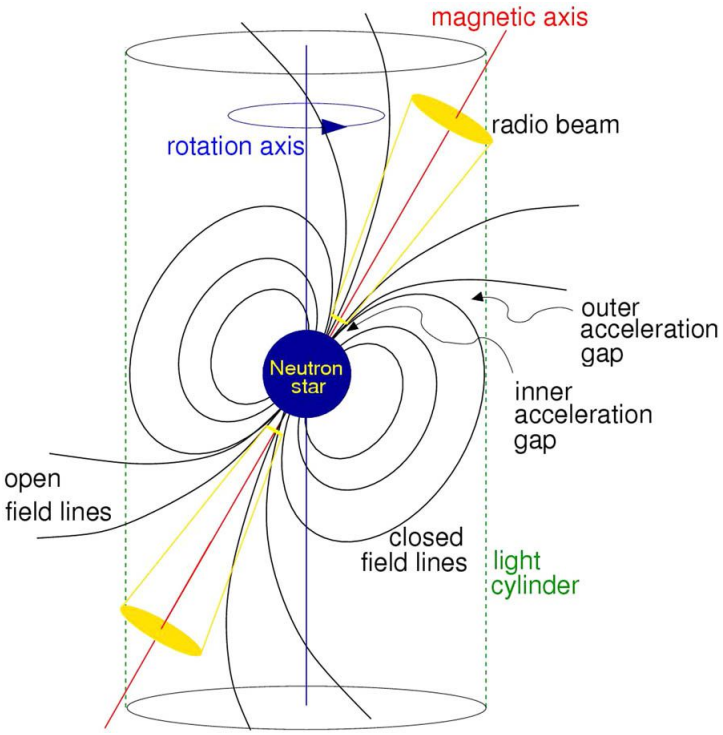

Fig. 6.2: Sketch of a pulsar displaying its key features. The neutron star is centrally located and both the closed and open magnetic field lines can be seen emanating from it. Also shown, is the rotation axis and the radio beam resultant from synchrotron emission of charged particles liberated from the surface. The figure also demarcates the light cylinder, a cylinder at which co-rotating plasma at the outermost radius is travelling at the speed of light. Image taken from [243]

As seen in the previous section a reduction in the spin velocity of the pulsar leads to the loss of energy from the system. The loss of energy from the pulsar is facilitated by the emission of particles from the pulsar's surface and their subsequent radiation of photons.

For a dipole magnetic field, the equatorial magnetic field strength at the surface is given by the equation

$$B_{\rm p} = 3.2 \times 10^{19} (P\dot{P})^{\frac{1}{2}} \ \ {\rm G} \tag{6.9}$$

for millisecond pulsars this can reach values of $> \ 10^{15}$ G.

Figure 6.2, shows a rudimentary diagram of the basic features of a pulsar, including the light cylinder. The intense magnetic fields of a pulsar ensure that any plasma in the immediate vicinity of the neutron star will co-rotate. However, at increasing radii, plasma must rotate with increasing velocity. At sufficiently large radii the

plasma can no longer co-rotate with the pulsar as it has reached the speed of light. The radius at which this happens is $R_{\rm LC} = \frac{\Omega}{c}$, where c (m s^{-1}) is the speed of light and $R_{\rm LC}$ (m) is the light cylinder radius. Extrapolating this radius around the rotational axis of the pulsar we obtain the light-cylinder. Within this cylinder, the magnetic field is primarily dipolar. As seen in Fig. 6.2, field lines emanating from the polar regions cross this light cylinder and remain open, formally violating Maxwellian electrodynamics.

In a simplified model the extremely rapid rotation of the pulsar's magnetic field, through the conductive medium of the plasma around it, sets up a potential between the surface of the pulsar and its outer regions. The strength of this potential is extremely large ($\sim 10^{15}$ to 10^{16} V) and is thought to be sufficient to tear away electrons from the surface of the star, immediately accelerating them to ultra-relativistic energies. The strength of the magnetic field, however, necessitates that the freed electron (in most cases) must move along the field lines. Of course, the movement of such a high-energy charged particle in a magnetic field releases synchrotron radiation, and the photons emitted will themselves also be of ultra-relativistic energies. This results in the near-immediate pair production of an electron-positron pair. The newly produced pair now themselves undergo the same process (with positrons moving in the opposite direction), forming a cascade of emission. The light produced here is highly polarised by the strong magnetic field resulting in the formation of beams.

Eventually, the number of charges will result in the collapse of the potential. With no potential, the particles in the magnetosphere are ejected into the surrounding region of the pulsar at relativistic speeds forming the pulsar wind. This causes the potential to re-establish repeating the process. Additionally, particles following open magnetic field lines near the poles will be ejected.

Material near the pulsar will also be accelerated away at extremely-high energies. Thus, the acceleration and ejection of particles from both the pulsar and its surrounding region form a powerful wind streaming outward. The collision of this relativistic wind with nearby ambient media forms a pulsar wind nebula (see [244] for a review).

6.5 Particle Acceleration

In order to produce the TeV gamma-ray flux observed in astrophysical systems, particles must first be accelerated to extremely-high energies before undergoing

non-thermal radiative interactions. The spectrum of cosmic rays seen on Earth implies a plethora of differing acceleration mechanisms spanning a large energy range and facilitating the spectrum seen in 5.2 (see Sec. 5.2 for further details). In the context of gamma-ray binaries, shock front processes and diffusion are the most commonly cited methods of particle acceleration. The following sections will focus on acceleration mechanisms pertinent to gamma-ray binaries, however, for a full and detailed overview of astrophysical acceleration mechanisms see [245] [232].

6.5.1 Fermi Acceleration

Fermi acceleration, named after Enrico Fermi who first postulated the theory [246], is an acceleration mechanism in which charged particles gain energy from an environment through repeated reflection. Originally, the mechanism was derived in order to explain the power-law spectrum of cosmic rays on Earth. Two orders of Fermi acceleration exist depending on the acceleration site: first-order (occurring in shock fronts) and second-order (occurring in fast-moving magnetised gas clouds). In both these cases, the environment is collisionless as charged particles can only undergo Fermi acceleration if they have energies far greater than the thermal energies of the environment (as collisions will cause high-energy losses in particles).

Second-order Fermi Acceleration

The original mechanism proposed by Fermi involved particle acceleration in a highly magnetised cloud of velocity v. An incident particle to the cloud will enter and diffuse through a random-walk path, dictated by elastic scattering off the highly turbulent magnetic fields within the cloud. These scatterings have a distribution of interaction directions with respect to the velocity of the cloud. Scattering will therefore lead to a gain in energy (for interactions head-on to the cloud's motion) or a loss of energy (for interactions tail-on to the cloud's motion) proportional to $(\frac{v}{c})^2$. A schematic diagram of this is seen in Fig.6.3. Head-on collisions are on average the more likely interaction leading to a net gain in particle energy through this mechanism. The overall energy gain of a particle is

$$\left\langle \frac{\delta E}{E} \right\rangle = \frac{8}{3}\left(\frac{v}{c}\right)^2 \tag{6.10}$$

which is derived from the consideration of both reference frames and the transformation between them [246] [232]. While the model is theoretically sound, the

frequency of interactions with these clouds is rare and their average velocities are low, meaning it is unlikely to produce the majority of cosmic rays. Moreover, having originally set out to explain the observed power-law spectrum of cosmic rays, this process offers no physical reasoning as to why a power law of a similar index to the one observed would be produced.

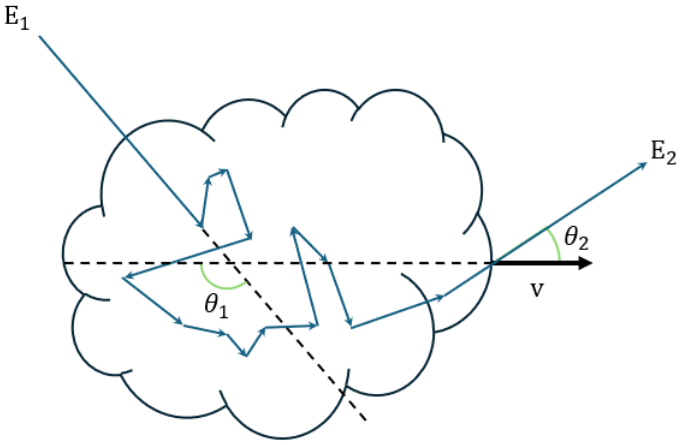

Fig. 6.3: Diagram demonstrating the principle of second-order Fermi acceleration. Here the cloud moves with velocity v, and a particle enters with energy E_1 at an angle of θ_1 to the direction of the cloud's motion. The particle will undergo a random walk within the cloud, gaining energy from head-on collisions. The particle will then leave with an energy E_2, at an angle of θ_2 to the direction of the cloud's motion. Figure adapted from [212]

First-order Fermi Acceleration

First-order Fermi acceleration, also called diffusive shock acceleration, is the primary acceleration mechanism of particles at shock boundaries. A shock propagating through a medium with velocity v, a speed greater than the upstream sound speed, will act as a site of acceleration as particles are able to repeatedly cross the shock front and extract energy with each crossing. First-order Fermi acceleration occurs in non-relativistic shocks where the extent of the shock front s is negligible when compared to the Larmor radius of the accelerated particles r_g (also referred to as the radius of gyration).

A shock itself is a discontinuity in the measurable variables of the local medium. It represents the point at which the temperature, pressure, density and velocity between the upstream (unshocked media into which the shock is propagating) and downstream (shocked media through which the shock has propagated) media

discontinuously change. From these two perspectives, as well as the reference frame of the shock itself, the process can be deconstructed. In the frame of the shock at velocity v (m s^{-1}), upstream material approaches at $v_{\rm u} = v$ and the downstream recedes at $v_{\rm d}$. These velocities are related to the upstream and downstream density ($\rho_{\rm u}$ and $\rho_{\rm d}$ respectively, kg m^{-3}) via the continuity equation.

$$v_{\rm u}\rho_{\rm u} = v_{\rm d}\rho_{\rm d} \tag{6.11}$$

For an ideal gas, one can express this ratio in terms of a compression factor, which for a strong shock is

$$\text{Compression Ratio} = \frac{\rho_{\rm d}}{\rho_{\rm u}} = \frac{\Gamma + 1}{\Gamma - 1} = 4 \tag{6.12}$$

where the adiabatic index of an ideal gas ($\Gamma = \frac{5}{3}$) has been substituted. Substituting this into Eq.6.11, results in $v_{\rm d} = \frac{1}{4}v_{\rm u}$ which in turn implies $v_{\rm d} = \frac{1}{4}v$.

In the upstream frame, the shock approaches with velocity v and the downstream media therefore approaches with velocity $\frac{3}{4}v$. Vice-versa, from the perspective of downstream the shock recedes at $\frac{1}{4}v$ and the upstream approaches with $\frac{3}{4}v$. A particle that is in equilibrium with its surrounding media will, therefore, gain energy upon crossing the shock front (in either direction) and undergoing multiple reflections by the magnetic fields of the new region. This can be demonstrated by considering a particle in the upstream medium in equilibrium with the isotropic distribution of upstream particles. As the shock passes through its vicinity it will cross the shock front into the downstream and gain an energy of $\frac{\Delta E}{E} \propto \frac{v}{c}$. Fluctuations in the downstream magnetic field will then cause the particle to scatter in a random walk until it reaches equilibrium with the velocity of the downstream material. The particle will then (once again) cross the shock front, now into the upstream, gaining energy. After this, the particle will continue a random walk, either once again gaining isotropic velocity to the local medium and repeating the cycle, or escaping the shock region. For a relativistic particle with initial energy E_0, the energy gain for a single cycle can be expressed as

$$\frac{\Delta E}{E} = \beta - 1 = \frac{4}{3}\frac{(v_{\rm u} - v_{\rm d})}{c} \tag{6.13}$$

where $\beta = \frac{E}{E_0}$. It therefore follows that for n cycles, a particle will have an energy of $E = \beta^n E_0$.

The probability at which a particle will escape the system is $P_{\rm esc} = \frac{v}{c}$ it, therefore, follows that the probability that the particle will remain in the system is $P = 1 - P_{\rm esc}$.

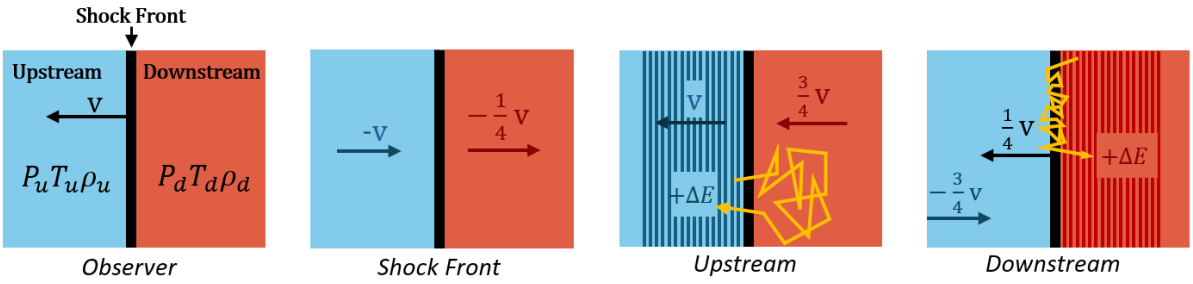

Fig. 6.4: A series of diagrams depicting the process of diffusive shock acceleration from different reference frames (with the reference frame written under each respective image). In each image, the blue region denotes the upstream and the red region denotes the downstream, while the central black line indicates the shock front. Parallel coloured lines indicate magnetic fields in the region of the respective colour, while orange lines indicate the path taken by a particle travelling between the two regions. From the frame of the observer (far left), the shock is moving with velocity v. In the reference frame of the shock front however (centre left), the upstream approaches with a velocity of v, while it sees the downstream recede at $-\frac{1}{4}v$. In the upstream frame of reference (centre right), the downstream approaches at $\frac{3}{4}v$. By entering the downstream, particles can scatter and become isotropic before returning to the upstream with an energy gain of ΔE. Finally in the downstream frame of reference (far right), the upstream is seen to approach with velocity $\frac{3}{4}v$, thus particles crossing the shock front can similarly extract an energy of ΔE from the upstream.

Similarly to the case of the energy gain, for an initial particle population of N_0 and n cycles, the number of particles remaining in the system with an energy of E or higher will be $N = N_0 P^n$. The differential energy spectrum of the system's particles is therefore

$$\frac{\mathrm{d}N}{\mathrm{d}E}\mathrm{d}E \propto E^{\frac{\ln(P)}{\ln(\beta)}-1}\mathrm{d}E \tag{6.14}$$

which for an ideal gas yields a power law of index 2. For this reason, first-order Fermi acceleration results naturally in the production of the observed cosmic ray power-law spectrum[2] as seen on Earth.

6.6 Particle Diffusion

The process underpinning and enabling both of the previously detailed acceleration mechanisms is diffusive propagation. Diffusive propagation represents particle transfer, which is achieved in first and second-order Fermi acceleration by the scattering of particles off magnetic fields. Diffusion is therefore related to the average magnetic field strength B (G). Given that turbulence in magnetic fields

[2]Though notable variations to the power-law index exist at key points within the SED, see Sec.5.2.

provides sites for charged particle scattering, diffusion is additionally related to the turbulence of a magnetic field δB providing that the turbulence occurs on relevant particle scales (typically the Larmor radius). These factors are related by the diffusion coefficient D ($\mathrm{m}^2\ \mathrm{s}^{-1}$), which is a measure of diffusion in a given magnetic field.

Commonly, astrophysical diffusive shocks are assumed to be in the Bohm-regime and therefore undergo Bohm Diffusion [247]. Here it is assumed that the relativistic particles involved have a mean free path similar to their Larmor radius. In this case, the diffusion coefficient can be approximated as

$$D_{\mathrm{Bohm}} = \frac{1}{16}\frac{k_{\mathrm{B}}T}{eB} \approx \eta\,\frac{cR_{\mathrm{l}}}{3} \tag{6.15}$$

where k_{B} ($\mathrm{J\ K}^{-1}$) is the Boltzmann constant, T (K) the plasma temperature, e (C) the electron charge and B (T) the magnetic field strength. Additionally, R_{l} (m) is the Larmor/gyro radius, c (ms^{-1}) the speed of light and $\eta = (\frac{\delta B}{B})^{-2}$. This equation reaches its limit where $\eta = 1$, referred to as the Bohm limit, where the speed of diffusion reaches its lowest possible value.

6.7 Non-thermal Radiation

Particles accelerated at astrophysical sites can undergo numerous processes through which their energy is reduced. Crucially, many of these processes result in the production of non-thermal radiation, emission produced by interactions unrelated to thermal processes. The non-thermal emission produced by a particle is directly proportional to its total energy, therefore, VHE gamma rays (such as those detected by IACTs) are indicative of extremely energetic particle populations and acceleration sites. Whilst non-thermal emission exists across the EM spectrum, this thesis will focus on processes resulting in the production of gamma rays.

High-energy particles interacting with ambient matter, local EM fields or photon fields, can undergo radiative losses via the production of photons in a number of processes. These processes fall into two distinct groups depending on the particle involved in the interaction, leptonic emission and hadronic emission.

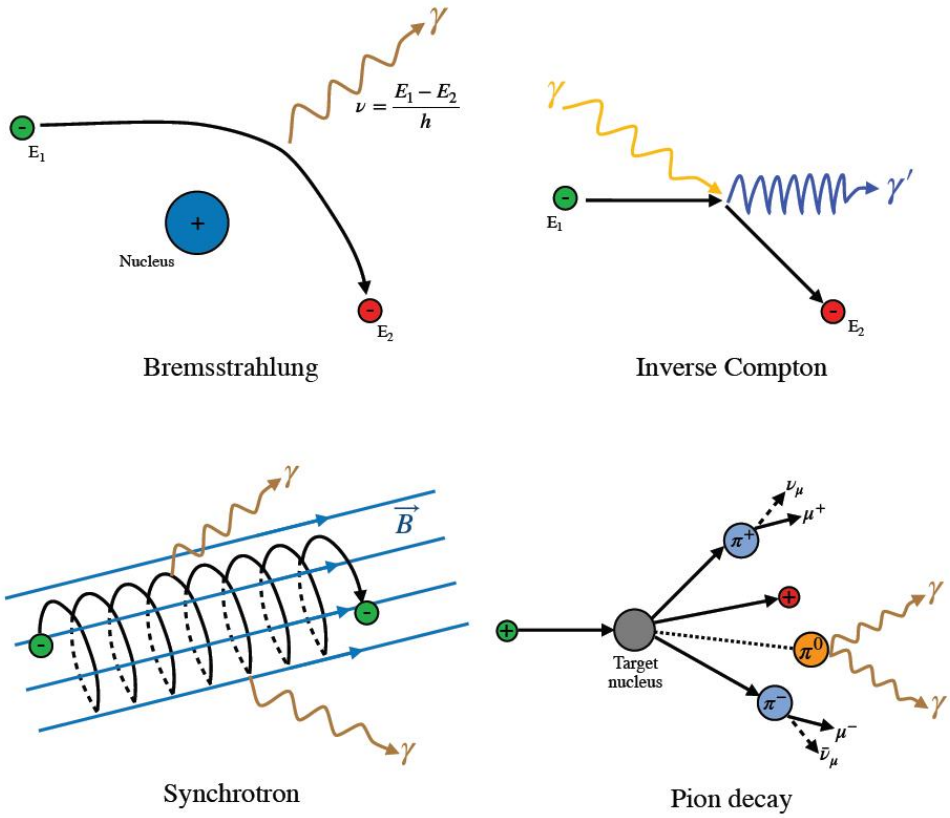

Fig. 6.5: Figure displaying possible radiative emission processes. Inverse Compton scattering, synchrotron emission and bremsstrahlung all represent leptonic emission mechanisms, while pion decay is a hadronic process. Figure taken from [248].

6.7.1 Hadronic Gamma-ray Emission

The acceleration of hadrons can lead to detectable gamma-ray emission through interactions with other particles in the vicinity. Protons and heavier nuclei, having attained high energies at acceleration sites, can undergo radiative losses through the production of neutral pions via interactions with nearby matter and photon fields. Shock fronts and other astrophysical acceleration sites are often naturally situated in the vicinity of these, making hadronic emission very probable. The interaction of protons with ambient matter or photons leads to the following processes

$$\mathrm{pp} \longrightarrow \sum \pi^{\pm,0} \tag{6.16}$$

$$\mathrm{p}\gamma \longrightarrow \begin{cases} \Delta^+ \longrightarrow \mathrm{p}\pi^0 \\ \Delta^+ \longrightarrow \mathrm{n}\pi^+ \\ \sum \pi^{\pm,0} \end{cases} \tag{6.17}$$

where the production of pions occurs through every channel. After production, pions will soon decay. For charged pions the most likely decay process is

$$\pi^{\pm} \longrightarrow \mu^{\pm} + \nu_{\mu} \longrightarrow (e^{\pm} + \nu_{e} + \nu_{\mu})\nu_{\mu} \tag{6.18}$$

and critically, for neutral pions, the overwhelmingly likely decay follows the form

$$\pi^{0} \longrightarrow \gamma\gamma \tag{6.19}$$

Which is the channel responsible for the production of hadronic gamma-ray emission. To kinematically enable this interaction, a proton energy of $E_{\mathrm{p}} \approx 280$ MeV is required [232]. To a good approximation, pp interactions result in $\sim 50\%$ of the energy being carried off by the leading nucleon, leaving only half of the energy available for pion production. This, combined with the fact that the remaining energy is shared equally by the production of either one of the two charged pions or a neutral pion, means that the resultant gamma rays have only $\frac{1}{6}E_{\mathrm{p}}$. A diagram of this process can be seen in Fig. 6.5.

This emission results in the characteristic "pion bump" in the SED of hadronic emission spectra (see Fig. 6.6). This feature is a characteristic symmetrical bump in the spectrum, where the energy range it covers is proportional to the energy spectrum of the primary hadrons.

6.7.2 Leptonic Gamma-ray Emission

Relativistic leptons, most commonly electrons, undergo radiative losses via three processes: Inverse Compton (IC) scattering, synchrotron radiation and bremsstrahlung.

Inverse Compton Scattering

IC scattering is broadly defined as a process in which an ambient photon is up-scattered by a relativistic electron, as shown in Fig. 6.5. The subsequent inelastic scattering of the photon involves a transfer of energy and momentum causing the ambient photon to gain large amounts of energy [250]. This high-energy photon then radiates away from the system allowing for its subsequent detection. The process takes its name from being the inverse of the groundbreaking mechanism proposed by Arthur Compton whereby a photon could up-scatter an electron [251].

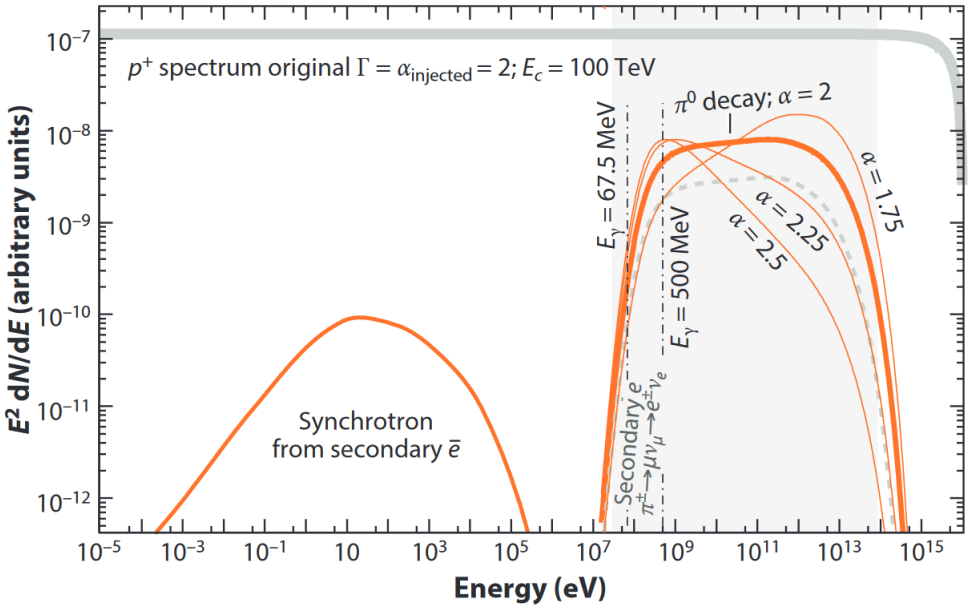

Fig. 6.6: The spectral energy distribution of gamma rays resulting from the hadronic interactions of an injected spectrum of protons (injected with a power-law index of 2 and a cutoff at 100 TeV) with the ISM. The resultant gamma-ray emission is marked by the orange curves, while the grey-shaded region denotes the sensitivity range of current gamma-ray detectors. This gamma-ray emission is dominated by neutral pion decay and, as such, the so-called "pion bump" (characterised by a steep spectral rise, plateau, and a sharp fall) is clearly visible in the right-hand feature. Also visible in the left-hand feature is the synchrotron emission of secondary electrons. Secondary electrons are produced from the inelastic collisions of two protons. For the synchrotron emission, a magnetic field of $B = 30$ μG has been assumed. Figure taken from [249].

In the case of IC, both relativistic electrons and a target field of low-energy photons are required to enable the up-scattering. Typically, the photon field is provided by ambient photons in the CMB, stellar photons, or infrared radiation from ISM dust emission. Depending on the energy of the photon (E_γ, eV) in the rest frame of the electron (with energy E_e, eV), there are two distinct physical regimes in which IC operates.

Thomson scattering is the dominant effect that applies when the equality $4E_\gamma E_e \ll m_e c^2$ holds. Particles undergoing IC via Thomson scattering mostly scatter elastically, meaning that the transfer of energy is minimal. Scattering is here defined by the Thomson cross section, σ_{T} (m^2)

$$\sigma_{\text{T}} = \frac{8\pi}{3}\left(\frac{e^2}{m_e c^2}\right)^2 \tag{6.20}$$

where m_e (kg) is the mass of the electron. Electrons undergoing Thomson scattering have an associated energy loss rate of $\dot{E}_{\rm Thom} \propto E_e^2$.

At sufficient photon and electron energies ($4E_\gamma E_e \gg m_e c^2$) the interaction will transition into the Klein-Nishina regime. Contrary to Thomson scattering, Quantum Electrodynamics (QED) corrections become non-negligible in this regime, requiring a more rigorous approach to the calculation of the cross section [252]. The resultant scattering between the electrons and ambient photons is far more inelastic leading to a larger transfer of energy. This will lead to an energy loss rate of $\dot{E}_{\rm KN} \propto \ln E_e$.

The transition between these two regimes naturally leads to a characteristic break in the SED of any population undergoing this change. Following the formalism of [253], for an electron population with an energy spectrum following a power law of $\frac{{\rm d}N}{{\rm d}E} \propto E^{-\alpha}$ the spectral index Γ will be

$$\Gamma_{\rm Thom} = \frac{\alpha + 1}{2} \tag{6.21}$$

$$\Gamma_{\rm KN} = \alpha + 1 \tag{6.22}$$

Thus, even for an injected spectrum following a power law, the transition between the two regimes will unavoidably lead to a discontinuity in the spectrum as it softens.

As demonstrated in [254] the energy peak for each regime can be calculated. Given a black body photon field, the energy of the photons can be approximated as $E_\gamma = 2.8\, k_{\rm B} T$ where T (K) is the black body temperature and $k_{\rm B}$ (J K^{-1}) is the Boltzmann constant. The spectral peak of gamma rays produced from IC is therefore

$$E_{\gamma,{\rm Thom}}^{\rm peak} \approx 33 E_e^2 k_{\rm B} T_e \tag{6.23}$$

$$E_{\gamma,{\rm KN}}^{\rm peak} \approx E_e \tag{6.24}$$

Bremsstrahlung

The deceleration of a charged particle within an electric field results in the emission of the lost kinetic energy as electromagnetic radiation, ensuring the conservation of energy [253]. This process is bremsstrahlung[3], and most commonly occurs astrophysically when an electron is deflected by a nearby atomic nucleus (a diagram of this process can be seen in Fig. 6.5). Because the rate of emission is directly proportional to the density of the target material and primary electron energy, VHE

[3] Literally "braking-radiation" from the German "bremsen" – to brake, and "Strahlung" – radiation

emission via bremsstrahlung necessitates both an acceleration site and a high-density region. VHE emission from bremsstrahlung is therefore not typically a dominant or detectable effect outside of extremely dense regions.

Synchrotron Radiation

Charged particles that are accelerated perpendicular to their velocity emit electromagnetic radiation known as synchrotron radiation. This usually occurs in astrophysical sources whereby a population of high-energy electrons enter a region of high magnetic field strength. These electrons are deflected by the magnetic field, taking a new helical trajectory parallel to the magnetic field lines as shown in Fig. 6.5. This deflection results in a loss of kinetic energy, which is re-emitted as synchrotron radiation via the conservation of energy. The energy of a synchrotron photon, naturally, depends on the strength of the magnetic field (B) as well as the energy of the incident charged particle. For a population of mono-energetic electrons with an isotropic distribution of pitch angles the energy of a synchrotron photon is given by [249]

$$E_{\text{sync}} = 0.2 \frac{B}{10\ \mu\text{G}} \left(\frac{E_e}{1\ \text{TeV}} \right)^3\ \text{eV} \tag{6.25}$$

Although this process can occur with any charged particle, the dependence of the energy loss rate on m^{-4} dictates that synchrotron emission for protons is extremely suppressed when compared to electrons. A characteristic synchrotron bump in the SED (combined with an IC bump at higher energies) is therefore highly indicative of a high-energy electron population. Where, for an injected population of electrons described by $\frac{\mathrm{d}N}{\mathrm{d}E} \sim E^{-\alpha}$, the synchrotron emission will follow a power law of spectral index $\Gamma = \frac{\alpha+1}{2}$ [253]. A characteristic SED of synchrotron emission is shown in Fig. 6.7.

6.8 PSR J2032+4127

PSR J2032+4127 is an example of a long-period gamma-ray binary system that shares many properties with PSR B1259-63/LS 2883. Additionally, it is one of the three gamma-ray binary systems in which the compact object has been identified as a pulsar. This makes it a prime candidate for the study of non-thermal emission in gamma-ray binaries and for the modelling of such systems. The source was first discovered when pulsed emission was detected from PSR J2032+4127 at GeV energies by *Fermi-LAT* [239]. Subsequent radio observations confirmed the nature

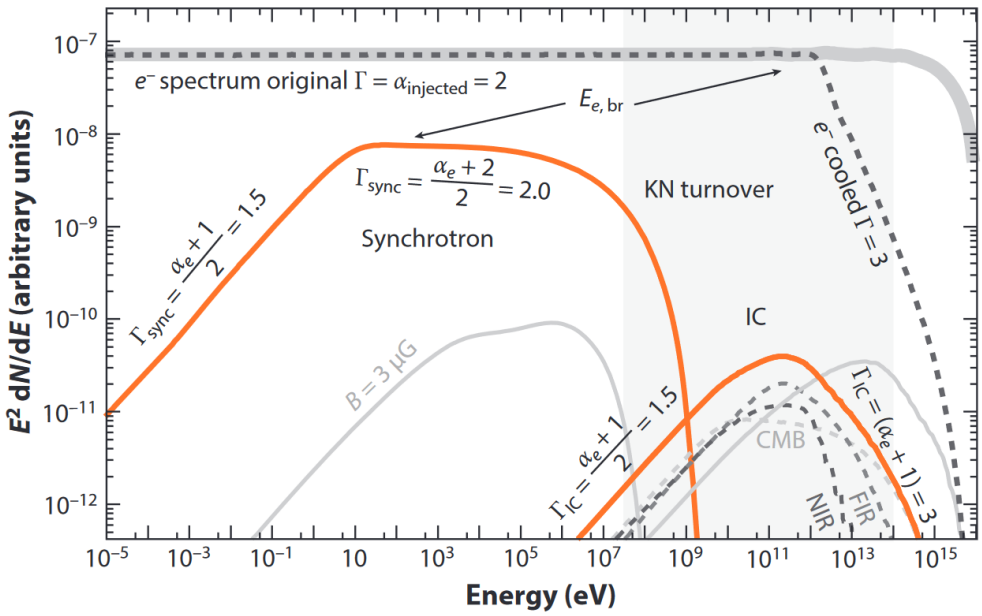

Fig. 6.7: A simulated SED for a population of electrons injected with a spectral slope of $\alpha = 2.0$ (light grey) at a typical galactic source ($t_{age} = 1000$ years, $B = 100$ μG). The SED is denoted here by the orange line. Additionally, the state including cooling is shown via the dashed grey line. The figure displays the characteristic leptonic emission profiles from synchrotron and Inverse Compton emission. Of additional note is the drop in the various elements of the SED around the energies at which Klein-Nishina cooling occurs due to the high-energy loss of the electrons in this regime. The shaded grey band denotes the energy range of contemporary gamma-ray telescopes. Figure taken from [249].

of the object as a ~ 143 ms gamma-ray pulsar. PSR J2032+4127 was originally thought to be an isolated pulsar [255], but further observations of the source in the radio regime detected a rapid acceleration in the spin-down rate of the pulsar. This evidence confirmed that the pulsar was not in fact isolated and was rather almost certainly a member of a binary with a highly eccentric orbit. Subsequent observations confirmed that the pulsar was indeed in an eccentric orbit ($e = 0.961$) around the Be star MT91 213 (also known to host a decretion disc) [256], with a separation of ~ 1 au at periastron [257]. The orbital period of the system is, however, much larger than that of PSR B1259-63/LS 2883, with a period in the range of $16,000$ to $17,670$ days (~ 43.8 to 48.4 years) [258]. The extensive period of the system provides limited opportunity to monitor its periastron passages. However, somewhat serendipitously, the latest periastron of the system occurred in November of 2017 ($t_{\rm p} = $ MJD 58069 days [258]) allowing observations of the system spanning the electromagnetic spectrum. X-ray observations of the system confirmed a strong brightening of the source in X-rays as it approached periastron, with the source in

2016 being reported as 20 times brighter than in 2010 [258]. In a similar manner to that of PSR B1259-63/LS 2883, this brightening is thought to be connected to the pulsar wind colliding with an increasing density of wind emanating from the Be star.

Around the periastron passage, the system displays some interesting non-thermal emission in X-rays. While an increasing level of flux is seen on the approach to periastron, this peaks at $t_{\rm p} - 20$ days[4] before a dip at periastron is observed. This is followed by a sharp rise to a second peak at $t_{\rm p} + 10$ days and a gradual drop off (see Fig. 6.8). This behaviour is mimicked in the spectral index of the X-ray emission, as well as in the equivalent width of the optical observations. This drop in flux is sometimes attributed to the geometry of the system with respect to the Earth and its inclination angle. However, most commonly it is thought to be a result of the pulsar either leaving the disc briefly or entering a sparser region causing a drop in the synchrotron emission responsible for the X-ray flux. Interestingly though, this feature of a double peak in the X-ray flux profile is also present in other gamma-ray binaries [257]. As opposed to the dynamic spectral and flux behaviour seen at X-ray energies, the periastron passage in the GeV band is marked by a constant and stable flux and spectral index before, during and after the periastron passage [259].

During the periastron passage, significant VHE emission was detected in the TeV band with VERITAS and MAGIC, leading to the detection of PSR J2032+4127 as a point source at these energies [260]. The TeV light curve (though with somewhat sparse sampling), seen in Fig. 6.8, showed a base level of VHE flux building to a peak at periastron in TeV. Following this the flux levels dropped down once again to the baseline level of emission [260]. The spectral behaviour of the source at these energies also displayed a preference for a power law during the periastron passage, with times prior to this displaying a preference for a cut-off power law. The spectra derived from the MAGIC and VERITAS observations are displayed in Fig. 6.9.

The TeV emission is most commonly attributed to the interaction of electrons in the termination shock between the stellar wind and the pulsar wind and corresponds to the IC emission of the same electron population responsible for the synchrotron emission seen in X-rays.

[4]Where $t_{\rm p}$ is the time of periastron.

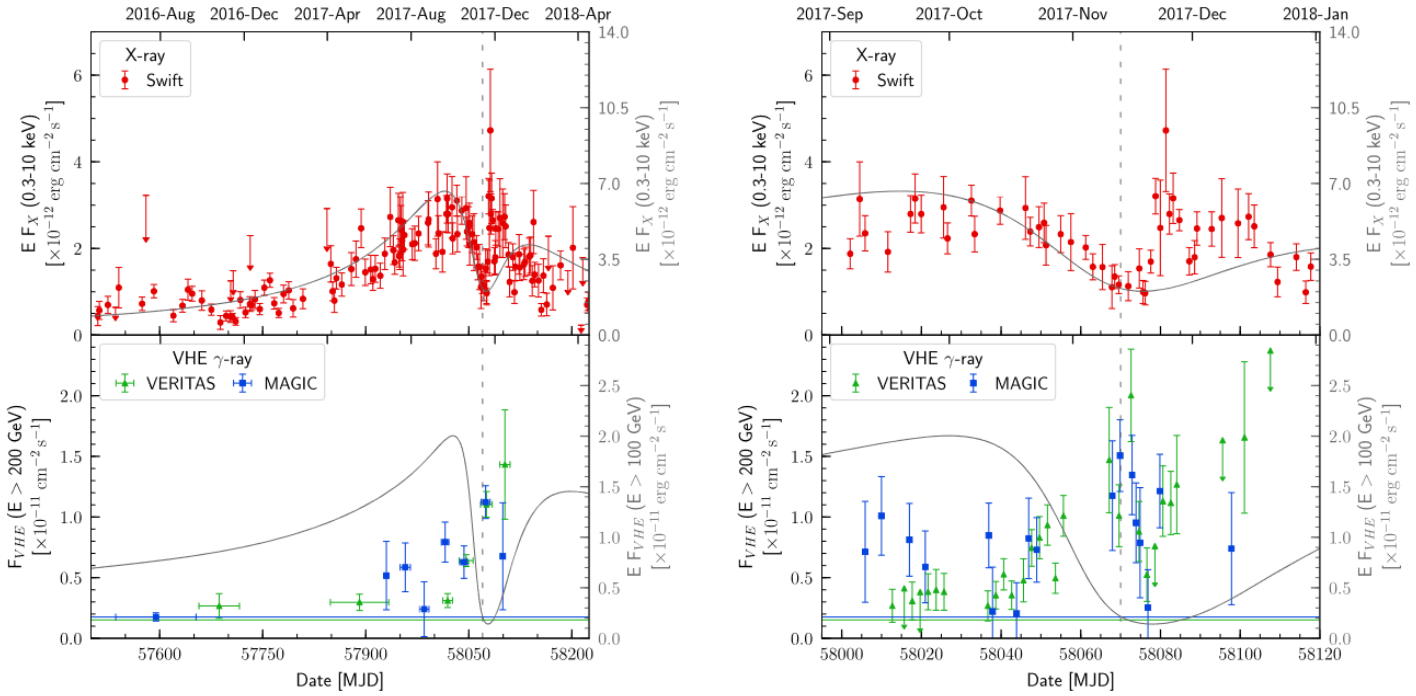

(a) Full Dataset

(b) Periastron

Fig. 6.8: This figure displays two different time resolutions of the X-ray energy-flux light curve ($0.3-10.0$ keV, top) and the VHE photon-flux light curve (> 200 GeV, bottom) of the 2017 periastron passage of PSR J2032+4127/MT91 213. The left-hand set of figures shows the full data set, whereas the right-hand set of figures shows exclusively the months around periastron. Red circles indicate Swift-XRT points (where observations of a duration of less than 1.4 ks are omitted), blue squares show MAGIC flux points and green triangles represent VERITAS flux points. The solid coloured lines in the VHE portion of the light curves represent the average flux levels in years prior to 2017 for each array. Solid grey lines indicate the predicted flux profile from modelling, and the dashed grey line shows the point of periastron. Figure taken from [260].

6.9 LS I +61° 303

Of the three gamma-ray binary systems with identified companions, LS I +61° 303 is the system in which the compact object has most recently been categorised. LS I +61° 303 was detected as a periodic radio source in the early 1980s [261], however, it was not detected in the VHE band until 2005/2006 [262]. Despite a historical catalogue of observations of the source, it was not possible to discern the nature of the companion until recently. Contemporary observations of the source with Five-hundred-meter Aperture Spherical radio Telescope (FAST), however, revealed transient radio pulsations (at a significance of $> 20\ \sigma$) of period $P =$

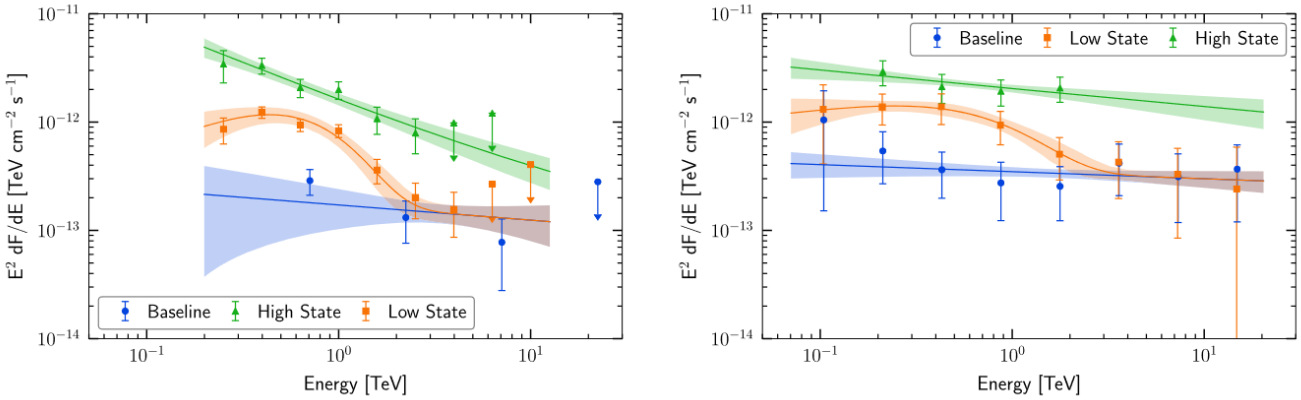

Fig. 6.9: The spectral energy distributions of the 2017 periastron passage of PSR J2032+4127/MT91 213, as recorded by the VERITAS (left) and MAGIC (right) arrays. To create the different spectra the arrays have binned the data into three different time periods. The baseline data (blue) represents the spectrum of data from prior to 2017, in which only baseline TeV emission was detected. The low state (orange) encompasses the time period in 2017 prior to the periastron passage (MJD 57928–58056 days). Finally, the high state is defined as periods around the periastron passage during which the TeV flux was greater than 1×10^{-11} cm^{-2} s^{-1} (MJD 58057–58074 days and 58080–58110 days). As can be seen, the high flux state is preferentially fit with a power-law model, whereas the low flux flux state is preferentially fit with a cut-off power law. Figure taken from [260], see citation for further details on the spectral properties of the system.

269.15508 ± 0.00016 ms for the first time, confirming the companion as a pulsar [240].

This (long suspected) pulsar is a member of a binary system and is, once again, in an eccentric ($e = 0.55$-0.72) orbit around a large, rapidly rotating star. Through 20 years worth of radio data, the system's period has been calculated at $P = 26.496$ days, making it the gamma-ray binary with the shortest period among those with confirmed compact objects [263] [264] [265]. The optical companion is a B0Ve star, which undergoes mass loss via equatorial winds, acquiring an equatorial decretion disc [263].

As is characteristic of gamma-ray binary systems LS I +61° 303 is host to a range of non-thermal emission around its periastron passage, spanning many wavelengths. Due to the shorter orbital period of the system, units of orbital phase are used preferentially over time from periastron. Phase $\Phi = 0$ was set at Julian Date 2443366.775 days [261] [266]. The periastron passage itself is thought to be in the range of $\Phi_{\rm p} = 0.2 - 0.5$ [263]. This value was later constrained to be $\Phi_{\rm p} = 0.23$ (with apastron at $\Phi_{\rm p} = 0.73$) [267]. More recent studies of the orbital parameters, on the other hand, cast this result into contention. The study outlined in [268],

concludes that the orbit has a far lower eccentricity than previously thought and is in fact nearly circular ($e < 0.15$). This study also concluded that the periastron is at $\Phi_{\rm p} = 0.6$, a result which would better match the observed emission.

In the radio band, a regular and intense radio flux outburst is seen at $\Phi = 0.6$, thought to be attributed to interactions of the pulsar wind with the decretion disc [269]. In addition to this emission, low-intensity outbursts are often detected at phases of $\Phi = 0.45 - 0.95$. These are thought to originate from interactions of the pulsar wind with ejected/disrupted material from the stellar disc [266] [264] [265]. The comparison of these radio outbursts to the periastron passage phases of this system leads to one of the major unknowns of the system, in that it is unclear as to why the radio outbursts appear to occur away from the periastron passage. Alternatively, this could be a result of an incorrect value of the periastron phase, and when adopting the periastron orbital phase of the more recent study ([268]), the emission corresponds well.

Periodic emission from the source is also detected in X-rays with a periodicity of $P = 26.7 \pm 0.2$ days [270]. This period clearly coincides with that of the radio emission [269] and repeatedly occurs in the orbital phase period $\Phi = 0.44 - 0.47$. What is curious about the X-ray emission from the source is that it is offset from the radio emission by several days, with no clear explanation as to why.

The GeV emission from the source is once again repeatedly seen in the orbital cycle. However, as opposed to the radio, X-ray and TeV emission which all occur around $\Phi \approx 0.6$ the GeV emission occurs at $\Phi = 0.25$ and is thus anti-correlated. The GeV spectrum is best described by a cut-off power law, featuring an exponential cutoff at 3.9 GeV.

Finally, the VHE emission follows a similar trend to the X-ray and radio flux, demonstrating a peak at around $\Phi = 0.6$. The singular VHE peak is seen repeatedly at this orbital phase and has been observed using the VERITAS array. The most recent VHE study of this object utilised upwards of 150 hours of VERITAS data and detected periodic behaviour of the source at TeV energies, as seen in Fig. 6.10. This study also concluded that the SED was best fit by a power-law model with a best fit spectral index value of $\Gamma = -2.55 \pm 0.05$ [271].

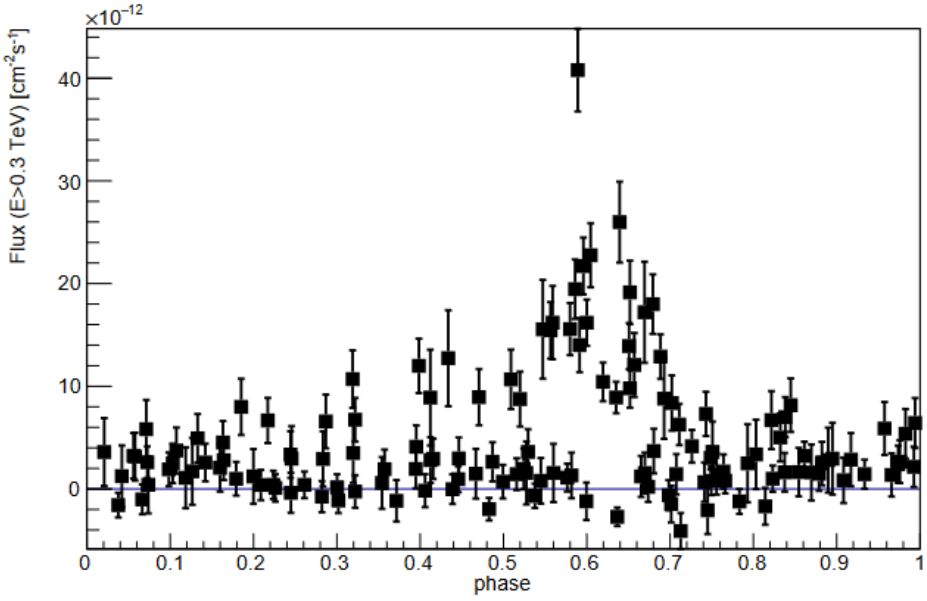

Fig. 6.10: The VHE light curve of the gamma-ray binary LS I +61° 303, comprising 163 hours of VERITAS data. The points displayed are binned by night. The figure begins at MJD 43366.8 days and assumes an orbital period of 26.496 days. Figure taken from [271].

6.10 PSR B1259-63/LS 2883

Discovered in 1992 during a radio survey conducting a search for nearby pulsars [238], PSR B1259-63/LS 2883 (PSR B1259-63) is a gamma-ray binary system consisting of a non-accreting pulsar in an eccentric orbit around an O9.5Ve type[5] star [238]. At the time of writing, it is one of three gamma-ray binary systems, alongside PSR J2032+4127 and LS I+61 303 [239, 240], where the companion has been confirmed as a neutron star[6]. PSR B1259-63 is uniquely positioned both as a member of a novel category of objects and as having a well-identified companion. It is therefore imperative for study to further the understanding of gamma-ray binary systems, and the physical processes involved in HE and VHE emission (such as IC emission and γ–γ absorption, see [274] for example).

[5]LS 2883 is nominally an O-type star, however Oe and Be stars are frequently grouped together as Be stars due to their similar properties [272]. For this reason, one may see LS 2883 referred to as a Be-type star in literature.

[6]The gamma-ray binary LS 5039, has also recently been tentatively suggested as hosting a pulsar due to the claimed detection of hard X-ray pulsations [273].

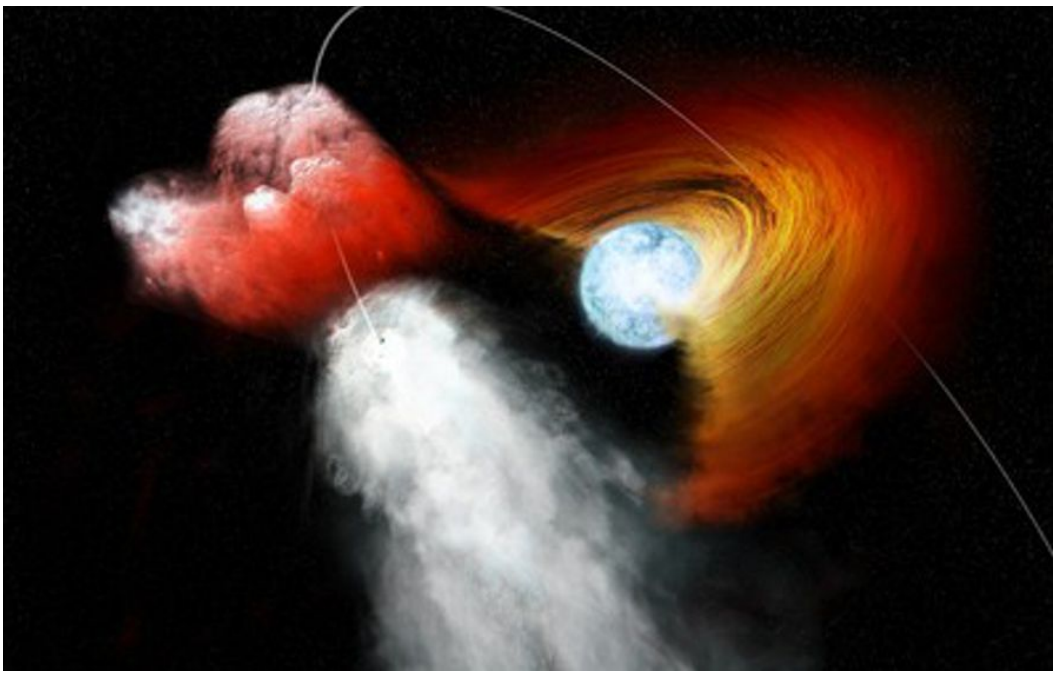

Fig. 6.11: Artist's impression of the periastron passage of gamma-ray binary system. Here, the pulsar is seen crossing the decretion disc of the star, disrupting the disc material. Image credit: NASA/CXC/M.Weiss.

6.10.1 System Properties

The PSR B1259-63/LS 2883 system undergoes periastron every ~ 3.4 years, corresponding to the point of the pulsar's orbit at which it is closest to its stellar companion. The properties of both objects in the system, as well as general properties of the system itself, are listed in Tab. 6.1. Orbital phases around the periastron passage are typically those in which the bulk of the non-thermal emission is detected. This emission is typically accredited to the interaction of the pulsar wind with the stellar wind, in particular, the stellar disc formed by the slower and denser equatorial wind [238, 275]. The interaction of these two winds is often assumed to form the shape of a conical termination shock around the pulsar facing the star [276]. This provides an acceleration site as per the classical plerionic binary scenario [277].

The stellar companion of PSR B1259-63, LS 2883, has been classified as an O9.5Ve type star. This denotes it as spectral class O with emission lines present. Additionally, 9.5 is an indicator specifically for O-type stars, where 9.5 indicates a weak He^{+} line and a strong He^{0} line. The luminosity class has been categorised as V, indicating the LS 2883 is a main sequence star.

The circumstellar disc of LS 2883 is composed of expelled stellar material and coalesces in the equatorial plane of the star, extending up to 20 stellar radii [275]. Measurements of the pulsed radio emission, and its subsequent disappearance and reappearance at ± 16 days, suggest that the disc is inclined with respect to the orbit of the pulsar. This in turn suggests that the pulsar likely crosses the disc twice during each orbit at these times.

Oe-type stars are known to also host a second distinct wind emanating from their poles. This polar wind typically has a vastly different density and velocity profile to that of the equatorial wind and is typically a lot sparser but faster [278].

The combination of these two wind components is a source of ambiguity in modelling, as their distinct profiles make for vastly different acceleration sites and therefore particle processes. It is, however, largely believed that the bulk of the emission in the system originates from the pulsar wind interacting with the circumstellar wind.

Additionally, the area around the star and disc is thought to host significant numbers of large clumps of matter, likely as a result of clumpy wind outflows or from the coalescence of disc ejecta caused by the pulsar's passage through the disc. These clumps are observed to emit X-rays as they are ejected from the system at least once per orbit [279, 280, 281]. The detection of the ejected objects implies a large number of clumps in the vicinity of the star as a result, with the periastron passage causing the expulsion of a small population of these.

6.11 Non-thermal Emission From PSR B1259-63/LS 2883

PSR B1259-63 is characterised by its non-thermal emission at orbital phases around the periastron passage. At these orbital phases, the system is detected across large swathes of the EM spectrum with each wavelength displaying a characteristic flux behaviour. Although periastron-to-periastron variation exists, largely (prior to 2021) most of this non-thermal emission followed a similar form across periastron passages.

Property	Value	Reference
RA, J2000	13h 02m 47.65s	[238]
DEC, J2000	$-63°\ 50'\ 8.6''$	[238]
Distance, d [kpc]	2.39	[282]
Eccentricity, e	0.87	[283]
Orbital Period, T [days]	1236.724526	[284]
Separation at Periastron [AU]	0.9	[285]
Inclination Angle of Disc, $\theta_{\rm i}$ [°]	154	[286]
Compact Object	**Neutron Star**	
Pulsar Period, $P_{\rm P}$ [ms]	47.76	[238]
Spin Down Luminosity, $L_{\rm SD}$ [erg s^{-1}]	8.2×10^{35}	[287]
Magnetic Field, B [G]	3×10^{11}	[283]
Companion Star	**O9.5Ve**	
Bolometric Luminosity, L_* [erg s^{-1}]	$(0.3 - 2.2) \times 10^{38}$	[288]
Temperature, T [K]	$(2.3 - 2.7) \times 10^4$	[288]
Mass, M [M$_\odot$]	$15 - 31$	[286]
Radius, R [R$_\odot$]	6	[289]

Tab. 6.1: Table detailing the values of various physical parameters of the gamma-ray binary system PSR B1259-63/LS 2883, along with the references from which they were taken. The table is subdivided into (top-down) general parameters of the system, parameters of the compact object and parameters of the companion star.

6.11.1 Radio Emission

As previously mentioned, PSR B1259-63 was discovered during a high-frequency radio survey of the southern galactic plane. This survey utilised the 64m Parkes telescope[7] to perform a search (at 660 MHz and 1520 MHz), where it detected the PSR B1259-63 system, and confirmed the companion to be a neutron star from its pulsed emission [238]. From this radio emission key orbital parameters were derived, many of which are listed in Tab. 6.1.

Since its discovery, PSR B1259-63 has been regularly monitored at radio wavelengths. Observations of the source have been taken at a variety of orbital phases, though much of the observational time is centred on the object's various periastron passages due to the phenomenon of the unpulsed non-thermal emission. The first recorded periastron passage of the system in 1994 was monitored in the radio band by the Australian Telescope Compact Array (ATCA) [290]. Following this, the system has been observed in the radio band during every subsequent periastron passage by a variety of radio telescopes, particularly with the ATCA (see [287] and references within).

[7] The titular star of the Australian comedy film "The Dish".

Across these periastron passages, the system has displayed several characteristic and recurrent features at radio frequencies. Namely, the radio emission of PSR B1259-63 is dominated by the pulsed emission of the neutron star until orbital phases close to the periastron passage. At ~ 20 days before periastron, a strong unpulsed flux component is detected and sharply rises to exceed the flux levels of the pulsed emission by several factors of 10 [272]. This unpulsed emission appears to last up to ~ 100 days after periastron, with the pulsed emission reappearing at ~ 20 days after periastron [289]. A key feature of the radio light curve, observed over multiple periastron passages, is the presence of two maxima at $t_{\rm p}$[8] ± 16 days. Several archival radio light curves are displayed in Fig. 6.12. These maxima are often attributed to the pulsar crossing the circumstellar disc due to its inclination to the orbital plane.

The unpulsed component of the emission is largely expected to originate from a population of electrons accelerated to high energies in the region where the pulsar and stellar wind meet during the periastron passage (see 6.5 for further details on particle acceleration). The radio emission of the unpulsed signal reportedly is consistent with optically thin synchrotron emission [272].

Because of this, models (see [287]) often explain X-ray and radio emission as synchrotron emission by a single electron population. This necessitates a spectrum of electrons that also reaches lower energies to explain the observed radio emission. To obtain a spectrum spanning such an energy range, the synchrotron emission would likely originate from a population of electrons that have already undergone IC cooling, producing higher energy emission.

Understanding the site of the radio emission provides a challenge to explanations of the emission mechanisms. Radio emission produced in the tip of the interaction cone would quickly become attenuated by the strong levels of free-free absorption. This would naively imply that the emission site is likely to be found far from the energetic particles resulting from the interaction of the two winds, i.e. in the tail of the shock region. However, this would further imply a delay between the X-ray and radio emission which is not seen, as well as distinctly different emissions given the changes in magnetic fields in the two environments. Moreover, the strong correlation seen between the unpulsed radio emission and X-ray emission seen in previous periastron passages provides compelling evidence that these two emissions are linked and are of synchrotron origin [287]. With regards to the electron population, however, it should be noted that recent spectral studies of the radio and X-ray emission tentatively suggest results that are inconsistent with a single population of electrons [272].

[8] $t_{\rm p}$ is defined as the time of periastron for a given periastron passage.

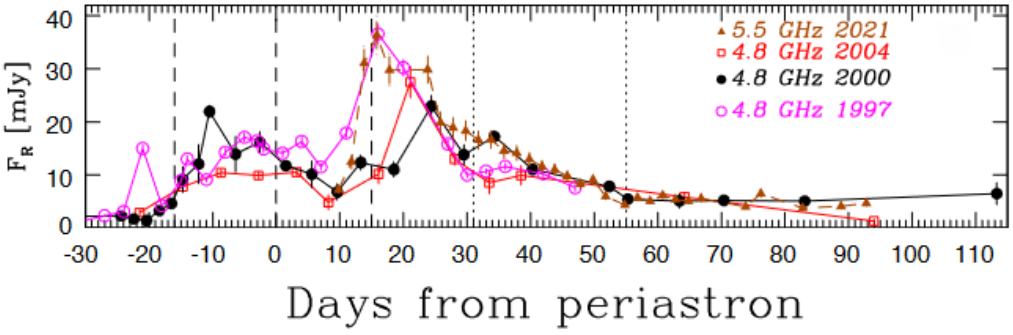

Fig. 6.12: Radio light curve of PSR B1259-63 covering multiple archival periastron passages. Light curve points represent radio flux densities in mJy. In this light curve the two peaked profile, thought to result from the disc crossing, can be seen with radio maxima at $t_{\rm p} - 16$ days and $t_{\rm p} + 16$ days. Figure adapted from [287].

6.11.2 X-ray Emission

At keV energies, the gamma-ray binary was first detected during its 1994 periastron by the ROSAT satellite [291]. The X-ray behaviour of the source has since proved a vital tool in understanding the physical processes underlying the system. As such, PSR B1259-63 has been monitored frequently at X-ray energies. These observations, again, largely focus on the system's periastron passages, of which every passage to date has been monitored by a host of X-ray instruments such as SWIFT, NICER and Chandra.

The X-ray behaviour of the system is characterised by unpulsed and non-thermal emission, detected at all orbital phases from periastron to apastron. Similarly to the case in radio, however, this emission increases at phases closer to the periastron and is at its minimum at apastron. Much like the emission characteristic of the radio band, the X-ray light curve also typically hosts two distinct maxima at times roughly corresponding to the disappearance and reappearance of pulsed emission ($t_{\rm p} \pm 16$ days). These peaks are, therefore, once again interpreted as originating from the pulsar crossing the inclined disc. Whilst small-scale variations in these maxima have been reported (for example between the periastron passage of 2014 and 2017 see [276] for further details), prior to the 2021 periastron passage the X-ray emission remained largely similar. However, for the first time in the observed history of the system, during the 2021 periastron passage a third X-ray peak (occurring between $\sim t_{\rm p} + 30$ days and $\sim t_{\rm p} + 50$ days) was observed, in addition to the expected X-ray maxima at $t_{\rm p} \pm 16$ days. The presence of this third peak constitutes a challenge for existing models of the system and implies novel behaviour in the 2021 periastron

passage. Archival light curves, as well as the 2021 periastron light curve, are shown in Fig. 6.13.

The origin of the X-ray emission in the system is still an area of active debate within the community. It is clear that the injected spectrum of particles must have sufficient energies to achieve radiative emission in the X-ray band from cooling. This, in turn, implies a production site close to the tip of the interaction. Such a scenario could provide the site for the acceleration of electrons to very high energies, allowing their subsequent radiative cooling via IC and synchrotron processes, producing TeV and X-ray photons respectively.

Such a scenario is supported by the, previously referenced, strong correlation between unpulsed radio and X-ray emission across multiple periastron passages. This correlation strongly implies that these two emissions are linked by a common particle population, possessing an injected energy spectrum spanning these energies. An alternative explanation suggested by [292] (among others) is that the X-ray emission is produced by MeV photons that have undergone IC scattering on photons from the stellar photon field. It should be noted that in a recent work, models that fit the X-ray to TeV data reasonably well, underpredict radio flux significantly [272]. This could hint towards either effective cooling (requiring a magnetic field of 50 G) or perhaps a second population of electrons [272].

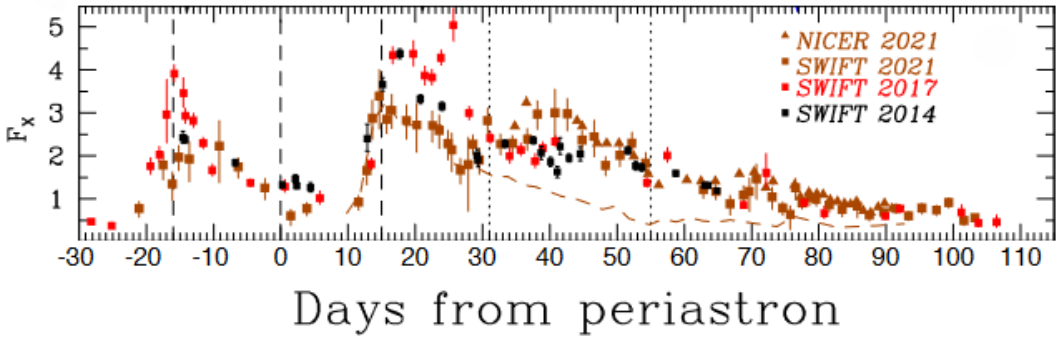

Fig. 6.13: X-ray light curve of PSR B1259-63 covering multiple archival periastron passages. Light curve points represent absorbed 1-10 keV X-ray flux in units of 10^{-11} erg cm^{-2} s^{-1}. Also depicted with the gold dashed line are the scaled 5.5 GHz radio data from 2021. The two peaked profile (thought to result from the disc crossing) seen in radio is also seen in archival X-ray observations at $t_{\rm p} - 16$ days and $t_{\rm p} + 16$ days. However, a third X-ray peak is present in the 2021 light curve. Figure adapted from [287].

6.11.3 GeV Emission

The GeV monitoring of PSR B1259-63 began following its detection by *Fermi-LAT* in 2011 [293] and (due to *Fermi-LAT's* unique all-sky data acquisition style, see Sec.2.8) has been monitored almost continuously since. The GeV behaviour of the system remains one of the most enigmatic and erratic features of the emission profile, with large variations in the GeV band observed between each periastron passage. Prior to $\sim t_{\rm p} - 30$ days only upper limits are detected from the source in the GeV band, however, between $t_{\rm p} - 30$ days to $t_{\rm p} + 30$ days the system enters a state of low GeV flux. This period also features mild variability in the flux, however, it is not possible to quantify this further given that the light curve during this time is largely composed of upper limits.

Following this phase comes an intense and extended high-flux state referred to as the "GeV flare[9]". This outburst of GeV emission has been observed following all periastron passages observed in the GeV band to date, from 2010/2011[10] to 2021 (for studies of the individual GeV flares for 2010, 2014, 2017 and 2021 see [294, 295, 296, 297]). Interestingly, this GeV emission appears to occur at times well after the periastron and after the pulsar is thought to have exited the disc. In fact, the GeV flare is notable in that (prior to the third X-ray peak observed in 2021) it occurs when almost all emission at other wavelengths are decreasing towards their respective minima.

The timing of the GeV flare remains an unpredictable feature of the system. The GeV flares in the 2010 and 2014 periastron passages, for example, began at $\sim t_{\rm p}+30$ days. Whereas in 2017 and 2021, the GeV flares started at $t_{\rm p} + 50$ days, a significant delay compared to previous periastron passages. Moreover, the flares in 2017 and 2021 showed evidence of extremely rapid and energetic sub-flares (exceeding ~ 30 times the spin-down luminosity of the pulsar), occurring on the scale of ~ 10 minutes. See Fig. 6.14 for the GeV light curve of PSR B1259-63 over multiple periastron passages.

Though the GeV emission remains difficult to explain, some models try to provide an explanation through interactions of the shock front with the observed clumps in the stellar wind. In the scenario proposed by [276], these stellar wind clumps are able to penetrate the shock front into the conical region immediately surrounding

[9] Given its detection and monitoring by the *Fermi-LAT* instrument (in turn, because of *Fermi-LAT's* monopoly at GeV energies) this is also sometimes referred to as the "*Fermi* flare".

[10] While the point of periastron technically occurred on the $10^{\rm th}$ December 2010, its proximity to the new year meant many observations of the latter stages of the periastron passage occurred in 2011. The passage is therefore sometimes reported in the literature as the 2011 periastron passage.

the pulsar. Inside this region, it is proposed that the clumps are able to interact with the unshocked/weakly shocked electrons of the pulsar wind, through a combination of IC and bremsstrahlung. This in turn produces GeV emission, with bremsstrahlung cited as being responsible for the flares and the IC interactions responsible for the more stable GeV emission.

In order for this to explain the erratic nature and luminosity of the emission it must, by nature, be anisotropic. In [276], this is explained by GeV emission only being visible to an observer looking through the base of the cone formed from the confluence of the two shocks. The tip of this cone is located between the pulsar and the star, with the ram pressure of the stellar wind causing the shock front to stream back beyond the pulsar, resulting in a conical shape. This also forms an opening directly behind the pulsar from the star's perspective, where there is a reduced/minimal shock front.

This means that the timing of emission can only occur while the base (opening) of the cone is in the observer's line of sight, and when the GeV clumps have penetrated beyond the shock giving rise to the seemingly unpredictable nature of the emission. Moreover [287], posits that the reasoning for a lower GeV flux level in 2021 is that the GeV emission detected is inversely proportional to the opening angle of the cone. This means a sparser disc (which could have been the case in the 2021 periastron) will produce a wider cone opening angle and therefore diminished GeV emission.

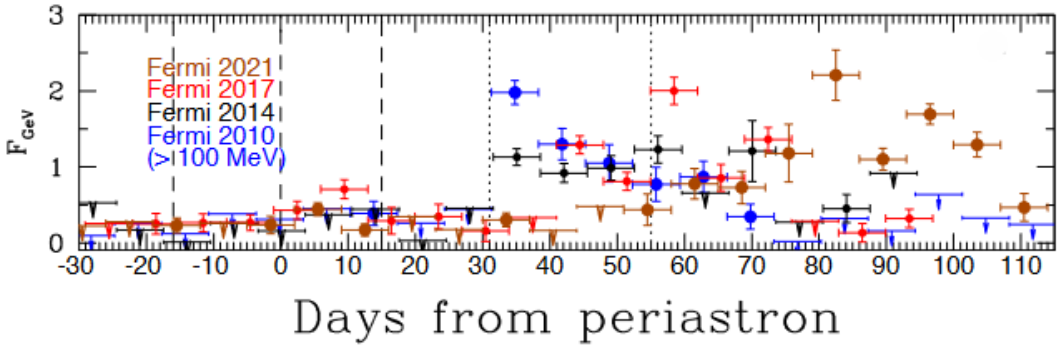

Fig. 6.14: GeV light curve of PSR B1259-63 covering multiple archival periastron passages. Points are *Fermi-LAT* flux measurements in the E $>$ 100 MeV energy range, binned into weekly bins. This light curve clearly displays the GeV low flux state present at times before periastron and the GeV flaring events at later times. Figure adapted from [287].

6.11.4 Very-high-energy Emission

PSR B1259-63 was not detected in the VHE band (TeV energies) until 2004[11] [298], when VHE emission from the periastron passage was detected by the H.E.S.S. array. Subsequently, H.E.S.S. has monitored the system during every periastron passage to date. Each of these periastron passages is collated and summarised in [299] (for the individual VHE analyses of the 2004, 2007, 2011 and joint 2014/2017 periastron passages see [298, 300, 301, 299] respectively).

VHE emission is commonly attributed to IC interactions of high-energy electrons accelerated in the shock, scattering off of UV photons from the stellar photon field [288]. In some models this strongly links the two wavelengths, suggesting a common particle population is responsible for both X-ray and VHE emission [287]. Previously, models involving a hadronic circumstellar disc were invoked, suggesting that VHE emission arose from hadronic interactions and subsequent π^0 decay, resulting from the pulsar crossing the disc [302]. However, these models have since become less plausible, as the increased resolution of the VHE spectra and flux behaviour suggest a greater likelihood of a leptonic emission origin.

VHE Flux Behaviour

The flux behaviour of the source at VHE energies is often difficult to discern on the scale of a single periastron passage due (in part) to the sun/moon, weather, scheduling and visibility constraints of IACTs. For example, a combination of these constraints in 2017 meant that the array was only able to observe 6 hours of the periastron passage at limited orbital phases [299]. The stacked VHE light curve of all periastron passage analyses, presented in [299], shows a distinct asymmetric double peak profile (see Fig. 6.15). A Bayesian block analysis of this light curve further reveals the presence of two distinct VHE maxima, with the first between $t_{\rm p} - 32$ days and $t_{\rm p} - 26$ days (at 12.1σ), and the second between $t_{\rm p} + 16$ days and $t_{\rm p} + 57$ days (with a significance of 39.8σ). Notably, this second peak is roughly coincident with the time of the pulsar exiting the equatorial disc, and with the novel third X-ray peak (though, it should be noted that this peak in VHE continues for far longer than its X-ray counterpart).

While the features of this stacked analysis provide interesting insight into the average flux behaviour of the system, it cannot be assumed that the orbit-to-orbit flux profile

[11] Though this emission was predicted, the instrumentation was not available for VHE monitoring due to the associated challenges discussed in Sec.5.3.

variability is non-existent. The observational constraints placed on the H.E.S.S. array make it difficult to discern whether indeed this asymmetric double peak profile is present in all periastron passages. Moreover, the sun/moon constraints limit the possibility of continuous observations at VHE energies, meaning short-scale investigations into the variability of the source are not possible. Evidence across the VHE observational history of the source does tentatively suggest that this profile is present in all periastron passages. However, the extent of its variability is not known. Naturally, the discovery of variability in the VHE light curve would have to be considered in the modelling of the VHE emission.

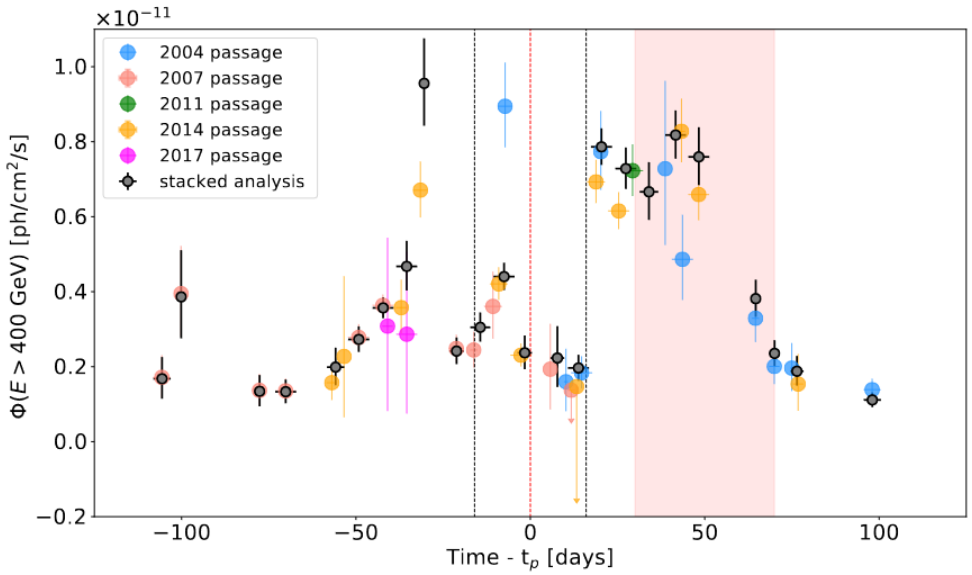

Fig. 6.15: VHE light curve of PSR B1259-63 covering multiple archival periastron passages, as well as the stacked analysis of previous periastron passages. Flux points are grouped into weekly bins, including the stacked analysis, and are derived assuming a photon index of 2.7. Additionally, the down arrows are 68% c.i. upper limits. The dashed lines at $t_{\mathrm{p}} - 16$ days and $t_{\mathrm{p}} + 16$ days correspond to the times at which the pulsar is thought to cross the disc, and the central black line at $\mathrm{Time} - t_{\mathrm{p}} = 0$ days marks the point of periastron. Here, the red-shaded area represents the period of the 2014 GeV flare. As can be seen in the figure, archival VHE observations appear to show an asymmetric double peak profile. Figure taken from [299].

VHE Spectral Behaviour

The VHE spectral behaviour of PSR B1259-63 is a crucial piece of information for understanding the particle acceleration processes present, and the respective emission of the system as a whole. The VHE spectrum is also representative of the highest energy particle populations present in the system, an area of particular

interest in gamma-ray binary emission mechanisms (and more generally in the ongoing search for galactic "PeVatrons"[12]).

The H.E.S.S. array has therefore calculated the spectrum of emission from the source during each recorded periastron passage. These are shown in Fig. 6.16. As can be seen over the variety of periastron passages, the VHE emission is best fit consistently with a power-law model. The parameters of all the VHE spectra derived from previous years agree within error with each other, with the system showing no signs of spectral variation between periastron passages.

Data Set	**Time Period** days	Γ	ϕ(1 TeV) 10^{-12} TeV^{-1} cm^{-2} s^{-1}
2004	$t_{\rm p} - 7$ to $t_{\rm p} + 98$	$2.64 \pm 0.06_{\rm stat} \pm 0.10_{\rm sys}$	$0.97 \pm 0.05_{\rm stat} \pm 0.19_{\rm sys}$
2007	$t_{\rm p} - 110$ to $t_{\rm p} + 11$	$2.84 \pm 0.08_{\rm stat} \pm 0.10_{\rm sys}$	$0.93 \pm 0.05_{\rm stat} \pm 0.19_{\rm sys}$
2011	$t_{\rm p} + 26$ to $t_{\rm p} + 32$	$2.7 \pm 0.1_{\rm stat} \pm 0.1_{\rm sys}$	$2.4 \pm 0.3_{\rm stat} \pm 0.5_{\rm sys}$
2014	$t_{\rm p} - 39$ to $t_{\rm p} + 78$	$2.84 \pm 0.05_{\rm stat} \pm 0.10_{\rm sys}$	$1.89 \pm 0.07_{\rm stat} \pm 0.38_{\rm sys}$
2021	$t_{\rm p} - 23$ to $t_{\rm p} + 127$	$2.65 \pm 0.04_{\rm stat} \pm 0.10_{\rm sys}$	$1.13 \pm 0.04_{\rm stat} \pm 0.23_{\rm sys}$

Tab. 6.2: Best fit parameters when a power-law model is applied to the various TeV data sets from PSR B1259-63 across multiple periastron passages recorded by the H.E.S.S. array. The $t_{\rm p}$ value represents the time of periastron for that respective row. The Γ parameter is the photon index of the best-fit power law $\mathrm{d}N/\mathrm{d}E = F_0(E/E_0)^{-\Gamma}$ to the best-fit normalisation level at the decorrelation energy. The spectral properties correspond to H.E.S.S. stereo analysis of the data acquired during the periastron passage, taken from [299]. The properties of the 2021 periastron are taken from [4]. Note, the spectral details of the 2017 periastron passage are not included due to the fact there were insufficient statistics to calculate a spectrum during the observations of this periastron passage [299]. The two errors associated with each value are representative of, first, the magnitude of the statistical uncertainty in the value at 95% c.i., and secondly the systematic error in the measurements as estimated following the method within [303]. The energy range for each spectral analysis was defined such that the energy reconstruction bias (which itself was calculated from Monte Carlo simulations), is lower than 10% of the energy. Additionally, the effective area calculated for each data set had to exceed 10% of the maximum value.

6.12 Summary

The subject of this chapter has been gamma-ray binary systems and their particle acceleration mechanisms. An overview of these subjects has been given to supplement the results presented in the work in chapter 7. In this chapter, the various broad categories of gamma-ray binary objects were introduced including

[12] Colloquial term for sources with the energetic capability to produce cosmic rays of up to PeV energies when incident at Earth.

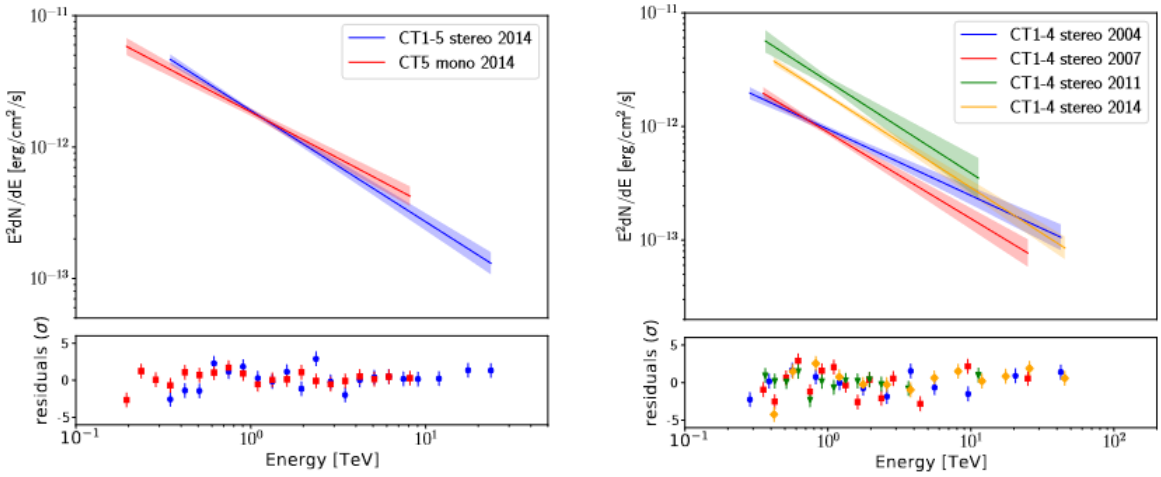

Fig. 6.16: A comparison of the TeV spectral energy distributions derived from multiple periastron passages of PSR B1259-63 with H.E.S.S. *Left:* the 2014 results with both stereo and mono observations in blue and red respectively. *Right:* archival spectra from 2004, 2007, 2010 and 2014 taken in stereo configuration. Spectral points in both plots are binned such that they have a significance of 2σ (with the exception of 2014's spectrum where the highest-energy flux point only has a significance of 1.5σ). In both plots, the best-fit power law is shown in the upper panel (with the coloured bands representing 1σ statistical uncertainties on the fits), with the lower panel showing the residuals of the data to the best spectral fit. Figure taken from [299].

microquasars, colliding wind binaries and (the object most pertinent to this thesis) gamma-ray binaries. Due to their presence in many gamma-ray binaries (including PSR B1259-63), Oe-Be stars and pulsars were introduced to give an explanation of their emission and how high-energy emission can form from these systems. In addition to the introduction of different objects, this chapter has described various methods of high-energy particle acceleration. This, of course, was supplemented by the mechanisms of non-thermal radiation produced by high-energy particles in both the hadronic and leptonic regimes.

Finally, since it is the subject of the study presented in chapter 7, extensive details of the gamma-ray binary PSR B1259-63/LS 2883 were given. This included an overview of the properties of the system, as well as a more detailed description of the characteristic non-thermal emission present around its periastron passages.

7

VHE Analysis of the 2021 Periastron of PSR B1259-63/LS 2883

Gamma-ray binary systems are unique and rare objects that exhibit interesting non-thermal emission (across the EM spectrum) around their periastron passages. Unfortunately, due to the scarcity of their detection so far, and their complex behaviour, much mystery still surrounds these objects. The observation and analysis of their non-thermal emission is paramount in understanding this enigmatic class of objects and the physical processes occurring within them. In particular, the VHE emission from these sources, seen at orbital phases close to the periastron, can provide a unique insight into the underlying mechanisms of particle acceleration and radiation.

The following work reports on the extensive H.E.S.S. observation campaign of the 2021 periastron passage of the gamma-ray binary PSR B1259-63/LS 2883. This system hosts a pulsar in an eccentric, 3.4 year, orbit around an O9.5Ve type star. The star hosts a decretion disc of gas and dust which is thought to be at an oblique angle to the pulsar's orbital plane, causing the pulsar to pass through this disc twice per orbit (thought to occur at $t_{\mathrm{p}} \pm 16$ days).

The 2021 periastron of this source was notable for a deviation from the usual trends seen in X-ray emission, in that a third X-ray peak appeared in addition to the usual two seen. Thus, the VHE results are an imperative piece of the puzzle to understand this novel behaviour. This work reports on the flux and spectral analysis of the source during the ~ 100 hour observation campaign from the H.E.S.S. array. An analysis is also conducted into a potential correlation between X-ray and TeV data around the periastron passage, as well as GeV and TeV data in the same time period. Finally, an extensive discussion regarding the ramifications of the findings for system models and particle acceleration is given.

7.1 H.E.S.S. Observations of the 2021 Periastron Passage of PSR B1259-63/LS 2883

Astronomy & Astrophysics manuscript no. output
May 6, 2024

H.E.S.S. observations of the 2021 periastron passage of PSR B1259-63/LS 2883

H.E.S.S. Collaboration, F. Aharonian[1,2,3], F. Ait Benkhali[4], J. Aschersleben[5], H. Ashkar[6], M. Backes[7,8], V. Barbosa Martins[9], R. Batzofin[10], Y. Becherini[11,12], D. Berge[9,13], K. Bernlöhr[2], M. Böttcher[8], C. Boisson[14], J. Bolmont[15], M. de Bony de Lavergne[16], J. Borowska[13], M. Bouyahiaoui[2], R. Brose[1], A. Brown[17], F. Brun[16], B. Bruno[18], T. Bulik[19], C. Burger-Scheidlin[1], S. Caroff[20], S. Casanova[21], J. Celic[18], M. Cerruti[11], T. Chand[8], S. Chandra[8], A. Chen[22], J. Chibueze[8], O. Chibueze[8], G. Cotter[17], J. Damascene Mbarubucyeye[9], J. Devin[23], J. Djuvsland[2], A. Dmytriiev[8], K. Egberts[10], S. Einecke[24], J.-P. Ernenwein[25], G. Fontaine[6], S. Funk[18], S. Gabici[11], Y.A. Gallant[23], D. Glawion[18], J.F. Glicenstein[16], P. Goswami[11], G. Grolleron[15], L. Haerer[2], B. Heß[26], W. Hofmann[2], T. L. Holch[9], M. Holler[27], Zhiqiu Huang[2], M. Jamrozy[28], F. Jankowsky[4], V. Joshi[18], I. Jung-Richardt[18], E. Kasai[7], K. Katarzyński[29], D. Khangulyan[30], R. Khatoon[8], B. Khélifi[11], W. Kluźniak[31], Nu. Komin[22], K. Kosack[16], D. Kostunin[9], A. Kundu[8], R.G. Lang[18], S. Le Stum[25], F. Leitl[18], A. Lemière[11], M. Lemoine-Goumard[32], J.-P. Lenain[15], F. Leuschner[26], J. Mackey[1], D. Malyshev[26,⋆], G. Martí-Devesa[27], R. Marx[4], A. Mehta[9], P.J. Meintjes[33], A. Mitchell[18], R. Moderski[31], L. Mohrmann[2], A. Montanari[4], E. Moulin[16], T. Murach[9], M. de Naurois[6], J. Niemiec[21], S. Ohm[9], E. de Ona Wilhelmi[9], M. Ostrowski[28], S. Panny[27], M. Panter[2], R.D. Parsons[13], U. Pensec[15], G. Peron[11], D.A. Prokhorov[34], G. Pühlhofer[26,⋆], M. Punch[11], A. Quirrenbach[4], M. Regeard[11], A. Reimer[27], O. Reimer[27], I. Reis[16], H. Ren[2], F. Rieger[2], B. Rudak[31], E. Ruiz-Velasco[2], V. Sahakian[3], H. Salzmann[26], A. Santangelo[26], M. Sasaki[18], J. Schäfer[18], F. Schüssler[16], H.M. Schutte[8], J.N.S. Shapopi[7], S. Spencer[18], Ł. Stawarz[28], R. Steenkamp[7], S. Steinmassl[2], C. Steppa[10], K. Streil[18], I. Sushch[8,⋆], T. Takahashi[35], T. Tanaka[36], A.M. Taylor[9], R. Terrier[11], C. Thorpe-Morgan[26,⋆], M. Tluczykont[37], T. Unbehaun[18], C. van Eldik[18], B. van Soelen[33], M. Vecchi[5], C. Venter[8], J. Vink[34], T. Wach[18], S.J. Wagner[4], F. Werner[2], A. Wierzcholska[21], M. Zacharias[4,8], A.A. Zdziarski[31], A. Zech[14], and N. Żywucka[8]

(Affiliations can be found after the references)

May 6, 2024

ABSTRACT

PSR B1259-63/LS 2883 is a gamma-ray binary system that hosts a pulsar in an eccentric orbit, with a 3.4 year period, around an O9.5Ve star (LS 2883). At orbital phases close to periastron passages, the system radiates bright and variable non-thermal emission, for which the temporal and spectral properties of this emission are, for now, poorly understood. In this regard, very high-energy (VHE) emission is especially useful to study and constrain radiation processes and particle acceleration in the system. We report on an extensive VHE observation campaign conducted with the High Energy Stereoscopic System, comprised of approximately 100 hours of data taken over five months, from $t_\mathrm{p} - 24$ days to $t_\mathrm{p} + 127$ days around the system's 2021 periastron passage (where t_p is the time of periastron). We also present the timing and spectral analyses of the source. The VHE light curve in 2021 is consistent overall with the stacked light curve of all previous observations. Within the light curve, we report a VHE maximum at times coincident with the third X-ray peak first detected in the 2021 X-ray light curve. In the light curve – although sparsely sampled in this time period – we see no VHE enhancement during the second disc crossing. In addition, we see no correspondence to the 2021 GeV flare in the VHE light curve. The VHE spectrum obtained from the analysis of the 2021 dataset is best described by a power law of spectral index $\Gamma = 2.65 \pm 0.04_\mathrm{stat} \pm 0.04_\mathrm{sys}$, a value consistent with the spectral index obtained from the analysis of data collected with H.E.S.S. during the previous observations of the source. We report spectral variability with a difference of $\Delta\Gamma = 0.56 \pm 0.18_\mathrm{stat} \pm 0.10_\mathrm{sys}$ at 95% confidence intervals, between sub-periods of the 2021 dataset. We also detail our investigation into X-ray/TeV and GeV/TeV flux correlations in the 2021 periastron passage. We find a linear correlation between contemporaneous flux values of X-ray and TeV datasets, detected mainly after $t_\mathrm{p} + 25$ days, suggesting a change in the available energy for non-thermal radiation processes. We detect no significant correlation between GeV and TeV flux points, within the uncertainties of the measurements, from $\sim t_p - 23$ days to $\sim t_p + 126$ days. This suggests that the GeV and TeV emission originate from different electron populations.

1. Introduction

Gamma-ray loud binaries (GRLBs) are a subclass of high-mass and intermediate-mass binary systems characterised by their energy spectra peaking above 1 MeV, but typically at $E \gtrsim 100$ MeV, and extending to beyond 1 TeV.

⋆ Corresponding authors;
e-mail: contact.hess@hess-experiment.eu

Article published by EDP Sciences, to be cited as https://doi.org/10.1051/0004-6361/202449612

While hundreds of high-mass binaries have been detected in the X-ray band, the current generation of Cherenkov telescopes and gamma-ray satellites have only been able to detect about a dozen GRLB systems (see, e.g., Dubus 2013; Chernyakova et al. 2019, for recent reviews). The physical environments and mechanisms leading to the production of such energetic radiation in these systems are not firmly established.

GRLB systems are comprised of a massive early-type star (spectral class O or B) and a compact object (a neutron star or a black hole). The nature of this compact object is difficult to discern in the majority of cases, in several systems however, the compact object has been identified as a non-accreting pulsar such as in the cases of PSR B1259-63/LS 2883, PSR J2032+4127 and LS I+61 303 (Johnston et al. 1992; Abdo et al. 2009; Weng et al. 2022). Additionally, evidence of hard X-ray pulsations have been reported in the system LS 5039 (Yoneda et al. 2020), tentatively suggesting a neutron star companion as well.

The PSR B1259-63/LS 2883 system was discovered during a high-frequency radio survey intending to search for nearby pulsars (Johnston et al. 1992). Subsequent radio and optical observations resulted in the identification of the compact object in the system as a young radio pulsar (spin period ~ 48 ms), in a highly eccentric ($e = 0.87$) 3.4-year ($1236.724526 \pm 6 \times 10^{-6}$ day) orbit around the O9.5Ve star LS 2883 (Johnston et al. 1992, 1994; Negueruela et al. 2011; Shannon et al. 2014; Miller-Jones et al. 2018).[1] The system is located at a distance of 2.39 ± 0.19 kpc from Earth (Gaia Collaboration et al. 2018), and recent measurements of the inclination angle suggest that the binary orbit is observed at an angle of 154° to the line of sight (Miller-Jones et al. 2018). The projected semi-major axis is $a \sin i = 1296.27448 \pm 0.00014$ lt-s (Miller-Jones et al. 2018), which for the pulsar's orbital eccentricity corresponds to apastron and periastron separations of 11 AU and 0.8 AU, respectively. Additionally, the spin-down luminosity of the pulsar was estimated to be $L_{\rm sd} = 8.2 \times 10^{35}$ erg s^{-1} (Johnston et al. 1994), with a characteristic age of 330 kyr (Johnston et al. 2005).

The companion star LS 2883 has a bolometric luminosity of $L_* = 2.3 \times 10^{38}$ erg s^{-1} (Negueruela et al. 2011) and hosts a decretion disc that extends up to at least 20 stellar radii (Johnston et al. 1992; Negueruela et al. 2011; Chernyakova et al. 2014) from the star (0.56 AU). The radius of LS 2883 is about $10 R_\odot$ (0.05 AU) (Negueruela et al. 2011), and its mass is $\sim 24\ M_\odot$(Shannon et al. 2014). The disappearance of pulsed radio emission at $\sim t_{\rm p} - 16$ days (where $t_{\rm p}$ is the time of periastron), and its reappearance at $\sim t_{\rm p} + 16$ days (Johnston et al. 2005), as well as observations of the dispersion measure along the periastron passage, both suggest that the stellar decretion disc is inclined with respect to the orbital plane (Johnston et al. 1996). Measurements of this inclination angle between the plane of the pulsar's orbit and the circumstellar disc suggest an angle of $\sim 35°$ (Johnston et al. 1994; Shannon et al. 2014).

Following its optical and radio detection, the system was later detected in the X-ray band with the *ROSAT* satellite (Cominsky et al. 1994). In the X-ray regime, PSR B1259-63/LS 2883 is detected during its entire orbit with a non-thermal, non-pulsed spectrum (Marino et al. 2023). While the X-ray flux level is minimal around apastron, close to the periastron passage the keV light curve is typically characterised by two maxima roughly coinciding with the times of the disappearance and re-appearance of pulsed radio emission (see e.g. Chernyakova et al. 2015). These peaks are usually interpreted as being connected to the pulsar crossing the Oe stellar disc. During the 2021 periastron passage, the X-ray light curve exhibited a third maximum between $\sim t_p$+30 and $t_{\rm p}$+50 days (Chernyakova et al. 2021) (henceforth referred to as the third X-ray peak), in addition to the two X-ray peaks at $\sim t_p \pm 16$ days detected in all observed periastron passages.

PSR B1259-63/LS 2883 was detected in the GeV band with *Fermi*-LAT (Abdo et al. 2011; Tam et al. 2011). At these energies, the system is characterised by a relatively low flux level in the period between $t_{\rm p} - 30$ and $t_{\rm p} + 30$ days. It later enters a high flux state (coined as the "GeV flare") that has been detected following all periastron passages observed with *Fermi*-LAT to date (2010 – 2021 Abdo et al. 2011; van Soelen & Meintjes 2015; Caliandro et al. 2015; Wood et al. 2018; Chang et al. 2021). However, for all periastron passages to date during which very high-energy (VHE; $\gtrsim 100$ GeV) observations were taken contemporaneously with the corresponding GeV flare, no clear counterpart at very high energies has been seen (H. E. S. S. Collaboration et al. 2013; H.E.S.S. Collaboration et al. 2020). The GeV flare in 2017 began after a noticeable delay, starting at up to $\sim$ 50 days after the periastron passage (Chang et al. 2021). The light curve of the GeV flare obtained from the 2017 periastron passage also showed a number of extremely strong and rapid sub-flares on timescales as short as $\sim$ 10 minutes. The observed luminosity of these sub-flares reached values of 30 times the spin-down luminosity of the pulsar (Johnson et al. 2018).

In the VHE band, PSR B1259-63/LS 2883 was detected with the High Energy Stereoscopic System (H.E.S.S.) for the first time in 2004 (Aharonian et al. 2005b), after which the array regularly observed the system at orbital phases close to its periastron passages. VHE observations of PSR B1259-63/LS 2883 are summarised in H.E.S.S. Collaboration et al. (2020) which reports on five (2004 – 2017) periastron passages observed with H.E.S.S. (see also Aharonian et al. 2005c, 2009; H. E. S. S. Collaboration et al. 2013; H.E.S.S. Collaboration et al. 2020, for individual analyses of the 2004–2017 periastron passages, respectively). See Tab. 1 for specific periastron passage dates and a summary of each passage's VHE observation campaign.

The VHE light curve obtained from the stacked analysis of the orbital-period folded data collected during the previous observations of the system indicate the presence of an asymmetric double peak profile (H.E.S.S. Collaboration et al. 2020). Maxima derived from a Bayesian block analysis of stacked data from previous periastron passages were reported between $t_{\rm p} - 32$ and $t_{\rm p} - 26$ days (with a hint of a sub-peak at around $t_{\rm p} - 15$ days) and between $t_{\rm p} + 16$ and $t_{\rm p} + 57$ days, with significances of 12.1σ and 39.8σ, respectively.

In this work we present the results of the most recent H.E.S.S. observational campaign on PSR B1259-63/LS 2883, performed around the 2021 periastron passage. Extensive coverage of the system during this observation campaign has allowed an unprecedented amount of observational data to be taken post-periastron passage. In

[1] In the following, we assume that the 2021 periastron of PSR B1259-63/LS 2883 occurred at $t_{\rm p} = 59254.867359$ MJD.

particular, observations extended up to the largest post-periastron orbital phase interval in the TeV band to date (29 days more than the previous longest in 2004), see Tab. 1 for details.

Following this introduction, Sec. 2 outlines the methodology and details of the H.E.S.S. array and its data pipeline. Moreover, this section covers specific details of prior H.E.S.S. observation campaigns and data analysis of the source during periastron passages up to and including 2021. In Sec. 3 the results of the analysis are presented, including studies of the flux behaviour and light curve trends, as well as spectral analysis of the source with a search for spectral variability. In this section we also present our investigation into a correlation between the X-ray / TeV flux and the GeV / TeV flux in the 2021 periastron passage. In Sec. 4 these results are discussed in the context of previous periastron passages and in the context of the unique findings at other wavelengths in 2021. We also present some theoretical interpretation of the findings of this study. Finally, Sec. 5 contains our concluding remarks.

2. Method

H.E.S.S. is an array of five imaging atmospheric Cherenkov telescopes (IACTs), where each telescope is abbreviated and numbered CT1-5, and is located in the Khomas Highlands of Namibia (see Aharonian et al. 2006; H.E.S.S. Collaboration et al. 2020, for detailed descriptions of the H.E.S.S. array).

In order to detect Cherenkov light, H.E.S.S. can only be operated under dark conditions. Because of this, H.E.S.S. is not operated during periods of bright moonlight (defined as above $\sim 40\%$ illumination). This results in a cycle-wise data taking period of 28 days. The fundamental data-taking unit of the H.E.S.S. array is an observational run, defined as a period of data acquisition lasting ~ 28 mins.

The VHE data presented in this paper are exclusively taken from runs where a minimum of three telescopes from CT1-4 were present (stereo mode). We use CT1-4 data to allow unbiased direct comparison to the majority of the other periastron passages covered by H.E.S.S., in which only CT1-4 data was available. For this reason CT5 data were not used in the analysis. The analysis presented in this paper used the reflected regions background method, for light curve production and spectral analysis, as well as the ring background method for the creation of maps (see Berge et al. 2007, for further details of these anaylsis methods). Observations were performed using pointing offsets from the source position, all offsets were exclusively performed along right ascension due to the presence of the nearby bright source HESS J1303-631 at an angular separation of 0.75° North from PSR B1259-63/LS 2883. The dataset contained almost exclusively 0.5° telescope offsets with two runs of 221 (the total run number after data quality selection cuts had been applied) at an offset of 0.7°.

Prior to 2021, H.E.S.S. observed PSR B1259-63/LS 2883 covering a number of orbital phases close to previous periastron passages. These include the 2004 (Aharonian et al. 2005c), 2007 (Aharonian et al. 2009), 2011 (H. E. S. S. Collaboration et al. 2013), 2014, and most recently the 2017 periastron passages (see H.E.S.S. Collaboration et al. 2020, for both the 2014 and 2017 periastron passages). See Tab. 1 for details of observations in previous periastron passages.

During the 2021 periastron passage H.E.S.S. attained a total of 100 h of observations in the stereo configuration after data quality selection cuts had been applied. See Tab. 1 for details of the 2021 observations.

The results presented in this paper were produced using the HAP (H.E.S.S. Analysis Package)/ImPACT (Image Pixel-wise fit for Atmospheric Cherenkov Telescopes) template-based method chain (Parsons & Hinton 2014). Results have been cross-checked using the Paris Analysis chain (de Naurois & Rolland 2009).

All light curves and spectra in this work were produced from data that had passed the spectral quality selection cuts, representing the strictest cut criterion for H.E.S.S. data (Aharonian et al. 2006). The data were also subject to a maximum event offset of 2.5°.

To estimate the systematic uncertainties we adopt the values outlined in Aharonian et al. (2006) for stereo analyses, as well as compare the reconstructed fluxes and spectral indices between the two major H.E.S.S. analysis chains. This study indicated a systematic uncertainty in the flux at an estimated level of 20% and an uncertainty in spectral indices of 0.1. Statistical uncertainties on values/figures in this work (with the exception of spectral parameters that are reported at 95% confidence interval –c.i.–) are given at 68% c.i., unless explicitly stated otherwise.

In calculating the spectra in this study we utilise the forward-folding method (see Piron et al. 2001, for further information on the forward folding method).

3. Results

The PSR B1259-63/LS 2883 system is located at the J2000 coordinates $RA = 13\mathrm{h}02\mathrm{m}47.65\mathrm{s}$, $Dec = -63°50'8.6''$ and is situated in the Galactic plane (Johnston et al. 1992). It is near to by the bright source HESS J1303–631, a pulsar wind nebula that is spatially coincident with the pulsar PSR J1301-6305 (H. E. S. S. Collaboration et al. 2012). The significance map of the source and its surrounding region are shown in Fig. 1 using Li and Ma significances (Li & Ma 1983) and were created by utilising all H.E.S.S. data passing spectral cuts from the 2021 periastron passage ($t_\mathrm{p} - 23$ days to $t_\mathrm{p} + 127$ days). HESS J1303–631 is known to have an energy-dependent morphology with a large spillover at GeV energies (H. E. S. S. Collaboration et al. 2012; Acero et al. 2013). This spillover corresponds to an extended and energy dependent emission profile of the source, to a degree that it has the potential to contaminate the emission of nearby sources such as PSR B1259-63/LS 2883. This required us to ensure that the effect of spillover was non-existent or negligible at very-high energies by measuring the effect of the spillover in runs far from the periastron passage (using combined data in the period of $\sim t_\mathrm{p} + 100$ days to $t_\mathrm{p} + 500$ days) where VHE emission from PSR B1259-63/LS 2883 was consistent with zero. No evidence of contaminant emission at VHE energies was found.

During the analysis of PSR B1259-63/LS 2883 a standard angular distance cut for point sources of 0.005 deg^2 was applied (defined as the angular distance between a reconstructed event and the expected source position).

The background acceptance ratio between the ON and OFF region had a value of $\alpha = 0.07$, resulting in a total excess of 1668.40 events. In total, for an acceptance corrected live time of 100.02 hours, we obtain a Li and Ma significance of 36.0 from PSR B1259-63/LS 2883.

		2004	2007	2011	2014	2017	2021
	Start Date	Feb 27	Apr 09	Jan 10	Mar 07	Aug 10	Jan 16
	End Date	Jun 15	Aug 08	Jan 16	Jul 21	Aug 20	Jun 16
	Time $-$ t_p [days]	-7 to +98	-110 to +11	+26 to +32	-39 to +78	-42 to -37	-23 to +127
CT5 Mono	N_{runs}	-	-	-	141	12	(216)
	t_L $[h]$	-	-	-	62.2	6	(99.4)
	θ [°]	-	-	-	41.8	57	(42.8)
CT1-4 Stereo	N_{runs}	138	213	11	163	-	221
	t_L $[h]$	57.1	93.9	4.8	68.1	-	100.0
	θ [°]	42.5	45.1	47.6	41.9	-	42.8

Table 1: Summary of analysed H.E.S.S. observations of PSR B1259-63/LS 2883 from 2004 to 2021. The number of runs passing spectral quality selection cuts in a given periastron passage is defined as N_{runs} (see text for further details), t_L refers to a periastron passage's total acceptance-corrected observation time, and finally θ indicates the mean zenith angle of the periastron passage's observations. Values for years prior to 2021 are taken from H.E.S.S. Collaboration et al. (2020) and references therein. CT1-4 stereo data are those runs in which third or more of the CT1-4 telescopes were active. CT5 mono data corresponds to the data obtained from only the central (and largest) telescope CT5. The 2021 CT5 mono observations are displayed in brackets as they are not presented or utilised in this study.

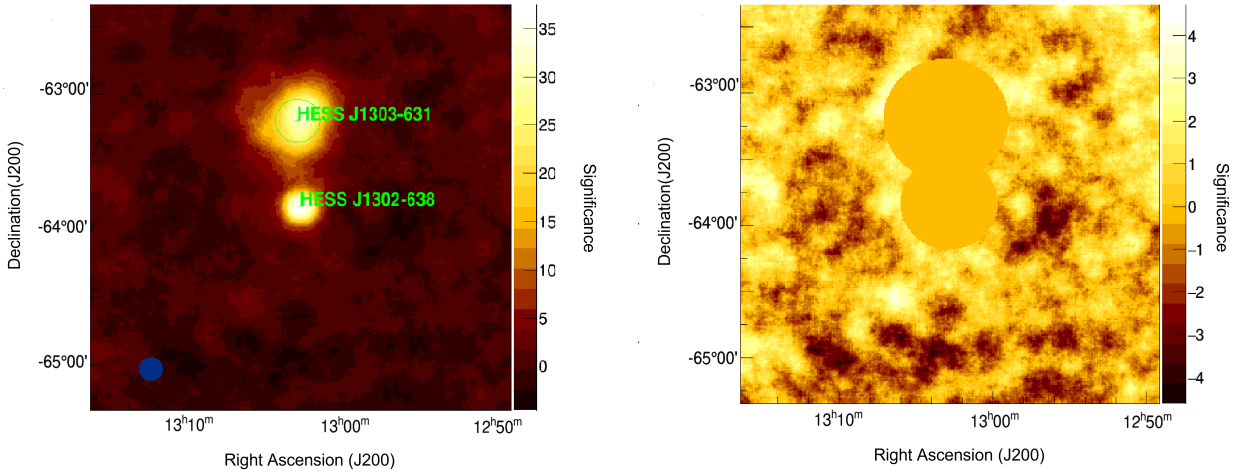

Fig. 1: Significance and excluded significance maps. **Left panel:** VHE significance map displaying PSR B1259–63/LS 2883 (here labelled as HESS J1302-638) and the surrounding region. PSR B1259-63/LS 2883 itself is the central object in the image, where also of note is the nearby pulsar wind nebula HESS J1303–631 (Aharonian et al. 2005c) directly to the north (see text for further details on this source). Also shown in blue in the lower left of the image, is the 68% c.i of the point spread function for these observations. **Right panel:** the significance map of PSR B1259-63/LS 2883 and its surrounding region after masking the two sources.
The bins in both maps are correlated within a circle of radius 0.1°.

3.1. Spectral analysis

A full investigation into the VHE spectral properties of the system during the periastron passage was undertaken and several spectra were derived. The total spectrum of the available periastron passage data was calculated, and the spectra of key intervals were created to investigate spectral variability. The first of these time frames included the two H.E.S.S. observational cycles (from $t_p - 3.9$ days to $t_p + 15.3$ days) that occurred concurrently with the periastron passage. Secondly, we created a spectrum for the period in which the peak levels of VHE flux were measured (here defined as $t_p + 25$ days to $t_p + 36$ days). Additionally, we created a spectrum from the data contemporaneous with the 2021 GeV flare (here referring to the period $t_p + 55$ days to $t_p + 108$ days as defined in Chernyakova et al. 2021). Finally, we created a spectrum of the data from the final two H.E.S.S. observational cycles from $\sim t_p + 81$ days to $\sim t_p + 127$ days (from now on referred to as the "TeV low flux" period). These datasets will henceforth be referred to as A, B, C, and D, respectively (please refer to Tab. 2). Each spectrum of these periods was fit with a power-law model, $\mathrm{d}N/\mathrm{d}E = \phi_0 (E/E_0)^{-\Gamma}$, where Γ represents the photon index of the power law with a normalisation ϕ_0 and a decorrelation energy of E_0. The best-fit parameters of these models are presented at 95% c.i. unless otherwise stated.

To define the energy range for the spectral analysis, two different approaches were used. For the total 2021 spectrum the lower energy bound, at 0.27 TeV, was defined using Monte Carlo simulations which ensure that the energy reconstruction bias is less than 10% of the energy (Aharonian et al. 2006). The upper bound of the energy range was defined by the highest energy bin that could be fit with a significance of 2σ. Henceforth we refer to this energy range as unfixed.

However, for the total spectrum used for comparison to the sub-periods, and for the sub-periods themselves, a fixed energy range was applied allowing accurate comparison of the different spectra. Thus, we apply an energy fitting range of (0.4 - 10.0) TeV for these sub-periods. The lower bound was chosen such that it supersedes the safe energy threshold for any of the data subsets. The higher energy threshold was chosen to ensure sufficient statistics up to the cut energy for all subsets.

Figure 2 shows the total 2021 periastron passage spectrum where no pre-fixed energy range for the fit was applied. This spectrum includes all the data taken with H.E.S.S. during the 2021 periastron passage and spans the energy range (0.30−39.6) TeV (the centres of the lowest and highest energy bins, respectively). Figure 2, shows that the data largely follow a power law, however, there are hints that the spectrum may contain substructure. These substructures could be a result of systematic effects, though an investigation into these effects is beyond the scope of this paper.

Figure 3 displays two of the three sub-spectra (datasets B and D) created to investigate the spectral behaviour of the system over the course of a single periastron passage. The inclusion of dataset D (the TeV low flux period) allows direct comparison between two unique flux states of the system to search for spectral variability. Additionally the total spectrum of the periastron passage, calculated with a fixed energy range, is shown in this figure. The data points in both Fig. 2 and for the sub-spectra in Fig. 3 were binned to ensure that every flux point has a statistical significance of at least 2σ.

We find a spectral index for the total periastron passage of $\Gamma = 2.78 \pm 0.05_{\rm stat} \pm 0.10_{\rm sys}$ (for the fixed energy range spectrum) which is consistent with the spectral index of previous years, $\Gamma = 2.76 \pm 0.03_{\rm stat} \pm 0.10_{\rm sys}$ (H.E.S.S. Collaboration et al. 2020).

We note a statistically significant difference between the spectral indices obtained through the power-law model describing dataset B and D (See Tab. 2). Accounting for the uncertainties, the spectral index change between these two datasets is $\Delta\Gamma = 0.56 \pm 0.18_{\rm stat} \pm 0.10_{\rm sys}$, implying a sub-orbital spectral variation at a c.i. of greater than 95%.

For the total unfixed spectrum, we attempted to fit an exponentially cut-off power-law model in order to determine if the data shows a preference for a high-energy cut-off. This revealed that a model with a cutoff is not preferred, with a lower limit on the cut-off energy of $E_C^{95\%} = 27.1$ TeV.

3.2. Flux analysis

For the 2021 periastron passage dataset, light curves were produced for the H.E.S.S. data in two different integration timescales, see Fig. 4. These were: night-wise binning and cycle-wise binning – grouping runs to individual observational cycles of ~ 28 days.

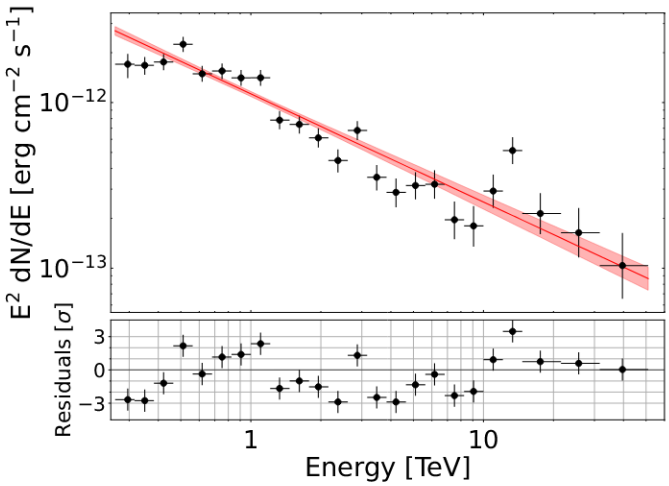

Fig. 2: Total spectrum of PSR B1259-63/LS 2883's 2021 periastron passage. The spectrum was produced from all data taken with H.E.S.S. during the 2021 periastron passage observations of PSR B1259-63/LS 2883, using an unfixed energy range. The spectrum has been fit with a power-law model. For details on the properties of the spectra displayed see Tab. 2. The red band indicates the 68% c.i. of the statistical error for the fitted model.

Individual flux points and their uncertainties were calculated using a reference spectrum, in this work this was a a power-law model in the energy range (0.4 - 100.0) TeV. An index of $\Gamma = 2.65$ was used, corresponding to the total 2021 dataset spectral index value.

We performed a search for variability in PSR B1259-63/LS 2883 over a number of different timescales, however, statistical uncertainties prevented us from establishing the presence of variability on run-to-run timescales[2]. Our analysis of the VHE data at $25 - 35$ days after periastron (the time period of fastest VHE flux increase) indicates that a model with a linearly increasing flux is a better fit to the data in this period than a constant flux model. This was determined by comparing the chi-squared values of a linear increase model, and a constant flux model, in this time period. The comparison of the fits of these methods showed that a linear flux increase is preferred at a $\sim 4\sigma$ level. During this time period the flux increased by a factor of two. Other than this increase in a period of ~ 10 days, we did not find significant evidence for a linear flux increase at shorter timescales. Thus, we see variability on timescales of down to ~ 10 days. It is possible that there exists variability on shorter timescales, however, we are unable to probe this due to statistics.

We investigated the impact of using an assumed spectral index of $\Gamma = 2.65$ to calculate the night-wise fluxes, given the discovery of sub-orbital spectral index variation. We investigated this by calculating binned fluxes using the two extreme values of the spectral index $\Gamma = 2.42$ (from the spectrum of the emission from dataset D) and $\Gamma = 2.98$

[2] Most commonly, subsequent runs were taken during the same or the following night, with the exception of several breaks due to moonlight or bad weather. Thus, run-to-run timescales range from a few hours to a few days.

Dataset	**Time** $- t_{\rm p}$ days	**Spectral Index** (Γ)	**Normalisation** (ϕ_0) Decorrelation Energy (E_0) 10^{-12} TeV^{-1} cm^{-2} s^{-1}	**Normalisation** (ϕ_0) (1 TeV) 10^{-12} TeV^{-1} cm^{-2} s^{-1}
Total 2021 (0.27 - 33.6 TeV)	−23.58 to +127.26	$2.65 \pm 0.04_{\rm stat} \pm 0.10_{\rm sys}$	$1.28 \pm 0.05_{\rm stat} \pm 0.26_{\rm sys}$ (0.95 TeV)	$1.13 \pm 0.04_{\rm stat} \pm 0.23_{\rm sys}$
Total 2021 (0.4 - 10 TeV)	−23.58 to +127.26	$2.78 \pm 0.05_{\rm stat} \pm 0.10_{\rm sys}$	$1.31 \pm 0.05_{\rm stat} \pm 0.26_{\rm sys}$ (0.95 TeV)	$1.15 \pm 0.04_{\rm stat} \pm 0.23_{\rm sys}$
2021 Periastron Period (*Dataset A*) (0.4 - 10 TeV)	−3.9 to +15.3	$2.75 \pm 0.11_{\rm stat} \pm 0.10_{\rm sys}$	$1.52 \pm 0.12_{\rm stat} \pm 0.30_{\rm sys}$ (0.95 TeV)	$1.34 \pm 0.10_{\rm stat} \pm 0.27_{\rm sys}$
2021 Peak TeV Flux (*Dataset B*) (0.4 - 10 TeV)	+25 to +36	$2.98 \pm 0.07_{\rm stat} \pm 0.10_{\rm sys}$	$5.00 \pm 0.22_{\rm stat} \pm 1.00_{\rm sys}$ (0.79 TeV)	$2.45 \pm 0.12_{\rm stat} \pm 0.49_{\rm sys}$
2021 GeV Flare Period (*Dataset C*) (0.4 - 10 TeV)	+55 to +108	$2.42 \pm 0.10_{\rm stat} \pm 0.10_{\rm sys}$	$0.38 \pm 0.03_{\rm stat} \pm 0.08_{\rm sys}$ (1.27 TeV)	$0.68 \pm 0.06_{\rm stat} \pm 0.14_{\rm sys}$
TeV Low Flux Period (*Dataset D*) (0.4 - 10 TeV)	+81 to +127	$2.42 \pm 0.17_{\rm stat} \pm 0.10_{\rm sys}$	$0.17 \pm 0.02_{\rm stat} \pm 0.03_{\rm sys}$ (1.40 TeV)	$0.37 \pm 0.05_{\rm stat} \pm 0.07_{\rm sys}$
Average of Previous Periastron Passages	−106 to +98	$2.76 \pm 0.09_{\rm stat} \pm 0.10_{\rm sys}$	-	$1.55 \pm 0.12_{\rm stat} \pm 0.31_{\rm sys}$

Table 2: Comparison of the best-fitting spectral parameters when a power-law model is fit to different datasets within the 2021 periastron passage of PSR B1259-63/LS 2883. Γ represents the best-fit photon index of the power law $\mathrm{d}N/\mathrm{d}E = \phi_0(E/E_0)^{-\Gamma}$, with ϕ_0 denoting the best-fit normalisation level, and E_0 being the decorrelation energy (Abdo et al. 2009). Presented here are the spectral properties of the total dataset of the periastron passage (for both fixed and unfixed energy ranges), as well as four additional sub-orbital periods from the 2021 dataset. All 2021 spectra in this table (with the exception of the total periastron passage spectrum marked "unfixed energy range") are calculated using an energy range of (0.4 - 10.0) TeV to enable comparison. The average spectral properties of H.E.S.S. stereo analysis from previous periastron passages (2004, 2007, 2011 and 2014, taken from H.E.S.S. Collaboration et al. 2020) are also included for comparison, from an averaging of the values reported in these papers. The spectra of previous periastron passages, however, do not use the same fixed energy values as the 2021 data. The two errors associated with each value are representative of, first, the magnitude of the statistical uncertainty in the value at a 95% confidence level, and secondly the systematic error in the measurements as adopted from Aharonian et al. (2006).

(dataset B). We then evaluated the difference between the nightwise fluxes of the two light curves that these indices produced. The percentage difference between the flux of the two new light curves yielded a maximum systematic error in the flux of ± 10%, a comparable value to that of Aharonian et al. (2006) from which the systematic error values of this study were taken (see Sec. 2 for details). This value represents an additional systematic flux error in the light curves exclusively, and does not have an impact on any scientific conclusions in the paper.

Although the 2021 VHE light curve presented in Fig. 4 shows an overall trend similar to the light curve obtained from the stacked analysis of the orbital-period-folded data collected during previous observations (H.E.S.S. Collaboration et al. 2020), we argue that a detailed comparison of the system's flux behaviour is complicated by the different coverage of the H.E.S.S. datasets. Despite observing at orbital phases close to the second disc crossing in the 2021 dataset, we do not see a VHE flux enhancement around this time. However, we report a VHE maximum occurring between $t_{\rm p} + 20$ and $t_{\rm p} + 50$ days (seen during the period of the maximum reported in previous years, H.E.S.S. Collaboration et al. 2020).

3.3. 2021 GeV flare

The 2021 GeV flare (shown in Fig. 6) differed in considerable ways from those of previous periastron passages (although the GeV behaviour appears inherently variable between periastron passages). As in 2017, the 2021 GeV flare

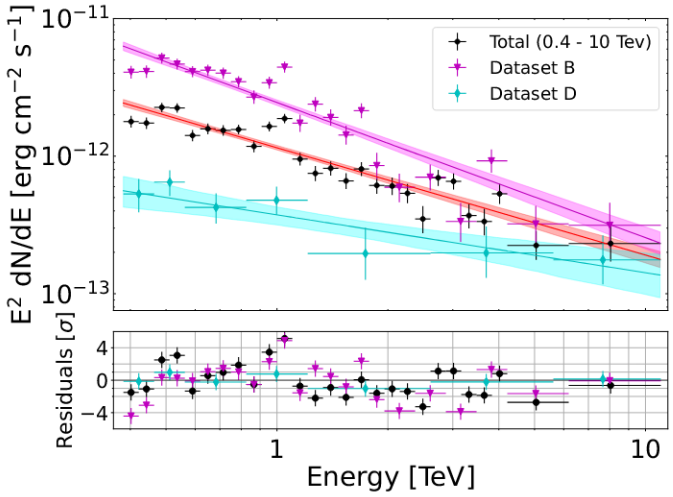

Fig. 3: Comparison of spectra from PSR B1259-63/LS 2883's 2021 periastron passage. Shown is the total spectrum of the 2021 periastron passage compared to two sub-spectra. Each model was calculated with the forward-folding method, using a power law in an energy range of (0.4 - 10.0) TeV to allow a comparison between them. Comparing spectra allowed us to search for VHE spectral variability on the scale of a single periastron passage. Displayed in red (black circles) is the spectrum of the total 2021 periastron passage, in cyan (cyan diamonds) the spectrum from the dataset D and in magenta (magenta triangles) the spectrum of dataset B. For details on the properties of the spectra displayed see Tab. 2. Shaded regions indicate the 68% c.i. for the fitted model.

started at $\sim t_{\rm p} + 55$ days with GeV activity extending to $\sim t_{\rm p} + 108$ days, see Chernyakova et al. (2021). The system underwent numerous rapid and energetic sub flares on very short timescales (in some cases as short as ~ 10 minutes) reaching up to 30 times the spin-down luminosity of the pulsar.

We see no correspondence to the 2021 GeV flare, from $\sim t_{\rm p} + 55$ days to $\sim t_{\rm p} + 108$ days, in the VHE light curve (see Sec. 3.5 for further investigation into this). We do, however, note that our ability to monitor this is somewhat complicated by a large gap in our observations during the 2021 GeV flare period, as no observations were performed in the time frame of $\sim t_{\rm p} + 65$ days to $\sim t_{\rm p} + 81$ days.

The spectrum of dataset C (derived during the 2021 GeV flare period) has a spectral index notably similar to that of dataset D. There is, therefore, also a discrepancy in the spectral index between datasets B and C at $\Delta\Gamma = 0.56 \pm 0.18$, the same level as the previously discussed discrepancy between dataset B and D.

3.4. X-ray-TeV correlation

We investigated a potential correlation between VHE and X-ray flux in the 2021 periastron passage data. In this study we utilise the results reported in Chernyakova et al. (2021), from the Neil Gehrels *Swift* (*Swift*) X-ray telescope (XRT) and the Neutron Star Interior Composition Explorer *NICER* (both in the $0.3-10$ keV range), covering the time period January, 19th, 2021 to May, 24th, 2021 ($t_{\rm p} - 21$ to $t_{\rm p} + 103$ days).

In order to perform the correlation study on timescales relevant to the system's behaviour, we binned the data from H.E.S.S. on a nightly basis, resulting in a total of 57 TeV points, compared to a total of 96 X-ray points binned by observations (32 of which from *NICER*, 64 from *Swift*). X-ray points had an average separation in time of 1.24 days (excluding time gaps of greater than a week) over the whole dataset.

A sub-selection of observations from both the TeV and X-ray datasets was made, ensuring the selection of only X-ray points occurring within one day of a TeV point. This correlation timescale of a day was selected because this is the shortest timescale in which the available statistics could confirm a lack of variability of PSR B1259-63/LS 2883 in X-rays. To make this sub-selection, we iterated over the data in steps of correlation timescale, where any TeV and X-ray points within this time became a correlated pair. Instances where two or more points of the same data type (X-ray or TeV[3]) were found to be within a single correlation timescale were handled by averaging the flux, time and uncertainties of the respective points. Any data points that did not contain a counterpart within one day of the point were not considered in the correlation study.

After this selection a total of 26 correlated pairs were found. This selection of correlated pairs and their distribution across the periastron passage can be seen in Fig. 6. The first correlated pair is at a time of $t_{\rm p} - 1.53$ days, extending up to the time of the final pair at $t_{\rm p} + 97.47$ days. The majority of pairs occurred at times later than $t_{\rm p} + 50$ days.

Figure 5 shows the results of the correlation investigation between the two datasets. By minimising η^2 (where η^2 is a linear combination of χ^2 tests, see appendix A for details of the η^2 test) we obtained the following best-fitting values of the linear fit parameters for the model $F_X = aF_{TeV} + b$: $a = 2.62^{+0.41}_{-0.38}$ and $b = 0.50^{+0.12}_{-0.13} \times 10^{-11}$ erg cm^{-2} s^{-1} (where F_X and F_{TeV} are the X-ray and TeV fluxes, respectively). These values of the fit gave a total $\eta^2 = 105.08$ for 26 correlated pairs, resulting in $\bar{\eta}^2 = 2.10$.

To estimate the statistical uncertainties we performed numerical simulations, considering $N = 10^6$ random trial datasets. The integrated X-ray and TeV photon flux for each trial dataset were simulated from the original data, assuming a Gaussian distribution of uncertainties. The quoted errors for each parameter correspond to a 68% c.i. of all best-fit values obtained during random trial datasets when fit with the same model. We estimated the chance probability of finding a correlation at $\bar{\eta}^2 = 2.10$ by comparing the number of trials that provided better η^2 values than the original data, to the number of trials with a worse η^2. Making this comparison we found a chance probability of 2.27×10^{-3}.

We therefore conclude that there is a positive correlation between the X-ray and TeV flux during the time periods of the 2021 perisatron that were probed by the study. While all points follow this linear trend, there are two notable outliers from the correlation. These pairs represent X-ray and TeV flux points that were measured shortly before $t_{\rm p} +$

[3] Formally, due to the TeV data being binned on a nightly basis it was not possible for two runs to occur within the same correlation timescale of a day. Thus this step only affected X-ray data points, which frequently occurred within a day of other X-ray points

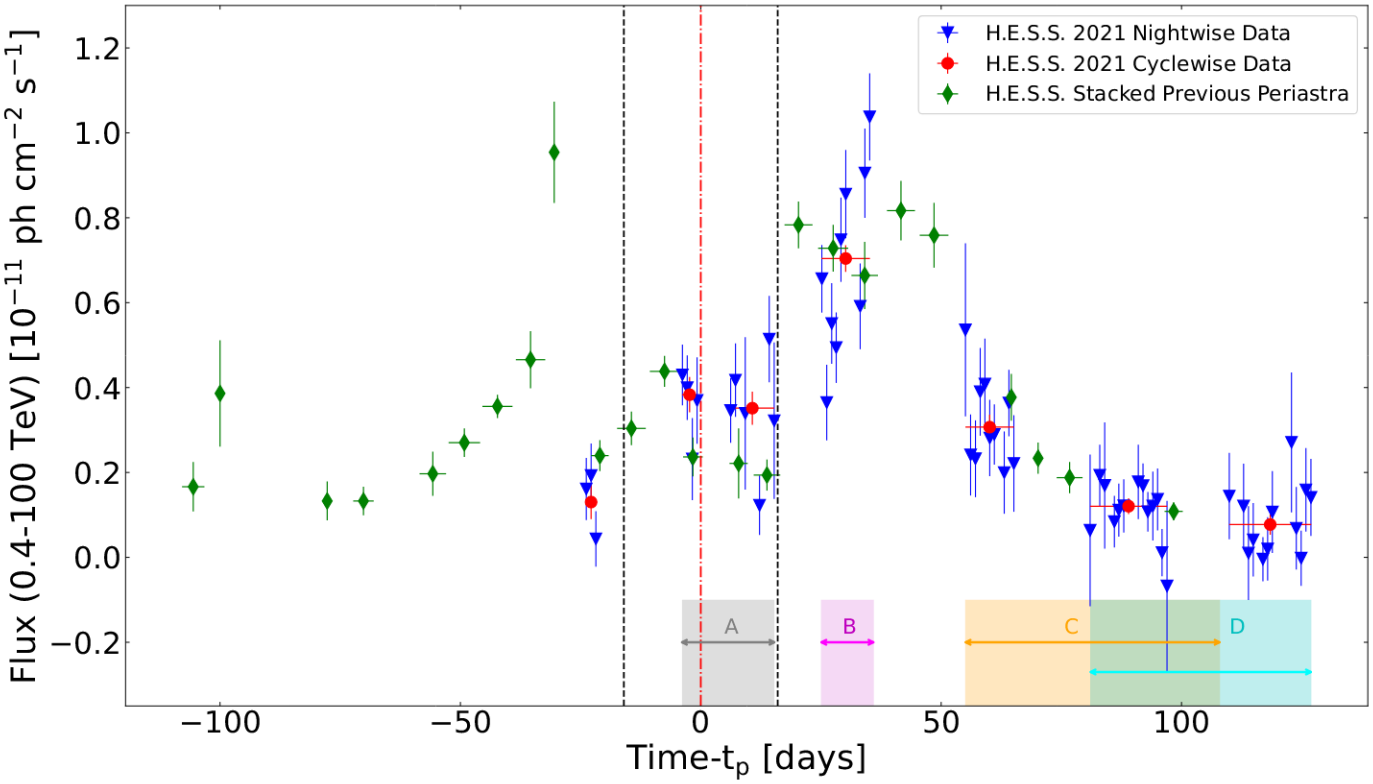

Fig. 4: VHE light curve of PSR B1259-63/LS 2883's 2021 periastron passage. VHE Data is shown in different binnings: night-wise binned fluxes (blue triangles), cycle-wise binned fluxes (red dots), and stacked data from H.E.S.S. observations of previous periastron passages (green diamonds). Horizontal error bars correspond to times of the earliest and latest runs that were merged to make the data point. Cycle-wise data contain the merged runs within one observational cycle ($\sim$ 28 days). Stacked data points have a weekly binning and correspond to data from the 2004, 2007, 2011, 2014 and 2017 periastron passages; these points were taken from H.E.S.S. Collaboration et al. (2020). The two dashed black lines at $t_p - 16$ days and $t_p + 16$ days correspond to the time at which the disc crossing is thought to occur, the dot-dashed red line at $t_p = 0$ days represents the point of periastron in the system. Finally, the shaded areas with arrows are displayed as a visual representation of the time periods from which sub datasets were taken. These regions are also marked with the letters of the dataset they represent. The grey region represents the time period encompassed by dataset A, the magenta region corresponds to the time period of dataset B, and the yellow region and the cyan regions indicate the time periods of datasets C and D, respectively; see Tab. 2 for the full details of these sub-periods.

16 days (see Figs. 6 and 5). With regards to the conclusion of a linear correlation, it is important to note that this initial study, which placed no restrictions on the time of the flux points used in the correlation, consisted mostly of flux points that were measured at times greater than t_p+25 days (see Fig. 6). This uneven sampling across the periastron passage prevents us from establishing the presence of such a correlation before this time period.

We separately assessed the correspondence of the VHE flux level to either the third X-ray peak or to the gradual decay seen in the X-ray flux profiles of previous years. To achieve this, we performed model fitting on the full dataset of 2021 VHE flux data, separately fitting both a negative exponential function and a negative exponential function combined with a Gaussian. Here, the negative exponential model is representative of the X-ray flux behaviour (corresponding well to the behaviour seen in previous years) and the Gaussian represents the flux profile of the third X-ray peak in 2021. In this comparison, the VHE data was better fit by the negative exponential function summed with a Gaussian, at a 5.5σ level. However, this fit is based on the available VHE data points that occur only immediately before the peak (see Fig. 6). Therefore, the limited number of points immediately after the peak makes it difficult to draw more robust claims.

In addition, we undertook a separate correlation study utilising only data occurring after the time of the second X-ray peak in 2021 ($t_p + 16$ days). The data from before this point, notably, were the cause of the blue coloured outliers at greater than 68% c.i. seen in the linear correlation in Fig. 5. We apply exactly the same method as described previously. This results in a goodness-of-fit value of $\eta^2 = 57.77$ that, for 22 correlated pairs, results in a $\bar{\eta}^2 = 1.38$ (compared to a value of $\bar{\eta}^2 = 2.10$ for the unrestricted dataset) and gave a chance probability of 8.3×10^{-4}.

3.5. GeV – TeV correlation

We also conducted a study into the correlation between the 2021 TeV and GeV datasets to further quantify the apparent absence of a TeV counterpart to the 2021 GeV flare. We utilise daily-binned GeV flux data from Chernyakova et al. (2021) for comparison with the nightly-binned TeV data. The method of correlation used was identical to that

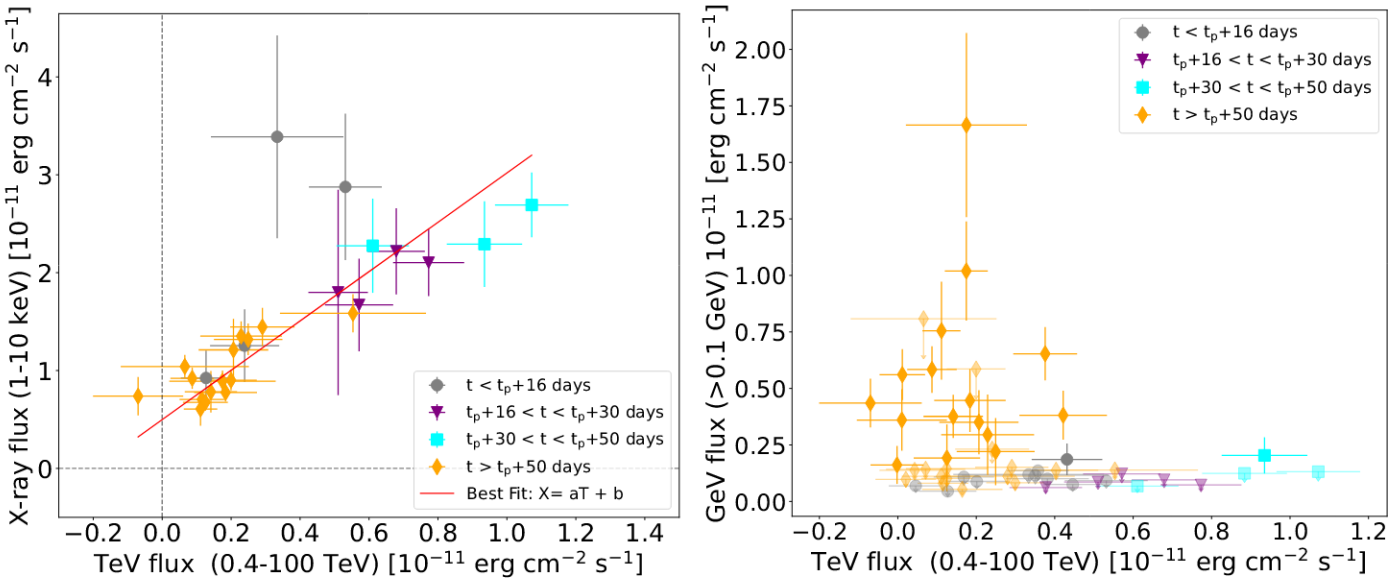

Fig. 5: Linear correlations between X-ray-TeV and GeV-TeV data sets. **Left panel:** Linear correlation ($F_X = aF_{TeV} + b$) between the flux of the TeV and X-ray datasets, where exclusively integrated energy flux points measured within a day of one another were utilised. Shown in red is the line of best-fit resulting from a linear fit with an offset. A large outlier can be seen at TeV flux $\sim 0.3 \times 10^{-11}$ erg cm^{-2} s^{-1}; this outlier originates from rapid X-ray variability in the period from periastron up to $\sim t_p + 16$ days. The dashed lines mark the zero points of each axis. As can be seen, there is a non-zero X-ray flux value at zero TeV flux in the fit.
Right panel: Correlation plot of the flux of the TeV and GeV datasets, where exclusively flux points measured within a day of one another were used. Note that transparent points correspond to upper limits taken from the *Fermi*-LAT daily light curve, where each upper limit has been assumed to have a flux of half the upper limit value and a flux error corresponding to a 95% c.i. on the *Fermi* upper limit. GeV flux points have been adapted from Chernyakova et al. (2021). In both figures the orbital phases from which correlation points are taken are denoted by their colour (see Fig. 6).

of the previous study between X-ray and TeV data. Despite known sub-flares at GeV energies, sometimes on timescales of ten minutes, we opted to utilise a timescale of one day. This correlation length matched the binning of the two light curves, and is also consistent with the X-ray – TeV correlation results.

Following the correlated pair selection, a total of 56 correlated pairs (from 57 TeV points and 187 GeV points) were selected. The first of these is at a time of $t_p - 23.5$ days, extending up to t_p+126.5 days. Because all but one TeV points are time-correlated with a GeV point, in the GeV/TeV correlation these pairs are relatively evenly sampled across the time range of the periastron passage, reflecting the distribution of the TeV points. The majority of the correlated GeV points, however, are upper limits from the *Fermi* analysis (144 of 187 points). We therefore tested for a correlation using several approaches. Firstly, we simply omitted the upper limits from the correlation study. This resulted in an $\bar{\eta}^2 = 11.56$. However such a selection introduces a bias towards high GeV fluxes and could mask an existing correlation. We therefore examined two approaches including upper limits, these methods corresponded to adopting a Gaussian distribution as the probability density function (PDF) for the upper limits (see Kelly 2007, for further details and alternative treatments of the PDF). The first of these approaches was to utilise half the upper limit value as the flux value and a dispersion corresponding to 95% c.i. of the *Fermi* upper limits. The second method utilised a zero value as the flux estimate (and once again a dispersion corresponding to 95% c.i. of the *Fermi* upper limits). The resulting $\bar{\eta}^2$ values were 15.02 and 10.67 for the Gaussian centered on half the upper limit value and the Gaussian centered at zero, respectively. All of these tests excluded a correlation at levels greater than 5σ. We conclude that (within the uncertainties of the measurements) we detect no significant GeV – TeV correlation throughout the entire probed time period.

4. Discussion

Understanding the broadband emission from GRLBs is a complex problem, which still awaits a definite solution. Despite the difficulties, some progress, however, has been made in the modeling of emission from these systems. PSR B1259-63/LS 2883 contains a non-accreting pulsar, thus, in what follows we discuss the properties of the emission in the framework of a binary pulsar model. This scenario implies that the relativistic outflow from a rotation powered pulsar interacts with the stellar wind which, in the case of PSR B1259-63/LS 2883, consists of a radiation-driven polar wind, and a significantly more dense Keplerian-like decretion disc.

4.1. Orbital dependence of the X-ray and TeV emission

The termination of the pulsar wind occurs at a distance of R_{ts} (from the pulsar) where the ram pressure of the stellar and pulsar winds are equal. Given the much higher anticipated speed of the pulsar wind, the energy injection of non-thermal particles into the interaction region is dominated

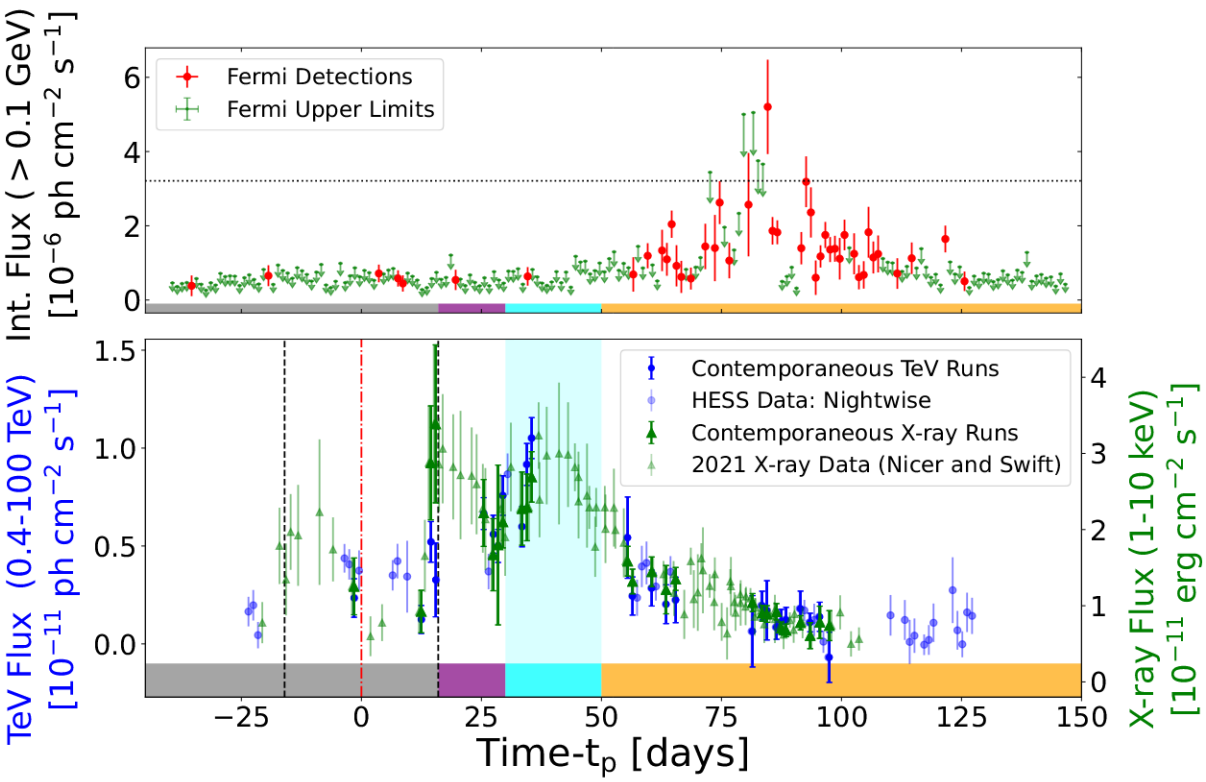

Fig. 6: Comparison of the 2021 GeV light curve to the correlated X-ray and VHE light curves. **Upper panel:** The GeV light curve of PSR B1259-63/LS 2883's 2021 periastron passage observed with *Fermi*-LAT ($0.1 - 10$ GeV). Figure adapted from Chernyakova et al. (2021). Data points represent daily binnings, with green points indicating 95% upper limits and red points denoting detections ($TS > 4$). The horizontal black dashed line marks the flux value corresponding to the spin-down luminosity of PSR B1259-63/LS 2883's pulsar $L_{\rm sd} = 8.2 \times 10^{35}$ erg s^{-1} (see Chernyakova et al. 2021). **Lower panel:** Light curve of PSR B1259-63/LS 2883's 2021 periastron passage displaying both VHE flux points from H.E.S.S. and X-ray data from the *Swift* and *NICER* observatories. Points with no transparency are points that were selected by the time correlation step and fell within a day of an alternate type of observation (see text for further details). Translucent points are data from each respective dataset that did not pass the time correlation step. The lines at $\sim t_{\rm p} \pm 16$ days represent the assumed disc crossing times and the line at $t_{\rm p} = 0$ days marks the time of periastron. In both panels, coloured regions correspond to the orbital phases of correlation points in Fig. 5 that share the same colour. Here the grey region represents orbital phases before $t_{\rm p} + 16$ days, the purple region represents the time frame $t_{\rm p} + 16$ to $t_{\rm p} + 30$ days, the cyan region is the time frame $t_{\rm p} + 30$ to $t_{\rm p} + 50$ days (coincident with the third X-ray peak reported in 2021 X-ray data), and the orange region corresponds to any time after $t_{\rm p} + 50$ days.

by contributions from the pulsar. Therefore, one expects that the radiation processes in binary pulsar systems are similar to those taking place in pulsar wind nebulae (Tavani et al. 1994; Tavani & Arons 1997), however, with the caveat of some important modifications.

Firstly, as the magnetic field is provided by the pulsar wind, a smaller termination distance necessarily implies a stronger magnetic field:

$$B \lesssim B_{\rm max} = \sqrt{\frac{L_{\rm sd}}{cR_{\rm ts}^2}} \approx 3 \left(\frac{L_{\rm sd}}{8.2\times10^{35}{\rm erg\,s^{-1}}}\right)^{1/2} \left(\frac{R_{\rm ts}}{0.1{\rm AU}}\right)^{-1} {\rm G}\,, \quad (1)$$

where $L_{\rm sd}$ is the pulsar's spin down luminosity. The second important difference is that the photon field is dominated by contributions from the optical companion. This provides an intense photon field with an energy density of

$$w_{\rm ph} = \frac{L_*}{4\pi cR^2} \approx 3 \left(\frac{L_*}{2.3\times10^{38}{\rm erg\,s^{-1}}}\right) \left(\frac{R}{1\,{\rm AU}}\right)^{-2} {\rm erg\,cm^{-3}}\,, \quad (2)$$

where R is the separation between the star and the pulsar (system separation). For simplicity, we assume that the production region is located close to the pulsar.

For a Gauss-strength magnetic field, VHE electrons generate synchrotron emission in the hard X-ray band. Binary pulsar systems were predicted, therefore, to be TeV sources, provided that the energy density of the stellar photon field is comparable to the expected energy density of the magnetic field (Kirk et al. 1999). For an accurate calculation of the expected TeV flux level, one needs to account for a number of effects including the Klein-Nishina cutoff, IC scattering in the anisotropic regime, and gamma-gamma attenuation (Kirk et al. 1999).

Under the assumption of isotropic winds, the pulsar wind termination distance is proportional to the system separation distance, $R_{\rm ts} \propto R$. Thus, the ratio of the photon to magnetic field energy density does not depend on the orbital phase, and one may expect quite similar X-ray and TeV light curves unless γ–γ attenuation is significant (Dubus 2006; Khangulyan et al. 2007; Sushch & van Soelen 2017; Sushch & van Soelen 2023). However, one needs to take into account that some physical parameters can change their values depending on the orbital phase. For example, the magnetic field strength, which is expected to be proportional to the distance to the termination shock, may undergo a significant change with orbital phase. Consequently, this may induce a change of the cooling regime and/or of the synchrotron component (Khangulyan et al. 2012; Dubus & Cerutti 2013).

Unless the stellar disc or locally generated fields provide significant targets for IC scattering, the temperature of the target photons does not vary with orbital phase. However, one needs to account for the change of the scattering angle. For an orbital inclination angle of $i \approx 154°$ (Miller-Jones et al. 2018), and for a production region in the orbital plane during the epochs of the H.E.S.S. observations (see Fig. 7), the IC scattering angle is approximately 65°. In this case,

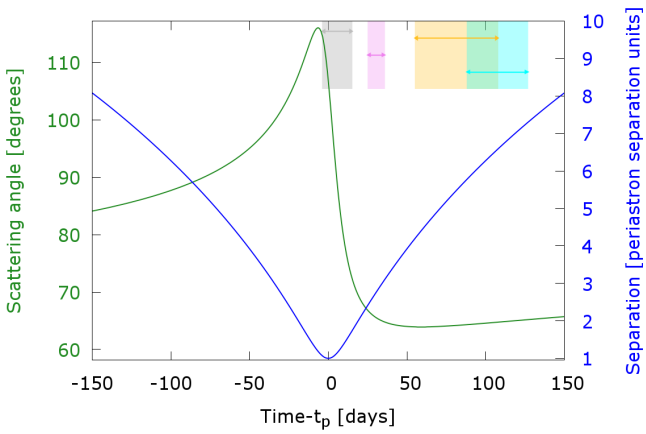

Fig. 7: Comparison of the scattering angle of IC processes to separation of the two objects comprising PSR B1259-63/LS 2883. **Left axis, green curve:** The angle between the line-of-sight and the direction from the optical star at the pulsar's location, as a function of time to periastron passage. If the production region is close to the pulsar, this angle is equal to the scattering angle for IC processes. **Right axis, blue curve:** The ratio of the separation distance, R, to the periastron separation. The shaded regions in this plot represent the periods of the sub spectra and are defined as in Fig. 4 (see Tab. 2 for the full details of these sub-periods).

an emission of energy 1 TeV may be generated by electrons with energy $E_{\rm TeV} \approx 1.6$ TeV; here we adopt a photon field temperature of $T_* \approx 3\times10^4$ K (Negueruela et al. 2011), and use the approximation from Khangulyan et al. (2014).

Because of the eccentric orbit of the pulsar in the system, the system separation changes by a factor of four during the period relevant for the H.E.S.S. observations. This will therefore induce a proportional change of the magnetic field strength in the production region, meaning that the energy of the X-ray emitting electrons may change by a factor of ≈ 2. For a typical X-ray spectrum slope of 1.5 (the average value obtained from *Swift* observations by Chernyakova et al. 2021), X-ray emitting electrons have an E^{-2} energy distribution and so, even in an idealised case of isotropic winds, the relationship between X-ray and TeV luminosity should depend on separation as:

$$L_X \propto L_{\rm TeV} R^{1/2}\,. \quad (3)$$

In Fig. 5, the linear fit is mostly constrained by pairs of correlated X-ray and TeV runs occurring at $t > t_{\rm p}+50$ days, i.e., when R is large and changes more slowly with time. For smaller separation distances, using Eq. (3) one should expect that the linear fit overestimates the X-ray flux level. However, from Fig. 5 one can see that for certain pairs the measured X-ray flux is significantly higher than the value given by the linear fit. This could be considered as a hint of the wind interaction in a non-isotropic regime (e.g a Keplerian decretion disc, a non-isotropic pulsar wind, or changes in the scattering angle between relativistic electrons and soft photons). Indeed, the points with high relative X-ray flux correspond to orbital phases close to $t_{\rm p}$ + 16 days, where the pulsar may interact with the stellar disc. Providing a significantly dense stellar disc, the pulsar wind

will terminate significantly closer to the pulsar, enhancing the magnetic field strength without a proportional enhancement of the photon field (Khangulyan et al. 2007; Takata et al. 2012; Sushch & Böttcher 2014). This results in increasing X-ray flux and a softer X-ray spectrum during the disc crossing, consistent with available observations (see e.g., Chernyakova et al. 2014).

Analysis of the X-ray – TeV emission correlation reveals that there is a contribution to the X-ray flux that depends weakly on the TeV flux level (the contribution due to the constant term in the linear relationship). This could indicate the presence of two or more zones that generate non-thermal emission. This is also supported by the absence of a strong correlation between the X-ray and radio emission. Up to about 30 days after periastron, radio and X-ray emission show a very good correlation, but following this the X-ray flux starts to increase while the radio flux continues decreasing (see in Chernyakova et al. 2021).

This third X-ray peak, occuring 30-50 days after periastron (Chernyakova et al. 2021), has not been reported in previous periastron passages. Although we lack TeV observations in 2021 during a larger fraction of this period, there is good evidence (from a significant TeV flux rise around $t_{\mathbf{p}} + 30$ days, a good correlation with X-ray data in this period, and from the light curve template fitting discussed in Sect. 3.2) that there is a correspondence of the third X-ray peak in the 2021 TeV light curve. However, because of the gap in TeV coverage after $t_{\mathbf{p}} + 35$ days, the time at which the maximum occurs in the TeV light curve is not well constrained and could be shifted with respect to the X-ray peak.

Summarising the multiwavelength data from Chernyakova et al. (2021) during the period 30-60 days post-periastron, we see that the radio emission decreases, X-ray emission increases and then decreases, GeV emission stays in a low-emission state. From the H.E.S.S. data, we see that the TeV emission increases and then decreases. Immediately following this period, the GeV emission increases strongly with no corresponding increase in any other band. Given the variation seen in emission profiles, it is difficult to reconcile all of these observational trends with a simple one-zone model for the post-periastron time-evolution of the non-thermal emission. A multi-zone configuration can be produced by the complex geometry and dynamics of the interaction between the pulsar and stellar winds (Bogovalov et al. 2008; Bosch-Ramon et al. 2012; Dubus et al. 2015; Huber et al. 2021), and it appears likely that such models are required to explain the data. The correlation of the TeV and X-ray light curves 30 days after periastron, suggests either that the electron population responsible for the third X-ray peak also emits in the TeV regime. Alternatively, given that the observed TeV light curve is compatible with previous periastron passages, it is possible that the X-ray emission accompanying the TeV peak was suppressed for some reason during previous periastron passages.

The nature of the GeV flare, which is not accompanied by an increase in emission at any other waveband, remains puzzling. This scenario could potentially be connected to a complex evolution of the wind termination shock, i.e. strong confinement of the pulsar wind due to either the eccentricity of the orbit (Barkov & Bosch-Ramon 2016), or the interaction with the circumstellar disc (Khangulyan et al. 2012) followed by a rapid expansion of the pulsar wind bubble later on.

4.2. Spectral variability

Another important finding in the H.E.S.S. 2021 dataset is spectral variability of the VHE emission. While in other GRLBs spectral variability is an established feature of the TeV emission (most notably in LS 5039, Aharonian et al. 2005a), the previously reported VHE spectra of PSR B1259-63/LS 2883 have a power-law shape with statistically indistinguishable photon indexes (H.E.S.S. Collaboration et al. 2020).

In the context of GRLBs there are three major factors that cause changes of the VHE spectral slope: γ–γ attenuation, anisotropic IC scattering, and changes in the distribution of emitting particles due to the orbital phase. In the specific case of PSR B1259-63/LS 2883, γ–γ attenuation might be relevant only at points close to the periastron passage which, most likely, has no significant impact during the orbital phases relevant for H.E.S.S. observations in 2021. Similarly, there is no significant change of the scattering angle during this period (see Fig. 7). With these aforementioned factors accounted for, the H.E.S.S. spectral variation measurement implies a hardening of the electron distribution that could, for example, be caused by a change of the cooling regime. If one assumes that the winds interact in an isotropic regime, then the rate of IC and synchrotron losses have a similar dependence ($\propto R^{-2}$) on the orbital phase. On the other hand, the rate of adiabatic losses scale differently, $\propto R^{-1}$ (see, e.g., Khangulyan et al. 2008b). Hence, one expects that at large system separations, the transition to an adiabatic loss-dominated cooling regime occurs at higher energies.

If this process indeed defines the hardening of the VHE spectrum, then one should also expect an analogous hardening during similar epochs prior to the periastron passage. The stacked analysis of the H.E.S.S. data collected in 2004, 2007, 2011, 2014, and 2017 indicates that VHE emission during the interval $t_{\rm p} - 109$ days to $t_{\rm p} - 47$ days has a photon index of $\Gamma = 2.7 \pm 0.1_{\rm stat} \pm 0.1_{\rm sys}$ (H.E.S.S. Collaboration et al. 2020) which is, in fact, significantly softer than the value obtained from "symmetric" orbital phases in 2021 (e.g., $\Gamma = 2.42 \pm 0.1_{\rm stat} \pm 0.1_{\rm sys}$ for the dataset C). A complicating factor is that during the pre-periastron passage period the IC scattering angle is larger (see in Fig. 7) and the resulting VHE spectrum is expected to be softer (see, e.g., Khangulyan et al. 2008a).

In summary, it appears that the observed spectral change can be explained in the context of a hardening of the electron spectrum. This is, in turn, driven by changes in the scaling of cooling timescales as a result of varying orbital separation. A detailed numerical model is required to quantitatively test the viability of such a scenario and is beyond the scope of this paper. The possible important role of adiabatic losses supports the general conclusion that in binary pulsar systems, (magneto)hydrodynamic processes play an essential role for non-thermal radiation formation (Bogovalov et al. 2008, 2012, 2019; Bosch-Ramon et al. 2012). Hydrodynamic processes may also lead to the formation of several distinct production regions (Zabalza et al. 2013; Dubus et al. 2015; Huber et al. 2021), and the existence of these seem to be supported by observational evidence. In particular we note the lack of a firm correlation between

X-ray and radio emission (Chernyakova et al. 2021), and the very different properties of the GeV and TeV emission detected from the system. A similar absence of correlation between GeV and TeV emission was seen during previous periastron passages (H.E.S.S. Collaboration et al. 2020).

5. Conclusions

This work summarises the results from the H.E.S.S. observations and analysis of the 2021 perisatron of the PSR B1259-63/LS 2883 system in the VHE band. As displayed in Tab. 2, our spectral studies reveal that the periastron-averaged spectrum can be described by a power-law model, with a spectral index of $\Gamma = 2.75 \pm 0.05_{\rm stat} \pm 0.1_{\rm sys}$. This value is consistent with the average value reported in previous periastron passages (H.E.S.S. Collaboration et al. 2020). We find that the fit has no preference to a power-law containing a cut-off component, with a lower limit on the cut-off energy of $E_C^{95\%} = 27.1$ TeV. We also present, for the first time, evidence of spectral variability on a sub-orbital scale. A difference of $\Delta\Gamma = 0.56 \pm 0.18_{\rm stat} \pm 0.10_{\rm sys}$ (at greater than 95% c.i.) is seen between the spectral slopes of datasets B and D, see Tab. 2. Since during the epochs corresponding to the datasets B and D, the γ–γ absorption is negligible and the change of the IC scattering angle is small, the revealed hardening indicates on a change of the energy distribution of the emitting particles, which can be caused by a change of the cooling regime.

The study of contemporaneous X-ray and TeV fluxes allowed the establishment of a linear correlation between the two energy bands. While the majority of the dataset is fitted relatively well by the applied linear fit (see in Fig. 6), two data pairs show significantly higher X-ray flux levels. The two outliers correspond to orbital phases when the pulsar likely interacts with the disc, therefore the structure of the flow deviates considerably from an axially-symmetric configuration. During this period, it is expected that the pulsar wind terminates at a significantly smaller distance, thereby strongly enhancing the magnetic field.

Regarding the TeV data taken during the time period of the third X-ray peak, we argue that there is good evidence for a correspondence of this TeV data to the third X-ray peak, in the 2021 TeV light curve. However, the time of the maximum in the TeV light curve is not well constrained because of a lack of data 35-55 days post-periastron. Nevertheless, this feature is very interesting and requires further investigation.

The correlation obtained contains a significant constant term, which implies a presence of X-ray emitting electrons with no proportional TeV component. This supports the existence of a multiple emission zone geometry within the system. The evidence for a multi-zone setup can also be obtained from the uncorrelated radiation in the GeV and TeV energy bands, as well as from the absence of a strong X-ray – radio correlation. The formation of a multi-zone setup can originate as a result of the complexity of the hydrodynamics within the pulsar and stellar wind interaction. The detection of spectral hardening at TeV energies after the 2021 periastron passage, together with the measured X-ray – TeV correlation, provide new constraints that will contribute to building a consistent physical model for the multiwavelength emission from PSR B1259-63/LS 2883.

Acknowledgements

The support of the Namibian authorities and of the University of Namibia in facilitating the construction and operation of H.E.S.S. is gratefully acknowledged, as is the support by the German Ministry for Education and Research (BMBF), the Max Planck Society, the Helmholtz Association, the French Ministry of Higher Education, Research and Innovation, the Centre National de la Recherche Scientifique (CNRS/IN2P3 and CNRS/INSU), the Commissariat à l'énergie atomique et aux énergies alternatives (CEA), the U.K. Science and Technology Facilities Council (STFC), the Irish Research Council (IRC) and the Science Foundation Ireland (SFI), the Polish Ministry of Education and Science, agreement no. 2021/WK/06, the South African Department of Science and Innovation and National Research Foundation, the University of Namibia, the National Commission on Research, Science & Technology of Namibia (NCRST), the Austrian Federal Ministry of Education, Science and Research and the Austrian Science Fund (FWF), the Australian Research Council (ARC), the Japan Society for the Promotion of Science, the University of Amsterdam and the Science Committee of Armenia grant 21AG-1C085. We appreciate the excellent work of the technical support staff in Berlin, Zeuthen, Heidelberg, Palaiseau, Paris, Saclay, Tübingen and in Namibia in the construction and operation of the equipment. This work benefited from services provided by the H.E.S.S. Virtual Organisation, supported by the national resource providers of the EGI Federation.

References

Abdo, A. A., Ackermann, M., Ajello, M., et al. 2011, ApJ, 736, L11
Abdo, A. A., Ackermann, M., Ajello, M., et al. 2009, Science, 325, 840
Abdo, A. A., Ackermann, M., Ajello, M., et al. 2009, The Astrophysical Journal, 707, 1310
Acero, F., Ackermann, M., Ajello, M., et al. 2013, The Astrophysical Journal, 773, 77
Aharonian, F., Akhperjanian, A. G., Anton, G., et al. 2009, A&A, 507, 389
Aharonian, F., Akhperjanian, A. G., Aye, K. M., et al. 2005a, Science, 309, 746
Aharonian, F., Akhperjanian, A. G., Aye, K.-M., et al. 2005b, A&A, 442, 1
Aharonian, F., Akhperjanian, A. G., Aye, K. M., et al. 2005c, A&A, 442, 1
Aharonian, F., Akhperjanian, A. G., Bazer-Bachi, A. R., et al. 2006, ApJ, 636, 777
Barkov, M. V. & Bosch-Ramon, V. 2016, MNRAS, 456, L64
Bausch, J. 2013, Journal of Physics A: Mathematical and Theoretical, 46, 505202
Berge, D., Funk, S., & Hinton, J. 2007, A&A, 466, 1219
Bogovalov, S. V., Khangulyan, D., Koldoba, A., Ustyugova, G. V., & Aharonian, F. 2019, MNRAS, 490, 3601
Bogovalov, S. V., Khangulyan, D., Koldoba, A. V., Ustyugova, G. V., & Aharonian, F. A. 2012, MNRAS, 419, 3426
Bogovalov, S. V., Khangulyan, D. V., Koldoba, A. V., Ustyugova, G. V., & Aharonian, F. A. 2008, MNRAS, 387, 63
Bosch-Ramon, V., Barkov, M. V., Khangulyan, D., & Perucho, M. 2012, A&A, 544, A59
Caliandro, G. A., Cheung, C. C., Li, J., et al. 2015, ApJ, 811, 68
Chang, Z., Zhang, S., Chen, Y.-P., et al. 2021, Universe, 7, 472
Chernyakova, M., Abdo, A. A., Neronov, A., et al. 2014, MNRAS, 439, 432
Chernyakova, M., Malyshev, D., Paizis, A., et al. 2019, A&A, 631, A177
Chernyakova, M., Malyshev, D., van Soelen, B., et al. 2021, Universe, 7, 242
Chernyakova, M., Neronov, A., van Soelen, B., et al. 2015, MNRAS, 454, 1358
Cominsky, L., Roberts, M., & Johnston, S. 1994, ApJ, 427, 978

de Naurois, M. & Rolland, L. 2009, Astroparticle Physics, 32, 231
Dubus, G. 2006, A&A, 451, 9
Dubus, G. 2013, A&A Rev., 21, 64
Dubus, G. & Cerutti, B. 2013, A&A, 557, A127
Dubus, G., Lamberts, A., & Fromang, S. 2015, A&A, 581, A27
Gaia Collaboration, Brown, A. G. A., Vallenari, A., et al. 2018, A&A, 616, A1
H. E. S. S. Collaboration, Abramowski, A., Acero, F., et al. 2012, A&A, 548, A46
H. E. S. S. Collaboration, Abramowski, A., Acero, F., et al. 2013, A&A, 551, A94
H.E.S.S. Collaboration, Abdalla, H., Adam, R., et al. 2020, A&A, 633, A102
Huber, D., Kissmann, R., Reimer, A., & Reimer, O. 2021, A&A, 646, A91
Johnson, T. J., Wood, K. S., Kerr, M., et al. 2018, ApJ, 863, 27
Johnston, S., Ball, L., Wang, N., & Manchester, R. N. 2005, MNRAS, 358, 1069
Johnston, S., Manchester, R. N., Lyne, A. G., et al. 1992, ApJ, 387, L37
Johnston, S., Manchester, R. N., Lyne, A. G., et al. 1996, MNRAS, 279, 1026
Johnston, S., Manchester, R. N., Lyne, A. G., Nicastro, L., & Spyromilio, J. 1994, MNRAS, 268, 430
Kelly, B. C. 2007, ApJ, 665, 1489
Khangulyan, D., Aharonian, F., & Bosch-Ramon, V. 2008a, MNRAS, 383, 467
Khangulyan, D., Aharonian, F. A., Bogovalov, S. V., & Ribó , M. 2012, The Astrophysical Journal, 752, L17
Khangulyan, D., Aharonian, F. A., & Kelner, S. R. 2014, ApJ, 783, 100
Khangulyan, D., Hnatic, S., Aharonian, F., & Bogovalov, S. 2007, Monthly Notices of the Royal Astronomical Society, 380, 320
Khangulyan, D. V., Aharonian, F. A., Bogovalov, S. V., Koldoba, A. V., & Ustyugova, G. V. 2008b, International Journal of Modern Physics D, 17, 1909
Kirk, J. G., Ball, L., & Skjæraasen, O. 1999, Astroparticle Physics, 10, 31
Li, T. P. & Ma, Y. Q. 1983, ApJ, 272, 317
Marino, A., Driessen, L., Lenc, E., et al. 2023, The Astronomer's Telegram, 15942, 1
Miller-Jones, J. C. A., Deller, A. T., Shannon, R. M., et al. 2018, Monthly Notices of the Royal Astronomical Society, 479, 4849
Negueruela, I., Ribó , M., Herrero, A., et al. 2011, The Astrophysical Journal, 732, L11
Parsons, R. & Hinton, J. 2014, Astroparticle Physics, 56, 26
Piron, F., Djannati-Atai, A., Punch, M., et al. 2001, A&A, 374, 895
Shannon, R. M., Johnston, S., & Manchester, R. N. 2014, MNRAS, 437, 3255
Sushch, I. & Böttcher, M. 2014, Journal of High Energy Astrophysics, 3, 18
Sushch, I. & van Soelen, B. 2017, ApJ, 837, 175
Sushch, I. & van Soelen, B. 2023, The Astrophysical Journal, 959, 30
Takata, J., Okazaki, A. T., Nagataki, S., et al. 2012, ApJ, 750, 70
Tam, P. H. T., Huang, R. H. H., Takata, J., et al. 2011, ApJ, 736, L10
Tavani, M. & Arons, J. 1997, ApJ, 477, 439
Tavani, M., Arons, J., & Kaspi, V. M. 1994, ApJ, 433, L37
van Soelen, B. & Meintjes, P. J. 2015, Mem. Soc. Astron. Italiana, 86, 123
Weng, S.-S., Qian, L., Wang, B.-J., et al. 2022, Nature Astronomy, 6, 698
Wood, K. S., Johnson, T., Ray, P. S., et al. 2018, in American Astronomical Society Meeting Abstracts, Vol. 231, American Astronomical Society Meeting Abstracts #231, 233.04
Yoneda, H., Makishima, K., Enoto, T., et al. 2020, Physical review letters, 125, 111103
Zabalza, V., Bosch-Ramon, V., Aharonian, F., & Khangulyan, D. 2013, A&A, 551, A17

[1] Dublin Institute for Advanced Studies, 31 Fitzwilliam Place, Dublin 2, Ireland
[2] Max-Planck-Institut für Kernphysik, P.O. Box 103980, D 69029 Heidelberg, Germany
[3] Yerevan State University, 1 Alek Manukyan St, Yerevan 0025, Armenia
[4] Landessternwarte, Universität Heidelberg, Königstuhl, D 69117 Heidelberg, Germany
[5] Kapteyn Astronomical Institute, University of Groningen, Landleven 12, 9747 AD Groningen, The Netherlands
[6] Laboratoire Leprince-Ringuet, École Polytechnique, CNRS, Institut Polytechnique de Paris, F-91128 Palaiseau, France
[7] University of Namibia, Department of Physics, Private Bag 13301, Windhoek 10005, Namibia
[8] Centre for Space Research, North-West University, Potchefstroom 2520, South Africa
[9] Deutsches Elektronen-Synchrotron DESY, Platanenallee 6, 15738 Zeuthen, Germany
[10] Institut für Physik und Astronomie, Universität Potsdam, Karl-Liebknecht-Strasse 24/25, D 14476 Potsdam, Germany
[11] Université de Paris, CNRS, Astroparticule et Cosmologie, F-75013 Paris, France
[12] Department of Physics and Electrical Engineering, Linnaeus University, 351 95 Växjö, Sweden
[13] Institut für Physik, Humboldt-Universität zu Berlin, Newtonstr. 15, D 12489 Berlin, Germany
[14] Laboratoire Univers et Théories, Observatoire de Paris, Université PSL, CNRS, Université Paris Cité, 5 Pl. Jules Janssen, 92190 Meudon, France
[15] Sorbonne Université, CNRS/IN2P3, Laboratoire de Physique Nucléaire et de Hautes Energies, LPNHE, 4 place Jussieu, 75005 Paris, France
[16] IRFU, CEA, Université Paris-Saclay, F-91191 Gif-sur-Yvette, France
[17] University of Oxford, Department of Physics, Denys Wilkinson Building, Keble Road, Oxford OX1 3RH, UK
[18] Friedrich-Alexander-Universität Erlangen-Nürnberg, Erlangen Centre for Astroparticle Physics, Nikolaus-Fiebiger-Str. 2, 91058 Erlangen, Germany
[19] Astronomical Observatory, The University of Warsaw, Al. Ujazdowskie 4, 00-478 Warsaw, Poland
[20] Université Savoie Mont Blanc, CNRS, Laboratoire d'Annecy de Physique des Particules - IN2P3, 74000 Annecy, France
[21] Instytut Fizyki Jądrowej PAN, ul. Radzikowskiego 152, 31-342 Kraków, Poland
[22] School of Physics, University of the Witwatersrand, 1 Jan Smuts Avenue, Braamfontein, Johannesburg, 2050 South Africa
[23] Laboratoire Univers et Particules de Montpellier, Université Montpellier, CNRS/IN2P3, CC 72, Place Eugène Bataillon, F-34095 Montpellier Cedex 5, France
[24] School of Physical Sciences, University of Adelaide, Adelaide 5005, Australia
[25] Aix Marseille Université, CNRS/IN2P3, CPPM, Marseille, France
[26] Institut für Astronomie und Astrophysik, Universität Tübingen, Sand 1, D 72076 Tübingen, Germany
[27] Universität Innsbruck, Institut für Astro- und Teilchenphysik, Technikerstraße 25, 6020 Innsbruck, Austria
[28] Obserwatorium Astronomiczne, Uniwersytet Jagielloński, ul. Orla 171, 30-244 Kraków, Poland
[29] Institute of Astronomy, Faculty of Physics, Astronomy and Informatics, Nicolaus Copernicus University, Grudziadzka 5, 87-100 Torun, Poland
[30] Department of Physics, Rikkyo University, 3-34-1 Nishi-Ikebukuro, Toshima-ku, Tokyo 171-8501, Japan
[31] Nicolaus Copernicus Astronomical Center, Polish Academy of Sciences, ul. Bartycka 18, 00-716 Warsaw, Poland
[32] Université Bordeaux, CNRS, LP2I Bordeaux, UMR 5797, F-33170 Gradignan, France
[33] Department of Physics, University of the Free State, PO Box 339, Bloemfontein 9300, South Africa
[34] GRAPPA, Anton Pannekoek Institute for Astronomy, University of Amsterdam, Science Park 904, 1098 XH Amsterdam, The Netherlands

[35] Kavli Institute for the Physics and Mathematics of the Universe (WPI), The University of Tokyo Institutes for Advanced Study (UTIAS), The University of Tokyo, 5-1-5 Kashiwa-no-Ha, Kashiwa, Chiba, 277-8583, Japan
[36] Department of Physics, Konan University, 8-9-1 Okamoto, Higashinada, Kobe, Hyogo 658-8501, Japan
[37] Universität Hamburg, Institut für Experimentalphysik, Luruper Chaussee 149, D 22761 Hamburg, Germany

Appendices

A. The η^2 parameter

In order to to include the uncertainties of both X-ray and TeV data, we utilise a linear combination of χ^2 tests (see e.g. Bausch 2013), denoted here as η^2, and defined as:

$$\eta^2(f,\Omega) = \sum_i \frac{(X_i - f(T_i,\Omega))^2}{\delta X_i^2} + \sum_i \frac{(T_i - f^{-1}(X_i,\Omega))^2}{\delta T_i^2} \tag{4}$$

where X_i and T_i are the i-th X-ray and TeV flux values from the time-correlated dataset. Accordingly δX_i and δT_i are the uncertainties of these values. The dependency between X-ray and TeV fluxes was assumed to have the functional form $X = f(T,\Omega)$ with Ω standing for the variable parameter(s) of the function f. The inverse function f^{-1} is given by: $T = f^{-1}(X,\Omega)$. For an accurate comparison between η^2 values, we also implement a method of reduced η^2, named $\bar{\eta}^2$. After summing the reduction of the two constituent χ^2 values, we reduce η^2 by applying

$$\bar{\eta}^2 = \frac{\eta^2}{2(N-1)}$$

where N is the number of correlated pairs.

We note that by design the η^2 test is symmetric with respect to the interchange of the $X \longleftrightarrow T$ datasets.

8 Conclusion

This thesis has presented a number of works on the topics of indirect dark matter detection and the VHE analysis of gamma-ray binaries. In addition to the work conducted on these subjects, significant theoretical background for the two subjects has been introduced to give context to the results presented.

Chapter 1 was dedicated to introducing the topic of dark matter. This included a brief history of the dark matter problem, the introduction of dark matter candidates/-models pertinent to later work, and the various search techniques employed in the search for DM. In particular, indirect dark matter searches were emphasised given the relevance to the work presented later in the thesis. This included a summary of dark matter signals from decay and annihilation, dark matter distributions and J-factors, as well as different search targets. Additionally, a summary of recent indirect dark matter searches was given.

Chapter 2, again, gave a theoretical background to the methods and techniques utilised in the acquisition and processing of data in X-ray and high-energy astronomy. This included a brief history of both X-ray astronomy and high-energy astronomy. Additionally, a summary of the methods and challenges in imaging astrophysical X-rays was given, alongside a breakdown of the components of X-ray data and its analysis. This chapter also featured introductions to several instruments. Details of the forthcoming THESEUS and eXTP missions were given to provide context for the later studies of their potential in dark matter detection. Finally, a summary of the instrumentation and data analysis pipeline for the *Fermi* satellite was given.

The first of the papers presented in this thesis is shown in Chapter 3, which details a study into the indirect detection of annihilating dark matter in nearby galaxy clusters using 12 years of Fermi-LAT data. The study utilised multiple profiles of 5 nearby galaxy clusters to obtain limits on annihilating WIMP dark matter. Specifically, this looked at the annihilation of WIMPs into the $b\bar{b}$, W^+W^- and $\gamma\gamma$ annihilation channels. The study did not detect any signal of dark matter, but instead placed limits upon the velocity averaged annihilation cross section ($\langle\sigma v\rangle$) of DM in the different channels. These limits were found to be comparable within a small factor to recent limits derived from DSph galaxies. The study also looked into the impact of boost factors (contributions from DM substructures) and compared various DM

distribution profiles. The study found the best limits were imposed by analysis of the Virgo cluster, in the $\gamma\gamma$ channel.

Chapter 4, contains the second and third published works presented in this thesis. These works detail the potential of the upcoming THESEUS and eXTP missions in their ability to detect decaying DM. The first of these works, concerned with the THESEUS mission, looks at the instrument's ability to detect signals from the decay of ALP, dark photon and νMSM sterile neutrino DM. Through a series of simulated blank sky observations (taking advantage of THESEUS's large FoV instruments), the level of flux that THESEUS could probe down to is shown. This study found THESEUS could make significant improvements to the exclusion of the parameter space for all three models (up to ~ 300 times in some cases). However, the control of systematics will be essential in determining its potential, as even minimal systematics can impair these limits significantly. The second work performs a similar study but for the forthcoming eXTP mission. Through simulated observations of DSph galaxies, the potential of the suite of instruments aboard eXTP was tested for their sensitivity in detecting the νMSM sterile neutrino. The study (once again), finds that the control of systematics will be quintessential in eXTP's ability to impose limits, however, that eXTP can improve νMSM sterile neutrino limits by a factor of 5-10.

In order to lay the foundations for the VHE analysis of the gamma-ray binary PSR B1259-63/LS 2883, chapter 5 introduces the principle of VHE gamma-ray astronomy. Specifically, this includes an overview of cosmic rays and the detection of VHE gamma rays. The topic of IACTs is covered in depth, including the formation of air showers/Cherenkov radiation, and how these are used in the reconstruction and detection of VHE gamma rays. Finally the H.E.S.S. array is introduced and an overview of its data reduction and analysis pipeline is given. This provides grounding for the later H.E.S.S. analysis.

Gamma-ray binary systems are then introduced in chapter 6 to familiarise the reader with, and describe the characteristics of, the object class to which PSR B1259-63/LS 2883 belongs. This includes a brief overview of the different types of GREB, as well as Oe/Be type stars and pulsars. Due to the prevalence of non-thermal emission in gamma-ray binary systems, particle acceleration, diffusion and non-thermal radiation methods are also described. Following this, details of the gamma-ray binary systems PSR J2032+4127 and LS I $+61^\circ$ 303 are given as examples of other sources in the class. Finally, a full introduction to PSR B1259-63/LS 2883 is given, detailing the system's properties and non-thermal emission behaviour around periastron passage.

Finally, chapter 7 contains the final paper presented in this thesis, the VHE analysis of the 2021 periastron of PSR B1259-63/LS 2883. This work comprises the H.E.S.S. analysis of ~ 100 hours of data taken around the 2021 periastron passage of the system. It details flux, spectral, X-ray/TeV flux correlation and GeV/TeV flux correlation analyses. The study finds, for the first time, spectral variation in the system on a sub-periastron timescale. The total spectral index is, however, consistent with the average of previous years. Additionally, the VHE flux profile of the system seems to generally display a similar asymmetric double peak profile to previous years. Finally, the results of the X-ray/TeV correlation seem to suggest a strong correlation at times following the periastron, whereas the GeV/TeV correlation suggests (at the level the study was able to probe) that there was no correlation between the emission.

Despite the vast differences between the two overarching topics presented in this thesis, each represents an intriguing mystery. Gamma-ray binaries with their potential to help our understanding of high-energy astrophysical phenomena and acceleration mechanisms in the Universe, and dark matter with its potential to revolutionise our understanding of cosmology and particle physics. Though many of the details of these topics yet remain enigmatic, it is the struggle of human ambition and curiosity towards the unknown that drives this field, and the species as a whole, towards wonders. The potential to chip away at the mysteries of the cosmos remains an entrancing endeavour and our skills to do so will only improve as we equip ourselves with an ever expanding repertoire of knowledge and instrumentation to answer ever bigger questions about the Universe. To put it shortly, it is an exciting time to be alive.

Bibliography

[1] Charles Thorpe-Morgan, Denys Malyshev, Christoph-Alexander Stegen, et al. Annihilating dark matter search with 12 yr of Fermi LAT data in nearby galaxy clusters. *MNRAS*, 502(3):4039–4047, April 2021.

[2] Charles Thorpe-Morgan, Denys Malyshev, Andrea Santangelo, et al. THESEUS insights into axionlike particles, dark photon, and sterile neutrino dark matter. *Phys. Rev. D*, 102(12):123003, December 2020.

[3] Denys Malyshev, Charles Thorpe-Morgan, Andrea Santangelo, et al. $extp$ perspectives for the $\nu\mathrm{MSM}$ sterile neutrino dark matter model. *Phys. Rev. D*, 101:123009, Jun 2020.

[4] H.E.S.S. Collaboration, F. Aharonian, F. Ait Benkhali, et al. H.e.s.s. observations of the 2021 periastron passage of psr b1259-63 ls 2883. *A&A*, 687:A219, 2024.

[5] Planck Collaboration, N. Aghanim, Y. Akrami, et al. Planck 2018 results. VI. Cosmological parameters. *A&A*, 641:A6, September 2020.

[6] William Thomson. Sir William Thomson's Baltimore Lectures. *Science*, 4(92):437–438, November 1884.

[7] J. C. Kapteyn. First Attempt at a Theory of the Arrangement and Motion of the Sidereal System. *ApJ*, 55:302, May 1922.

[8] J. H. Oort. The force exerted by the stellar system in the direction perpendicular to the galactic plane and some related problems. *Bull. Astron. Inst. Netherlands*, 6:249, August 1932.

[9] F. Zwicky. Die Rotverschiebung von extragalaktischen Nebeln. *Helvetica Physica Acta*, 6:110–127, January 1933.

[10] Edwin Hubble and Milton L. Humason. The Velocity-Distance Relation among Extra-Galactic Nebulae. *ApJ*, 74:43, July 1931.

[11] G. Bertone. *Particle Dark Matter: Observations, Models and Searches*. Cambridge University Press, 2010.

[12] V. C. Rubin, Jr. Ford, W. K., and N. Thonnard. Rotational properties of 21 SC galaxies with a large range of luminosities and radii, from NGC 4605 (R=4kpc) to UGC 2885 (R=122kpc). *ApJ*, 238:471–487, June 1980.

[13] M. S. Roberts and R. N. Whitehurst. The rotation curve and geometry of M31 at large galactocentric distances. *ApJ*, 201:327–346, October 1975.

[14] K. C. Freeman. On the Disks of Spiral and S0 Galaxies. *ApJ*, 160:811, June 1970.

[15] D. H. Rogstad and G. S. Shostak. Gross Properties of Five Scd Galaxies as Determined from 21-CENTIMETER Observations. *ApJ*, 176:315, September 1972.

[16] K. G. Begeman, A. H. Broeils, and R. H. Sanders. Extended rotation curves of spiral galaxies : dark haloes and modified dynamics. *MNRAS*, 249:523, April 1991.

[17] M. Milgrom. A modification of the Newtonian dynamics as a possible alternative to the hidden mass hypothesis. *ApJ*, 270:365–370, July 1983.

[18] A. Einstein. Die Grundlage der allgemeinen Relativitätstheorie. *Annalen der Physik*, 354(7):769–822, January 1916.

[19] Priyamvada Natarajan, Urmila Chadayammuri, Mathilde Jauzac, et al. Mapping substructure in the HST Frontier Fields cluster lenses and in cosmological simulations. *Monthly Notices of the Royal Astronomical Society*, 468(2):1962–1980, 02 2017.

[20] Maruša Bradač, Steven W. Allen, Tommaso Treu, et al. Revealing the Properties of Dark Matter in the Merging Cluster MACS J0025.4-1222. *ApJ*, 687(2):959–967, November 2008.

[21] Douglas Clowe, Anthony Gonzalez, and Maxim Markevitch. Weak-Lensing Mass Reconstruction of the Interacting Cluster 1E 0657-558: Direct Evidence for the Existence of Dark Matter. *ApJ*, 604(2):596–603, April 2004.

[22] M. Markevitch, A. H. Gonzalez, D. Clowe, et al. Direct Constraints on the Dark Matter Self-Interaction Cross Section from the Merging Galaxy Cluster 1E 0657-56. *ApJ*, 606(2):819–824, May 2004.

[23] Douglas Clowe, Maruša Bradač, Anthony H. Gonzalez, et al. A Direct Empirical Proof of the Existence of Dark Matter. *ApJ*, 648(2):L109–L113, September 2006.

[24] Peter Schneider. *Extragalactic Astronomy and Cosmology*. Springer Berlin Heidelberg, Berlin, Heidelberg, 2015.

[25] A. A. Penzias and R. W. Wilson. A Measurement of Excess Antenna Temperature at 4080 Mc/s. *ApJ*, 142:419–421, July 1965.

[26] L. Bergström and A. Goobar. *Cosmology and Particle Astrophysics*. Springer Praxis Books. Springer Berlin Heidelberg, 2006.

[27] P.J.E. Peebles, L.A. Page, and R.B. Partridge. *Finding the Big Bang*. Cambridge University Press, 2009.

[28] Planck Collaboration, N. Aghanim, Y. Akrami, et al. Planck 2018 results. VI. Cosmological parameters. *A&A*, 641:A6, September 2020.

[29] P. J. E. Peebles. Large-scale background temperature and mass fluctuations due to scale-invariant primeval perturbations. *ApJ*, 263:L1–L5, December 1982.

[30] G. R. Blumenthal, S. M. Faber, J. R. Primack, and M. J. Rees. Formation of galaxies and large-scale structure with cold dark matter. *Nature*, 311:517–525, October 1984.

[31] Volker Springel, Simon D. M. White, Adrian Jenkins, et al. Simulations of the formation, evolution and clustering of galaxies and quasars. *Nature*, 435(7042):629–636, June 2005.

[32] Robert A. Crain, Joop Schaye, Richard G. Bower, et al. The EAGLE simulations of galaxy formation: calibration of subgrid physics and model variations. *MNRAS*, 450(2):1937–1961, June 2015.

[33] Joop Schaye, Robert A. Crain, Richard G. Bower, et al. The EAGLE project: simulating the evolution and assembly of galaxies and their environments. *MNRAS*, 446(1):521–554, January 2015.

[34] Annalisa Pillepich, Volker Springel, Dylan Nelson, et al. Simulating galaxy formation with the illustristng model. *Monthly Notices of the Royal Astronomical Society*, 473(3):4077–4106, October 2017.

[35] Rainer Weinberger, Volker Springel, Lars Hernquist, et al. Simulating galaxy formation with black hole driven thermal and kinetic feedback. *Monthly Notices of the Royal Astronomical Society*, 465(3):3291–3308, November 2016.

[36] Elcio Abdalla, Guillermo Franco Abellán, Amin Aboubrahim, et al. Cosmology intertwined: A review of the particle physics, astrophysics, and cosmology associated with the cosmological tensions and anomalies. *Journal of High Energy Astrophysics*, 34:49–211, June 2022.

[37] Seth Koren. The Hierarchy Problem: From the Fundamentals to the Frontiers. *arXiv e-prints*, page arXiv:2009.11870, September 2020.

[38] Carlos Pérez de los Heros. Status, Challenges and Directions in Indirect Dark Matter Searches. *Symmetry*, 12(10):1648, October 2020.

[39] G. Hinshaw, J. L. Weiland, R. S. Hill, et al. Five-year wilkinson microwave anisotropy probe observations: Data processing, sky maps, and basic results. *The Astrophysical Journal Supplement Series*, 180(2):225–245, February 2009.

[40] Tracy R. Slatyer. TASI Lectures on Indirect Detection of Dark Matter. *arXiv e-prints*, page arXiv:1710.05137, October 2017.

[41] D. Hooper. TASI Lectures on Indirect Searches For Dark Matter. In *TASI 2018 - Theory in an Era of Data*, page 10, June 2018.

[42] Gary Steigman, Basudeb Dasgupta, and John F. Beacom. Precise relic WIMP abundance and its impact on searches for dark matter annihilation. *Phys. Rev. D*, 86(2):023506, July 2012.

[43] Lawrence J. Hall, Karsten Jedamzik, John March-Russell, and Stephen M. West. Freeze-In Production of FIMP Dark Matter. *JHEP*, 03:080, 2010.

[44] Howard Baer, Ki-Young Choi, Jihn E. Kim, and Leszek Roszkowski. Dark matter production in the early universe: Beyond the thermal wimp paradigm. *Physics Reports*, 555:1–60, 2015. Dark matter production in the early Universe: Beyond the thermal WIMP paradigm.

[45] Jennifer M. Gaskins. A review of indirect searches for particle dark matter. *Contemporary Physics*, 57(4):496–525, October 2016.

[46] Gianfranco Bertone, Dan Hooper, and Joseph Silk. Particle dark matter: evidence, candidates and constraints. *Phys. Rep.*, 405(5-6):279–390, January 2005.

[47] Leszek Roszkowski, Enrico Maria Sessolo, and Sebastian Trojanowski. Wimp dark matter candidates and searches—current status and future prospects. *Reports on Progress in Physics*, 81(6):066201, may 2018.

[48] Jonathan L. Feng. The WIMP paradigm: Theme and variations. *SciPost Phys. Lect. Notes*, page 71, 2023.

[49] Benjamin W. Lee and Steven Weinberg. Cosmological lower bound on heavy-neutrino masses. *Phys. Rev. Lett.*, 39(4):165–168, July 1977.

[50] Jonathan L. Feng and Jason Kumar. Dark-Matter Particles without Weak-Scale Masses or Weak Interactions. *Phys. Rev. Lett.*, 101(23):231301, December 2008.

[51] Stefano Profumo. TASI 2012 Lectures on Astrophysical Probes of Dark Matter. *arXiv e-prints*, page arXiv:1301.0952, January 2013.

[52] Patrick J Fox. TASI Lectures on WIMPs and Supersymmetry. In *Proceedings of Theoretical Advanced Study Institute Summer School 2018 -Theory in an Era of Data - PoS(TASI2018)*, volume 333, page 005, 2019.

[53] Juri Smirnov and John F. Beacom. Tev-scale thermal wimps: Unitarity and its consequences. *Phys. Rev. D*, 100:043029, Aug 2019.

[54] Stephen P. Martin. A Supersymmetry Primer. In *Perspectives on Supersymmetry*, pages 1–98. World Scientific Publishing Co. Pte. Ltd, 1998.

[55] Martin Schmaltz and David Tucker-Smith. Little higgs theories. *Annual Review of Nuclear and Particle Science*, 55(1):229–270, 2005.

[56] D Bailin and A Love. Kaluza-klein theories. *Reports on Progress in Physics*, 50(9):1087, sep 1987.

[57] G. Jungman, M. Kamionkowski, and K. Griest. Supersymmetric dark matter. *Phys. Rep.*, 267:195–373, March 1996.

[58] Achille Corsetti and Pran Nath. Susy dark matter, 2000.

[59] Riccardo Catena and Laura Covi. *SUSY dark matter(s)*. Springer Berlin Heidelberg, Berlin, Heidelberg, 2014.

[60] Joachim Kopp. Sterile neutrinos as dark matter candidates. *SciPost Phys. Lect. Notes*, page 36, 2022.

[61] Alexander Merle. keV Neutrino Model Building. *International Journal of Modern Physics D*, 22(10):1330020, August 2013.

[62] M. Goldhaber, L. Grodzins, and A. W. Sunyar. Helicity of Neutrinos. *Physical Review*, 109(3):1015–1017, February 1958.

[63] Arthur B. McDonald. Nobel lecture: The sudbury neutrino observatory: Observation of flavor change for solar neutrinos. *Rev. Mod. Phys.*, 88:030502, Jul 2016.

[64] J. Schechter and J. W. F. Valle. Neutrino masses in su(2) $\otimes$ u(1) theories. *Phys. Rev. D*, 22:2227–2235, Nov 1980.

[65] Samoil M. Bilenky. Neutrinos: Majorana or Dirac? *Universe*, 6(9):134, August 2020.

[66] M. Klasen, M. Pohl, and G. Sigl. Indirect and direct search for dark matter. *Progress in Particle and Nuclear Physics*, 85:1–32, November 2015.

[67] Takehiko Asaka and Mikhail Shaposhnikov. The νmsm, dark matter and baryon asymmetry of the universe. *Physics Letters B*, 620:17–26, 2005.

[68] K. N. Abazajian, M. A. Acero, S. K. Agarwalla, et al. Light sterile neutrinos: A white paper. *Preprint*, 2012.

[69] A. Boyarsky, M. Drewes, T. Lasserre, et al. Sterile neutrino Dark Matter. *Progress in Particle and Nuclear Physics*, 104:1–45, January 2019.

[70] Palash B. Pal and Lincoln Wolfenstein. Radiative decays of massive neutrinos. *Phys. Rev. D*, 25:766–773, Feb 1982.

[71] R. D. Peccei and Helen R. Quinn. CP conservation in the presence of pseudoparticles. *Phys. Rev. Lett.*, 38(25):1440–1443, June 1977.

[72] R. D. Peccei and Helen R. Quinn. Constraints imposed by CP conservation in the presence of pseudoparticles. *Phys. Rev. D*, 16(6):1791–1797, September 1977.

[73] Igor García Irastorza. An introduction to axions and their detection. *SciPost Phys. Lect. Notes*, page 45, 2022.

[74] F. Wilczek. Problem of strong P and T invariance in the presence of instantons. *Phys. Rev. Lett.*, 40(5):279–282, January 1978.

[75] Steven Weinberg. A new light boson? *Phys. Rev. Lett.*, 40(4):223–226, January 1978.

[76] Roberto D. Peccei. The Strong CP Problem and Axions. In Markus Kuster, Georg Raffelt, and Berta Beltrán, editors, *Axions*, volume 741, page 3. Springer Berlin, Heidelberg, 2008.

[77] David d'Enterria. Collider constraints on axion-like particles. *arXiv e-prints*, page arXiv:2102.08971, February 2021.

[78] L.F. Abbott and P. Sikivie. A cosmological bound on the invisible axion. *Physics Letters B*, 120(1):133–136, 1983.

[79] Michael Dine and Willy Fischler. The not-so-harmless axion. *Physics Letters B*, 120(1):137–141, 1983.

[80] John Preskill, Mark B. Wise, and Frank Wilczek. Cosmology of the invisible axion. *Physics Letters B*, 120(1):127–132, 1983.

[81] David J.E. Marsh. Axion cosmology. *Physics Reports*, 643:1–79, 2016. Axion cosmology.

[82] T.W.B. Kibble. Some implications of a cosmological phase transition. *Physics Reports*, 67(1):183–199, 1980.

[83] Georg G. Raffelt. *Stars as laboratories for fundamental physics*. University of Chicago Press, 1996.

[84] H. Primakoff. Photo-production of neutral mesons in nuclear electric fields and the mean life of the neutral meson. *Phys. Rev.*, 81:899–899, Mar 1951.

[85] Javier Redondo and Andreas Ringwald. Light shining through walls. *Contemporary Physics*, 52(3):211–236, 2011.

[86] Klaus Ehret, Maik Frede, Samvel Ghazaryan, et al. New alps results on hidden-sector lightweights. *Physics Letters B*, 689(4):149–155, 2010.

[87] R. Ballou, G. Deferne, M. Finger, et al. New exclusion limits on scalar and pseudoscalar axionlike particles from light shining through a wall. *Phys. Rev. D*, 92:092002, Nov 2015.

[88] P. Sikivie. Experimental tests of the "invisible" axion. *Phys. Rev. Lett.*, 51:1415–1417, Oct 1983.

[89] Vedran Brdar, Bhaskar Dutta, Wooyoung Jang, et al. Axionlike particles at future neutrino experiments: Closing the cosmological triangle. *Phys. Rev. Lett.*, 126:201801, May 2021.

[90] R. Essig, J. A. Jaros, W. Wester, et al. Dark Sectors and New, Light, Weakly-Coupled Particles. *arXiv e-prints*, page arXiv:1311.0029, October 2013.

[91] Maxim Pospelov, Adam Ritz, and Mikhail Voloshin. Bosonic super-WIMPs as keV-scale dark matter. *Phys. Rev. D*, 78(11):115012, December 2008.

[92] Theodor Kaluza. Zum Unitätsproblem der Physik. *Sitzungsberichte der Königlich Preußischen Akademie der Wissenschaften (Berlin*, pages 966–972, January 1921.

[93] Oskar Klein. The Atomicity of Electricity as a Quantum Theory Law. *Nature*, 118(2971):516, October 1926.

[94] Bernard J. Carr and Florian Kuhnel. Primordial black holes as dark matter candidates. *SciPost Physics Lecture Notes*, 2021.

[95] Jodi Cooley. Dark Matter direct detection of classical WIMPs. *SciPost Phys. Lect. Notes*, page 55, 2022.

[96] Marc Schumann. Direct detection of WIMP dark matter: concepts and status. *Journal of Physics G Nuclear Physics*, 46(10):103003, October 2019.

[97] Richard J. Gaitskell. Direct detection of dark matter. *Annual Review of Nuclear and Particle Science*, 54(1):315–359, 2004.

[98] R. Bernabei, P. Belli, F. Cappella, et al. Dark Matter: DAMA/LIBRA and its perspectives. *arXiv e-prints*, page arXiv:2209.00882, September 2022.

[99] XENON Collaboration, E. Aprile, K. Abe, et al. First Dark Matter Search with Nuclear Recoils from the XENONnT Experiment. *arXiv e-prints*, page arXiv:2303.14729, March 2023.

[100] J. Aalbers, D. S. Akerib, C. W. Akerlof, et al. First Dark Matter Search Results from the LUX-ZEPLIN (LZ) Experiment. *arXiv e-prints*, page arXiv:2207.03764, July 2022.

[101] Yue Meng, Zhou Wang, Yi Tao, et al. Dark matter search results from the pandax-4t commissioning run. *Phys. Rev. Lett.*, 127:261802, Dec 2021.

[102] Pietro Di Gangi. The xenon road to direct detection of dark matter at lngs: The xenon project. *Universe*, 7(8), 2021.

[103] CRESST Collaboration, G. Angloher, S. Banik, et al. Results on sub-GeV Dark Matter from a 10 eV Threshold CRESST-III Silicon Detector. *arXiv e-prints*, page arXiv:2212.12513, December 2022.

[104] SuperCDMS Collaboration, M. F. Albakry, I. Alkhatib, et al. A Strategy for Low-Mass Dark Matter Searches with Cryogenic Detectors in the SuperCDMS SNOLAB Facility. *arXiv e-prints*, page arXiv:2203.08463, March 2022.

[105] Julien Billard, Mark Boulay, Susana Cebrián, et al. Direct detection of dark matter—appec committee report*. *Reports on Progress in Physics*, 85(5):056201, apr 2022.

[106] Jessica Goodman, Masahiro Ibe, Arvind Rajaraman, et al. Constraints on dark matter from colliders. *Phys. Rev. D*, 82(11):116010, December 2010.

[107] Antonio Boveia and Caterina Doglioni. Dark Matter Searches at Colliders. *Annual Review of Nuclear and Particle Science*, 68:429–459, October 2018.

[108] Jonathan M. Cornell, Stefano Profumo, and William Shepherd. Dark matter in minimal universal extra dimensions with a stable vacuum and the "right" Higgs boson. *Phys. Rev. D*, 89(5):056005, March 2014.

[109] Tracy R. Slatyer. Les Houches Lectures on Indirect Detection of Dark Matter. *SciPost Phys. Lect. Notes*, page 53, 2022.

[110] NASA fermi gamma-ray space telescope-fermi searches for dark matter. `https://fermi.gsfc.nasa.gov/science/eteu/dm/`. Accessed: 2023-11-21.

[111] Carlos Pérez de los Heros. Status, challenges and directions in indirect dark matter searches. *Symmetry*, 12(10):1648, oct 2020.

[112] Julio F. Navarro, Aaron Ludlow, Volker Springel, et al. The diversity and similarity of simulated cold dark matter haloes. *MNRAS*, 402(1):21–34, February 2010.

[113] Anatoly Klypin, Gustavo Yepes, Stefan Gottlöber, et al. MultiDark simulations: the story of dark matter halo concentrations and density profiles. *MNRAS*, 457(4):4340–4359, April 2016.

[114] V. Springel, J. Wang, M. Vogelsberger, et al. The aquarius project: the subhaloes of galactic haloes. *Monthly Notices of the Royal Astronomical Society*, 391(4):1685–1711, dec 2008.

[115] Philip Bett, Vincent Eke, Carlos S. Frenk, et al. The spin and shape of dark matter haloes in the Millennium simulation of a Λ cold dark matter universe. *MNRAS*, 376(1):215–232, March 2007.

[116] Julio F. Navarro, Carlos S. Frenk, and Simon D. M. White. The Structure of Cold Dark Matter Halos. *ApJ*, 462:563, May 1996.

[117] Julio F. Navarro, Carlos S. Frenk, and Simon D. M. White. A Universal Density Profile from Hierarchical Clustering. *ApJ*, 490(2):493–508, December 1997.

[118] Oleg Y. Gnedin, Andrey V. Kravtsov, Anatoly A. Klypin, and Daisuke Nagai. Response of dark matter halos to condensation of baryons: Cosmological simulations and improved adiabatic contraction model. *The Astrophysical Journal*, 616(1):16–26, nov 2004.

[119] Oleg Y. Gnedin, Daniel Ceverino, Nickolay Y. Gnedin, et al. Halo Contraction Effect in Hydrodynamic Simulations of Galaxy Formation. *arXiv e-prints*, page arXiv:1108.5736, August 2011.

[120] Sergey Mashchenko, James Wadsley, and H. M. P. Couchman. Stellar feedback in dwarf galaxy formation. *Science*, 319(5860):174–177, jan 2008.

[121] A. V. Macciò , G. Stinson, C. B. Brook, et al. HALO EXPANSION IN COSMOLOGICAL HYDRO SIMULATIONS: TOWARD a BARYONIC SOLUTION OF THE CUSP/CORE PROBLEM IN MASSIVE SPIRALS. *The Astrophysical Journal*, 744(1):L9, dec 2011.

[122] HongSheng Zhao. Analytical models for galactic nuclei. *Monthly Notices of the Royal Astronomical Society*, 278(2):488–496, 01 1996.

[123] J. Einasto. On the Construction of a Composite Model for the Galaxy and on the Determination of the System of Galactic Parameters. *Trudy Astrofizicheskogo Instituta Alma-Ata*, 5:87–100, January 1965.

[124] Stacy S. McGaugh, Vera C. Rubin, and W. J. G. de Blok. High-Resolution Rotation Curves of Low Surface Brightness Galaxies. I. Data. *AJ*, 122(5):2381–2395, November 2001.

[125] Matthew G. Walker and Jorge Peñ arrubia. A METHOD FOR MEASURING (SLOPES OF) THE MASS PROFILES OF DWARF SPHEROIDAL GALAXIES. *The Astrophysical Journal*, 742(1):20, nov 2011.

[126] W. J. G. de Blok. The core-cusp problem. *Advances in Astronomy*, 2010:1–14, 2010.

[127] A. Burkert. The structure of dark matter halos in dwarf galaxies. *The Astrophysical Journal*, 447(1), jul 1995.

[128] Dragan Huterer. Weak lensing, dark matter and dark energy. *General Relativity and Gravitation*, 42(9):2177–2195, jul 2010.

[129] Dean E. McLaughlin. Evidence in Virgo for the Universal Dark Matter Halo. *ApJ*, 512(1):L9–L12, February 1999.

[130] Akira Tokiwa, Masahiro Takada, Tian Qiu, et al. Study of structural parameters and systemic proper motion of Sextans dwarf spheroidal galaxy with Subaru Hyper Suprime-Cam data. *arXiv e-prints*, page arXiv:2302.06071, February 2023.

[131] Aldée Charbonnier, Céline Combet, and David Maurin. clumpy: A code for gamma-ray signals from dark matter structures. *Computer Physics Communications*, 183(3):656–668, 2012.

[132] G. Kauffmann, S. D. M. White, and B. Guiderdoni. The formation and evolution of galaxies within merging dark matter haloes. *MNRAS*, 264:201–218, September 1993.

[133] Anatoly Klypin, Andrey V. Kravtsov, Octavio Valenzuela, and Francisco Prada. Where Are the Missing Galactic Satellites? *ApJ*, 522(1):82–92, September 1999.

[134] Ben Moore, Sebastiano Ghigna, Fabio Governato, et al. Dark Matter Substructure within Galactic Halos. *ApJ*, 524(1):L19–L22, October 1999.

[135] Michael Boylan-Kolchin, James S. Bullock, and Manoj Kaplinghat. Too big to fail? The puzzling darkness of massive Milky Way subhaloes. *MNRAS*, 415(1):L40–L44, July 2011.

[136] Michael Boylan-Kolchin, James S. Bullock, and Manoj Kaplinghat. The Milky Way's bright satellites as an apparent failure of ΛCDM. *MNRAS*, 422(2):1203–1218, May 2012.

[137] Shea Garrison-Kimmel, Michael Boylan-Kolchin, James S. Bullock, and Evan N. Kirby. Too big to fail in the Local Group. *MNRAS*, 444(1):222–236, October 2014.

[138] Jeremiah P. Ostriker, Ena Choi, Anthony Chow, and Kundan Guha. Mind the gap: Is the too big to fail problem resolved? *The Astrophysical Journal*, 885(1):97, nov 2019.

[139] Jan Conrad and Olaf Reimer. Indirect dark matter searches in gamma and cosmic rays. *Nature Physics*, 13(3):224–231, March 2017.

[140] Lisa Goodenough and Dan Hooper. Possible Evidence For Dark Matter Annihilation In The Inner Milky Way From The Fermi Gamma Ray Space Telescope. *Preprint*, 10 2009.

[141] Qiang Yuan and Bing Zhang. Millisecond pulsar interpretation of the Galactic center gamma-ray excess. *Journal of High Energy Astrophysics*, 3:1–8, September 2014.

[142] Martin Pohl, Oscar Macias, Phaedra Coleman, and Chris Gordon. Assessing the Impact of Hydrogen Absorption on the Characteristics of the Galactic Center Excess. *ApJ*, 929(2):136, April 2022.

[143] Alan W. McConnachie. THE OBSERVED PROPERTIES OF DWARF GALAXIES IN AND AROUND THE LOCAL GROUP. *The Astronomical Journal*, 144(1):4, jun 2012.

[144] Louis E Strigari. Dark matter in dwarf spheroidal galaxies and indirect detection: a review. *Reports on Progress in Physics*, 81(5):056901, mar 2018.

[145] Joshua W. Foster, Marius Kongsore, Christopher Dessert, et al. Deep search for decaying dark matter with xmm-newton blank-sky observations. *Physical Review Letters*, 127(5), jul 2021.

[146] A. Neronov and D. Malyshev. Toward a full test of the νMSM sterile neutrino dark matter model with athena. *Phys. Rev. D*, 93:063518, Mar 2016.

[147] Scott Tremaine and James E. Gunn. Dynamical role of light neutral leptons in cosmology. *Phys. Rev. Lett.*, 42(6):407–410, February 1979.

[148] Alexey Boyarsky, Oleg Ruchayskiy, and Dmytro Iakubovskyi. A lower bound on the mass of dark matter particles. *Journal of Cosmology and Astroparticle Physics*, 2009(03):005, mar 2009.

[149] Pasquale D. Serpico and Georg G. Raffelt. Lepton asymmetry and primordial nucleosynthesis in the era of precision cosmology. *Phys. Rev. D*, 71:127301, Jun 2005.

[150] Nathalie Palanque-Delabrouille, Christophe Yèche, Julien Baur, et al. Neutrino masses and cosmology with lyman-alpha forest power spectrum. *Journal of Cosmology and Astroparticle Physics*, 2015(11):011, nov 2015.

[151] Matteo Viel, Julien Lesgourgues, Martin G. Haehnelt, et al. Constraining warm dark matter candidates including sterile neutrinos and light gravitinos with wmap and the lyman-α forest. *Phys. Rev. D*, 71:063534, Mar 2005.

[152] Esra Bulbul, Maxim Markevitch, Adam Foster, et al. Detection of an unidentified emission line in the stacked x-ray spectrum of galaxy clusters. *The Astrophysical Journal*, 789(1):13, jun 2014.

[153] A. Boyarsky, O. Ruchayskiy, D. Iakubovskyi, and J. Franse. Unidentified line in x-ray spectra of the andromeda galaxy and perseus galaxy cluster. *Phys. Rev. Lett.*, 113:251301, Dec 2014.

[154] Christopher Dessert, Joshua W. Foster, Yujin Park, and Benjamin R. Safdi. Was There a 3.5 keV Line? *arXiv e-prints*, page arXiv:2309.03254, September 2023.

[155] Kenny C. Y. Ng, Brandon M. Roach, Kerstin Perez, et al. New constraints on sterile neutrino dark matter from nustar m31 observations. *Phys. Rev. D*, 99:083005, Apr 2019.

[156] Sebastian Hoof, Alex Geringer-Sameth, and Roberto Trotta. A global analysis of dark matter signals from 27 dwarf spheroidal galaxies using 11 years of Fermi-LAT observations. *J. Cosmology Astropart. Phys.*, 2020(2):012, February 2020.

[157] H. Abdalla, F. Aharonian, F. Ait Benkhali, et al. Search for Dark Matter Annihilation Signals in the H.E.S.S. Inner Galaxy Survey. *Phys. Rev. Lett.*, 129(11):111101, September 2022.

[158] Christoph Keller. X-rays from the sun. *Experientia*, 51:710–720, 07 1995.

[159] Riccardo Giacconi, Herbert Gursky, Frank R. Paolini, and Bruno B. Rossi. Evidence for x rays from sources outside the solar system. *Phys. Rev. Lett.*, 9:439–443, Dec 1962.

[160] J.E. Trümper and G. Hasinger. *The Universe in X-Rays*. Astronomy and Astrophysics Library. Springer Berlin Heidelberg, 2008.

[161] Hans Wolter. Spiegelsysteme streifenden Einfalls als abbildende Optiken für Röntgenstrahlen. *Annalen der Physik*, 445(1):94–114, January 1952.

[162] Jessica Gaskin, Ronald Elsner, Brian Ramsey, et al. Superhero: Design of a new hard-x-ray focusing telescope. In *2015 IEEE Aerospace Conference*, pages 1–15, 2015.

[163] L. Strüder, U. Briel, K. Dennerl, et al. The European Photon Imaging Camera on XMM-Newton: The pn-CCD camera. *A&A*, 365:L18–L26, January 2001.

[164] Gregory Prigozhin, Keith Gendreau, John P. Doty, et al. NICER instrument detector subsystem: description and performance. In Jan-Willem A. den Herder, Tadayuki Takahashi, and Marshall Bautz, editors, *Space Telescopes and Instrumentation 2016: Ultraviolet to Gamma Ray*, volume 9905 of *Society of Photo-Optical Instrumentation Engineers (SPIE) Conference Series*, page 99051I, July 2016.

[165] Chandra an x-ray data primer. `https://cxc.cfa.harvard.edu/cdo/xray_primer.pdf`. Accessed: 2023-12-05.

[166] Keith A. Arnaud, Randall K. Smith, and Aneta Siemiginowska. *Handbook of X-ray Astronomy*. Cambridge Observing Handbooks for Research Astronomers. Cambridge University Press, 2011.

[167] P. Predehl, R. Andritschke, V. Arefiev, et al. The eROSITA X-ray telescope on SRG. *A&A*, 647:A1, March 2021.

[168] P. Morrison. On gamma-ray astronomy. *Il Nuovo Cimento*, 7(6):858–865, March 1958.

[169] NASA'S HEASARC Observatories explorer 11. `https://heasarc.gsfc.nasa.gov/docs/heasarc/missions/explorer11.html`. Accessed: 2023-07-18.

[170] NASA compton gamma-ray observatory. `https://science.nasa.gov/mission/cgro`. Accessed: 2024-01-09.

[171] ESA Operational and Post-operational Missions integral. `https://www.cosmos.esa.int/web/integral/science`. Accessed: 2023-08-10.

[172] NASA'S HEASARC Observatories agile. `https://heasarc.gsfc.nasa.gov/docs/heasarc/missions/agile.html`. Accessed: 2023-08-10.

[173] NASA fermi gamma-ray space telescope. `https://fermi.gsfc.nasa.gov/`. Accessed: 2023-10-25.

[174] P. O'Brien, E. Bozzo, R. Willingale, et al. The Soft X-ray Imager (SXI) on-board the THESEUS mission. *Mem. Soc. Astron. Italiana*, 89:130, January 2018.

[175] Claudio Labanti, Lorenzo Amati, Filippo Frontera, et al. The X/Gamma-ray Imaging Spectrometer (XGIS) on-board THESEUS: design, main characteristics, and concept of operation. *arXiv e-prints*, page arXiv:2102.08701, February 2021.

[176] Diego Götz, Stéphane Basa, Frédéric Pinsard, et al. The Infra-Red Telescope (IRT) on board the THESEUS mission. *arXiv e-prints*, page arXiv:2102.08696, February 2021.

[177] L. Amati, P. O'Brien, D. Götz, et al. The THESEUS space mission concept: science case, design and expected performances. *Advances in Space Research*, 62(1):191–244, July 2018.

[178] S. N. Zhang, M. Feroci, A. Santangelo, et al. eXTP: Enhanced X-ray Timing and Polarization mission. In Jan-Willem A. den Herder, Tadayuki Takahashi, and Marshall Bautz, editors, *Space Telescopes and Instrumentation 2016: Ultraviolet to Gamma Ray*, volume 9905 of *Society of Photo-Optical Instrumentation Engineers (SPIE) Conference Series*, page 99051Q, July 2016.

[179] Jean J. M. in't Zand, Enrico Bozzo, JinLu Qu, et al. Observatory science with eXTP. *Science China Physics, Mechanics, and Astronomy*, 62(2):29506, February 2019.

[180] ShuangNan Zhang, Andrea Santangelo, Marco Feroci, et al. The enhanced X-ray Timing and Polarimetry mission—eXTP. *Science China Physics, Mechanics, and Astronomy*, 62(2):29502, February 2019.

[181] W. B. Atwood, A. A. Abdo, M. Ackermann, et al. The Large Area Telescope on the Fermi Gamma-Ray Space Telescope Mission. *ApJ*, 697(2):1071–1102, June 2009.

[182] M. Ackermann, M. Ajello, A. Albert, et al. The Fermi Large Area Telescope on Orbit: Event Classification, Instrument Response Functions, and Calibration. *ApJS*, 203(1):4, November 2012.

[183] M. Ajello, W. B. Atwood, M. Axelsson, et al. Fermi Large Area Telescope Performance after 10 Years of Operation. *ApJS*, 256(1):12, September 2021.

[184] W. B. Atwood, A. A. Abdo, M. Ackermann, et al. The large area telescope on the fermi gamma-ray space telescope mission. *The Astrophysical Journal*, 697(2):1071, may 2009.

[185] The fermi-lat instrument. `https://www-glast.stanford.edu/instrument.html`. Accessed: 2023-12-13.

[186] W. Atwood, A. Albert, L. Baldini, et al. Pass 8: Toward the Full Realization of the Fermi-LAT Scientific Potential. *arXiv e-prints*, page arXiv:1303.3514, March 2013.

[187] M. Aguilar, L. Ali Cavasonza, G. Ambrosi, et al. The alpha magnetic spectrometer (ams) on the international space station: Part ii — results from the first seven years. *Physics Reports*, 894:1–116, 2021. The Alpha Magnetic Spectrometer (AMS) on the International Space Station: Part II - Results from the First Seven Years.

[188] Stanford fermi-lat performance for pass8 (v. p8r3_v3). `https://www.slac.stanford.edu/exp/glast/groups/canda/lat_Performance.htm`. Accessed: 2024-02-28.

[189] S. Abdollahi, F. Acero, M. Ackermann, et al. Fermi large area telescope fourth source catalog. *The Astrophysical Journal Supplement Series*, 247(1):33, mar 2020.

[190] J. Ballet, P. Bruel, T. H. Burnett, et al. Fermi Large Area Telescope Fourth Source Catalog Data Release 4 (4FGL-DR4). *arXiv e-prints*, page arXiv:2307.12546, July 2023.

[191] CERN timeline: Victor hess discovers cosmic rays. https://timeline.web.cern.ch/victor-hess-discovers-cosmic-rays-0. Accessed: 2024-01-09.

[192] Kenneth Greisen. End to the cosmic-ray spectrum? *Phys. Rev. Lett.*, 16:748–750, Apr 1966.

[193] G. T. Zatsepin and V. A. Kuz'min. Upper Limit of the Spectrum of Cosmic Rays. *Soviet Journal of Experimental and Theoretical Physics Letters*, 4:78, August 1966.

[194] Carmelo Evoli. The cosmic-ray energy spectrum, May 2023.

[195] NASA. U.S. standard atmosphere. *Legacy CDMS*, October 1976.

[196] H. Bethe and W. Heitler. On the Stopping of Fast Particles and on the Creation of Positive Electrons. *Proceedings of the Royal Society of London Series A*, 146(856):83–112, August 1934.

[197] Ralph Engel, Dieter Heck, and Tanguy Pierog. Extensive Air Showers and Hadronic Interactions at High Energy. *Annual Review of Nuclear and Particle Science*, 61(1):467–489, November 2011.

[198] W. Heitler. *Quantum theory of radiation*. Clarendon Press, Oxford, 1954.

[199] David Berge. *A detailed study of the gamma-ray supernova remnant RX J1713.7-3946 with H.E.S.S.* Theses, Ruperto-Carola University of Heidelberg, February 2006.

[200] J. Matthews. A heitler model of extensive air showers. *Astroparticle Physics*, 22(5):387–397, 2005.

[201] Marco Barrantes, Jose Valdes, O Musalem, et al. Atmospheric corrections of the cosmic ray fluxes detected by the solar neutron telescope at the summit of the sierra negra volcano in mexico. *Geofísica Internacional*, 57:253–275, 10 2018.

[202] F. Aharonian, J. Buckley, T. Kifune, and G. Sinnis. High energy astrophysics with ground-based gamma ray detectors. *REPORTS ON PROGRESS IN PHYSICS Rep. Prog. Phys*, 71:96901–56, 09 2008.

[203] PA Cherenkov. Visible luminescence of pure liquids under the influence of γ-radiation. In *Dokl. Akad. Nauk SSSR*, volume 2, pages 451–454, 1934.

[204] I. M. Frank and Igor Y. Tamm. Coherent visible radiation of fast electrons passing through matter. *Physics-Uspekhi*, 93:388–393, 1937.

[205] Armelle Jardin-Blicq. *The TeV γ-ray emission of the Galactic Plane. HAWC and H.E.S.S. observations of the Galactic Plane and detailed study of the region surrounding 2HWC J1928+177*. Theses, Ruperto-Carola University of Heidelberg, June 2019.

[206] Christian Spiering. Cherenkov detectors in astroparticle physics. *Nuclear Instruments and Methods in Physics Research A*, 1056:168573, November 2023.

[207] T. C. Weekes, M. F. Cawley, D. J. Fegan, et al. Observation of TeV Gamma Rays from the Crab Nebula Using the Atmospheric Cerenkov Imaging Technique. *ApJ*, 342:379, July 1989.

[208] F. Aharonian, A. G. Akhperjanian, A. R. Bazer-Bachi, et al. The H.E.S.S. Survey of the Inner Galaxy in Very High Energy Gamma Rays. *ApJ*, 636(2):777–797, January 2006.

[209] John M. Davies and Eugene S. Cotton. Design of the quartermaster solar furnace. *Solar Energy*, 1(2):16–22, 1957.

[210] S. Funk, G. Hermann, J. Hinton, et al. The trigger system of the H.E.S.S. telescope array. *Astroparticle Physics*, 22(3-4):285–296, November 2004.

[211] H. E. S. S. Collaboration, H. Abdalla, R. Adam, et al. H.E.S.S. and Fermi-LAT observations of PSR B1259-63/LS 2883 during its 2014 and 2017 periastron passages. *A&A*, 633:A102, January 2020.

[212] Cosimo Nigro, Tarek Hassan, and Laura Olivera-Nieto. Evolution of data formats in very-high-energy gamma-ray astronomy. *Universe*, 7(10), 2021.

[213] F. Aharonian, A.G. Akhperjanian, K.-M. Aye, et al. Calibration of cameras of the h.e.s.s. detector. *Astroparticle Physics*, 22(2):109–125, 2004.

[214] B. Bi, M. Barcelo, C. Bauer, et al. Performance of the new FlashCam-based camera in the 28m telescope of H.E.S.S. In *37th International Cosmic Ray Conference*, page 743, March 2022.

[215] Alison Mitchell, Vincent Marandon, and Robert Daniel Parsons. A Generic Algorithm for IACT Optical Efficiency Calibration using Muons . *PoS*, ICRC2015:756, 2016.

[216] A. M. Hillas. Cerenkov Light Images of EAS Produced by Primary Gamma Rays and by Nuclei. In *19th International Cosmic Ray Conference (ICRC19), Volume 3*, volume 3 of *International Cosmic Ray Conference*, page 445, August 1985.

[217] F. Aharonian, A. G. Akhperjanian, A. R. Bazer-Bachi, et al. Observations of the Crab nebula with HESS. *A&A*, 457(3):899–915, October 2006.

[218] R.D. Parsons and J.A. Hinton. A monte carlo template based analysis for air-cherenkov arrays. *Astroparticle Physics*, 56:26–34, 2014.

[219] Marianne Lemoine-Goumard, B. Degrange, and Martin Tluczykont. Selection and 3d-reconstruction of gamma-ray-induced air showers with a stereoscopic system of atmospheric cherenkov telescopes. *Astroparticle Physics*, 25:195–211, 2006.

[220] Mikaël Jacquemont, Thomas Vuillaume, Alexandre Benoît, et al. Gammalearn: A deep learning framework for iact data. *Proceedings of 36th International Cosmic Ray Conference — PoS(ICRC2019)*, 2019.

[221] F. A. Aharonian, A. G. Akhperjanian, J. A. Barrio, et al. The energy spectrum of tev gamma rays from the crab nebula as measured by the hegra system of imaging air cerenkov telescopes. *The Astrophysical Journal*, 539(1):317, aug 2000.

[222] H. J. Völk and Konrad Bernlöhr. Imaging very high energy gamma-ray telescopes. *Experimental Astronomy*, 25:173–191, 2008.

[223] S. Ohm, C. van Eldik, and K. Egberts. gamma/hadron separation in very-high-energy gamma-ray astronomy using a multivariate analysis method. *Astroparticle Physics*, 31(5):383–391, 2009.

[224] Christoph Deil, Catherine Boisson, Karl Kosack, et al. Open high-level data formats and software for gamma-ray astronomy. In *6th International Symposium on High Energy Gamma-Ray Astronomy*, volume 1792 of *American Institute of Physics Conference Series*, page 070006, January 2017.

[225] T. P. Li and Y. Q. Ma. Analysis methods for results in gamma-ray astronomy. *ApJ*, 272:317–324, September 1983.

[226] D. Berge, S. Funk, and J. Hinton. Background modelling in very-high-energy γ-ray astronomy. *A&A*, 466(3):1219–1229, May 2007.

[227] H. E. S. S. Collaboration, H. Abdalla, A. Abramowski, et al. The H.E.S.S. Galactic plane survey. *A&A*, 612:A1, April 2018.

[228] J. R. Mattox, D. L. Bertsch, J. Chiang, et al. The Likelihood Analysis of EGRET Data. *ApJ*, 461:396, April 1996.

[229] Alexander Etz. Introduction to the concept of likelihood and its applications. *Advances in Methods and Practices in Psychological Science*, 1, 10 2017.

[230] A. Avakyan, M. Neumann, A. Zainab, et al. XRBcats: Galactic low-mass X-ray binary catalogue. *A&A*, 675:A199, July 2023.

[231] M. Neumann, A. Avakyan, V. Doroshenko, and A. Santangelo. XRBcats: Galactic High Mass X-ray Binary Catalogue. *A&A*, 677:A134, September 2023.

[232] Malcolm S. Longair. *High Energy Astrophysics*. Cambridge University Press, 2011.

[233] H. Schatz and K.E. Rehm. X-ray binaries. *Nuclear Physics A*, 777:601–622, 2006. Special Isseu on Nuclear Astrophysics.

[234] I. F. Mirabel and L. F. Rodríguez. Sources of relativistic jets in the galaxy. *Annual Review of Astronomy and Astrophysics*, 37(1):409–443, 1999.

[235] A. Abramowski, F. Acero, F. Aharonian, et al. HESS observations of the carina nebula and its enigmatic colliding wind binary eta carinae. *Monthly Notices of the Royal Astronomical Society*, 424(1):128–135, jun 2012.

[236] H. E. S. S. Collaboration, H. Abdalla, R. Adam, et al. Detection of very-high-energy γ-ray emission from the colliding wind binary η Car with H.E.S.S. *A&A*, 635:A167, March 2020.

[237] Marco Tavani and Jonathan Arons. Theory of high-energy emission from the pulsar/be star system psr 1259–63. i. radiation mechanisms and interaction geometry. *The Astrophysical Journal*, 477:439 – 464, 1996.

[238] S. Johnston, R. N. Manchester, A. G. Lyne, et al. PSR 1259-63 - A binary radio pulsar with a Be star companion. *ApJ*, 387:L37–L41, March 1992.

[239] A. A. Abdo, M. Ackermann, M. Ajello, et al. Detection of 16 Gamma-Ray Pulsars Through Blind Frequency Searches Using the Fermi LAT. *Science*, 325(5942):840, August 2009.

[240] Shan-Shan Weng, Lei Qian, Bo-Jun Wang, et al. Radio pulsations from a neutron star within the gamma-ray binary LS I +61° 303. *Nature Astronomy*, 6:698–702, March 2022.

[241] I. F. Mirabel. Very energetic gamma-rays from microquasars and binary pulsars. *Science*, 312(5781):1759–1760, 2006.

[242] Henny J. G. L. M. Lamers, Franz-Josef Zickgraf, Dolf de Winter, et al. An improved classification of B[e]-type stars. *A&A*, 340:117–128, December 1998.

[243] Duncan Ross Lorimer and Michael Kramer. *Handbook of pulsar astronomy*, volume 4. Cambridge university press, 2005.

[244] A. M. W. Mitchell and J. Gelfand. Pulsar Wind Nebulae. In *Handbook of X-ray and Gamma-ray Astrophysics*, page 61. Springer, 2022.

[245] Thomas K. Gaisser, Ralph Engel, and Elisa Resconi. *Cosmic Rays and Particle Physics*. Cambridge University Press, 2 edition, 2016.

[246] ENRICO Fermi. On the origin of the cosmic radiation. *Phys. Rev.*, 75:1169–1174, Apr 1949.

[247] Andrew Guthrie and R. K. Wakerling. The Characteristics of Electrical Discharges in Magnetic Fields. *Journal of the American Medical Association*, 144(2):209–209, 09 1949.

[248] Yu Wun Wong. *Diffuse γ-Ray Emission from the Galactic Centre with H.E.S.S.* PhD thesis, Erlangen - Nuremberg U., 2023.

[249] Stefan Funk. Ground- and Space-Based Gamma-Ray Astronomy. *Annual Review of Nuclear and Particle Science*, 65:245–277, October 2015.

[250] E. Feenberg and H. Primakoff. Interaction of Cosmic-Ray Primaries with Sunlight and Starlight. *Physical Review*, 73(5):449–469, March 1948.

[251] Arthur H. Compton. A quantum theory of the scattering of x-rays by light elements. *Phys. Rev.*, 21:483–502, May 1923.

[252] O. Klein and T. Nishina. Über die Streuung von Strahlung durch freie Elektronen nach der neuen relativistischen Quantendynamik von Dirac. *Zeitschrift fur Physik*, 52(11-12):853–868, November 1929.

[253] George R. Blumenthal and Robert J. Gould. Bremsstrahlung, Synchrotron Radiation, and Compton Scattering of High-Energy Electrons Traversing Dilute Gases. *Reviews of Modern Physics*, 42(2):237–271, January 1970.

[254] J.A. Hinton and W. Hofmann. Teraelectronvolt astronomy. *Annual Review of Astronomy and Astrophysics*, 47(1):523–565, sep 2009.

[255] F. Camilo, P. S. Ray, S. M. Ransom, et al. Radio detection of lat psrs j1741–2054 and j2032+4127: No longer just gamma-ray pulsars. *The Astrophysical Journal*, 705(1):1, oct 2009.

[256] A. G. Lyne, B. W. Stappers, M. J. Keith, et al. The binary nature of PSR J2032+4127. *Monthly Notices of the Royal Astronomical Society*, 451(1):581–587, 05 2015.

[257] M Chernyakova, D Malyshev, P Blay, et al. Multiwavelength observations of PSR J2032+4127 during the 2017 periastron passage. *Monthly Notices of the Royal Astronomical Society*, 495(1):365–374, 05 2020.

[258] Wynn C. G. Ho, C.-Y. Ng, Andrew G. Lyne, et al. Multiwavelength monitoring and X-ray brightening of Be X-ray binary PSR J2032+4127/MT91 213 on its approach to periastron. *Monthly Notices of the Royal Astronomical Society*, 464(1):1211–1219, 09 2016.

[259] K. L. Li, J. Takata, C. W. Ng, et al. The x-ray modulation of psr j2032+4127/mt91 213 during the periastron passage in 2017. *The Astrophysical Journal*, 857(2):123, apr 2018.

[260] A. U. Abeysekara, W. Benbow, R. Bird, et al. Periastron observations of tev gamma-ray emission from a binary system with a 50-year period. *The Astrophysical Journal Letters*, 867(1):L19, oct 2018.

[261] A. R. Taylor and P. C. Gregory. Periodic radio emission from LS I + 61 303. *ApJ*, 255:210–216, April 1982.

[262] J. Albert, E. Aliu, H. Anderhub, et al. Periodic Very High Energy γ-Ray Emission from LS I +61°303 Observed with the MAGIC Telescope. *ApJ*, 693(1):303–310, March 2009.

[263] J. B. Hutchings and D. Crampton. Spectroscopy of the unique degenerate binary star LS I +61 303. *PASP*, 93:486–489, August 1981.

[264] P. C. Gregory. Bayesian Periodic Signal Detection. I. Analysis of 20 Years of Radio Flux Measurements of the X-Ray Binary LS I +61°303. *ApJ*, 520(1):361–375, July 1999.

[265] P. C. Gregory. Bayesian Analysis of Radio Observations of the Be X-Ray Binary LS I +61°303. *ApJ*, 575(1):427–434, August 2002.

[266] J. M. Paredes, R. Estalella, and A. Rius. Observations at 3.6 CM wavelength of the radio light curve of LSI +61 303. *A&A*, 232:377, June 1990.

[267] J. Casares, I. Ribas, J. M. Paredes, et al. Orbital parameters of the microquasar LS I +61 303. *MNRAS*, 360(3):1105–1109, July 2005.

[268] Vadim Kravtsov, Andrei V. Berdyugin, Vilppu Piirola, et al. Orbital variability of the optical linear polarization of the γ-ray binary LS I +61° 303 and new constraints on the orbital parameters. *A&A*, 643:A170, November 2020.

[269] M. Massi. LS I +61°303 in the context of microquasars. *A&A*, 422:267–270, July 2004.

[270] J. M. Paredes, J. Marti, M. Peracaula, and M. Ribo. Evidence of X-ray periodicity in LSI+61 303. *A&A*, 320:L25–L28, April 1997.

[271] David Kieda et al. Very High Energy Gamma-ray Emission from the Binary System LS I +61 303. *PoS*, ICRC2021:832, 2021.

[272] M. Chernyakova, D. Malyshev, B. van Soelen, et al. The radio to GeV picture of PSR B1259-63 during the 2021 periastron passage. *MNRAS*, January 2024.

[273] Hiroki Yoneda, K Makishima, T Enoto, et al. Sign of hard-x-ray pulsation from the gamma-ray binary system ls 5039. *Physical review letters*, 125:111103, 09 2020.

[274] Iurii Sushch and Brian van Soelen. Gamma-Gamma Absorption in the γ-ray Binary System PSR B1259-63/LS 2883. *ApJ*, 837(2):175, March 2017.

[275] Ignacio Negueruela, Marc Ribó , Artemio Herrero, et al. ASTROPHYSICAL PARAMETERS OF LS 2883 AND IMPLICATIONS FOR THE PSR b1259-63 GAMMA-RAY BINARY. *The Astrophysical Journal*, 732(1):L11, apr 2011.

[276] M. Chernyakova, D. Malyshev, S. Mc Keague, et al. New insight into the origin of the GeV flare in the binary system PSR B1259-63/LS 2883 from the 2017 periastron passage. *MNRAS*, 497(1):648–655, July 2020.

[277] C. F. Kennel and F. V. Coroniti. Confinement of the Crab pulsar's wind by its supernova remnant. *ApJ*, 283:694–709, August 1984.

[278] Lewis Ball, Andrew Melatos, Simon Johnston, and Olaf Skjæraasen. Origin of the transient, unpulsed radio emission from the PSR b1259-63 binary system. *The Astrophysical Journal*, 514(1):L39–L42, mar 1999.

[279] George G. Pavlov, Chulhoon Chang, and Oleg Kargaltsev. Extended emission from the psr b1259-63/ss 2883 binary detected with chandra. *The Astrophysical Journal*, 730(1):2, feb 2011.

[280] George G. Pavlov, Jeremy Hare, Oleg Kargaltsev, et al. An extended x-ray object ejected from the psr b1259–63/ls2883 binary. *The Astrophysical Journal*, 806(2):192, jun 2015.

[281] George Pavlov, Jeremy Hare, and Oleg Kargaltsev. High-speed ejecta from the gamma-ray binary psr b1259–63/ls 2883. *Rendiconti Lincei. Scienze Fisiche e Naturali*, 30, 02 2019.

[282] Gaia Collaboration, A. G. A. Brown, A. Vallenari, et al. Gaia Data Release 2. Summary of the contents and survey properties. *A&A*, 616:A1, August 2018.

[283] S. Johnston, R. N. Manchester, A. G. Lyne, et al. Radio and Optical Observations of the PSR:B1259-63 / SS:2883 Be-Star Binary System. *MNRAS*, 268:430, May 1994.

[284] R. M. Shannon, S. Johnston, and R. N. Manchester. The kinematics and orbital dynamics of the PSR B1259-63/LS 2883 system from 23 yr of pulsar timing. *MNRAS*, 437(4):3255–3264, February 2014.

[285] M. Chernyakova, A. Neronov, B. van Soelen, et al. Multi-wavelength observations of the binary system PSR B1259-63/LS 2883 around the 2014 periastron passage. *Monthly Notices of the Royal Astronomical Society*, 454(2):1358–1370, 10 2015.

[286] J C A Miller-Jones, A T Deller, R M Shannon, et al. The geometric distance and binary orbit of PSR B1259–63. *Monthly Notices of the Royal Astronomical Society*, 479(4):4849–4860, 07 2018.

[287] Maria Chernyakova, Denys Malyshev, Brian van Soelen, et al. Multi-Wavelength Properties of the 2021 Periastron Passage of PSR B1259-63. *Universe*, 7(7):242, July 2021.

[288] D. Khangulyan, S. Hnatic, F. Aharonian, and S. Bogovalov. TeV light curve of PSR b1259-63/SS2883. *Monthly Notices of the Royal Astronomical Society*, 380(1):320–330, aug 2007.

[289] N. Wang, S. Johnston, and R. N. Manchester. 13 years of timing of PSR B1259-63. *MNRAS*, 351:599–606, June 2004.

[290] Simon Johnston, R. N. Manchester, D. McConnell, and D. Campbell-Wilson. Transient radio emission from the PSR B1259-63 system near periastron. *MNRAS*, 302(2):277–287, January 1999.

[291] Lynn Cominsky, Mallory Roberts, and Simon Johnston. Detection of X-Ray Emission from the PSR 1259-63/SS 2883 Binary System. *ApJ*, 427:978, June 1994.

[292] M. Chernyakova, A. Neronov, F. Aharonian, et al. X-ray observations of PSR B1259-63 near the 2007 periastron passage. *Monthly Notices of the Royal Astronomical Society*, 397(4):2123–2132, 08 2009.

[293] A. A. Abdo, M. Ackermann, M. Ajello, et al. Discovery of High-energy Gamma-ray Emission from the Binary System PSR B1259-63/LS 2883 around Periastron with Fermi. *ApJ*, 736:L11, July 2011.

[294] A. A. Abdo, M. Ackermann, M. Ajello, et al. Discovery of High-energy Gamma-ray Emission from the Binary System PSR B1259-63/LS 2883 around Periastron with Fermi. *ApJ*, 736:L11, July 2011.

[295] G. A. Caliandro, C. C. Cheung, J. Li, et al. Gamma-Ray Flare Activity from PSR B1259-63 during 2014 Periastron Passage and Comparison to Its 2010 Passage. *ApJ*, 811(1):68, September 2015.

[296] Kent S. Wood, Tyrel Johnson, Paul S. Ray, et al. The 2017 Periastron Passage of PSR B1259-63 in Gamma-rays and X-rays. In *American Astronomical Society Meeting Abstracts #231*, volume 231 of *American Astronomical Society Meeting Abstracts*, page 233.04, January 2018.

[297] Zhi Chang, Shu Zhang, Yu-Peng Chen, et al. Fermi-LAT Observation of PSR B1259-63 during Its 2021 Periastron Passage. *Universe*, 7(12):472, December 2021.

[298] F. Aharonian, A. G. Akhperjanian, K.-M. Aye, et al. Discovery of the binary pulsar PSR B1259-63 in very-high-energy gamma rays around periastron with HESS. *A&A*, 442:1–10, October 2005.

[299] H.E.S.S. Collaboration, H. Abdalla, R. Adam, et al. H.E.S.S. and Fermi-LAT observations of PSR B1259-63/LS 2883 during its 2014 and 2017 periastron passages. *A&A*, 633:A102, January 2020.

[300] F. Aharonian, A. G. Akhperjanian, G. Anton, et al. Very high energy γ-ray observations of the binary PSR B1259-63/SS2883 around the 2007 Periastron. *A&A*, 507(1):389–396, November 2009.

[301] H. E. S. S. Collaboration, A. Abramowski, F. Acero, et al. H.E.S.S. observations of the binary system PSR B1259-63/LS 2883 around the 2010/2011 periastron passage. *A&A*, 551:A94, March 2013.

[302] Andrii Neronov and Maria Chernyakova. Radio-to-TeV γ-ray emission from PSR B1259 63. *Ap&SS*, 309(1-4):253–259, June 2007.

[303] F. Aharonian, A. G. Akhperjanian, A. R. Bazer-Bachi, et al. The H.E.S.S. Survey of the Inner Galaxy in Very High Energy Gamma Rays. *ApJ*, 636(2):777–797, January 2006.

List of Figures

List of Tables

List of Acronyms

ΛCDM Λ Cold Dark Matter. 13, 14, 15, 44

νMSM Sterile neutrino (ν) Minimal extension to the Standard Model. 21, 36, 49, 91, 202

ADC Analogue Digital Converter. 129

AGILE Astro-Rivelatore Gamma a Immagini Leggero. 65

AGN Active Galactic Nuclei. 42, 56, 68, 70, 146

ALP Axion-like Particle. 23, 91, 202

AMS Alpha Magnetic Spectrometer. 73

ARF Ancillary Response File. 60, 61

ATCA Australian Telescope Compact Array. 172

BDT Boosted Decision Tree. 133

C Charge-conjugation symmetry. 23

c.i. confidence interval. 15

CCD Charge-coupled Device. 56

CDM Cold Dark Matter. 13, 18, 24, 41

CGRO Compton Gamma Ray Observatory. 64, 65

CMB Cosmic Microwave Background. 8, 11, 12, 13, 15, 16, 21, 115

CR Cosmic Rays. 114, 115, 117

CTA Cherenkov Telescope Array. 125

CWB Colliding Wind Binary. 146

CXO Chandra X-ray Observatory. 58

DAQ Data Acquisition System. 128, 129

DL Data Level. 73, 128

DM Dark Matter. 7, 8, 9, 11, 15, 16, 17, 18, 19, 20, 21, 22, 23, 25, 27, 28, 29, 30, 31, 32, 34, 35, 36, 37, 38, 39, 40, 41, 44, 45, 46, 48, 49, 50, 51, 52, 77, 79, 91, 201, 202

DSph Dwarf Spheroidal. 43, 46, 50, 91, 201, 202

EAS Extensive Air Shower. 117, 118, 119, 120, 121, 123, 124, 125, 130, 131, 132, 134, 142, 236

EM Electromagnetic. 28, 66, 70, 71, 114, 117, 120, 121, 122, 123, 132, 158, 171, 183

EO Einstein Observatory. 56

ER Electron Recoil. 32

ESA European Space Agency. 66, 67

eXTP Enhanced X-ray Timing and Polarimetry. 68, 77, 91, 201, 202

FACT First G-APD Cherenkov Telescope. 125

FAST Five-hundred-meter Aperture Spherical radio Telescope. 166

FoV Field of View. 37, 48, 56, 66, 67, 68, 69, 70, 72, 126, 127, 138, 202

FWHM Full Width at Half Maximum. 68

GBM Fermi Gamma-ray Burst Monitor. 70

GLAST Gamma-ray Large Area Space Telescope. 69

GRB Gamma-ray Burst. 63, 65, 66, 67, 68, 70

GREB Gamma-ray Emitting Binary. iii, iv, vi, 146, 202

H.E.S.S. High Energy Stereoscopic System. 125, 126, 127, 128, 129, 130, 132, 136, 139, 142, 143, 178, 179, 180, 183, 202, 203

HAP H.E.S.S. Analysis Program. 139, 140

HE High-energy. 55, 116, 139, 145, 146, 147, 169

HEGRA High-energy Gamma Ray Astronomy. 125

HG High Gain. 129

HMXBs High-mass X-ray Binaries. 145

IACT Imaging Atmospheric Cherenkov Telescope. 117, 120, 121, 123, 124, 125, 126, 131, 135, 136, 137, 138, 139, 142, 158, 178, 202

IC Inverse Compton. 160, 161, 162, 163, 165, 169, 173, 175, 177, 178

ICM Intra-cluster Medium. 44, 45

ImPACT Image Pixel-wise fit for Atmospheric Cherenkov Telescopes. 131

INTEGRAL INTErnational Gamma-Ray Astrophysics Laboratory. 65

IRF Instrument Response Function. 60, 73, 74, 75, 76, 77, 128, 133, 141

IRT Infra-red Telescope. 67

ISM Interstellar Medium. 66, 161

LAD Large Area Detector. 68

LAT Fermi Large Area Telescope. 46, 70, 71, 72, 74, 77, 79, 176

LED Light Emitting Diode. 129

LG Low Gain. 129

LHC Large Hadron Collider. 35

LMXBs Low-mass X-ray Binaries. 145

LSP Lightest Supersymmetric Particle. 19, 20

MACHO Massive Compact Halo Object. 16

MAGIC Major Atmospheric Gamma Imaging Cherenkov Telescopes. 125, 165

MOND Modified Newtonian Dynamics. 9, 11, 29

NICER Neutron Star Interior Composition Explorer Mission. 59

NR Nuclear Recoil. 32

NSB Night Sky Background. 130

NuSTAR Nuclear Spectroscopic Telescope Array. 58

P Parity symmetry. 23

PFA Polarimetry Focusing Array. 69

PHA Pulse Height Amplitude. 59

PI Pulse Invariant. 59

PMT Photomultiplier Tube. 32, 124, 126, 129

PQ Peccei-Quinn. 23, 24, 26

PSF Point Spread Function. 134

QCD Quantum Chromodynamics. 23

QED Quantum Electrodynamics. 162

RMF Redistribution Matrix File. 59, 61

ROI Region Of Interest. 75, 135, 136, 137

RSP Response. 61

SAS-2 Small Astronomy Satellite - 2. 63

SDD Silicon Drift Detector. 67, 68

SED Spectral Energy Density. 39, 157, 160, 162, 163, 168

SFA Spectroscopic Focusing Array. 68

SM Standard Model. 7, 14, 15, 18, 19, 20, 21, 22, 23, 24, 28, 29, 30, 31, 34, 35, 36, 37, 38, 48, 49, 50, 79

SUSY Supersymmetric extension to the Standard Model. 18, 19, 20

SXI Soft X-ray Imager. 66

TD Topological Defects. 25

THESEUS Transient High Energy Sky and Early Universe Surveyor. 66, 67, 77, 91, 201, 202

TS Test Statistic. 138

VERITAS Very Energetic Radiation Imaging Telescope Array System. 125, 165, 168

VHE Very-high-energy. iv, 71, 113, 116, 117, 123, 135, 138, 139, 141, 142, 145, 146, 147, 158, 162, 163, 165, 166, 168, 169, 178, 179, 180, 183, 201, 202, 203, 241

WFM Wide Field Monitor. 68

WIMP Weakly Interacting Massive Particle. 18, 19, 20, 23, 29, 31, 32, 33, 37, 39, 49, 51, 53, 79, 201

XGIS X and Gamma-ray Imager and Spectrometer. 66, 67

XRBs X-ray Binaries. 56, 145

Declaration

I hereby declare that the thesis I submit for my doctorate with the title: "Astrophysical Frontiers: The Indirect Detection of Dark Matter & the Analysis of Gamma-ray Binary Systems" is my own independent work, that I used only the sources and resources cited and have clearly indicated all content adopted either word-for-word or in substance. I declare that the University of Tübingen's guidelines to ensure good academic practice (Senate decision of 25.5.2000) have been observed. I solemnly swear that this information is true and that I have not concealed any relevant information. I am aware that making a false declaration is punishable by a fine or by a prison term of up to three years.

Moreover, I declare that only the parts of this thesis that are clearly indicated (and accompanied by the relevant documents and approvals) have been published previously and that no part of this thesis has been submitted in part or its entirety as a doctoral thesis or any other piece of assessed work at this or any other institution. I also confirm that, at the time of submission, I have not been accepted at any other university as a doctoral candidate. I furthermore declare that there are no prior abandoned/completed doctoral qualification processes or relevant examination processes that I have partaken in.

Finally, I declare, that I did not take part in any commercially arranged agreements with regard to my Ph.D. project. I especially did not contact any organizations, which engage in the active search for supervisors for Ph.D. theses and receive money for their services. I furthermore state that I did not use such organizations, which adopt the applicant's obligations and take care of the academic requirements partially or entirely. Furthermore, I state that I am aware of the legal consequences of using a commercial thesis-writing agency (disqualification as a doctoral student, elimination of acceptance to the doctoral qualification process, termination of the Ph.D. examination procedure, and annulment of the degree in accordance).

Tübingen, 21st October, 2024

Charles Thorpe-Morgan